

中国科学技术大学

博士学位论文



ATLAS 实验上 $VH(H \rightarrow WW^*)$ 过程的截面测量及抗辐照 LGAD 的研制

作者姓名： 杨霄

学科专业： 粒子物理与原子核物理

导师姓名： 刘衍文教授

完成时间： 二〇二三年八月二日



University of Science and Technology of China
A dissertation for doctor's degree



**Measurement of $VH(H \rightarrow WW^*)$
process in ATLAS and development
of radiation hard LGAD**

Author: Xiao Yang

Speciality: Particle Physics and Nuclear Physics

Supervisor: Prof. Yanwen Liu

Finished time: August 2, 2023

中国科学技术大学学位论文原创性声明

本人声明所呈交的学位论文，是本人在导师指导下进行研究工作所取得的成果。除已特别加以标注和致谢的地方外，论文中不包含任何他人已经发表或撰写过的研究成果。与我一同工作的同志对本研究所做的贡献均已在论文中作了明确的说明。

作者签名：_____

签字日期：_____

中国科学技术大学学位论文授权使用声明

作为申请学位的条件之一，学位论文著作权拥有者授权中国科学技术大学拥有学位论文的部分使用权，即：学校有权按有关规定向国家有关部门或机构送交论文的复印件和电子版，允许论文被查阅和借阅，可以将学位论文编入《中国学位论文全文数据库》等有关数据库进行检索，可以采用影印、缩印或扫描等复制手段保存、汇编学位论文。本人提交的电子文档的内容和纸质论文的内容相一致。

控阅的学位论文在解密后也遵守此规定。

☒ 公开 ☐ 控阅（____年）

作者签名：_____

导师签名：_____

签字日期：_____

签字日期：_____

摘 要

本博士学位论文研究了粒子物理中两个关键课题，探讨了自然界未解的基本问题和下一代对撞机实验的技术挑战。论文研究内容集中在 ATLAS 实验中希格斯玻色子 (H) 与矢量玻色子 (V) 协同产生并且希格斯玻色子衰变到 W 玻色子对过程的截面测量，以及抗辐照的低增益雪崩探测器在高粒度计时探测器升级中的研制，范围包括从概念设计、工艺与器件仿真、探测器的制造加工、以及表征测试。

本论文首先对粒子物理的标准模型理论框架进行了总结，介绍了希格斯玻色子的性质，包括希格斯机制、产生和衰变模式，以及目前在 LHC 上的观测结果。论文还对大型强子对撞机 (LHC)、ATLAS 实验及其探测系统进行了概述，讨论了高亮度 LHC 升级计划以及 ATLAS 第二阶段升级计划中的高粒度计时探测器项目。

在物理分析部分，本论文探讨了使用 ATLAS 探测器在 2015-2018 期间获取的 139 fb^{-1} 数据测量希格斯玻色子与矢量玻色子协同产生并且衰变到 W 玻色子对过程的截面。这部分内容包括物理背景、分析中使用的数据和蒙特卡洛样本概述、本底估计、系统误差、统计分析方法和结果。论文通过多参数拟合降低了本底贡献的不确定度，使得测量精度比之前大幅提高。经过多参数统计拟合分析，论文得到的 WH 信号、ZH 信号以及它们的联合 VH 信号的观测 (预期) 统计显著性分别是 1.5 (3.3)、4.6 (3.1) 和 4.6 (4.7) 倍的标准偏差，对应截面 WH: $0.13^{+0.08}_{-0.07}$ (统计误差) $^{+0.05}_{-0.04}$ (系统误差) pb、ZH: $0.31^{+0.09}_{-0.08}$ (统计误差) ± 0.03 (系统误差) pb 和 VH: 0.44 ± 0.10 (统计误差) $^{+0.06}_{-0.05}$ (系统误差) pb。论文中测量结果与标准模型理论的预言一致。

在探测器研发部分，本论文介绍了硅探测器及其在粒子物理实验中的应用。本论文重点介绍了一种用于 ATLAS 实验高粒度计时探测器 (HGTD) 升级的新型硅探测器技术——低增益雪崩探测器 (LGAD)，并综述了 LGAD 技术的发展、计时性能、抗辐照性能、增益层退化、不同类型的 LGAD 设计以及潜在应用。

本论文还展示了科大和中科院微电子研究所 (微电子所) 在抗辐照 LGAD 加工工艺与批量生产方面的合作研究。针对高粒度计时探测器升级的要求，作者使用思科公司的 TCAD EDA 软件对 LGAD 结构进行了系统性的工艺仿真，建立了一套适用于微电子所的工艺参数并进行优化，结合电学仿真提供了较完备的结构设计。论文中所设计的器件在微电子所的 8 寸线上进行了加工流片。通过与微电子所合作，经过系统性的调试，作者开发了一套相对成熟的 LGAD 生产工艺。论文中制得的 LGAD 样品与 HGTD 组的其他样品进行了多种方法的性能表

征。使用的测试系统包括高压探针台，锶-90 β 射线测试系统，红外激光瞬态电流测试系统（TCT），以及位于德国汉堡的 DESY 以及欧洲核子研究中心（CERN）的 PS/SPS 带电粒子束流设施。通过以上研究，作者得到了器件击穿电压，漏电流，电荷收集效率，时间分辨等关键参数。最终结果显示，器件辐照前时间分辨优于 35 ps，电荷收集效率大于 10 fC。

通过对中子辐照前后器件的测试结果进行对比，作者标定了器件的抗辐照性能。此外作者进一步开发并优化了掺碳工艺，优化后的器件实现了领先的抗辐照性能。通过测量得到样品的受子移除系数为 $1.23 \times 10^{-16} \text{ cm}^2$ ，达到了世界领先水平。在 HGTD 要求的最高辐照剂量（ $2.5 \times 10^{15} \text{ cm}^{-2}$ 1 MeV 中子当量）之后，所设计探测器依然可以实现优于 50 ps 的时间分辨与 5 fC 的收集电荷。样品性能显著优于日本滨松的对应产品，完全满足 HGTD 合作组的指标要求。

作者还在科大微纳研究与制造中心成功开发了基于 6 寸硅片加工平台的 LGAD 加工制造工艺。通过充分利用中心微纳加工平台的条件与设备，作者经过多次摸索和调试，成功研制了交流耦合的 LGAD（AC-LGAD）器件，又称为阻性硅探测器（RSD）。测试结果显示，探测器样品时间分辨接近 30 ps，且通过电荷重心法重建的空间分辨测量优于 $5 \mu\text{m}$ ，符合设计预期。这方面的工作为未来进一步的新型半导体探测器研发奠定了基础。本论文系统地总结了作者在 LGAD 技术开发、制造、表征方面的工作，以及将 LGAD 应用于 ATLAS 实验高粒度计时探测器升级的研究。

关键词：希格斯粒子截面测量；抗辐照硅探测器；超快定时探测器；强子对撞实验；

ABSTRACT

This doctoral thesis investigates two key topics in particle physics, addressing the fundamental unsolved questions of nature and the technical challenges of next-generation collider experiments. The research focuses on the measurement of Higgs boson production in association with vector bosons and with the Higgs boson decaying into W boson pairs in the ATLAS experiment, as well as the development of the radiation-resistant Low-Gain Avalanche Detector (LGAD) for the high-granularity timing detector upgrade, covering conceptual design, simulation, fabrication, and characterization.

The thesis begins with a summary of the theoretical framework of particle physics, including the Standard Model and an overview of the Large Hadron Collider (LHC) and the ATLAS experiment. It also discusses the high-luminosity LHC upgrade and the High-Granularity Timing Detector (HGTD) for the second phase of the ATLAS upgrade. Following this, the thesis summarizes the properties of the Higgs boson, including the Higgs mechanism, production and decay modes, and observations at the LHC.

The study delves into the measurement of Higgs boson production in association with vector bosons, with the Higgs boson decaying into W boson pairs using 139 fb^{-1} data collected by the ATLAS detector from 2015 to 2018. This part includes physical motivation, data and Monte Carlo sample overview, background estimation, systematic uncertainties, statistical treatment, and results. By using a global fitting to constrain the backgrounds, the measurement precision has been significantly improved. The statistical significance for WH , ZH , and their combined VH signals are 1.5 (3.3), 4.6 (3.1), and 4.6 (4.7) standard deviations, respectively. The corresponding cross-sections for WH are $0.13^{+0.08}_{-0.07}$ (statistical error) $^{+0.05}_{-0.04}$ (systematic error) pb, ZH : $0.31^{+0.09}_{-0.08}$ (statistical error) ± 0.03 (systematic error) pb, and VH : 0.44 ± 0.10 (statistical error) $^{+0.06}_{-0.05}$ (systematic error) pb, which are consistent with the theoretical prediction from the Standard Model.

In addition, the thesis discusses silicon detectors and their applications in particle physics experiments. It investigates a new type of silicon detector technology, Low Gain Avalanche Diodes (LGAD), for the HGTD of the ATLAS upgrade. It discusses the development of LGAD technology, timing performance, radiation resistance, gain layer degradation, different types of LGAD designs, and potential applications.

The thesis showcases the collaborative research between USTC and the Institute of Microelectronics (IME) on the radiation-resistant LGAD fabrication process and production. To meet the requirements of the high-granularity timing detector upgrade, the author used Synopsys' TCAD EDA software for LGAD process simulation, established process parameters and optimized them, and provided a relatively optimized structural design in conjunction with guidelines from electric simulations. The designed devices were manufactured in collaboration with IME in an 8-inch wafer fabrication line, and a relatively mature LGAD production process was developed. The fabricated LGAD samples were characterized using various methods together with LGAD samples from other producers, including high-voltage probe testing, Strontium-90 beta radiation sources, infrared laser TCT, and particle beam testing at DESY in Hamburg, Germany, and CERN's PS/SPS facilities. Key parameters such as breakdown voltage, leakage current, charge collection efficiency, and timing resolution were obtained. The pre-irradiation timing resolution is better than 35 ps and collected charge is larger than 10 fC.

By comparing the test results before and after neutron irradiation, the radiation resistance of the devices was calibrated. The author further developed and optimized the carbon-doping process, resulting in devices with leading radiation resistance performance. The neutron removal cross-section reached $1.23 \times 10^{-16} \text{ cm}^2$, a world-leading level. After the highest irradiation dose required by HGTD, $2.5 \times 10^{15} \text{ cm}^{-2}$ of 1 MeV neutron equivalent fluences, the devices can still achieve a timing resolution better than 50 ps and a collected charge of 5 fC, significantly outperforming the corresponding products from Hamamatsu, Japan, and fully meeting the requirements of the HGTD project.

The author also developed an LGAD manufacturing process based on a 6-inch silicon wafer processing platform at the USTC center for micro- and nanoscale research and fabrication (NRFC). By fully utilizing the conditions and equipment of the micro-nano processing platform and going through multiple explorations, the author successfully developed AC-coupled LGAD (AC-LGAD), also called Resistive Silicon Detector (RSD). The resulting devices achieved a timing resolution close to 30 ps and a spatial resolution better than 5 μm measured using the center of gravity reconstruction method. These results agree with the expectations of the design. This work lays the foundation for the future development of new semiconductor detectors. The thesis systematically summarizes the author's work in LGAD technology development, manufacturing, characterization, and the application of LGADs for the HGTD of the ATLAS upgrade.

Key Words: Higgs cross-section measurement; Radiation-resistant silicon detectors;
Ultra-fast timing detector; LHC

Acknowledgements

First and foremost, I would like to express my profound appreciation to Prof. Yanwen Liu. Thanks for your guidance, support, and encouragement throughout my journey in the realm of particle physics. This thesis would not have been possible without your invaluable assistance. I am grateful for the opportunity to study such an intriguing topic under your tutelage. Since attending my first Classical Mechanics class taught by Prof. Liu, I have been captivated by your rigorous and optimistic approach, coupled with a keen sense of humor that enlivens the study of physics. Prof. Liu's ability to identify the crux of physical problems, whether in meetings or private conversations, has been truly inspiring. I am deeply thankful for your unwavering dedication to your student's growth and for providing resources, courage, and opportunities to develop my research skills. Your patience in addressing all my queries, regardless of their magnitude or nature, has been invaluable. I am grateful for your guidance during times of indecision and for rekindling my passion for physics.

I would like to extend my sincere gratitude to the Department of Modern Physics and the State Key Laboratory of Particle Detection and Electronics for providing a conducive environment, high-performance computing resources, and a dedicated server for TCAD EDA simulations. Without these resources, many aspects of my research would have been unattainable. I am also grateful to the graduate school for providing me with the opportunity for a one-year visit to CERN, where I learned new research methods and approaches. I appreciate the support of the laboratory, which enabled me to attend several workshops and conferences for academic communication, which was crucial for my research.

I would like to express my appreciation to the professors and engineers at IME, as well as the engineers at USTC NRFC, especially F.F. Peng, W. Liu, J. Sun, J.L. Peng, Y. Wei, H.T. Liu, L. Chen, L.J. Wang and S. Wu, for sharing your knowledge and experience in this new area. I am grateful for your dedication to the fabrication process, even when it required working late hours and handling non-standard requirements. I would also like to thank the engineers from SINANO, particularly R.K. Ji and X. Zhang, as well as Prof. Xu at the School of Microelectronics, for your assistance with device characterization and simulation.

My gratitude also extends to Prof. G. Kramberger from JSI, Prof. Hartmut F.-W. Sadrozinski from UCSC, Dr. S. Guindon, Dr. D. Dominik from CERN, and Prof. L. C. Garcia for your guidance in various aspects of my LGAD research and for providing me with the opportunity to work on the DAQ demonstrator. This experience greatly enhanced my understanding of the integration of detectors into the ATLAS system with the digital part. I would also like to thank R. Gugel, R. Ospanov, A. Farilla, C. Burgard, and B. Winter for your assistance with the HWW, VH analysis, and the statistical framework with CAF.

Moreover, I would like to express my gratitude to every member of the HGTD group at USTC, especially J.J. Ge, C.Li, T.Wang, and H.Chen without your help the work is not possible, also I want to thank X.X Zheng, K.Ma, H.Li, A.N. Wang, Y.K. Cai, Z. Li thanks for your valuable contributions to the simulations, tests, and discussions that are essential to this research. I would also like to thank Prof. Z.Zhao, Prof. Y.Wu, Prof. Y.Song, Prof. L.Xu and Prof. J.Liu. Your support and guidance are crucial and benefit all of us in many aspects.

Lastly, but most importantly, I would like to express my deepest gratitude to my parents, Mrs. Yang and Ms. Chang. Your material and emotional support have allowed me to focus on my studies and pursue my ambitions without any distractions. Although they may not fully comprehend the scope of my work, Your optimism and earnest attitude have been a constant source of inspiration. As my first teacher, Your influence has been the key factor in my ability to make progress in my work. I would like to thank my entire family for being my steadfast support system as I chase the beauty of science.

Acronyms and notations

A_{\max}	Maximum Amplitude of the waveform xviii, xxxii, 168–170
C_p	Pad Capacitance xviii, xxxvii, 166, 190
$\text{Noise}_{\text{RMS}}$	RMS of the initial part of the waveform xviii, 168
Pulse integral	Integral of the waveform around the peak xviii, 168
T_{\max}	Peak time of the waveform xviii, xxxii, 168–170
V_{BD}	Breakdown Voltage xviii, xxix, xxx, xxxii, xxxiii, xxxvi, 99, 108, 109, 119, 120, 128, 133, 150, 151, 159, 160, 163, 164, 166, 172–174, 176, 178, 191–193, 209
V_{BK}	Bulk Depletion Voltage xviii
V_{FD}	Full Depletion Voltage xviii, xxxvi, xxxvii, 119, 145, 160, 166, 171, 172, 176, 189, 190
V_{GL}	Gain Layer Depletion Voltage xviii, xxxii, xxxvi, 100, 119, 134, 160, 163, 166, 171–174, 176, 177, 188, 189
V_{OP}	Operation Voltage xviii, xxxvi, 160
n^+	Heavily n-type doped xviii, 109–111, 156
n^-	Lightly n-type doped xviii
AC-LGAD	AC-coupled Low Gain Avalanche Detetor xviii, xxiii, xxxi, xxxiii, xxxiv, 4, 105, 109, 144, 197, 203, 204, 206, 208–212, 216
ANN	Artificial Neural Network xviii, xxvi, xxvii, xxxv, 42–46, 49–53, 56, 57, 59
BDT	Boosted Decision Tree xviii, xxvii, 42, 60
BOE	Buffered Oxide Etch xviii, 145

Acronyms and notations

C-V	Capacitance-voltage xviii, xxii, xxx–xxxii, xxxvi, xxxvii, 86, 99, 100, 116, 119, 134, 149, 155, 163–166, 171–174, 176–178, 189–191, 194, 208
CFD	Constant Fraction Discrimination xviii
CKM	Cabibbo-Kobayashi-Maskawa xviii, 9, 10
CTD	Constant Threshold Discrimination xviii
DLTS	Deep Level Transient Spectroscopy xviii, 99, 100
DNN	Deep Neural Network xviii
DRIE	Deep Reactive-ion Etching xviii, 90, 104
DUT	Device under Test xviii, xxxiii, 168–170, 181, 182, 186, 187
EDA	Electronic Design Automation xviii
GR	Guard Ring xviii
HGTD	High-granularity Timing Detector xviii, xix, xxi, xxii, xxv, xxxiii, xxxv, 2, 3, 18–22, 99, 102, 107–110, 112, 114, 116, 118, 120, 122, 124, 126, 128–130, 132, 134, 136, 138, 140, 142, 144, 146, 148, 150–152, 154–156, 161, 178, 185, 188, 191, 197, 198
HV	High Voltage xviii
I-V	Current-voltage xviii, xxii, xxiii, xxx–xxxiii, xxxvi, 85, 99, 116, 119, 134, 149, 155, 162–166, 171–174, 176–179, 191–194, 208, 209
IME	Institute of Microelectronics , CAS xviii, xxxii, 4, 138, 177, 191
IP	Inter-pad xviii
IPA	Isopropyl Alcohol xviii, 205
LCR	Inductance, Capacitance, Resistance xviii, 166

LGAD	Low Gain Avalanche Detetor xviii
MIP	Minimum Ionizing Particle xviii
MVA	Multi-variable Analysis xviii, 42
NIEL	Non-ionizing Energy Loss xviii, xxv, xxviii, 21, 92
NMP	N-Methyl-2-pyrrolidone xviii, 205
NRFC	USTC Center for Micro- and Nanoscale Research and Fabrication xviii, xxiii, xxxiii, xxxiv, 161, 166, 203–205, 208–211
POI	Parameter of Interest xviii, xxvii, xxviii, xxxv, xxxvi, 53, 55, 57, 59, 60, 63, 70, 72, 74–76, 79
QA	Quality Assurance xviii
QC	Quality Control xviii
QC-TS	Quality Control Test Structures xviii
RNN	Recurrent Neural Network xviii, xxvi, xxxv, 46–48, 64, 79
RSD	Resistive Silicon Detector xviii, 203
SEB	Single Event Burnout xviii, 102, 103, 109, 150, 199
SINANO	Suzhou Institute of Nano-tech and Nano-bionics, CAS xviii
SMU	Source Measure Unit xviii, 161
TCAD	Technology Computer Aided Design xviii, xxi, xxix, xxx, 113, 115–117, 119, 121, 123, 125, 127, 129, 131, 133, 151, 197
TCT	Transient Current Technique xviii, xxxii, xxxiii, 99, 102, 149, 168, 208, 209
TDAQ	Trigger and Data Acquisition xviii, xxvi, 18, 38

Acronyms and notations

TLU	Trigger Logic Unit xviii, 182
TOA	Time of Arrival xviii, 168, 170, 183
TOF	Time of Flight xviii
TOT	Time over Threshold xviii
TSC	Thermally Stimulated Current xviii, xxix, 99, 100, 102
UFSD	Ultra Fast Silicon Detector xviii

Contents

Acronyms and notations	xv
1 Introduction	1
2 Standard Model, ATLAS experiment and HGTD	5
2.1 The Standard Model in particle physics	5
2.2 Electro-weak symmetry breaking	6
2.3 The Brout-Englert-Higgs mechanism	7
2.4 The Large Hadron Collider and the ATLAS experiment	10
2.5 The ATLAS detector	11
2.5.1 Inner detector	12
2.5.2 Calorimeter system	13
2.5.3 Muon spectrometer	14
2.6 The high luminosity upgrade of the LHC	16
2.7 The ATLAS phase 2 upgrade and the high-granularity timing detector	17
2.7.1 Preparing ATLAS for the future – The ATLAS phase 2 upgrade	17
2.7.2 The high-granularity timing detector (HGTD) in ATLAS phase 2	18
I Measurement of associate production of vector and Higgs bosons with the $H \rightarrow WW^*$ decay mode at ATLAS	23
3 Higgs Boson Production and Property Studies at the ATLAS Experiment	25
3.1 Higgs production at LHC	25
3.2 Higgs decay modes	27
3.3 Experimental observations	29
4 Measurement of the Vector Boson Associated Production with the $H \rightarrow WW^*$ Decay	35
4.1 Motivation	35
4.2 Overview of the analysis	35
4.3 Data and MC samples	37
4.4 Reconstruction of objects and events	40
4.5 Event selection	42
4.5.1 Definition of the channels	42
4.5.2 Opposite-sign 2ℓ channel	43
4.5.3 Same-sign 2ℓ channel	46
4.5.4 3ℓ channel	49
4.5.5 4ℓ channel	53

Contents

4.6	Background estimation	56
4.6.1	Opposite-sign 2ℓ channel	56
4.6.2	Same-sign 2ℓ channel	56
4.6.3	3ℓ channel	58
4.6.4	4ℓ channel	59
4.6.5	Background from fake-leptons	60
4.7	Systematic uncertainties	62
4.7.1	Experimental uncertainties	64
4.7.2	Theoretical uncertainties	65
4.8	Statistical Treatment	66
4.8.1	Statistical Framework	66
4.8.2	Binning	68
4.8.3	Fitting procedure	70
4.8.4	Asimov results and uncertainties impacts	70
4.9	Results	72
 II Low-Gain Avalanche Detector Development at USTC for the HGTD and Future Experiments		81
5	Working Principles of a Silicon Detector	83
5.1	Properties of the silicon material	83
5.1.1	Drift of charge carrier and material resistivity	84
5.1.2	P-N junction	84
5.1.3	Avalanche and breakdown	85
5.1.4	Leakage current	85
5.1.5	Capacitance	86
5.2	Silicon for particle detection	87
5.2.1	Electron-hole generation	87
5.2.2	Signal induction	87
5.2.3	Layout of the detector	88
5.2.4	Architecture of the junction	89
5.3	Radiation damage on the silicon detector	90
5.3.1	Bulk damage	91
5.3.2	Surface damage	93
5.4	Summary	93
6	The Low Gain Avalanche Detector History and its Principle	95
6.1	Technology motivation	95
6.2	Timing performance of the LGAD	97
6.3	Radiation hardness of the LGAD	99
6.3.1	Gain layer degradation – Acceptor removal	100
6.3.2	High voltage operation – Single-event burnout effect	102
6.4	Different types of the LGAD design	103
6.4.1	Inverse LGAD	104

6.4.2	Trench isolated LGAD	104
6.4.3	Deep junction LGAD	104
6.4.4	AC coupled LGAD (RSD)	105
6.5	Summary	105
7	Simulation and Fabrication of the USTC-IME LGADs for the HGTD Upgrade	107
7.1	The structure of the LGAD sensor	107
7.1.1	Substrate - Where everything is based on	107
7.1.2	Multiplication layer (p-well) - Heart of LGAD	108
7.1.3	n^+ layer - We got the signal? Read it out!	109
7.1.4	Junction termination extension - Stop break at the edge!	110
7.1.5	Field plate - Make the field smooth.	110
7.1.6	Guard-ring - For those signals and current we don't want!	111
7.1.7	Float guard ring - Lower the potential step by step.	111
7.1.8	P-stop - Keep the electrodes isolated.	111
7.1.9	C-stop - Don't touch the defects!	112
7.2	technology computer aided design (TCAD) simulation	113
7.2.1	Mobility	113
7.2.2	Recombination	114
7.2.3	Avalanche	115
7.3	Results from the TCAD simulation for the LGAD structures	115
7.3.1	Overview of the LGAD model in TCAD	115
7.3.2	Optimization of the substrate	116
7.3.3	Optimization of the p-well (gain-layer)	119
7.3.4	Optimization of the guard-ring	120
7.3.5	Optimization of the p-stop	123
7.3.6	Optimization of the field plate	125
7.3.7	Optimization of the field plate of GR	126
7.3.8	Optimization of the floating GR	129
7.3.9	Inter-pad gap for the 2×2 array	130
7.3.10	Conclusion and design for prototype production	131
7.4	USTC-IME 1st batch fabrication	134
7.4.1	Fabrication process preparation	135
7.4.2	Mask preparation	138
7.4.3	Wafer preparation and field oxide growing/etching	145
7.4.4	JTE and p/c-stop implantation and diffusion	145
7.4.5	Carbon infusion	145
7.4.6	n^+ and p-well implantation	146
7.4.7	Contact etching	146
7.4.8	Metallization and passivation	147
7.4.9	Splits of the wafers	147
7.5	USTC-IME 2nd batch fabrication	148
7.5.1	Mask preparation	148
7.5.2	Improvement of the contact design	150
7.5.3	Improvement of the carbon infusion	150

Contents

7.5.4	Improvement of the gain layer	150
7.5.5	Improvement of the inter-pad gap and slim-edge design	151
7.5.6	Splits of the wafers	151
7.6	Design for the production of the USTC-IME LGADs for HGTD	155
7.6.1	The 15×15 array layout	155
7.6.2	QC-TS structures	155
7.7	Summary	156
8	Characterization and Performance of the HPK and USTC-IME LGADs	159
8.1	Overview	159
8.2	The laboratory setup for characterization of the LGADs at USTC	161
8.2.1	Probe-station setup for IV/CV measurement	161
8.2.2	I-V measurement setup	163
8.2.3	C-V measurement setup	166
8.2.4	TCT and β -scope setup	166
8.2.5	Data analysis for the transient test	168
8.3	Results from laboratory test	171
8.3.1	I-V/ C-V results of the HPK LGADs	171
8.3.2	Impact of the neighboring floating pads	174
8.3.3	Measurements of the first batch USTC-IME LGADs	176
8.3.4	Measurements of the second batch USTC-IME LGADs	178
8.4	Test with charged particle beams at CERN PS/SPS and DESY	181
8.4.1	Setup of the test beam	181
8.4.2	Trigger and DAQ	181
8.4.3	Track reconstruction for data from EUDET-type telescope	182
8.4.4	Treatment of the oscilloscope waveform	183
8.4.5	Data analysis	184
8.5	Results from the test beam	184
8.5.1	Time resolution and charge collection	184
8.5.2	Inter-pad gap distance	186
8.6	Radiation hardness of the USTC-IME LGAD	188
8.7	Postmortem analysis of the production	191
8.7.1	Wafer-level uniformity study evaluation	191
8.7.2	Yield estimation of the full-size array	191
8.8	Summary	194
9	Conclusions and Future Prospective	197
9.1	Conclusions	197
9.1.1	The $H \rightarrow WW^*, VH$ analysis	197
9.1.2	The LGAD development	197
9.2	Future prospective	198
9.2.1	The $H \rightarrow WW^*, VH$ analysis in the ATLAS run 3 and HL-LHC	198
9.2.2	Current limitations and possible solutions of the LGAD technology for future application	198

Appendix	203
A Development of the AC-coupled low gain avalanche detector (AC-LGAD)s at the USTC Nano-Fabrication and Research Center	203
A.1 Advantages of the AC-LGAD	203
A.2 Capacity of the USTC USTC center for micro- and nanoscale research and fabrication (NRFC)	203
A.3 Design of the AC and DC coupled LGADs	205
A.4 Fabrication of the AC and DC LGADs with the 6-inch processes at NRFC	208
A.5 Performance of the AC and DC LGADs produced at NRFC	208
A.5.1 I-V and Timing performance	208
A.5.2 Spatial results from the laser-TCT	209
A.6 Summary	212

List of Figures

2.1	The elementary particles in the SM [9]. The chart is similar to the periodic table in chemistry but is more fundamental.	6
2.2	The LHC accelerator complex for the hadron collision experiment at $\sqrt{s} = 14$ TeV. . .	11
2.3	The ATLAS detector and subsystems [44].	12
2.4	Schematic view of the ATLAS inner detector system [44].	13
2.5	Schematic view of the ATLAS calorimeter system [44].	14
2.6	Schematic view of the ATLAS muon spectrometer system [44].	15
2.7	The LHC/HL-LHC project schedule (updated in February 2022).	16
2.8	Novel technologies to be used for the high-luminosity LHC.	17
2.9	A simulated $t\bar{t}$ event at average pile-up of 200 collisions per bunch crossing at the ATLAS in HL-LHC phase [54].	18
2.10	The simulated interaction distributions in both the Spatial axis (direction along the LHC beam line) and Timing axis (time from the center of time for bunch crossing) from one HL-LHC bunch crossing. Around 200 pile-up interaction vertices are shown by the stars. The pile-up vertices are shown in black. One hard scattering vertex is shown by the red star. The nominal ITk resolution in the forward region, 2 mm, for the soft particles is shown by the red band for spatial direction and the expected time resolution of HGTD (50 ps) is shown by the green band in timing direction. (Figure adapted from [57]).	19
2.11	The position of HGTD in the ATLAS detector at the HL-LHC [57].	20
2.12	The composition of the HGTD system [57].	20
2.13	The simulated non-ionizing radiation fluences in the HGTD area. (a) Expected nominal Si 1 MeV _{eq} fluence dose as functions of the radius in the outermost sensor layer of the HGTD for 4000 fb ⁻¹ , i.e. before including safety factors. (b)The non-ionizing energy loss (NIEL) fluence of the HGTD region for the HL-LHC with 1.5 safe factor applied and considering ring replacements. [57].	21
2.14	Schematic drawing of two adjacent modules on the top side and one on the bottom side of the cooling plate [57].	21
3.1	The Feynman diagrams for the Higgs production and decay [15].	25
3.2	Predicted SM Higgs production cross-sections for different modes at the LHC with the mass of 125 GeV [68]. The theory uncertainties are shown by line widths. . . .	27
3.3	The predicted branching fractions of the different Higgs boson decay modes in the SM. The branching ratios at different Higgs mass points are shown in (a) [68]. The theory uncertainties are shown by line widths. The pie chart is shown in (b), and only the modes with branch ratios larger than 0.5% are shown. (chart is made with data from [9])	28

List of Figures

3.4	The recent results of the Higgs mass measurement from (a) ATLAS and (b) CMS detectors. The results between ATLAS and CMS have good agreement within the uncertainties, showing a combined Higgs mass near 125 GeV.	29
3.5	The measurement of the Higgs mass and width performed on the ATLAS detector. (a) The four-lepton invariant mass distribution from all subchannels combined (black points) in $H \rightarrow ZZ^* \rightarrow 4\ell$ channel is shown along with the post-fit signal and background distributions (red line) [72]. (b) The likelihood profile as a function of the ratio between the hypothesized and SM expected Higgs width in the combined on-shell and off-shell $H \rightarrow ZZ^* \rightarrow 4\ell$ and $H \rightarrow ZZ^* \rightarrow 2\ell 2\nu$ analysis [73].	30
3.6	The measurement of the Higgs spin and parity with the $H \rightarrow ZZ^* \rightarrow 4\ell$, $H \rightarrow WW^* \rightarrow e\nu\mu\nu$ and $H \rightarrow \gamma\gamma$ channels at ATLAS detector with 7 and 8 TeV data. The distribution of the test statistic for the (a) 0^+ and 0^- as well as (b) 0^+ and 2^+	31
3.7	The recent results on the Higgs coupling measurements at the (a) ATLAS [15] and (b) CMS [14] experiments. The results are presented by the ratio of the observed rate to the predicted SM event rate for different combinations of Higgs boson production and decay processes. The results show good agreement between the observed data and the prediction.	33
4.1	Feynman diagrams for the signal topologies at tree-level considered by the analysis of VH , $H \rightarrow WW^*$ measurement.	36
4.2	The trigger and data acquisition (TDAQ) used in the ATLAS run 2 data-taking with specific focus given to the components of the L1 Trigger system [95].	38
4.3	The integrated luminosity (a) and the number of interactions per crossing (pile-up) distribution (b) for the overall ATLAS 2015 to 2018 data taking in LHC run 2 [96].	38
4.4	The illustration of the detector and algorithm for reconstruction and identification of the electrons in ALTLAS detector [157].	41
4.5	The performance of the artificial neural network $(\text{ANN})_{\text{VHOS}}^{\text{VH}}$ used in the analysis. The distributions on the signal and background for the VH , top, Z+jets, and WW node.	45
4.6	Post-fit distribution of $\text{ANN}_{\text{VHOS}}^{\text{VH}}$ in the opposite-sign 2ℓ SR. In all subsequent post-fit distributions, “Misid.” refers to the mis-identified lepton background which is primarily from the $W + jets$	46
4.7	Post-fit distributions of the recurrent neural network (RNN) discriminant in (a) $\text{SS}2\mu$, (b) $\text{SS}2e$, and (c) SSDF signal region categories.	48
4.8	The performance of the RNN used in the same-sign 2ℓ channel analysis. (a) The distribution of the RNN output on the signal and background for the trained and tested samples is shown. (b) The background rejection as a function of the signal efficiency in the train and test samples.	49
4.9	The performance of the ANN_{Zdom} used in the analysis. (a) The distribution of the ANN_{Zdom} on the signal and background for the trained and tested samples is shown. (b) The background rejection as a function of the signal efficiency in the train and test samples.	50

4.10	The performance of the ANN_{Zdep} used in the analysis. (a) (c) (e) The distribution of the ANN_{Zdom} on the signal and background for the trained and tested samples on the output nodes for $t\bar{t}$, WWW , WZ regarding to the WH node. (b) (d) (f) The background rejection as a function of the signal efficiency in the train and test samples on the output nodes for $t\bar{t}$, WWW , WZ regarding to the WH node.	52
4.11	Post-fit distributions of (a) ANN_{Zdom} in the Z-dominated SR and (b) $\text{ANN}_{\text{Zdep}}^{\Delta}$ in the Z-depleted SR. The lower panel shows the ratio of the data to the sum of the fitted signal and background. The hatched band in the upper panel and the shaded band in the lower panel show the total uncertainty. The post-fit results are obtained from the combined 2 parameter of interest (POI) fit described in Sec. 4.8.3.	53
4.12	Post-fit distributions of the BDT in (a) the 1-SFOS category and (b) the 2-SFOS category. The lower panel shows the ratio of the data to the sum of the fitted signal and background. The hatched band in the upper panel and the shaded band in the lower panel show the total uncertainty. The post-fit results are obtained from the combined 2 POI fit described in Sec. 4.8.3.	55
4.13	The performances of the BDTs used in the analysis are shown by the distribution of the signal and background for the trained and tested samples. The BDT is trained and applied individually for (a) 1-SFOS and (b) 2-SFOS categories.	55
4.14	Post-fit distributions of (a) $\text{ANN}_{\text{VHOS}}^{\text{top}}$ in the top CR, (b) $\text{ANN}_{\text{VHOS}}^{\text{Z+jets}}$ in the Z+jets CR, and (c) $\text{ANN}_{\text{VHOS}}^{\text{WW}}$ in the WW CR of the opposite-sign 2ℓ channel. The lower panel shows the ratio of the data to the sum of the fitted signal and background. The hatched band in the upper panel and the shaded band in the lower panel show the total uncertainty. The post-fit results are obtained from the combined 2 POI fit described in Sec. 4.8.3.	57
4.15	Post-fit distributions of ANN_{Zdom} in the (a) $W(Z/\gamma^*)$ CR with no jets and (b) $W(Z/\gamma^*)$ CR with at least one jet and of $\text{ANN}_{\text{Zdep}}^{\Delta}$ in the (c) $W(Z/\gamma^*)$ CR with no jets and (d) $W(Z/\gamma^*)$ CR with at least one jet. The lower panel shows the ratio of the data to the sum of the fitted signal and background. The hatched band in the upper panel and the shaded band in the lower panel show the total uncertainty. The post-fit results are obtained from the combined 2 POI fit described in Sec. 4.8.3.	59
4.16	Post-fit distributions of the (a) 1-SFOS boosted decision tree (BDT) output and (b) 2-SFOS BDT output in the ZZ CR. The lower panel shows the ratio of the data to the sum of the fitted signal and background. The hatched band in the upper panel and the shaded band in the lower panel show the total uncertainty. The post-fit results are obtained from the combined 2 POI fit described in Sec. 4.8.3.	60
4.17	The uncertainties breakdown on (a) μ_{WH} and (b) μ_{ZH} of each contribution source with total statistical uncertainties are shown.	71
4.18	The 2D likelihood 1 to 5 sigma contours (a) of the μ_{WH} and μ_{ZH} and profile likelihood curves of μ_{WH} , μ_{ZH} (b) and of μ_{VH} (c) from the VH combined fit.	73
4.19	Best-fit values of the total WH , ZH , and VH cross-sections times the $H \rightarrow WW^*$ branching ratio. Each measurement is normalized to its SM prediction. The black error bars, orange boxes, and blue boxes show the total, statistical, and systematic uncertainties in the measurements, respectively. The gray bands represent the theory uncertainty of the corresponding Higgs production mode.	75

List of Figures

4.20	Observed profile likelihood as a function of $\sigma \times \mathcal{B}_{H \rightarrow WW^*}$ normalized by the SM expectation for (a) the VH and WH/ZH measurements from the combined 1- and 2 POI fits, respectively, and (b) the single-channel measurements.	75
4.21	Two-dimensional likelihood contours of the measured values of $\sigma_{ZH} \times \mathcal{B}_{H \rightarrow WW^*}$ vs. $\sigma_{WH} \times \mathcal{B}_{H \rightarrow WW^*}$ for 68% and 95% confidence levels (CLs) compared with the predictions from the SM. The 68% confidence level on the SM predictions for the ZH and WH cross-sections times branching fraction is indicated by the magenta ellipse.	78
5.1	Examples of the silicon hole generation in the n-in-p silicon detector.	88
5.2	Here are examples of the drift potential (a) and weighted potential (b) generated with the <i>Weightfield2</i> simulation software [194]. The electrode have 50 μm width and 120 μm pitch with 120 V bias applied.	89
5.3	Here are examples of the detector with different layouts, the pixel detector(a) and strip detector(b).	89
5.4	Here are examples of the different architecture in the active area. The planar sensor(a) and 3D sensor(b).	90
5.5	The NIEL which using the Displacement damage function $D(E)$ normalized to 95 MeV \cdot mb for neutrons, protons, pions and electrons [188].	92
5.6	Energy level of defects caused by the displacement damage in silicon and their consequences.	93
6.1	(a) The schematic view of the LGAD structure. The p-type implantation is placed near the surface, creating a strong local electric field where the electron avalanche would happen. (b) Examples of the electric-field strength in LGAD with 300 μm thickness and external bias at 50 V, 200 V, 600 V. The 300 μm in a 300 μm PIN diode without gain and biased to 600 V is also drawn for comparison. The x-axis is the depth starting from the sensor surface in a logarithm scale [206].	96
6.2	(a) The shape of the LGAD signal with fixed gain and different thickness indicates that the fast-rising edge with the highest slew rate can be achieved with the thin LGADs. (b) The simulated timing resolution by <i>Weightfield2</i> with different detector thickness. The contributions from Jitter and Landau noise are shown separately [206].	98
6.3	The signal composition of the LGAD with gain = 10, the simulation is done with the <i>Weightfield2</i> [194], and the thickness is set to 50 μm . The total signal and the composition from primary electrons, gain electrons, primary holes, and gain holes are shown. The MIP signal is simulated, and the Landau noise can be seen in the rising edge.	98
6.4	Two different approaches of the irradiation hard LGADs by selecting the different gain layer depth. (a) The two-gain layer simulated the doping profile. (b) The electric field is calculated by the corresponding doping profile.	99
6.5	The B_iO_i formation from the B_i and O_i created by the interstitials Si_i created under the irradiation shown in the band gap.	100

6.6	The gain of the electron is calculated by the integration of the multiplication factor derived by the Massey model with the two doping profiles. Both before and after, a fixed fraction of the acceptor removed gain layer after irradiation is plotted. The curves indicate that the loss of the gain in the deep gain layer LGAD can be compensated with less increase in the bias voltage after irradiation.	101
6.7	The interactions of the defects created by the displacement damage and the formation of the B_iO_i complex formation after the irradiation (a) [209]. The formation of the B_iO_i complex measured by the thermally stimulated current (TSC) technique with the p-type silicon samples irradiated at different fluences [208]. We can see the increments of the B_iO_i peak when the fluence gets higher.	102
6.8	(a) Microscopic photo of a typical burn mark observed in ATLAS proton beam tests at Fermilab in 2018 in a CNM LDA35 sensor [213]. (b) Minimal SEB threshold vs. thickness of the sensor.	103
6.9	The legacy LGAD structure schematic layout.	103
6.10	The novel LGAD structures have been developed for better performance and more wide application scenarios.	104
7.1	The illustration of typical LGAD structures, including the multiplication layer, n^+ layer, JTE, field-plate, p-stop, and guard ring.	107
7.2	The impact of the field plate on the edge of the depletion region [191].	110
7.3	The impact of the float guard ring on the edge of the depletion region surface [191].	111
7.4	The schematic illustration of the c-stop in the peripheral region of the LGAD design. (a) The depletion region arrived at the cutting edge of the device where the defects and contaminations concentrate. This will lead to an increment in the leakage current. (b) The depletion region is constrained by the p-type c-stop implantation and kept away from the cutting edge.	113
7.5	The LGAD model created by the process simulation of the TCAD for the electric properties' validation and optimization. The simulation of the single pad device is only performed on half of the device and focuses on the peripheral region since its symmetric. For the doping concentration scale, the positive value corresponds to the donor-enriched region and the negative value corresponds to the acceptor-enriched region.	116
7.6	The electric simulation of the LGAD peripheral regions. The study is focused on the optimization of the electric field strength (the top figure) and the potential distribution (the bottom figure) to avoid the formation of a strong local field, which may cause premature breakdown and an increment of leakage current, especially after irradiation.	117
7.7	The simulated electric potential distribution at different substrate concentrations (a) $5 \times 10^{12} \text{ cm}^{-3}$, (a) $1 \times 10^{13} \text{ cm}^{-3}$, (a) $5 \times 10^{13} \text{ cm}^{-3}$. The same bias (120 V) is used for each simulation.	118
7.8	The V_{BD} dependence on the substrate concentration from the simulation shown in Fig. 7.7. The trendline is plotted for guiding eyes.	119
7.9	The $1/C^2 - V$ of the device with different p-well dose with the fixed substrate concentration and the $1/C^2 - V$ of the different substrate concentration but fixed p-well design.	120

List of Figures

7.10	The optimization of the p-well and the gain as well as the V_{BD} dependence of the p-well doping. The 1000 keV implantation energy is used in the simulation.	120
7.11	The optimization of the guard ring. The impact of floating or grounding the guard ring are shown in the figures. (a), (b) are the electric field strength distributions, and the (c), (d) are the current (charge carrier drift) paths, from which we can see without the guard ring grounded the signal and current in the peripheral region are collected by the guard ring without contributed to the central pad.	122
7.12	The two p-stop model is shown. Such a design can have stronger isolation for the guard ring and the central pad.	123
7.13	The comparison of the simulated results of the single p-stop (a), (c) and the dual p-stop (b), (d). The electric-field distributions are shown on the (a), (b), and the current density distributions are on the (c), (d).	124
7.14	The comparison of the simulated results of the design of the p-stop with (a) 25 μm and (b) 50 μm distance to the JTE of the central pad.	125
7.15	The comparison of the simulated results of the design on the field-plate with L_{FP} to be (a) 10 μm and (b) 20 μm	126
7.16	The comparison of the simulated results of the design on the field-plate for the guard ring with L_{GRFP} to be (a) 0, (b) 5 μm , (c) 10 μm , and (d) 15 μm	127
7.17	The validation of the optimized structure dimensions by a scan for the V_{BD}	128
7.18	The zoomed electric field strength and potential contours for the $L_{GRFP} = 10 \mu\text{m}$ design is shown. We can see a smoother field at the edge of the guard ring with the GRFP introduced.	129
7.19	The structure of the floating guard ring for smoothing the potential drop in the peripheral region (a) [189] and the implementation for the TCAD model of the LGAD is shown in (b).	129
7.20	The comparison of the simulated electric potential with one float guard ring added at the outside of the guard ring. We can see that the electric-potential drop is shared by the added guard ring and mitigated the forthcoming of the local strong electric field. .	130
7.21	The simulated inter-pad gap design for the large array with $D_{IP} = 50 \mu\text{m}$	130
7.22	The finalized and the converged model based on the above simulation for the mask design of the fabrication.	132
7.23	The simulated V_{BD} at different p-well dose for the validation of the peripheral design. In the region where the dose is low, the V_{BD} keeping constant means the breakdown is dominated by the peripheral region. When the dose is higher than $1.5 \times 10^{12} \text{ cm}^{-2}$, the V_{BD} gets lower, which means the breakdown is dominated by the central pads. .	133
7.24	The simulated I-V and C-V curves are based on the finalized models with splits of gain layer design. The energy and the dose of the gain layer are shown in the legend of the figure. The doses are shown by the arbitrary unit with the split-2 as 1.0 U. . . .	134
7.25	The designed layout of the 1×1 and 2×2 used in the first batch production of the USTC-IME LGADs.	134
7.26	The schematic view for illustration of the processes in the LGAD fabrication with the 50 μm thickness silicon wafer.	137
7.27	The layer 1-4 (FO, JTE, PSTOP, NPLUS) of the designed 1×1 LGAD used in the first batch production of the USTC-IME LGADs.	139

7.28	The layer 5-8 (PWELL, CONT, METAL, PASS) of the designed 1×1 LGAD used in the first batch production of the USTC-IME LGADs.	140
7.29	The designed layout of the reticle to be used in the first batch production of the USTC-IME LGADs.	143
7.30	The 1×1 and 2×2 LGADs layout with different geometry parameters used in the first batch production of the USTC-IME LGADs.	143
7.31	The designed layout of the 5×5 and 15×15 used in the first batch production of the USTC-IME LGADs.	144
7.32	The auxiliary devices layout with different geometry parameters used in the first batch production of the USTC-IME LGADs. The candidate AC-LGADs layouts with different pixel sizes are shown in (d).	144
7.33	The USTC-IME design of the carbon infusion for the protection of the gain layer boron from the impact of acceptor removal.	146
7.34	Photo of the wafer with USTC-IME version 1.1 LGADs at the first batch.	148
7.35	The designed reticle layout of (a) the small array devices wafer and (b) full size 15×15 array wafer (left) used in the second batch production of the USTC-IME LGADs.	149
7.36	The layout of the 2×2 LGAD array with different inter-pad gap distance and slim edge used in the second batch production of the USTC-IME LGADs. (a) 2×2 IP3SE3 with $30 \mu\text{m}$ inter-pad gap and $300 \mu\text{m}$ slim edge. (b) 2×2 SE4IP5 with $50 \mu\text{m}$ inter-pad gap and $400 \mu\text{m}$ slim edge. (c) 2×2 SE5IP7 with $70 \mu\text{m}$ inter-pad gap and $500 \mu\text{m}$ slim edge. (d) 5×5 SE4IP5 with $50 \mu\text{m}$ inter-pad gap and $400 \mu\text{m}$ slim edge.	152
7.37	Photo of the wafer of the USTC-IME second batch. (a) the five wafers with different layouts and gain layer designs. (b) The wafer with 15×15 full-size LGADs arrays.	153
7.38	Photo of the wafers with (a) small arrays (1×1 , 2×2 , 5×5) and (b) large arrays (15×15) LGADs at the USTC-IME second batch.	154
7.39	The layout of the 15×15 LGAD array with the requirement from the collaboration specification implemented.	155
7.40	The layout of the QC test structures for the production phase.	156
7.41	The layout of the reticle to be used in the production phase with the requirement from the collaboration specification implemented.	156
8.1	The manual probe station with an 8-inch trunk is used for the room temperature IV/CV test at stage-1.	161
8.2	The probe station with a 4-inch trunk for the room and low-temperature IV/CV test at stage-2.	162
8.3	The setup of the automatic probe station at the USTC for the wafer-level IV/CV test.	162
8.4	(a) The dedicated software for the I-V and C-V measurement was developed with <i>Qti5</i> and the <i>pymeasure</i> backends. (b) schematic layout of the cable connection for performing the I-V test on the 2×2 LGAD arrays, the test of the single pad and larger arrays uses similar cable connections.	164
8.5	The schematic view of the circuit with the digital switch boards for (a) I-V and (b) C-V test of the 5×5 and 15×15 large array LGADs [228].	165

List of Figures

8.6	The setup of the β -scope system for the charge collection and timing performance test of LGAD with ^{90}Sr beta source. The schematic view (a) and a photo of the setup (b) are shown.	167
8.7	The setup of the laser transient current technique (TCT) system for the inter-pad gap and jitter measurement at fixed position charge deposition, frequency under high rate. The 1064 nm infra-red laser is equipped for the silicon device test.	168
8.8	The USTC-IME LGAD sensor on the pre-amplifier board for the charge collection and timing resolution test.	169
8.9	The simplified schematic of the LGAD pre-amplifier.	169
8.10	(a) The illustration of the variables being extracted from the waveforms. (b) The 2D distribution of the peak time of the waveform (T_{max}) and maximum amplitude of the waveform (A_{max}) for all events recorded and before the selection applied.	170
8.11	The (a) I-V and (b) C-V curves of the HPK prototype 1.1, 1.2, 2, 3.1, 3.2 LGADs.	171
8.12	The N-V curves used for the V_{GL} determination, as we can see, for prototypes that have high bulk resistance, a dip can be clearly observed in the N-V curve.	173
8.13	The I-V (a) and C-V (b) curves of the HPK prototype 3.2 5×5 LGADs measured with the probe card by USTC.	173
8.14	The V_{BD} distribution of the HPK prototype 3.2 5×5 LGADs measured from I-V.	173
8.15	The V_{GL} distribution of the HPK prototype 3.2 5×5 LGADs measured from (a) C-V and from (b) I-V.	174
8.16	The correlation of the V_{GL} (left from C-V measurement and right from I-V measurement) and V_{BD} for the HPK prototype 3.2 5×5 LGADs.	174
8.17	The leakage current distribution in 3 circumstances to study floating pad impact.	175
8.18	The I-V and C-V curves measured for the first batch USTC-IME wafers.	177
8.19	(a) The IV of the carbon enriched USTC institute of microelectronics, CAS (IME) LGADs after the different fluence. (b) The dependency of measured V_{GL} on the different fluence irradiated LGADs.	177
8.20	The measured result of the USTC-IME first batch LGADs with β -source.	178
8.21	The I-V results of the USTC-IME batch 2 LGADs with different gain layer designs.	179
8.22	The LGAD wafers at the automatic probe station(left) and microscopic version of the LGAD wafers at the automatic probe station (right)	179
8.23	(a) Charge collection and (b) timing resolution of the USTC-IME version 2.1 LGADs. The measurements are performed under -30°C with the beta source. The green and red lines specify the requirements corresponding to the initial and end-of-life performances in the specifications.	180
8.24	A photo of the test beam setup at DESY TB 22 beam station with 5 GeV electron for the LGAD performance test. The EUDET beam telescope with MIMOSA pixel is used for tracking. Similar hardware setup and the data acquisition system are used at CERN PS/SPS test beam for other campaigns.	181
8.25	3D-proto-tracks are reconstructed from the three MIMOSA planes before the DUTs (“upstream triplets”), and other 3D-proto-tracks are reconstructed from the three MIMOSA planes after the DUTs (“downstream triplets”). The downstream triplets must coincide with a hit in the FE-I4 plane.	183

8.26	The measured results of the three carbonated LGAD prototypes from USTC-IME as well as IHEP-IME and FBK after the highest required fluence. The distribution of the collected charge under the beam is shown in (a), the collected charge at different bias voltages is shown in (b), the time resolution at different bias voltages is shown in (c), the efficiency in 1 dimension is shown in (d). The HGTD required performance is shown by the dashed line. The results demonstrated the good performance of USTC-IME LGADs that exceeded the requirement by a significant margin.	185
8.27	The inter-pad gap distance measured by the charged particle beam at CERN/SPS with the EUTelescope. The track is constructed with the six MIMOSA pixel detector planes placed on both downstream and upstream of the beam, and the tracks are reconstructed and extrapolated to the device under test (DUT) plane for the hit position determination.	187
8.28	The distribution of the (a) breakdown voltage and (b) leakage current. The uniformity is observed on the wafer. Similar pattern is observed in other wafers produced by IME. Later studies have confirmed its due to the 1% level dose variation when performing the implantation of the gain layer.	191
8.29	The distribution of the V_{BD} from the on-wafer I-V test for the USTC-IME second batch version 1 wafers for the uniformity evaluate and yield estimation.	192
8.30	The distribution of the V_{BD} from the on-wafer I-V test for the USTC-IME second batch version 2 wafers for the uniformity evaluate and yield estimation.	193
8.31	Overview of the c-factor evolution and comparison with other vendors for the radiation hard LGAD research from the most promising sample of each batch.	195
A.1	Overview of the NRFC major equipments for 6-inch silicon wafers fabrication. . . .	204
A.2	The simulation of the AC LGAD signal readout with (a) the hit in the middle of the sensor. The hit in the position displaced to the middle by a distance of d is shown by the blue arrow. The signals for the hit in the middle being read out at different pixels are shown in (b). The signals for the hit at different positions with a step of $50\ \mu\text{m}$ and being read out in the middle pixel are shown in (c).	206
A.3	The designed reticle layout used in the 6-in AC and DC coupled LGADs production on the 6-in wafers at NRFC. The size is designed with $10 \times 10\ \text{mm}^2$ and the LGADs with size of 1×1 , 2×2 are placed for layout optimization.	207
A.4	(a) Photo of the wafer of AC/DC LGADs produced at USTC NRFC. (b) The microscopic photo of the USTC NRFC LGADs.	208
A.5	(a) The bonding of USTC NRFC AC LGAD sensor on the 9-channel pre-amplifier board for the charge collection, position, and timing resolution test. (b) The electrodes in the AC-LGAD used in the TCT test.	209
A.6	The test results of the LGAD samples produced by NRFC at USTC. (a) I-V curves measured for the W3 and W4 where a V_{BD} in the range of 150 to 220 V is found for the W3-ER W4-OR . Different depths of the gain layer are realized by the different implantation energies. (b) The timing resolution of the NRFC LGADs measured by the β -scope, a time resolution better than 40 ps is achieved by the W3-ER . The LGADs fabricated at USTC-IME are also measured for comparison.	209
A.7	The average amplitude of the signal obtained from different NRFC AC-LGAD strips as a function of the laser spot position. The signals from the DC ring are also read out for comparison.	210

List of Figures

A.8	The average amplitude of the signal obtained from different NRFC AC-LGAD pixels as a function of the laser spot position. The labeling of the pixels can be found in Fig. A.9.	211
A.9	The scan is performed along the Y direction. The X position is fixed in the center of the two columns of pads (200 μm) in the scan.	212
A.10	The signal waveform and the amplitude used for the position determination. (a) The signal observed from different pixel of AC-LGAD for the same hit. (b) The measured $F(Y)$ function with the calibration data.	212
A.11	The measured position resolution with the test data in (a) X direction and (b) Y direction. The 640 points are used in the estimation in the range of 150 to 250 μm for the direction under measurement and 175 to 215 μm for the direction not measured. .	213

List of Tables

2.1	Main parameters of the HGTD design. The table is taken from [57] with the recent updates implemented.	22
4.1	MC generators used to model the signal and background processes. Alternative generators or parton shower models used to estimate systematic uncertainties are shown in parenthesis. In the last column, the prediction order (in QCD, unless specified otherwise) for the total cross-section is shown.	39
4.2	The event categories definition before the multivariate analysis treatment applied. . .	43
4.3	ANN input variables used in the opposite-sign 2ℓ channel.	44
4.4	Input variables for the RNN in the same-sign 2ℓ channel.	47
4.5	Summary of input variables for the ANNs in the Z-dominated (left) and Z-depleted (right) categories.	51
4.6	Summary of input variables for the BDTs in the 4ℓ channel.	54
4.7	The background modeling of each channel. At least one reconstructed misidentified lepton in the data-driven background processes.	56
4.8	The estimated muon fake-factor in the $VH\ 2\ell$ DFOS, $WH\ 2\ell$ same-sign and 3ℓ channels with the relative uncertainties	61
4.9	The estimated electron fake-factor in the $VH\ 2\ell$ DFOS, $WH\ 2\ell$ same-sign and 3ℓ channels with the relative uncertainties	62
4.10	Expected fake-lepton event yields as predicted by MC and by data-driven (DD) method. Total background includes MC-based fake estimation. Only MC statistical uncertainties are quoted.	63
4.11	Expected fake-lepton event yields as predicted by MC and by data-driven (DD) method. Total background includes MC-based fake estimation. Only MC statistical uncertainties are quoted.	63
4.12	Post-fit normalization factors which scale the corresponding estimated yields in the signal region. The quoted uncertainties include both statistical and systematic contributions. The post-fit results are obtained from the combined 2 POI fit	63
4.13	Summary of the optimized MVA output binning for each channel.	69
4.14	Regions and POIs used for each channel fitting. The fitted value and expected significance are also shown, both experimental and theoretical systematics are included in the fitting.	70
4.15	Results from VH combined asimov fit. All VH regions are included in the fitting. The Asimov dataset is used in the signal regions and the observed data are used in the control regions.	72

List of Tables

4.16	The measured values of the signal strengths and the corresponding sensitivities, Z_0 , for the single-channel fits as well as the combined 1- and 2 POI fits. For each fit, both the expected and measured results are shown. The uncertainties correspond to the total of all statistical and systematic sources.	76
4.17	Post-fit MC and observed data yields in each SR as measured by the 2-POI fit. The top and Z+jets processes for a given channel correspond to those with only prompt leptons, as described in Sec . The uncertainties correspond to the total of all statistical and systematic sources. The quadrature sum of the individual sources may differ from the total uncertainty due to correlations.	77
4.18	Breakdown of the average contributions to the total uncertainties in percentage on the observed values of the signal strengths for the combined 1 POI ($\sigma_{VH} \times \mathcal{B}_{H \rightarrow WW^*}$) and 2 POI ($\sigma_{WH} \times \mathcal{B}_{H \rightarrow WW^*}$ and $\sigma_{ZH} \times \mathcal{B}_{H \rightarrow WW^*}$) fits. Indentation is used to denote subcategories. “Floating normalization” refers to the uncertainties on the normalization factors obtained using control regions. The quadrature sum of the individual sources may differ from the total uncertainty due to correlations.	79
7.1	The designed fabrication process recipe with the main processes based on the simulation for the USTC-IME first batch.	136
7.2	Description of the eight layers of photolithographic mask used to fabricate the USTC-IME first batch LGAD	138
7.3	Summary of the USTC-IME wafers from the first batch (version 1.1) production and second batch productions (version 2.0 and 2.1). The wafer series number, the gain layer dose and energy, the type of the gain layer implantation, the layouts on the wafer, the breakdown voltage, the irradiation hardness c -factor, and the sites where the samples have been tested are listed.	154
8.1	HGTD electric requirements as well as timing and charge collection performance of the sensor as produced at operation voltage ($V_{OP} = 0.8 \cdot V_{BD}$ and $T = -30^\circ\text{C}$). . . .	160
8.2	HGTD sensor performance requirements after irradiated to highest fluences $2.5 \times 10^{15} \text{ n}_{eq}/\text{cm}^2$.160	
8.3	Summary of electric characterization platforms for LGAD tests at USTC	163
8.4	The information of the HPK sensor prototypes being tested.	172
8.5	The extracted V_{GL} , V_{FD} , V_{BD} from the I-V and C-V curves, which is important for the performance of the LGAD sensor for a stable operation.	172
8.6	Overview of the information and the main test results for the first batch USTC-IME LGADs.	176
8.7	Charge collection efficiency and Timing performance of the irradiated USTC-IME W11 carbonated LGADs.	178
8.8	The measured result of the collected charge and time resolution for carbonated LGAD sensor promising. The sensors tested are the most promising prototypes from IHEP-IME, USTC-IME and FBK.	186
8.9	The measured inter-pad distance for the USTC-IME W17 and W19 2×2 array with the nominal distance to be $30 \mu\text{m}$	187
8.10	Irradiation facilities and parameters and maximum achieved fluence and TID, as well as LGAD types irradiated.	188
8.11	The V_{GL} extracted from single sensors using CV methods.	189

List of Tables

8.12	The c -factor extracted from USTC-IME second batch single sensors using C-V method at room temperature.	189
8.13	The V_{FD} and C_p extracted from USTC-IME second batch single sensors using C-V method at room temperature.	190

1 Introduction

“Pursuit of understanding the basic elements of nature is deeply rooted in the core of science.”

Particle physics, as one of the fundamental physics, focuses on understanding the fundamental particles and forces. After decades of efforts of the particle physics community, mankind nowadays has a rather unified, beautiful, comprehensive theoretical framework, the Standard Model (SM), which serves as a vital foundation for understanding the building blocks and rules that govern our universe.

The SM in particle physics has proved its power in describing the interactions between elementary particles by three of the fundamental forces: electromagnetic, weak, and strong forces. Since the discovery of top [1, 2], bottom [3], and charm quarks [4, 5], the Z and W bosons [6, 7], and the gluon [8], the SM has been established from intertwined efforts in both theoretical and experimental communities. The model is further verified by the precision measurements of interaction coupling strengths and by the measurements of the fundamental particle properties like masses, spins, and decay widths [9]. Thanks to several decades of continuing work on both theoretical conjectures and experimental technologies that give us a clear picture of how our universe is made and behaves in the most fundamental level of current human knowledge. The most recent and important triumph in testing this model is that the last missing piece, the Higgs boson [10, 11], was eventually observed by the ATLAS and CMS experiments at the Large Hadron Collider in 2012 at CERN [12, 13] and further precision measurements verified the consistency of its properties with the SM prediction [14, 15].

Despite the success of the theory, there are still many open questions that cannot be answered by the SM, including the lack of explanation for the small masses of neutrinos and the mixing among them, the difficulty in describing the gravity force in the unified framework, hierarchy problem of the large discrepancy between the fundamental forces, and the elementary particle level constituents of dark matter.

Theoretical models beyond the SM (BSM) are proposed. Some of them are developed with extensions of the SM, including the Super-symmetry(SUSY) [16, 17], others are the brand new theoretical framework like string theory, extra dimensions. Those BSM theories can address some of the limitations mentioned above. However, up to now, none of them has solid experimental evidence.

The Higgs decays to a pair of W bosons is the channel with the second-largest branch ratio and can probe the Higgs coupling with the W boson. The $H \rightarrow WW^*$ decay with the Higgs produced by the fusions of the vector bosons or gluons has been observed with a significance of 6.1 standard deviations [18], due to that their cross-section is larger and the final states can be distinguished easily from the background. However, for the vector boson associated production, the leptonic decay of the W boson brings more than one neutrino in the final state and makes it difficult to fully reconstruct the final states. More challenges arise from the overwhelming background, such as diboson (WZ), triboson (VVV) and fake background in the final states. On the other hand, with the fast evolving of

1 Introduction

the machine learning techniques like novel neural network algorithms (eg. ANN, RNN, DNN), the analysis techniques (prompt lepton tagger, fake-factor method [19]), and the increased luminosity in the past years, the precision of the measurement has been well improved and will be described in detail in this thesis.

“The field of particle physics is constantly evolving, and upgrades to experimental setups are essential to keep up with the latest advancements.”

The Large Hadron Collider (LHC) [20], constructed and operated at CERN under the global collaboration of the particle physics community all over the world, has provided valuable data for studying various processes including very rare phenomena. However, higher statistics are needed for the precision measurements of processes [21, 22] with small cross-sections and for the search for BSM physics. In order to further improve the precision of SM and Higgs properties measurements and search for BSM physics with rare phenomena, the High Luminosity LHC (HL-LHC), as well as upgrade to the detector system, have been scheduled after the third run period of LHC [23, 24]. The HL-LHC will produce collisions at the same center of mass energy ($\sqrt{s} = 14$ TeV) as the LHC’s designed energy, with the instantaneous luminosity around $5\text{--}7 \times 10^{34} \text{ cm}^{-2}\text{s}^{-1}$, which corresponds to an increase of about a factor of five.

Moreover, the HL-LHC will enable ATLAS to measure the differential distributions of SM processes to high precision. Without increasing the collision energy, many new physics searches will shift from the “bump-hunting” analyses to search for discrepancies in the tails of distributions and other new methods. These searches will require a precise understanding of all reconstructed objects in the increased acceptance ($|\eta|$ up to 4) with the forward detector systems, which makes the improvements to the performances of the detectors in the forward region important.

The increase in the collision rate also poses new challenges for the detectors [25]. The detector system must be able to read out and record data at an unprecedentedly high rate and provide information for us to identify physics objects and reconstruct events with high efficiency. This will require significant upgrades to their readout and trigger systems in hardware and algorithms for data reconstruction and analysis in software. Additionally, the ability to distinguish signal events from background events of the detectors needs to be improved to ensure the accuracy of measurements for rare phenomena.

To further enhance the capabilities of the all-silicon Inner Tracker (ITk) [26, 27] of phase 2 ATLAS [28] in the forward region, between the inner tracker and calorimeter, a novel detector system called the HGTD has been designed [29]. This detector enables the measurement of charged-particle trajectories in both time and space (4-dimension tracking), aiming to mitigate the effects of the increased number of simultaneous interactions (pile-up) and offer a significant improvement of the performances including the isolation and identification in forward regions.

The HGTD will measure the time-of-flight of minimum-ionizing particles, and provide a time resolution of around 30 ps per track for minimum ionizing particles on average at the beginning of the HL-LHC operation, which will degrade to 50 ps by the end of the operation. By providing high-precision time measurements for charged particles, the HGTD will complement the ITk in the forward region to mitigate the pile-up effects at the HL-LHC.

The HGTD plays a significant role in improving the reconstruction of physics objects in the forward region of ATLAS [30], where the performance has been relatively worse compared to the central

detector regions. With the HGTD, the precision and fiducial phase space for these measurements will be increased, leading to a reduction in systematic uncertainties. This is essential for achieving high-precision measurements such as Higgs couplings and cross-sections of the SM processes.

Accurate luminosity determination is also critical for precision measurements. The HGTD is uniquely positioned to measure both the online luminosity on a bunch-by-bunch basis during HL-LHC running and the high-precision determination of the integrated luminosity offline. The luminosity uncertainty is already a leading uncertainty in several precision measurements of cross sections and couplings during the first two runs of the LHC. The HGTD will contribute to determine an accurate luminosity measurement for ATLAS precision measurements, including Higgs properties in HL-LHC period.

The Low Gain Avalanche Detector (LGAD) is a type of novel silicon planar sensor, proposed and developed by the CERN RD50 collaboration for several years. Such a detector can provide signals with moderate gain, fast response, and excellent timing resolution both before and after high fluences of irradiation. After several years of joint-force efforts of the RD50 and the ATLAS collaboration on R&D, LGAD sensors have been optimized and been proven to provide adequate performance for the HGTD [31]. The required timing precision of 30 ps has been achieved by the prototype sensors from multiple vendors. This level of precision is crucial for effectively disentangling the particles produced in different proton-proton collisions and reducing the impact of pile-up on the reconstruction of particle trajectories.

Although the LGAD has shown promising performance, by the time this technique is selected, there are still several key technical points that need to be addressed by further R&D work. The problems include insufficient radiation hardness to provide the required performance for the HL-LHC. The sensor burnout by a single event observed at test beams with irradiated sensors caused major concerns that need to be understood and mitigated. The design of the sensor edge and inter-pixel area need to be optimized for the final production. The comprehensive studies have been performed at USTC, starting from scratch, covering most of the key issues mentioned above. In particular, the simulation, design, fabrication, and characterization are included in this thesis. The LGAD sensors developed by the USTC and Institute of Microelectronics, Chinese Academy of Sciences (IME) have shown comparable performance with the best prototypes from other vendors [32], which make it one of the selected providers of sensors for the HGTD.

My Ph.D. research work focuses on two important topics in particle physics that face both the challenges on the unknown fundamental questions of nature and the challenges on the technical aspect of the next-generation collision experiment:

- Part I: the measurement of the associate production of vector and Higgs bosons in the $H \rightarrow WW^*$ decay mode at ATLAS.
- Part II: the development of the low-gain avalanche detector for the high-granularity timing detector upgrade from conceptual design to the systematic application.

Chapter 2 provides an overview of the SM of particle physics and the Large Hadron Collider (LHC), including the ATLAS experiment and its detector systems. This chapter also introduces the high-luminosity LHC upgrade and the high-granularity timing detector in the ATLAS phase 2 upgrade.

1 Introduction

Chapter 3 focuses on the properties of the Higgs boson, including the Brout-Englert-Higgs mechanism and the production and decay modes of Higgs. The mechanism of how elementary particles acquire masses and the discovery and measurement of the Higgs boson and its properties at the LHC are reviewed.

Chapter 4 presents a measurement of the Higgs boson production cross-section in the $H \rightarrow WW^*$, VH channel using the ATLAS detector. This chapter includes a discussion of the motivation for the measurement, an overview of the data and Monte Carlo samples used in the analysis, background estimation, systematic uncertainties, statistical treatment, and the results.

Chapter 5 provides an introduction to silicon detectors and their use in particle physics experiments. This chapter discusses the properties of silicon material, radiation damage, and an overview of different types of silicon detectors and their considerations.

Chapter 6 focuses on the low-Gain avalanche detector, a novel silicon detector technology that is being developed for the high-granularity timing detector upgrade at the ATLAS experiment. This chapter discusses the development of the LGAD technology, timing performance, radiation hardness, gain layer degradation, different types of LGAD design, and their potential applications.

Chapter 7 presents the simulation and fabrication of LGADs for the high-granularity timing detector upgrade under the collaboration of USTC and IME. This chapter includes a detailed discussion of the structure of the LGAD, such as the substrate, multiplication layer, n-plus, junction termination extension, field plate, guard-ring, float guard-ring, and p-stop.

Chapter 8 focuses on the characterization of the LGADs using various testing techniques, including current-voltage (IV) measurements, capacitance-voltage (CV) measurements, and pulse response measurements. This chapter discusses the methods and results of the characterization and the impact of the measurements on the LGAD design.

Finally, Chapter 9 presents a summary of the work carried out in this Ph.D thesis, including the contributions to the development of LGAD technology, the fabrication and characterization of LGADs, and the research and development for the use of LGADs in the high-granularity timing detector upgrade at the ATLAS experiment.

The discussion on the development of the fabrication technology for the production of AC-LGADs and DC-LGADs at USTC center for micro and nanoscale research and fabrication (NRFC) is also shown in Appendix A, which includes the development of the fabrication process for the novel silicon detector research.

Declaration

In this thesis, the Chapter 2, 3, 5, 6 are mostly review existing literature to introduce the background of the subject. Chapter 4 and 7, 8, Appendix A contain original research to which the author has contributed significantly and parts of the results have been published in journal articles. The work described in Chapter 4 is collaborative with the group, and the author's original contributions are the systematic and statistical treatment and interpretation, combination, and background modeling of the 2ℓ same sign channel.

2 Standard Model, ATLAS experiment and HGTD

2.1 The Standard Model in particle physics

The SM is a gauge field theory based on the symmetry group of $SU(3)_C \times SU(2)_L \times U(1)_Y$ that describes the fermionic constituents of matter and their interactions mediated by bosons [33–35]. It is the most successful theory in particle physics, explaining most of the experimental phenomena at the most fundamental level of today and providing very accurate predictions for a large variety of physical processes. However, it does not explain everything. It misses key items such as a description of the gravitational force or an explanation for dark matter, among other open questions in physics.

The elementary particles in the SM, including their masses, electric charges, spins, generation, and interaction with each other [9, 36] is shown by Fig. 2.1. The fermions are grouped into three generations with similar properties but different masses between different generations. The quarks are six strong interacting particles with fractional electric charge $+2/3$ (up, charm, and top) or $-1/3$ (down, strange, bottom). Leptons are transparent to the strong force and exist in three generations of negatively charged particles (electrons, muons, and tau leptons) and three flavors of neutral particles: their neutrino counterparts. Every fermion in SM has a corresponding anti-particle with the same mass but opposite electric charge and quantum numbers.

Electromagnetism, the strong force, and the weak interaction are mediated by spin-1 gauge fields. Massless gluons and photons are the carriers of the strong and electromagnetic forces [37], respectively, whereas the weak interaction is mediated by the massive W^\pm and Z bosons [33–35]. The masses of the W^\pm and Z bosons are the result of spontaneous symmetry breaking [10]. This mechanism also gives rise to a scalar particle – the Higgs boson. The framework of the SM has been introduced by several excellent references in literature [38–40] in detail. A brief review of the theoretical framework of the SM and how the Higgs boson is related to particles’ mass is given by Sec. 2.2 and Sec. 2.3.

2 Standard Model, ATLAS experiment and HGTD

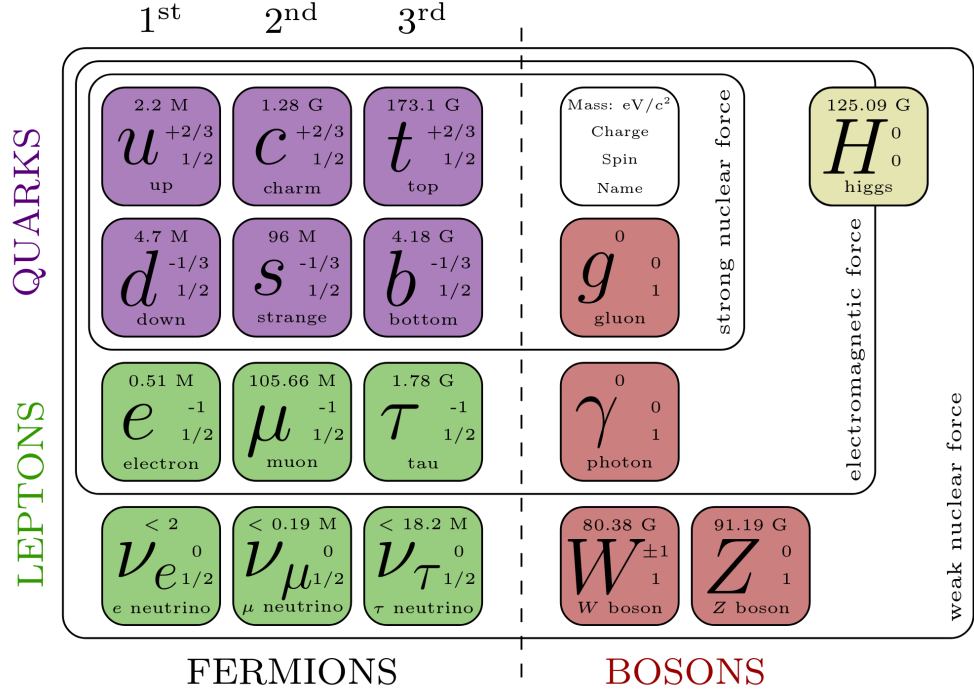


Figure 2.1: The elementary particles in the SM [9]. The chart is similar to the periodic table in chemistry but is more fundamental.

2.2 Electro-weak symmetry breaking

The whole SM theory is based on the symmetry of nature. S. L. Glashow, A. Salam, and S. Weinberg [33–35] proposed a $SU(2)_L \times U(1)_Y$ local gauge theory which unified the electromagnetism and the weak interaction. Fermions in the fundamental representation of this group appear as left-handed doublets and right-handed singlets, and they are classified by the quantum numbers of isospin charge I , associated with the $SU(2)$ symmetry group and the left-handed doublets and the hypercharge Y , associated with the right-handed singlets and the $U(1)$ symmetry group. The third component of the isospin charge I_3 and the weak hypercharge Y are related to the electric charge Q in this way [37]:

$$Y = 2(Q - I_3).$$

Therefore, in a field theory for electromagnetic and weak interactions, the Lagrangian must be invariant under gauge transformations of $SU(2) \times U(1)$. Additionally, this symmetry is broken by the Higgs mechanism down to the electromagnetic gauge symmetry in order for the W^\pm and Z bosons to acquire masses.

The full Lagrangian thus has a gauge field term \mathcal{L}_G , a Higgs field term describing its interaction with the gauge bosons \mathcal{L}_H [11, 41], a fermion-gauge boson interaction term \mathcal{L}_F and the fermion mass term \mathcal{L}_Y :

2.3 The Brout-Englert-Higgs mechanism

$$\mathcal{L}_{EWK} = \mathcal{L}_G + \mathcal{L}_H + \mathcal{L}_F + \mathcal{L}_Y.$$

For the gauge part, the isospin operators I_1, I_2, I_3 , and the hypercharge Y are each associated with a vector field. There is a triplet of vector fields W_μ^i for I_i ($i=1,2,3$) and a singlet field B_μ for Y . These define the field strength tensors:

$$W_{\mu\nu}^a = \partial_\mu W_\nu^a - \partial_\nu W_\mu^a + g_2 \epsilon_{abc} W_\mu^b W_\nu^c,$$

$$B_{\mu\nu} = \partial_\mu B_\nu - \partial_\nu B_\mu,$$

where g_2 is the non-Abelian SU(2) gauge coupling constant. Consequently, the gauge field Lagrangian can be written as

$$\mathcal{L}_G = -\frac{1}{4} W_{\mu\nu}^a W^{a,\mu\nu} - \frac{1}{4} B_{\mu\nu} B^{\mu\nu}.$$

2.3 The Brout-Englert-Higgs mechanism

The Higgs field is represented by a single complex scalar doublet field with hypercharge $Y = 1$. It couples with the other gauge fields and with itself through

$$\mathcal{L}_H = (D_\mu \Phi)^\dagger (D^\mu \Phi) - V(\Phi),$$

where the gauge invariant covariant derivative and the Higgs self-interaction are defined as

$$D_\mu = \partial_\mu + ig_2 W_\mu^a \frac{\tau^a}{2} + ig_1 \frac{Y}{2} B_\mu,$$

$$V(\Phi) = -\mu^2 \Phi^\dagger \Phi + \frac{\lambda}{4} (\Phi^\dagger \Phi)^2,$$

with g_1 being the Abelian U(1) coupling and where λ and μ are parameters. τ^a are the Pauli matrices, which constitute the generators for the Lie algebra of SU(2).

This potential has a vacuum expectation value of

$$\langle \Phi \rangle = \frac{1}{\sqrt{2}} \begin{pmatrix} 0 \\ v \end{pmatrix},$$

where

2 Standard Model, ATLAS experiment and HGTD

$$v = \frac{2\mu}{\sqrt{\lambda}}.$$

As a consequence, the bosonic fields and the Higgs field acquire the following masses:

$$m_W = \frac{vg_2}{2},$$

$$m_Z = \frac{v}{2}\sqrt{g_1^2 + g_2^2},$$

and

$$m_H = v\sqrt{2\lambda}.$$

The W and Z boson masses are related by the coupling constant, and the ratio between them can be associated with the weak mixing angle or Weinberg angle. This angle is the angle by which spontaneous symmetry breaking rotates the original W^3 and B vector boson plane, producing the Z boson and the photon as a result,

$$\frac{m_W}{m_Z} = \frac{g_2}{\sqrt{g_1^2 + g_2^2}} = \cos \theta_W,$$

$$\begin{pmatrix} \gamma \\ Z^0 \end{pmatrix} = \begin{bmatrix} \cos \theta_W & -\sin \theta_W \\ \sin \theta_W & \cos \theta_W \end{bmatrix} \begin{pmatrix} B \\ W^3 \end{pmatrix}.$$

The fermionic part of the Lagrangian has one term describing the interactions with the boson fields and one term where the Yukawa couplings between fermions and the Higgs boson give rise to the fermion masses. Given a family of fermions, taking the first generation of quarks as an example, we use this notation for the fermionic field:

$$\psi_1 = \begin{pmatrix} u \\ d \end{pmatrix}_L, \psi_2 = u_R, \psi_3 = d_R.$$

The same may be defined for leptons using ν_e and e instead of u and d , and for the other quark and lepton families. With this definition, the interaction between gauge boson fields and fermions can be written using the covariant derivative:

$$\mathcal{L}_F = \sum_j i\bar{\psi}_j(x)\gamma^\mu D_\mu \psi_j(x).$$

For the Yukawa Lagrangian, we can choose the following gauge to simplify the term:

2.3 The Brout-Englert-Higgs mechanism

$$\Phi = \begin{pmatrix} \Phi^+(x) \\ \Phi^0(x) \end{pmatrix} = \frac{1}{\sqrt{2}} \begin{pmatrix} 0 \\ v + H(x) \end{pmatrix},$$

which results in the simple expression for the fermion mass terms

$$\mathcal{L}_Y = - \sum_f m_f \bar{\psi}_f \psi_f - \sum_f \frac{m_f}{v} \bar{\psi}_f \psi_f H,$$

where $m_f = g_f \frac{v}{\sqrt{2}}$ is the mass of the fermions, which depends on the Yukawa coupling constants g_f .

With this Lagrangian, the mass eigenstates for fermions are defined, but for quarks, they do not coincide with the weak eigenstates. There is a mixing between flavors when there are charged currents involved (the W^\pm), which is represented by a unitary matrix (shown by Eq. 2.1) called Cabibbo-Kobayashi-Maskawa (CKM) matrix [42].

$$\begin{bmatrix} d' \\ s' \\ b' \end{bmatrix} = \begin{bmatrix} V_{ud} & V_{us} & V_{ub} \\ V_{cd} & V_{cs} & V_{cb} \\ V_{td} & V_{ts} & V_{tb} \end{bmatrix} \begin{bmatrix} d \\ s \\ b \end{bmatrix}. \quad (2.1)$$

The unitarity of the CKM matrix, $(VV^\dagger)_{ij} = (V^\dagger V)_{ij} = \delta_{ij}$, leads to twelve distinct complex relations among the matrix elements. The six relations with $i \neq j$ can be represented geometrically as triangles in the complex plane. Two of these

$$\begin{aligned} V_{ud}V_{ub}^* + V_{cd}V_{cb}^* + V_{td}V_{tb}^* &= 0, \\ V_{td}V_{ud}^* + V_{ts}V_{us}^* + V_{tb}V_{ub}^* &= 0, \end{aligned}$$

have terms of equal order, $\mathcal{O}(A\lambda^3)$, and so have corresponding triangles whose interior angles are all $\mathcal{O}(1)$ physical quantities that can be independently measured. The angles of the first triangle are given by

$$\begin{aligned} \alpha \equiv \phi_2 &\equiv \arg\left(-\frac{V_{td}V_{tb}^*}{V_{ud}V_{ub}^*}\right) \simeq \arg\left(-\frac{1-\rho-i\eta}{\rho+i\eta}\right), \\ \beta \equiv \phi_1 &\equiv \arg\left(-\frac{V_{cd}V_{cb}^*}{V_{td}V_{tb}^*}\right) \simeq \arg\left(\frac{1}{1-\rho-i\eta}\right), \\ \gamma \equiv \phi_3 &\equiv \arg\left(-\frac{V_{ud}V_{ub}^*}{V_{cd}V_{cb}^*}\right) \simeq \arg(\rho+i\eta). \end{aligned}$$

The angles of the second triangle are equal to (α, β, γ) up to corrections of $\mathcal{O}(\lambda^2)$. The notations (α, β, γ) and (ϕ_1, ϕ_2, ϕ_3) are both in common usage but, for convenience, we only use the first convention in the following.

2 Standard Model, ATLAS experiment and HGTD

With the decomposition as Eq. 2.2, where $s_{ij} = \sin \theta_{ij}$, $c_{ij} = \cos \theta_{ij}$, and δ is the phase for all CP -violating phenomena in the processes where flavor changed in the SM.

$$V_{\text{CKM}} = \begin{bmatrix} V_{ud} & V_{us} & V_{ub} \\ V_{cd} & V_{cs} & V_{cb} \\ V_{td} & V_{ts} & V_{tb} \end{bmatrix} = \begin{bmatrix} 1 & 0 & 0 \\ 0 & c_{23} & s_{23} \\ 0 & -s_{23} & c_{23} \end{bmatrix} \begin{bmatrix} c_{13} & 0 & s_{13}e^{-i\delta} \\ 0 & 1 & 0 \\ -s_{13}e^{i\delta} & 0 & c_{13} \end{bmatrix} \begin{bmatrix} c_{12} & s_{12} & 0 \\ -s_{12} & c_{12} & 0 \\ 0 & 0 & 1 \end{bmatrix}. \quad (2.2)$$

Thus, the CKM matrix can be defined by three angles and one CP -violating phase. There are four free parameters in the matrix of the SM that are experimentally measured. The results are interpreted by a global fit of several experiments simultaneously for the four free parameters [43], and the unitarity are verified.

2.4 The Large Hadron Collider and the ATLAS experiment

Pursuing the energy and precision frontier is always the goal for particle physics to further understand the composition and the evolution of our universe. By analyzing the fundamental particles and their interactions, physicists have gradually established the SM introduced in Sec. 2.1, which has successfully described all 3 of 4 known interactions in the universe. The experimental input is important for providing the validation of the current theory and potential hints for the new theory beyond our current understanding. In the experimental area, the top quark was successfully discovered in 1995 by the CDF and D0 experiment at the Tevatron accelerator at Fermilab [1, 2]. The W and Z bosons are found by the UA1 and UA2 experiments at Super Proton Synchrotron (SPS) at CERN [6, 7], providing further experimental proofs of the model. After the efforts of experimental physicists in the past decades, the SM has been well validated except for the Higgs boson that eluded the discovery for a long period until the operation of the new experiments with a more powerful collider – **The Large Hadron Collider**.

The LHC is the world's largest and most powerful particle accelerator, located at CERN in Geneva, Switzerland [20]. The LHC accelerator complex is designed to accelerate protons to extremely high energies (up to 14 TeV) and then collide them together in a controlled environment. The LHC accelerator complex is a chain of several accelerators that work together to progressively increase the energy of the protons, as shown in Fig. 2.2. The complex includes the following accelerators, listed in the order in which they are used to accelerate the protons:

- Linear Accelerator 2/4¹ (Linac2/Linac4): This accelerator provides the initial acceleration to the protons, bringing them up to an energy of 50 MeV.
- Proton Synchrotron Booster (PSB): The protons are then injected into the PSB, which further accelerates them to an energy of 1.4 GeV.
- Proton Synchrotron (PS): The protons out of PSB are sequentially accelerated by PS to an energy of 25 GeV.

¹The Linac4 replaced the Linac2 as the new linear accelerator to inject the protons for LHC since 2020.

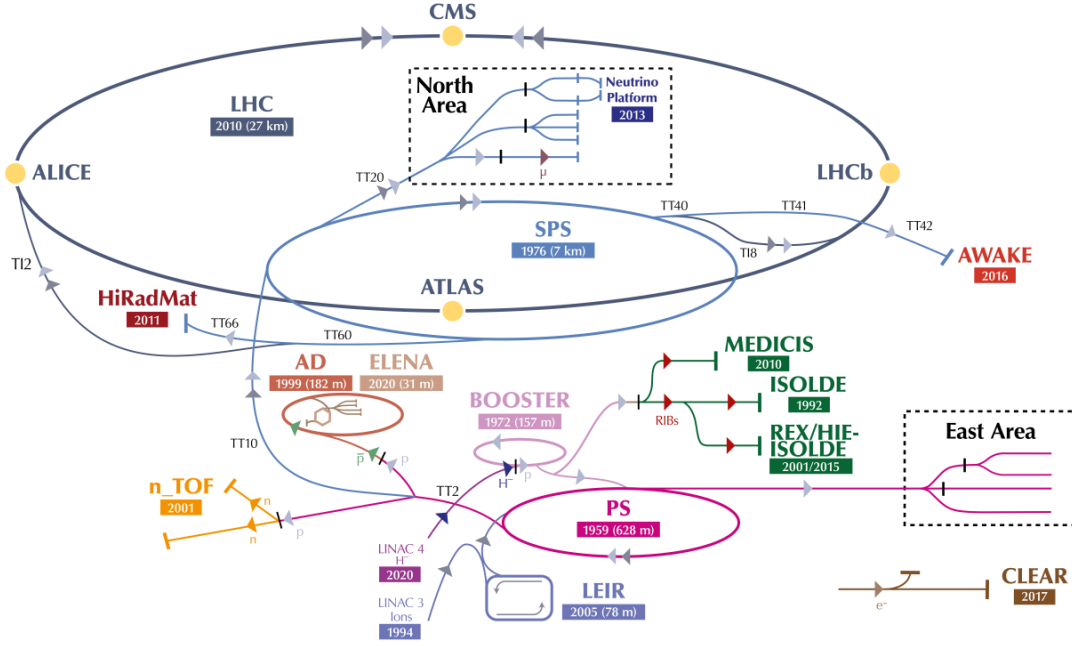


Figure 2.2: The LHC accelerator complex for the hadron collision experiment at $\sqrt{s} = 14$ TeV.

- Super Proton Synchrotron (SPS): Following this, the SPS accelerates them to an energy of 450 GeV.
- Large Hadron Collider (LHC): Finally, the protons are injected into the LHC, which accelerates them to their maximum energy of 6.5 (7.0)² TeV per proton, resulting in a total center-of-mass energy up to 14 TeV.

The LHC main ring has a length of 27 kilometers with superconducting magnets equipped, which are used to guide the protons flying along the ring and reaching almost the speed of light. It also has several radiofrequency (RF) cavities equipped for accelerating the charged particles by its high-frequency electric field. The protons are designed to travel in opposite directions and collide at the four main interaction points, where detectors are installed to record the final state particles of the collision events.

2.5 The ATLAS detector

The ATLAS detector, is one of the most complex and innovative instruments ever built by mankind [21]. It plays a critical role in the LHC experiments as a general-purpose detector. It enables physicists to study the fundamental building blocks of matter and the interactions among them. The whole detector is a complex system composite of several sub-detectors that work together (as shown in Fig. 2.3) to

² The maximum energy of the protons and the energy of the collision depends on the run period of the LHC and can be found in Fig. 2.7 in detail. The LHC uses the 13 TeV center of mass energy in its second run period and gradually increases to the maximum 14 TeV in high luminosity LHC runs.

2 Standard Model, ATLAS experiment and HGTD

detect particles produced from the collisions at the LHC and to measure their properties. The detector covers almost the entire solid angle around the collision point and is designed to capture varieties of different particles, including electrons, photons, muons, and hadrons. A detailed review of the system can be found in [44].

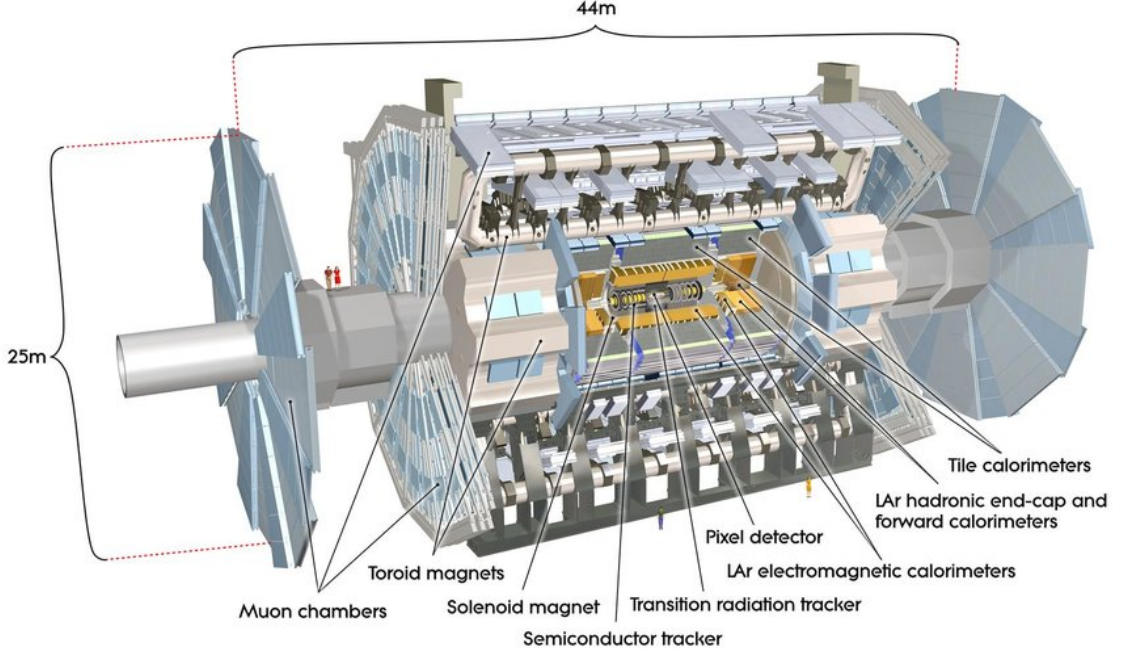


Figure 2.3: The ATLAS detector and subsystems [44].

The right-handed Cartesian coordinate system is used with the origin defined as the nominal collision point. The z -axis follows the beamline of the protons coming from the Geneva side to the direction of the Jura mountain. The x -axis points to the center of the LHC ring, and the y -axis goes upwards. The azimuthal angle ϕ in the range of $[0, 2\pi]$ is defined with respect to the x -axis in the x - y plane. The polar angle θ in the range of $[0, \pi]$ is defined with respect to the beam axis, and a more convenient definition, the pseudorapidity, is commonly used, which is defined by $\eta = -\ln \tan \frac{\theta}{2}$. By those definitions, the transverse momentum, as well as the energy, can be defined in the x - y plane, and the angular distance is defined by $\Delta R = \sqrt{\Delta\eta^2 + \Delta\phi^2}$. The intuitive visual illustration of the coordinate system for both ATLAS and CMS can be found in [45].

2.5.1 Inner detector

The inner detector (ID) system is one of the most crucial components of the ATLAS detector. It is situated in a 2 T axial magnetic field and provides charged-particle tracking in the range $|\eta| < 2.5$. The inner detector system is composed of three different detectors, each of which performs a specific function. The schematic view of the inner detector system is shown in Fig. 2.4.

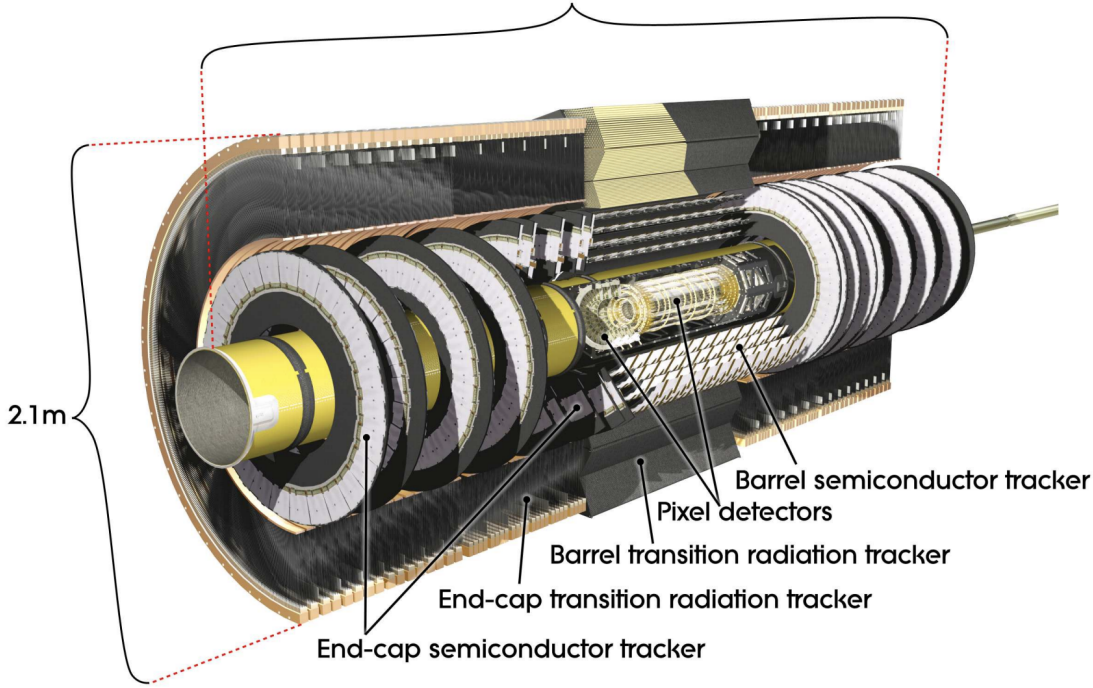


Figure 2.4: Schematic view of the ATLAS inner detector system [44].

The innermost detector in the inner detector system is the silicon pixel detector, which is responsible for detecting particles that pass through the vertex region. The silicon pixel detector provides four measurements per track and has an insertable B-layer (IBL) installed before the LHC Run 2 [46], which provides additional coverage and enhances the performance.

The silicon microstrip tracker (SCT) is outside the pixel detector [47]. It provides eight measurements per track and complements the silicon pixel detector in the detection of charged particles. The transition radiation tracker (TRT) is the outermost detector in the inner detector system [48]. It provides information about electron identification and enables radially extended track reconstruction up to $|\eta| = 2.0$. The TRT works by detecting the transition radiation emitted when an electron passes through the boundaries of different materials.

2.5.2 Calorimeter system

The electromagnetic and hadronic calorimeters are the sub-detectors outside the inner detector in ATLAS. They are responsible for measuring the energy and position of electrons, photons, and hadrons. The electromagnetic calorimeter is composed of lead and liquid argon and measures the energy of electrons and photons. The hadronic calorimeter is made of steel as absorber and liquid argon (scintillator tiles) as active material in barrel (endcap) regions. The schematic view of the calorimeter system is shown in Fig. 2.5.

2 Standard Model, ATLAS experiment and HGTD

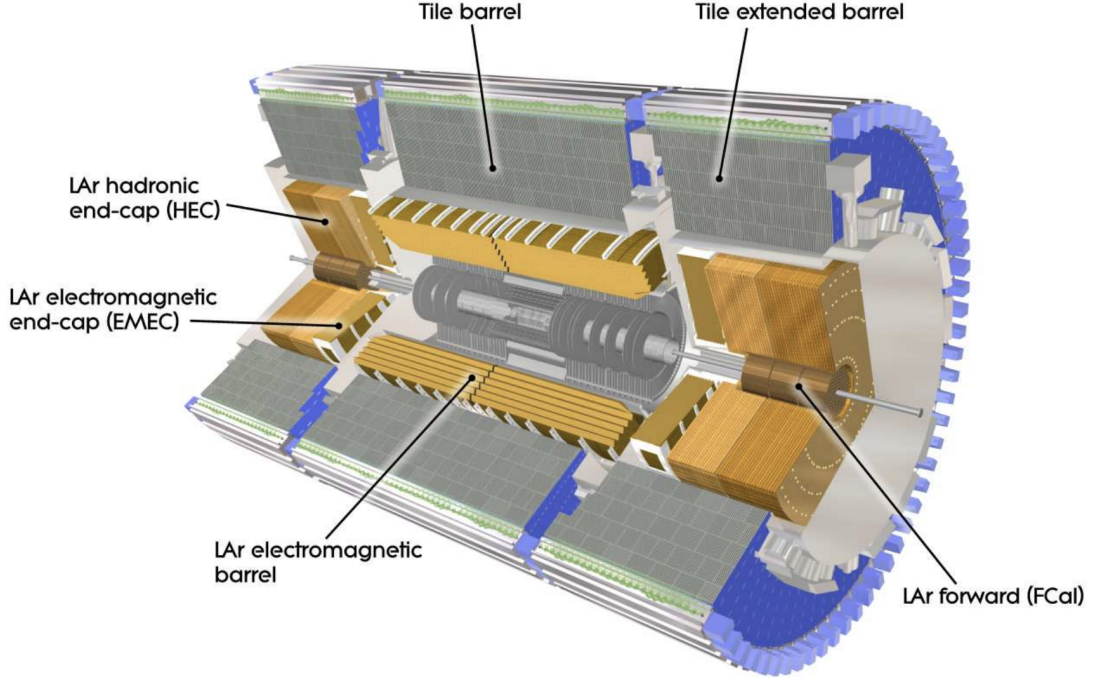


Figure 2.5: Schematic view of the ATLAS calorimeter system [44].

The calorimeter system covers a wide pseudorapidity range of $|\eta| < 4.9$. Within the pseudorapidity range $|\eta| < 3.2$, the electromagnetic calorimetry (EM) is provided by the combination of barrel and endcap high-granularity lead/liquid-argon (LAr) calorimeters [49]. These calorimeters are designed to provide accurate energy measurements of electrons and photons. Additionally, an extra thin LAr pre-sampler covers the range $|\eta| < 1.8$ to correct for energy loss in material upstream of the calorimeters.

The hadronic calorimeter is segmented into three barrel structures [50] within the range $|\eta| < 1.7$, and two copper/LAr hadron endcap calorimeters. These calorimeters are optimized to detect and measure the energy of hadrons and other particles. The solid angle coverage of the ATLAS detector is completed with forward copper/LAr and tungsten/LAr calorimeter modules that are optimized for electromagnetic and hadronic energy measurements, respectively.

2.5.3 Muon spectrometer

The muon spectrometer (MS) is the outermost sub-detector in the ATLAS detector. It incorporates three large superconducting air-core toroidal magnets and provides precise measurements of muon trajectories [51]. The muon spectrometer is designed to detect muons, which are produced in the collisions of protons. The schematic view of the muon spectrometer system is shown in Fig. 2.6.

The muon chambers are designed to identify muons efficiently and trigger the detectors to read out when an event with interesting properties is observed. The high-precision tracking chambers

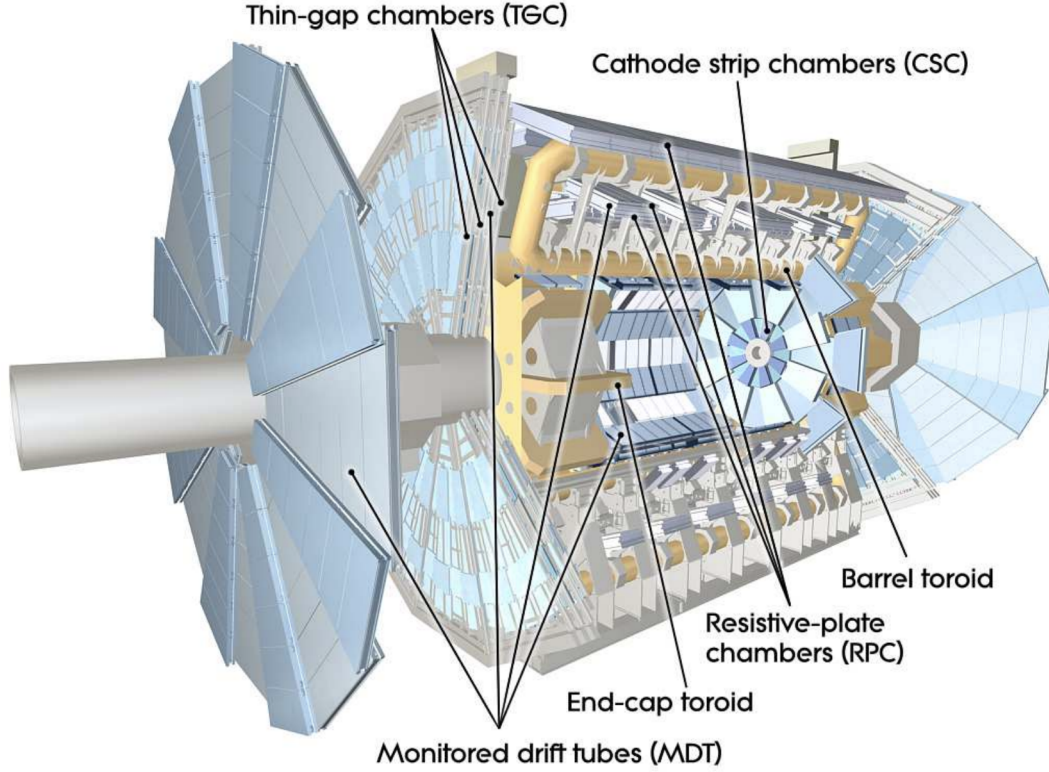


Figure 2.6: Schematic view of the ATLAS muon spectrometer system [44].

are used to measure the deflection of muons in a magnetic field generated by the superconducting air-core toroidal magnets. The field integral of the toroids ranges between 2.0 and 6.0 T · m, providing excellent measurement precision for the muons.

Three layers of precision chambers cover the region $|\eta| < 2.7$, each consisting of monitored drift tubes (MDT) that provide high-resolution tracking information. In the forward region, where the soft-scattering is dominant, cathode-strip chambers complement the precision chambers. The combination of precision and cathode-strip chambers allows for precise momentum measurements of muons across a wide range of angles.

The muon trigger system covers the range $|\eta| < 2.4$, using resistive-plate chambers (RPC) in the barrel and thin-gap chambers (TGC) in the endcap regions. With such layouts, the total uncertainty for the measurement of transverse momentum for muons is around 3% over a wide range of p_T and up to 10% for muons with 1 TeV of transverse momentum [52].

In conclusion, the ATLAS detector is an innovative and complex instrument that plays a critical role in LHC experiments. Its design and operation are essential for detecting and identifying particles produced in proton-proton collisions at the LHC, allowing physicists to study the fundamental properties of matter and the interactions between its building blocks.

2 Standard Model, ATLAS experiment and HGTD

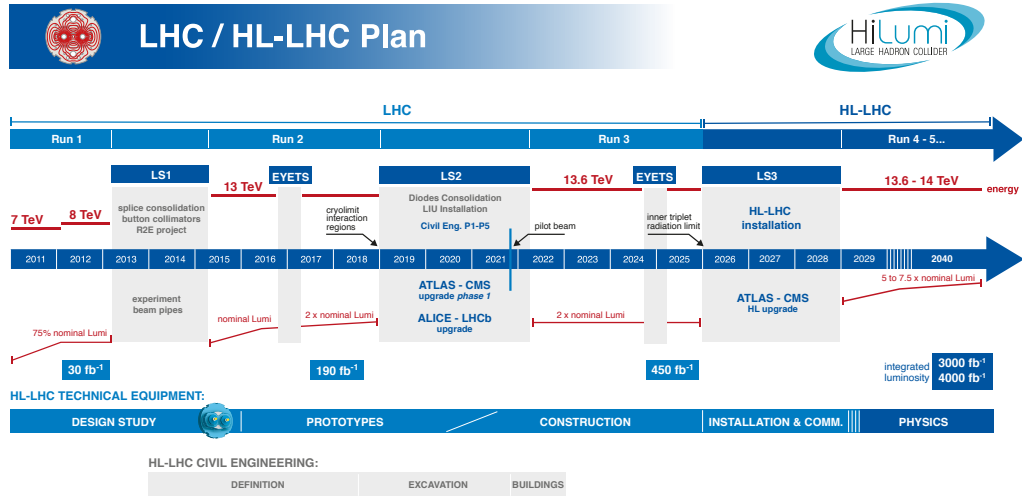


Figure 2.7: The LHC/HL-LHC project schedule (updated in February 2022).

2.6 The high luminosity upgrade of the LHC

The high luminosity LHC (HL-LHC) physics program promises to be an exciting time for researchers in the field. The upgraded accelerator is expected to provide a massive integrated luminosity of approximately 2500 fb^{-1} over the course of 10 years to the ATLAS and CMS detectors. This extended period of operation will enable scientists to probe deeper into the search for new physics, as well as to gain a more comprehensive understanding of the properties of the Higgs boson [53]. Several new technologies will be applied to realize this in the new phase of the LHC, which are shown and summarized in Fig. 2.7.

However, with the unprecedented proton-proton luminosity comes new experimental challenges. The experiments will need to address the aging of the current detectors under a radiation environment and develop new techniques to isolate and precisely measure the products of the most interesting collisions. These challenges require a great deal of skill and expertise from the researchers and engineers involved in the project, but the potential rewards are significant in terms of advancing our understanding of the universe and the fundamental laws that govern it. The most recent schedule of the HL-LHC upgrade is shown in Fig. 2.8.

2.7 The ATLAS phase 2 upgrade and the high-granularity timing detector

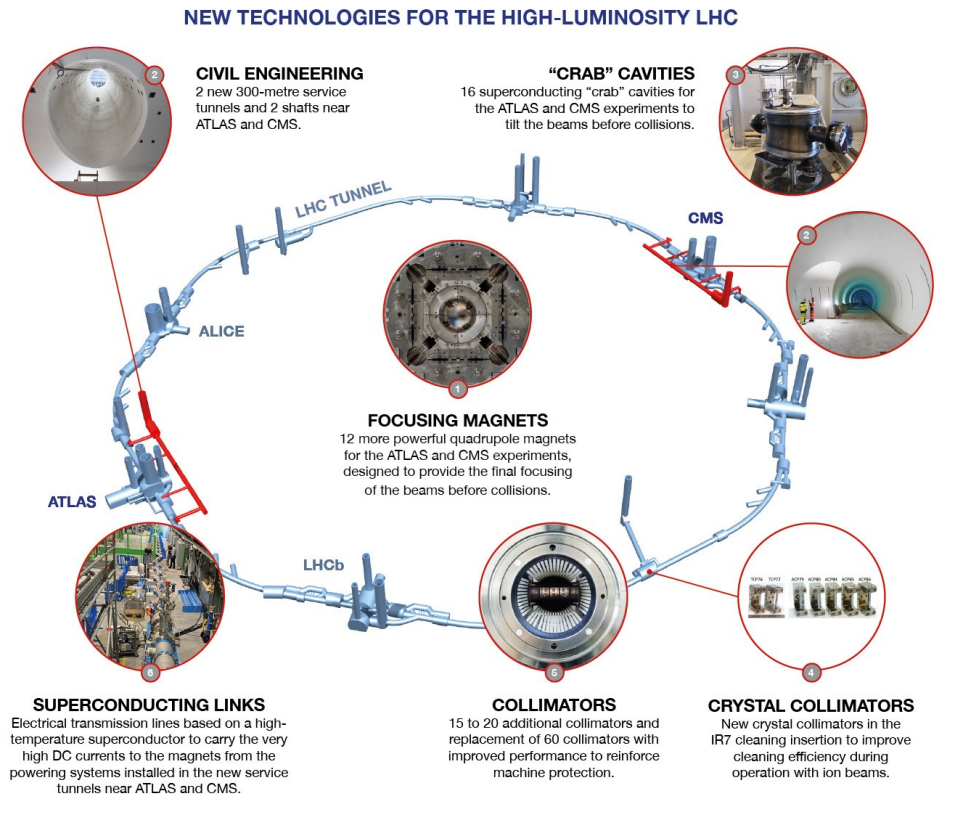


Figure 2.8: Novel technologies to be used for the high-luminosity LHC.

2.7 The ATLAS phase 2 upgrade and the high-granularity timing detector

2.7.1 Preparing ATLAS for the future – The ATLAS phase 2 upgrade

For the ATLAS detector, there are many issues that need to be addressed to make the detector work well under 5-8 times higher luminosity and benefit as much as possible from the upgrade of the HL-LHC. This major upgrade for the ATLAS detector scheduled for 2026-2028 of the LHC long shutdown 3 (LS3) is called "the phase 2 upgrade". The issues about the challenges that need to be considered for the ATLAS upgrade includes:

- the trigger and data acquisition system (higher trigger rate),
- the tracking system (the gas-based TRT outer tracker need to be upgraded to a full silicon version to record event at a higher rate and have better resolution for background rejection),
- the luminosity measurement system to achieve the precision measurement as discussed in Chapter 1,

2 Standard Model, ATLAS experiment and HGTD

- the muon spectrometer to have better efficiency, resolution, isolation, coverage,
- the rejection of significantly higher pile-up contributions in high luminosity operation (as shown in Fig. 2.9).

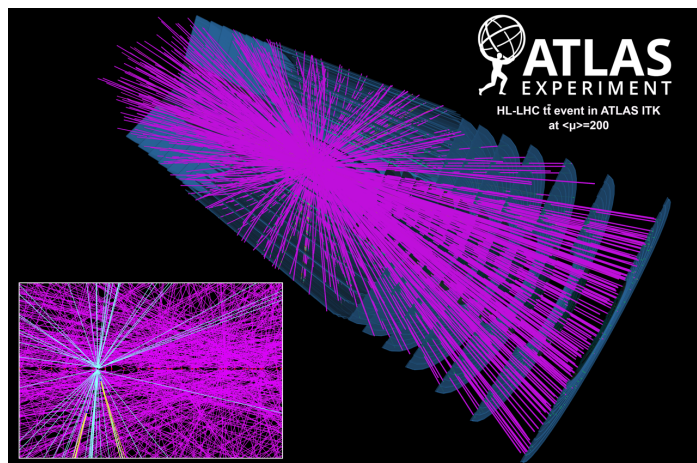


Figure 2.9: A simulated $t\bar{t}$ event at average pile-up of 200 collisions per bunch crossing at the ATLAS in HL-LHC phase [54].

The corresponding projects have been proposed and scheduled, including the Inner Tracker (ITk) Pixel [26] and Strip [27], the Liquid Argon Calorimeter (LAr) [55], the Tile Calorimeter [56], the High-Granularity Timing Detector (HGTD) [57], the Muon Spectrometer [58], and the TDAQ [59]. The work for this thesis would focus on the HGTD upgrade where a novel silicon detector technology and the concept of the 4-D tracking (shown in Fig. 2.10) at 30 ps is planned to be used in the particle experiment for the first time.

2.7.2 The HGTD in ATLAS phase 2

The HGTD is a proposed detector system [57, 60] for the ATLAS experiment as part of the phase 2 upgrade in preparation for the HL-LHC which is expected to start operations in 2029. The HL-LHC, being operated at a much higher luminosity, will result in a significant increase in collision rates. The HGTD is designed to handle this increased collision rate by providing high-precision timing measurements.

The HGTD plays a key role in mitigating the effects of pile-up, which is the phenomenon where multiple proton-proton collisions occur within the same bunch crossing, making it difficult to distinguish between the particles produced in each collision. The HGTD's timing resolution will allow to separate the signals from the different collisions, reducing the impact of pile-up on ATLAS measurements by the concept of 4-D tracking. As shown in Fig. 2.10, with the precise timing information provided by HGTD, the hard-scattering vertex (our signal candidate) can be more easily separated. In addition to its timing capabilities, the HGTD will also provide additional tracking information, which will allow for improved identification of particle types and the reconstruction of particle trajectories when matching with the inner tracker.

2.7 The ATLAS phase 2 upgrade and the high-granularity timing detector

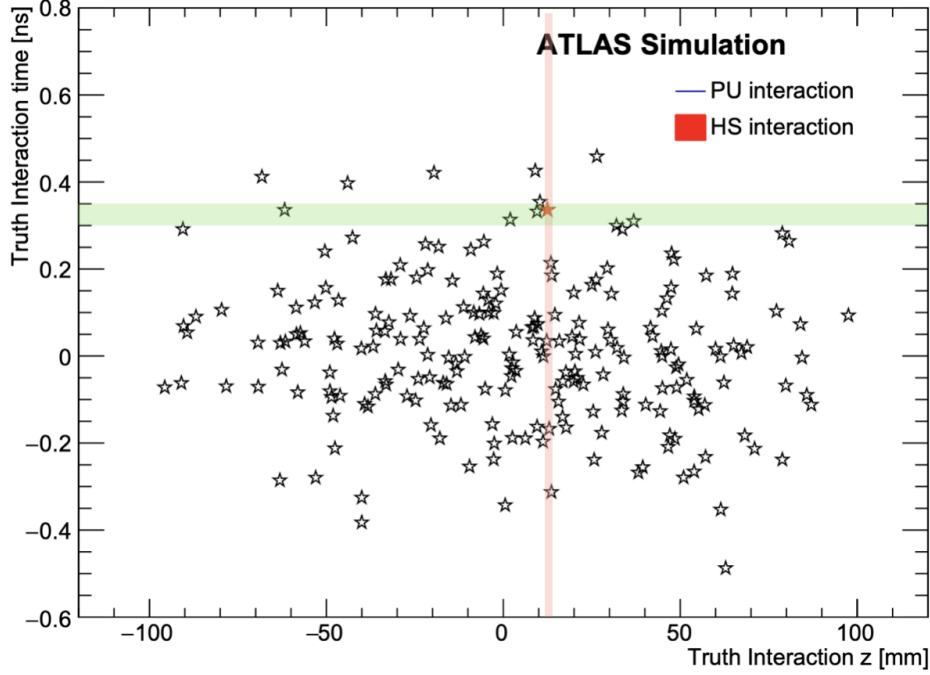


Figure 2.10: The simulated interaction distributions in both the Spatial axis (direction along the LHC beam line) and Timing axis (time from the center of time for bunch crossing) from one HL-LHC bunch crossing. Around 200 pile-up interaction vertices are shown by the stars. The pile-up vertices are shown in black. One hard scattering vertex is shown by the red star. The nominal ITk resolution in the forward region, 2 mm, for the soft particles is shown by the red band for spatial direction and the expected time resolution of HGTD (50 ps) is shown by the green band in timing direction. (Figure adapted from [57]).

The HGTD system consists of two hermetic vessels, each containing two instrumented double-sided layers mounted on cooling/support disks. The sensor technology for each of the layers is LGAD which are silicon sensors that provide a moderate gain for improved timing performance. The HGTD will be positioned in the gap region between the barrel and end-cap calorimeters (as shown by Fig. 2.11), approximately ± 3.5 m from the nominal interaction point, and will cover a pseudo-rapidity between 2.4 and 4.0. The HGTD will measure the times of arrival of minimum-ionizing particles with an average time resolution of approximately 30 ps per track at the beginning of the High Luminosity LHC and towards the end of the HL-LHC operation, the time resolution is expected to be degraded to 50 ps.

For the HGTD, the chosen layout of LGAD sensors (shown in Tab. 2.1) provides an active area per sensor of $19.5 \text{ mm} \times 19.5 \text{ mm}$, resulting in a total of 16064 sensors for total HGTD area with 15×15 pixel array on each sensor.

The detector is designed to cover a pseudo-rapidity range of $2.4 < |\eta| < 4.0$ by several layers of the LGAD sensors, which have an active thickness of $50 \text{ } \mu\text{m}$. It has a total of 3.6 million channels and an active area of 6.4 m^2 . The modules are sized $2 \text{ cm} \times 2 \text{ cm}$ with a pixel size of $1.3 \text{ mm} \times 1.3 \text{ mm}$. The collected charge per hit needs to be greater than 4.0 fC. The approximate average number of hits per track ranges from 2.0 to 2.6, depending on the pseudo-rapidity range. The average time resolution

2 Standard Model, ATLAS experiment and HGTD

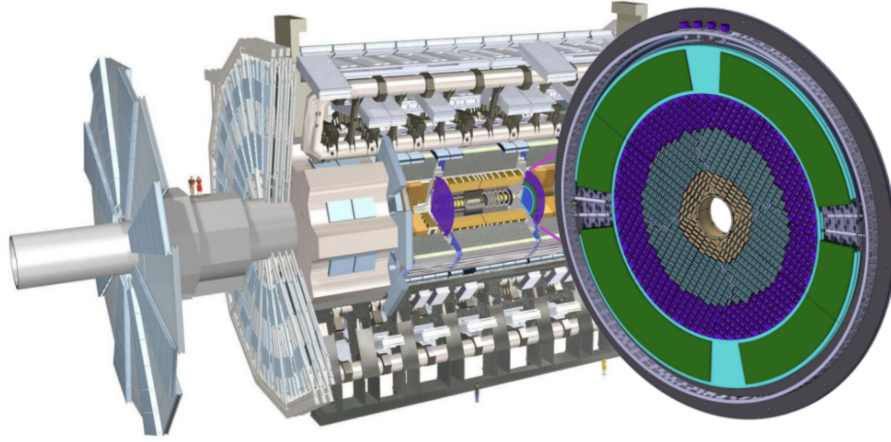


Figure 2.11: The position of HGTD in the ATLAS detector at the HL-LHC [57].

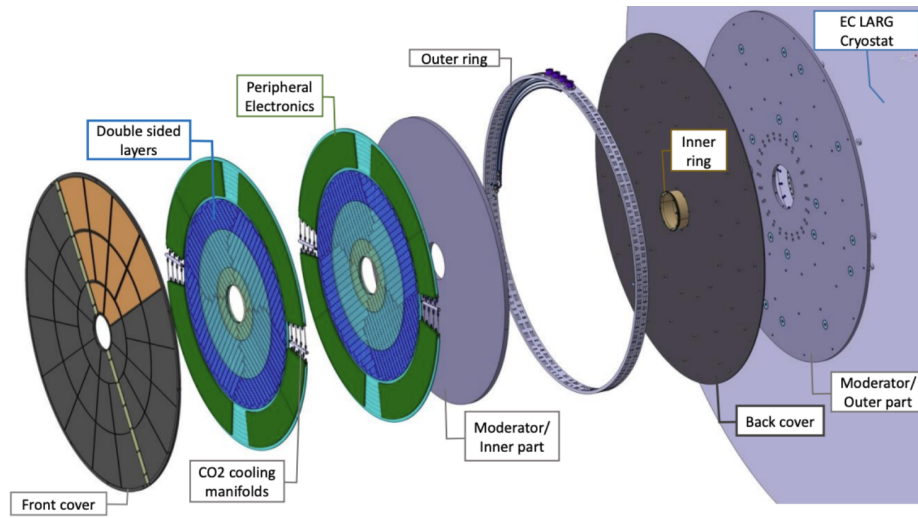


Figure 2.12: The composition of the HGTD system [57].

per hit at the start and end of the operational lifetime is ≈ 35 ps and ≈ 70 ps, respectively, while the average time resolution per track is ≈ 30 ps at the start and 50 ps at the end. The main parameters of the HGTD design are summarized in the Tab. 2.1.

2.7 The ATLAS phase 2 upgrade and the high-granularity timing detector

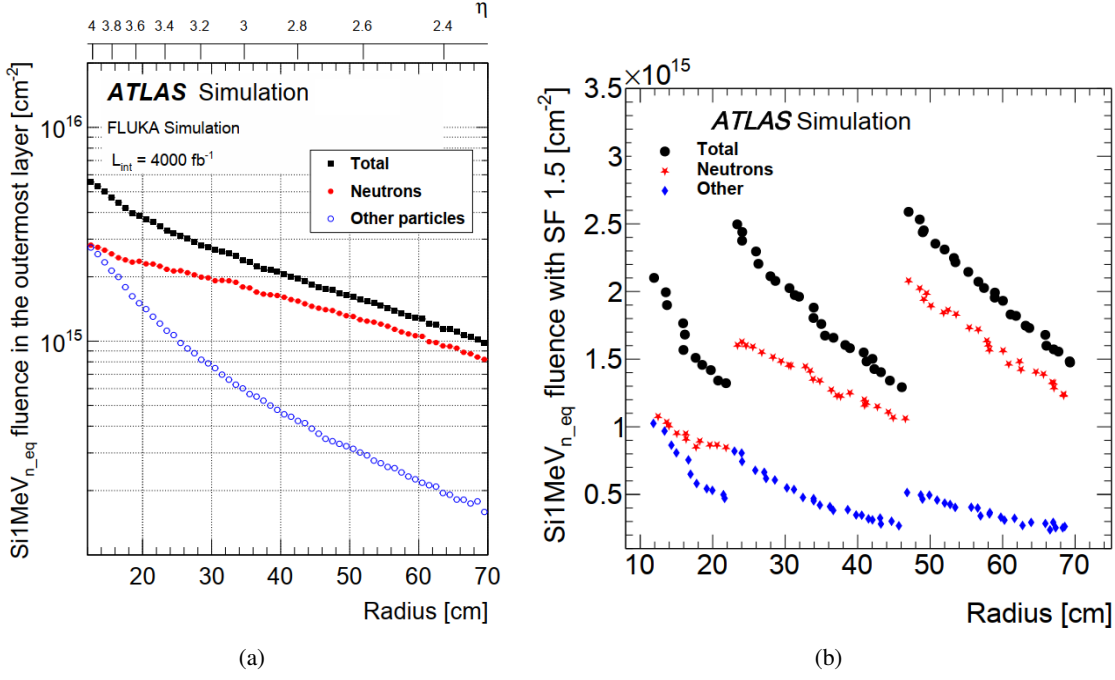


Figure 2.13: The simulated non-ionizing radiation fluences in the HGTD area. (a) Expected nominal Si 1 MeV_{n_eq} fluence dose as functions of the radius in the outermost sensor layer of the HGTD for 4000 fb⁻¹, i.e. before including safety factors. (b) The NIEL fluence of the HGTD region for the HL-LHC with 1.5 safe factor applied and considering ring replacements. [57].

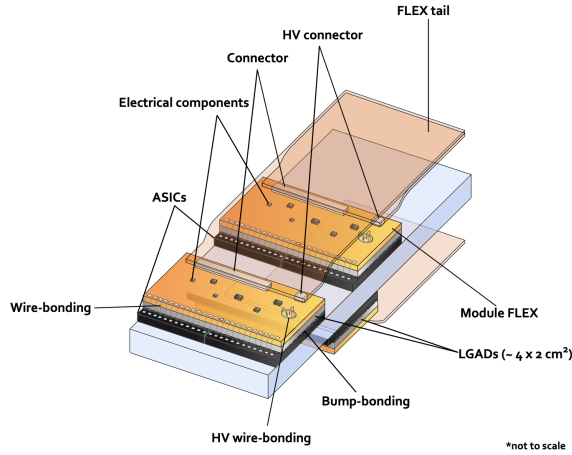


Figure 2.14: Schematic drawing of two adjacent modules on the top side and one on the bottom side of the cooling plate [57].

2 Standard Model, ATLAS experiment and HGTD

Table 2.1: Main parameters of the HGTD design. The table is taken from [57] with the recent updates implemented.

Pseudo-rapidity coverage	$2.4 < \eta < 4.0$
Thickness in z	75 mm(+50 mm moderator)
Position of active layers in z	± 3.5 m
Weight per end-cap	350 kg
Radial extension:	
Total	$110 \text{ mm} < r < 1000 \text{ mm}$
Active area	$120 \text{ mm} < r < 640 \text{ mm}$
Pad size	$1.3 \text{ mm} \times 1.3 \text{ mm}$
Active sensor thickness	$50 \mu\text{m}$
Number of channels	3.6 M
Active area	6.4 m^2
Module size	15×15 pads ($2 \text{ cm} \times 2 \text{ cm}$)
Modules	16064
Collected charge per hit	$> 4.0 \text{ fC}$
Average number of hits per track	
$2.4 < \eta < 2.7$ ($640 \text{ mm} > r > 470 \text{ mm}$)	≈ 2.0
$2.7 < \eta < 3.5$ ($470 \text{ mm} > r > 230 \text{ mm}$)	≈ 2.4
$3.5 < \eta < 4.0$ ($230 \text{ mm} > r > 120 \text{ mm}$)	≈ 2.6
Average time resolution per hit (start and end of operational lifetime)	
$2.4 < \eta < 4.0$	$\approx 35 \text{ ps}$ (start), $\approx 70 \text{ ps}$ (end)
Average time resolution per track (start and end of operational lifetime)	$\approx 30 \text{ ps}$ (start), $\approx 50 \text{ ps}$ (end)

Part I

Measurement of associate production of vector and Higgs bosons with the $H \rightarrow WW^*$ decay mode at ATLAS

3 Higgs Boson Production and Property Studies at the ATLAS Experiment

3.1 Higgs production at LHC

The SM predicts four main Higgs boson production mechanisms processes that originate from proton-proton collisions at the LHC. Interaction between gluons and quarks produces a Higgs boson alone or in addition to other particles like vector bosons and quarks. The four dominant production mechanisms are shown in Feynman diagrams in Fig. 3.1, and the production cross-section through those different processes is presented in Fig. 3.2.

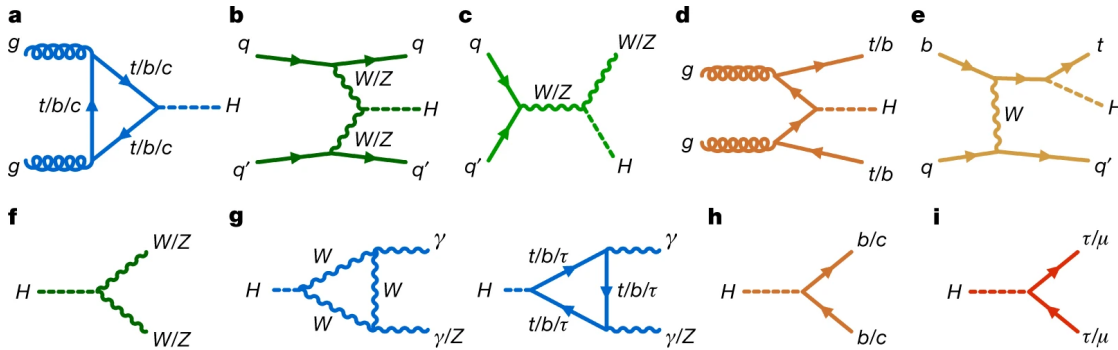


Figure 3.1: The Feynman diagrams for the Higgs production and decay [15].

Gluon fusion- ggF

The largest number of Higgs bosons are produced at the LHC through the gluon fusion (ggF) involving a fermion loop (Fig. 3.1 (a)). The dominant contribution to this process comes from top quark loops, while bottom quark loops and negative top-bottom interference can contribute up to 10%. However, perturbative expansion in QCD for the $pp \rightarrow H, ggF$ converges slowly, with significant corrections at NLO and NNLO. These corrections are comparable in size to or even larger than the uncertainties introduced by parton density functions and QCD scale variations [61]. Recently, researchers have calculated results up to NNNLO using an effective theory with the top-quark integrated out [62] (result shown in Fig. 3.2), and NLO electroweak corrections have also been computed with high precision. The final uncertainty is 5.6% for the theoretical calculation and 3.2% for PDF and α_s contribution.

3 Higgs Boson Production and Property Studies at the ATLAS Experiment

Vector boson fusion- VBF

The production of Higgs boson through the fusion of two vector bosons (VBF) (Fig. 3.1 (b)) is a significant contribution to the LHC, providing the second-largest cross-section. In order to target this production mechanism in the experiment, the two accompanying quark jets with high energy in the final state can be exploited to select events efficiently. The VBF process, $pp \rightarrow qqH$, has been accurately calculated to NNLO in QCD, along with NLO EW corrections. The calculation employs the description of double deep inelastic scattering, which is applied to the fusion of pure electroweak vector bosons into a colorless Higgs boson [63]. The correction 2% level uncertainties for total cross sections at the LHC from higher order corrections and the parton distribution uncertainties are achieved separately for the VBF production.

Vector boson associated production- VH

The production of Higgs bosons in association with a W or Z vector boson (Fig. 3.1 (c)), known as Higgs strahlung (VH), is being investigated experimentally as a potential mechanism for Higgs boson production at the LHC. In order to identify this production mechanism in the experiment among backgrounds, events with an additional vector boson in the final state can be specifically searched for. The VH processes $pp \rightarrow WH$ and $pp \rightarrow ZH$ has been calculated to NNLO in QCD [64, 65], with NLO EW corrections [66], utilizing a calculation that is split into four components: Drell-Yan induced, top-loop induced, photon-induced, and a $gg \rightarrow ZH$ component, which is calculated to NLO accuracy with NLL corrections added on top [67], for the ZH mode. The PDF and α_s uncertainties are estimated to be 3.8% for the WH process and 3.7% for the ZH process with a Higgs mass of 125 GeV.

Top and bottom quark associated production- $t\bar{t}H$ and bbH

Measuring Higgs boson production in association with top quarks ($t\bar{t}H$ or tH) or bottom quarks (bbH) poses a significant challenge compared to the aforementioned processes due to a lower production cross-section and less accessible final state. However, researchers are actively working to establish these mechanisms for Higgs boson production at the LHC. The $t\bar{t}H$ process (Fig. 3.1 (d)) has been calculated with NLO accuracy in both QCD and EW corrections [61] which achieved 7.8% uncertainty on the total cross section with Higgs mass to be 125 GeV. In contrast, the tH process calculations rely solely on NLO QCD predictions and include s-channel (Fig. 3.1 (e)) and t-channel diagrams. The bbH (Fig. 3.1 (d)) cross-section prediction combines results from an NNLO QCD calculation in a five-flavor scheme and an NLO QCD calculation in a four-flavor scheme. The four-flavor scheme does not include bottom quarks in the initial state but accounts for their presence via gluon splitting into b-quark pairs. For the t-channel, the tH production cross section is estimated to have 3.3% uncertainty for PDF+ α_s contribution and 9.6% uncertainty for the QCD scale and flavour-scheme ambiguities contribution. For the s-channel the cross section is estimated to have 2.2% uncertainty for PDF+ α_s contribution and 2.1% uncertainty for the QCD scale and contribution.

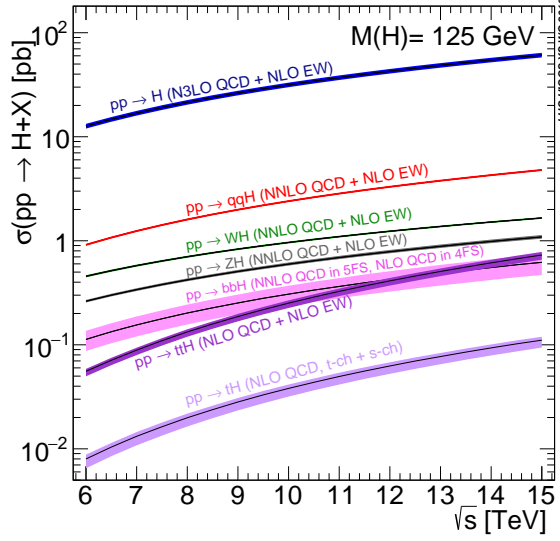


Figure 3.2: Predicted SM Higgs production cross-sections for different modes at the LHC with the mass of 125 GeV [68]. The theory uncertainties are shown by line widths.

3.2 Higgs decay modes

The SM Higgs boson exhibits a broad range of phenomenology with the major decay modes: $H \rightarrow b\bar{b}$, $H \rightarrow WW^*$, $H \rightarrow \gamma\gamma$ and $H \rightarrow ZZ^*$ at LHC. The total decay width of the Higgs boson is defined by the sum of the partial width of all possible decay channels. Thus, the branching ratio (BR) of a channel is defined by the ratio of each decay width and the total decay width,

$$BR_{H \rightarrow X} = \frac{\Gamma_{H \rightarrow X}}{\Gamma_H^{\text{tot}}}.$$

Fig. 3.3 depicts the principal branching fractions of Higgs boson decays.

As shown in Fig. 3.3, the $H \rightarrow b\bar{b}$ decay mode (Fig. 3.1 (h)) has the largest branch ratio (57.7%) for a Higgs boson mass of around 125 GeV. However, identifying these events at hadron colliders can be challenging due to the purely hadronic final state, necessitating the use of additional final state features to differentiate signal events from the background. Analyses concentrate on the VBF , VH , and $t\bar{t}H$ production modes rather than the dominant gluon fusion production mode. The $H \rightarrow WW^*$ decay mode has the second-largest branching fraction (21.5%) (Fig. 3.1 (f)). The final state with W boson decaying leptonically is easy to identify experimentally. Decays to gluons (8.60%) or charm quarks (2.90%) are difficult to distinguish from the overwhelming background. On the other hand, decays to pairs of Z bosons (2.64%) (Fig. 3.1 (f)) or to photons (0.23%) (Fig. 3.1 (g)) are easily identified because of excellent background control. Finally, the decays $H \rightarrow Z\gamma$ (0.15%) and $H \rightarrow \mu\mu$ (0.022%) (Fig. 3.1 (i)) are extremely rare and rather hard to accumulate enough statistics. Recent progress has shown a significant improvement with the new method applied and the full dataset accumulated in the recent years for these channels [69, 70].

3 Higgs Boson Production and Property Studies at the ATLAS Experiment

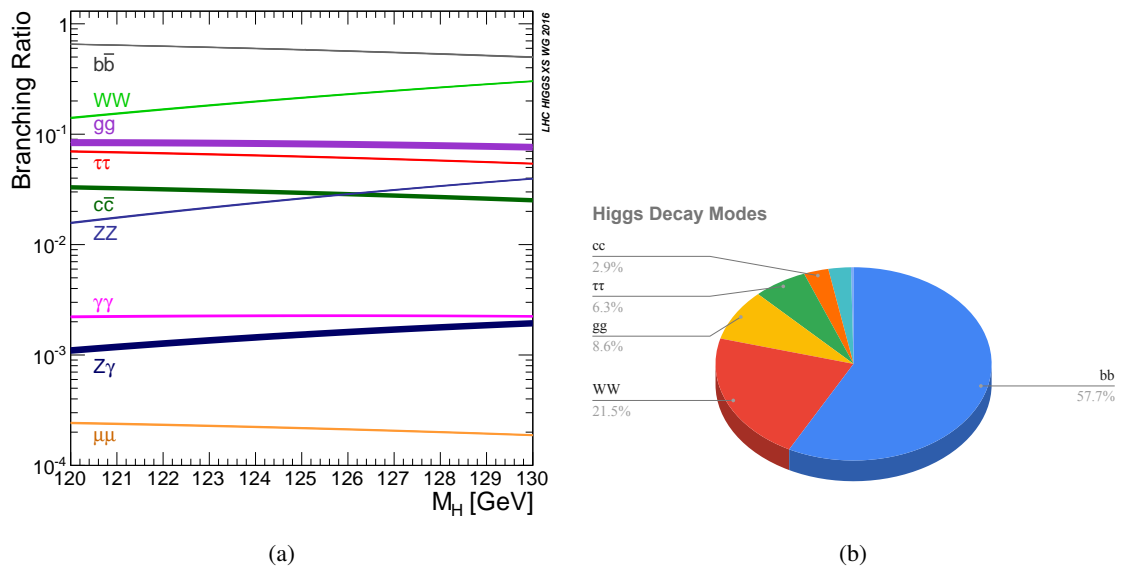
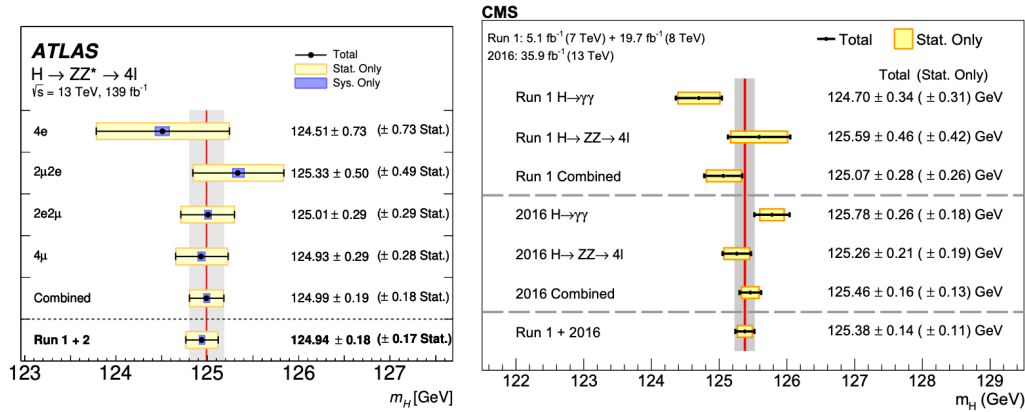


Figure 3.3: The predicted branching fractions of the different Higgs boson decay modes in the SM. The branching ratios at different Higgs mass points are shown in (a) [68]. The theory uncertainties are shown by line widths. The pie chart is shown in (b), and only the modes with branch ratios larger than 0.5% are shown. (chart is made with data from [9]).

3.3 Experimental observations

Mass, Width, Spin and Parity

Several measurements were made in LHC run 1 and run 2 to characterize the Higgs boson. The first is the determination of its mass. The mass is measured to be $m_H = 125.38 \pm 0.14$ GeV using the CMS detector in $H \rightarrow ZZ^* \rightarrow 4\ell$ and $H \rightarrow \gamma\gamma$ channels with Run 1 and partial Run 2 dataset collected in the year 2015 and 2016 [71]. The value is measured to be $m_H = 124.94 \pm 0.18$ GeV using the ATLAS detector in $H \rightarrow ZZ^* \rightarrow 4\ell$ channel with full run 2 dataset [72] as shown by the fit in Fig.3.5(a). The results for each channel and period are shown in Fig. 3.4 (a) for ATLAS and Fig. 3.4 (b) for CMS.



(a) Higgs mass measurement with ATLAS detector

(b) Higgs mass measurement with CMS detector

Figure 3.4: The recent results of the Higgs mass measurement from (a) ATLAS and (b) CMS detectors. The results between ATLAS and CMS have good agreement within the uncertainties, showing a combined Higgs mass near 125 GeV.

Given by the SM prediction, the on-shell Higgs boson production (gluon-gluon fusion in the equations below) is inversely proportional to the width:

$$\sigma_{gg \rightarrow H \rightarrow ZZ}^{\text{on-shell}} \sim \frac{g_{ggH}^2 g_{HZZ}^2}{m_H \Gamma_H},$$

while the off-shell Higgs boson production has no dependence on width:

$$\sigma_{gg \rightarrow H \rightarrow ZZ}^{\text{off-shell}} \sim \frac{g_{ggH}^2 g_{HZZ}^2}{m_H}.$$

Thus by measuring the ratio between the on-shell and off-shell productions of the Higgs boson, the total width of the Higgs boson is observed to have a value of $4.5^{+3.3}_{-2.5}$ MeV [73] as shown in Fig.3.5(b) and $3.2^{+2.4}_{-1.7}$ MeV [74] using the ATLAS and CMS detectors. The results are compatible with the SM prediction of 4.1 MeV.

3 Higgs Boson Production and Property Studies at the ATLAS Experiment

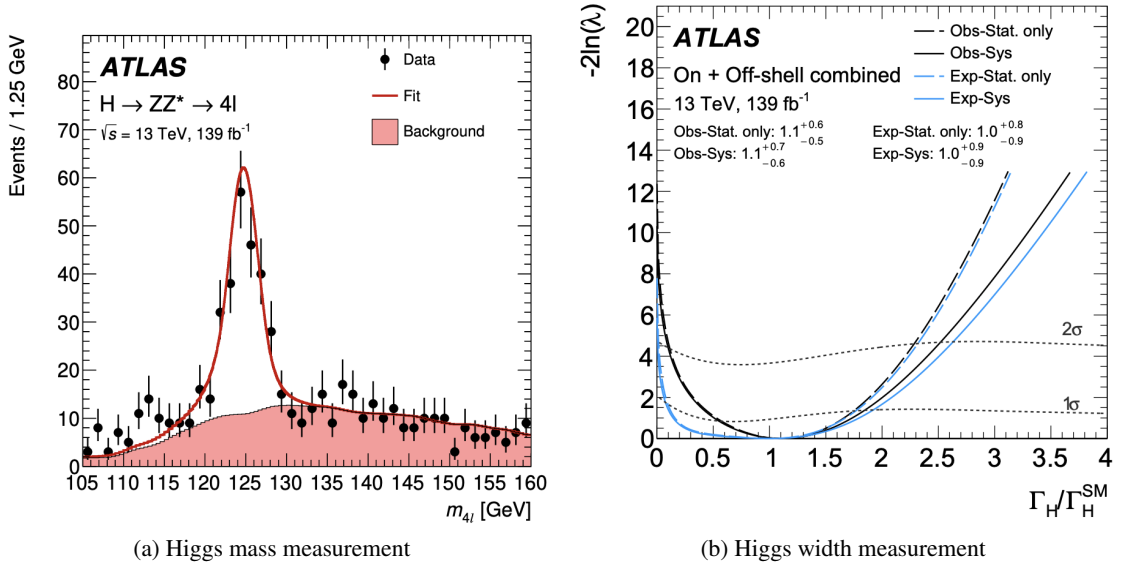


Figure 3.5: The measurement of the Higgs mass and width performed on the ATLAS detector. (a) The four-lepton invariant mass distribution from all subchannels combined (black points) in $H \rightarrow ZZ^* \rightarrow 4\ell$ channel is shown along with the post-fit signal and background distributions (red line) [72]. (b) The likelihood profile as a function of the ratio between the hypothesized and SM expected Higgs width in the combined on-shell and off-shell $H \rightarrow ZZ^* \rightarrow 4\ell$ and $H \rightarrow ZZ^* \rightarrow 2\ell 2\nu$ analysis [73].

The spin (J) and parity (P) of the Higgs boson were studied using events where the Higgs decays to other bosons: $H \rightarrow \gamma\gamma$, $H \rightarrow ZZ^* \rightarrow 4\ell$ and $H \rightarrow WW^* \rightarrow l\nu l\nu$. Hypotheses such as $J^P = 0^-$ or 2^+ were excluded in favor of the SM hypothesis of 0^+ [75, 76] as shown in Fig. 3.6 with the test statistic \tilde{q} based on a ratio of profiled likelihoods. The likelihood used in the analysis is constructed to be sensitive to the spin-parity J^P of the signal. All characteristics of the Higgs boson are similarly compared to the theoretical predictions up to now.

3.3 Experimental observations

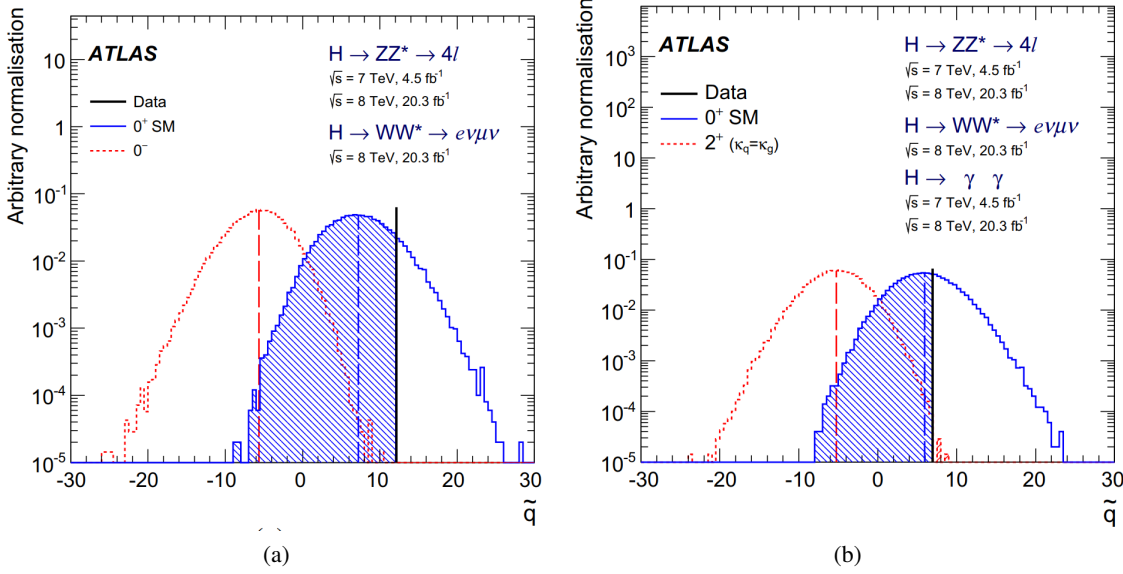


Figure 3.6: The measurement of the Higgs spin and parity with the $H \rightarrow ZZ^* \rightarrow 4\ell$, $H \rightarrow WW^* \rightarrow e\nu\mu\nu$ and $H \rightarrow \gamma\gamma$ channels at ATLAS detector with 7 and 8 TeV data. The distribution of the test statistic for the (a) 0^+ and 0^- as well as (b) 0^+ and 2^+ .

Production cross-section and decay branch ratio

The measurements of the Higgs production cross sections in the major decay channels are combined with the maximum profile likelihood fit method. The signal strength μ , is the parameter of interest in the fitting, which represents the measured yield of signal in data over the expected yields of signals from all SM processes. The significance of the signal is evaluated with a background-only hypothesis test with the profiled likelihood ratio test statistic. The details of the fitting can be found in Sec.4.8.3. With these definitions, the measured signal strength can be used to evaluate the cross-section with:

$$(\sigma \cdot BR_{H \rightarrow X})_{\text{obs}} = \mu(\sigma \cdot BR_{H \rightarrow X})_{\text{exp}},$$

where $(\sigma \cdot BR_{H \rightarrow X})_{\text{exp}}$ is the predicted cross-section times branch ratio of a Higgs decay channel by SM.

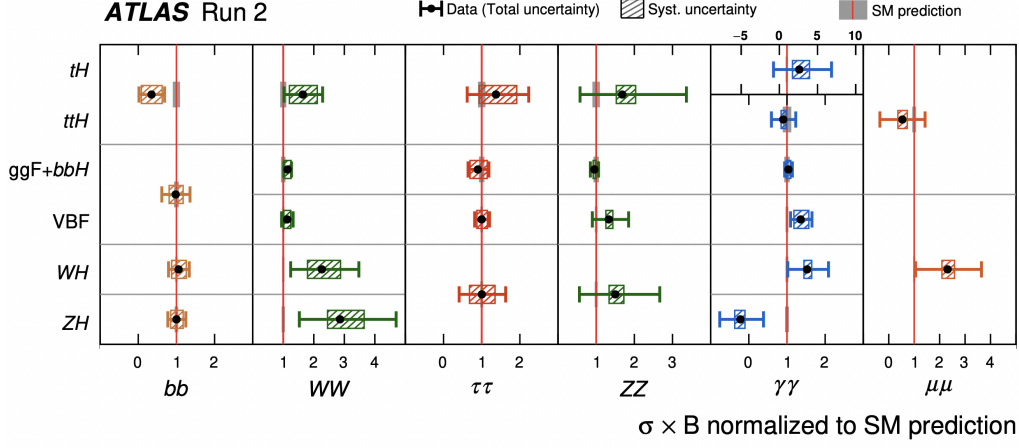
Both the Higgs boson production and decay have been validated in the ATLAS and CMS experiment with high precision level (shown in Fig. 3.7). The experiment results by the ATLAS [15] and CMS [14] keep good agreement with the theoretical prediction after ten years of Higgs boson discovery at LHC.

The latest measurements of the Higgs boson cross-section times branch ratio, normalized to the SM values, for various production and decay modes are summarized below for both experiments. The results agree with the SM within the total uncertainties. Though there are a few channels where the precision of the measurement needs to be further improved to further reduce the uncertainties. For

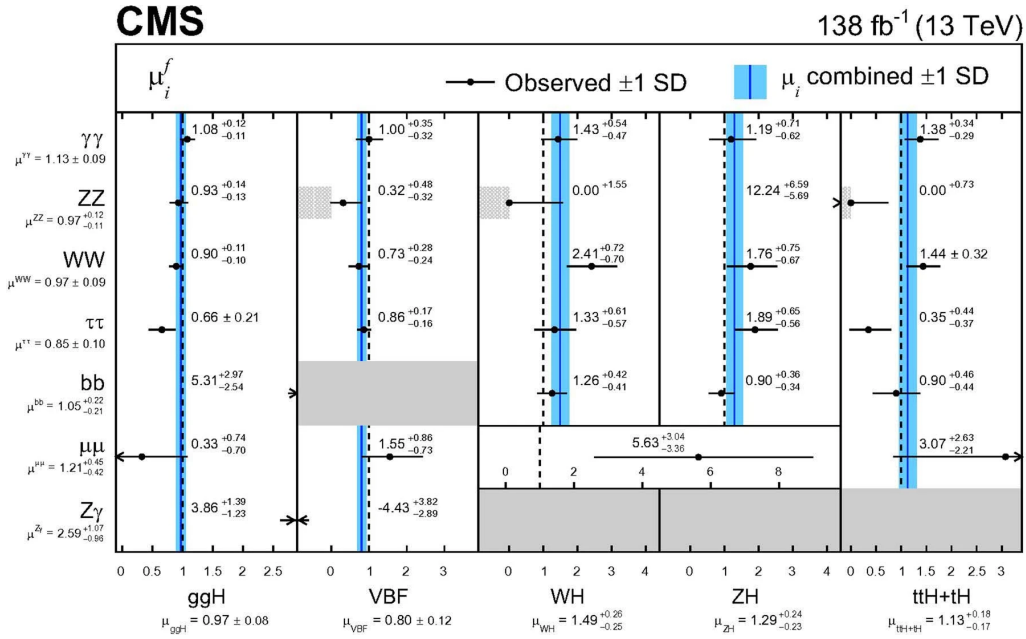
3 Higgs Boson Production and Property Studies at the ATLAS Experiment

instance, the signal strength of the $ttH + tH \rightarrow bb$ process is $0.348^{+0.341}_{-0.330}$ and the signal strength of the $ggF + VBF + bbH \rightarrow bb$ is $0.980^{+0.376}_{-0.363}$ measured with the ATLAS detector (shown in Fig. 3.7 (a)). Some modes, such as $WH \rightarrow WW$, show a signal strength of $2.264^{+1.212}_{-1.022}$. Other modes, like $ZH \rightarrow \gamma\gamma$, exhibit a negative value of $-0.221^{+0.606}_{-0.541}$. These results provide valuable insights into the Higgs boson's properties and its interactions with other particles. The measurement uncertainties from several channels are dominated by the statistics uncertainties, including the $H \rightarrow \mu\mu$ decay, the $H \rightarrow WW^*$ decay with VH production, and the $H \rightarrow ZZ^*$ decay with VH , $t\bar{t}H$, and tH production. With more statistics accumulated in future data taking (LHC run 3 and HL-LHC), a more precise check of the SM will be performed.

3.3 Experimental observations



(a) Results by the ATLAS experiment



(b) Results by the CMS experiment

Figure 3.7: The recent results on the Higgs coupling measurements at the (a) ATLAS [15] and (b) CMS [14] experiments. The results are presented by the ratio of the observed rate to the predicted SM event rate for different combinations of Higgs boson production and decay processes. The results show good agreement between the observed data and the prediction.

4 Measurement of the Vector Boson Associated Production with the $H \rightarrow WW^*$ Decay

4.1 Motivation

The associated production of the Higgs boson with either a W or a Z boson, known as the VH process (Fig. 3.1 (c)), provides us a direct probing of the couplings between Higgs and electroweak vector bosons. In particular, in the WH mode with subsequent $H \rightarrow WW^*$ decay (Fig. 4.1 (a)(b)(c)), the Higgs boson couples only to the W bosons both in the production vertex and decay vertex of the Feynman diagram, which make it more sensitive to the WH coupling constant measurement.

This channel is also potentially sensitive to some BSM theories that can modify this coupling or implies another scalar Higgs with a different isospin [77, 78].

4.2 Overview of the analysis

In this chapter, the measurement of the WH and ZH production cross-sections in the $H \rightarrow WW^*$ decay channel is introduced. The proton-proton collisions used in this study were carried out at a center-of-mass energy of $\sqrt{s} = 13$ TeV, and the data correspond to an integrated luminosity of 139 fb^{-1} for analysis. The ATLAS detector at LHC was used to record the data between 2015 and 2018. Earlier measurements were conducted by the ATLAS [79] and CMS [80] Collaborations at $\sqrt{s} = 7$ TeV and 8 TeV, respectively. The CMS Collaboration recently measured WH and ZH production [81] with 137 fb^{-1} data at $\sqrt{s} = 13$ TeV. The ATLAS Collaboration's latest results are based on data from 2015 and 2016, with an integrated luminosity of 36.1 fb^{-1} [82]. Other decay modes have been used to measure VH production at $\sqrt{s} = 13$ TeV, including $H \rightarrow ZZ^* \rightarrow 4\ell$ [83, 84], $H \rightarrow \gamma\gamma$ [85, 86], $H \rightarrow b\bar{b}$ [87, 88], $H \rightarrow \tau\tau$ [89, 90], and a search for VH production in the $H \rightarrow c\bar{c}$ decay [91, 92]. Four channels are used in this analysis depending on the number of the lepton and their charge and flavor to improve global sensitivity. The work described in this chapter is collaborative with the group, and the author's original contributions are mainly on the systematic and statistical treatment and interpretation, combination, and background modeling of the 2ℓ same sign channel.

Opposite-sign 2ℓ channel

The opposite-sign 2ℓ channel focuses on the process in which the associated weak boson V decays hadronically, producing two energetic jets. The $H \rightarrow WW^*$ decay produces two oppositely charged leptons, designated as ℓ_0 and ℓ_1 , as well as two neutrinos. By selecting two leptons of different flavors

4 Measurement of the Vector Boson Associated Production with the $H \rightarrow WW^*$ Decay

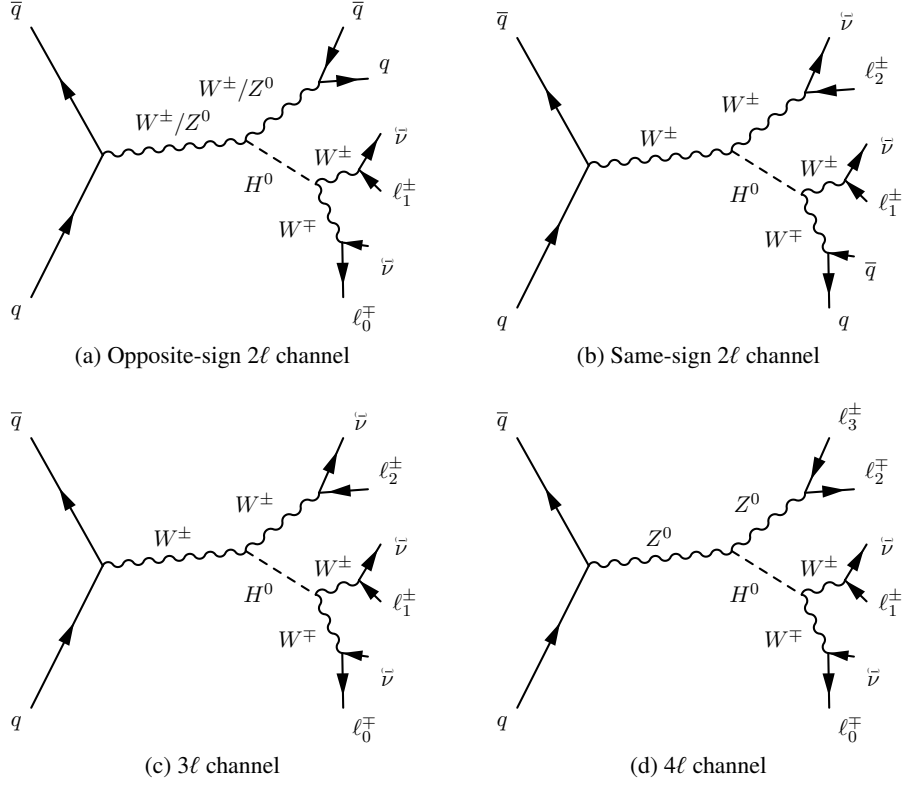


Figure 4.1: Feynman diagrams for the signal topologies at tree-level considered by the analysis of VH , $H \rightarrow WW^*$ measurement.

and carefully examining the kinematic properties of events, we can enhance the signal-to-background ratio. The primary backgrounds for this channel are $t\bar{t}$ and Wt processes, with $Z \rightarrow \tau\tau$ and WW production with two associated jets also making significant contributions. Final states containing W + jets and multijets may produce misidentified leptons, which can contaminate the signal region. Additional background sources include $W(Z/\gamma^*)$ production (comprising WZ and $W\gamma^*$ processes) and other processes involving the Higgs boson, particularly its production through gluon fusion (ggF).

Same-sign 2ℓ channel

The same-sign 2ℓ channel focuses on a different final state, in which the associated W boson decays leptonically, while the $H \rightarrow WW^*$ decay produces a W bosons that also decays leptonically, resulting in two leptons with the same charge, labeled as ℓ_1 and ℓ_2 , two neutrinos, and two energetic jets. The primary backgrounds in this channel include $W(Z/\gamma^*)$, $W\gamma^*$, and W + jets production, while WW , $Z + \gamma^*$, Z + jets, and top-quark processes also contribute to the final state.

3 ℓ channel

The 3 ℓ channel focuses on a WH final state in which the Higgs boson decays to W bosons pair. All weak bosons decay leptonically, producing three charged leptons and three neutrinos in the final state. The lepton with a unique charge is designated as ℓ_0 , while the lepton closest to ℓ_0 in the angular distance is designated as ℓ_1 , and the remaining lepton is designated as ℓ_2 . Leptons ℓ_0 and ℓ_1 are assumed to originate from the $H \rightarrow WW^*$ decay. The most significant background to this channel is $W(Z/\gamma^*)$ production, with non-resonant WWW production also contributing to the background.

4 ℓ channel

Finally, the 4 ℓ channel targets a ZH process in which the Higgs boson decays to a W boson pair, resulting in four charged leptons and two neutrinos in the final state. The leptons belonging to the same-flavor opposite-sign (SFOS) pair with an invariant mass closest to the Z boson mass are labeled as ℓ_2 and ℓ_3 , while the remaining leptons are labeled as ℓ_0 and ℓ_1 and are assumed to originate from the $H \rightarrow WW^*$ decay. The primary backgrounds to this channel are non-resonant ZZ and WWZ production.

4.3 Data and MC samples

The analysis presented in this study uses the full ATLAS Run 2 dataset, which includes proton-proton collision data produced at $\sqrt{s} = 13$ TeV between 2015 and 2018. Before analysis, the data undergo a series of quality checks and cleaning procedures [93], including the removal of events recorded when relevant detector components were not fully functional. This cleaning process results in a total integrated luminosity of 139 fb^{-1} (Fig. 4.3).

The process of selecting interesting events for analysis starts with the level-1 trigger (L1 trigger) system, which is implemented in the dedicated hardware [94]. This system accepts events from the 40 MHz bunch crossings and uses a set of pre-defined criteria to reduce the rate of accepted events to below 100 kHz. The events that pass this first selection are then processed by the high-level trigger (HLT), which applies more sophisticated algorithms implemented in software. The high-level trigger further reduces the event rate to about 1 kHz, ensuring that only the most interesting events are recorded to disk for further analysis. A schematic view of the trigger system components is shown in Fig. 4.2.

4 Measurement of the Vector Boson Associated Production with the $H \rightarrow WW^*$ Decay

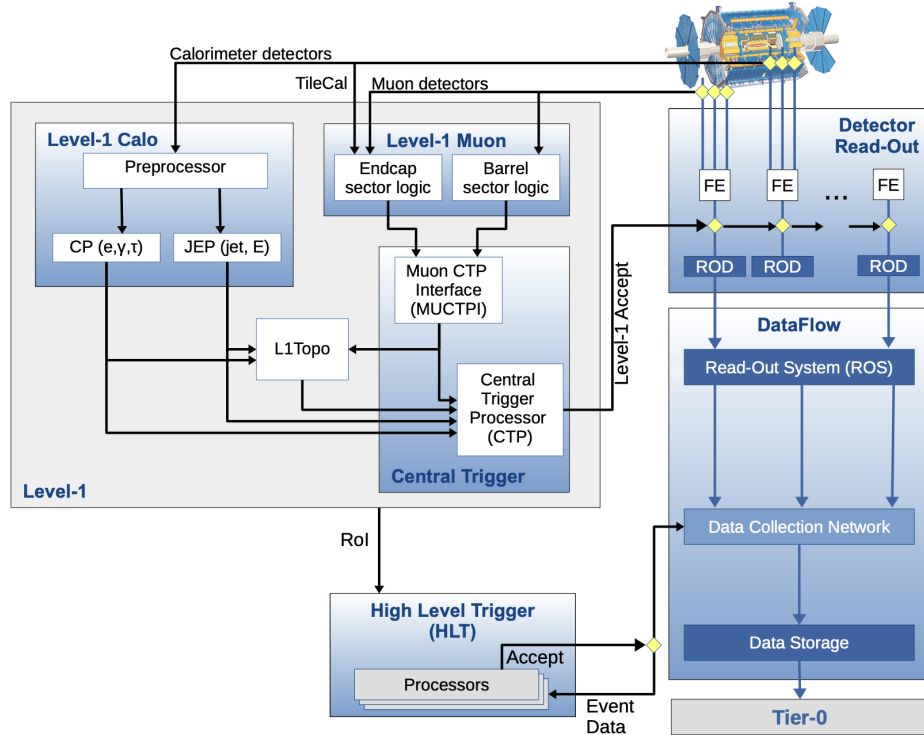


Figure 4.2: The TDAQ used in the ATLAS run 2 data-taking with specific focus given to the components of the L1 Trigger system [95].

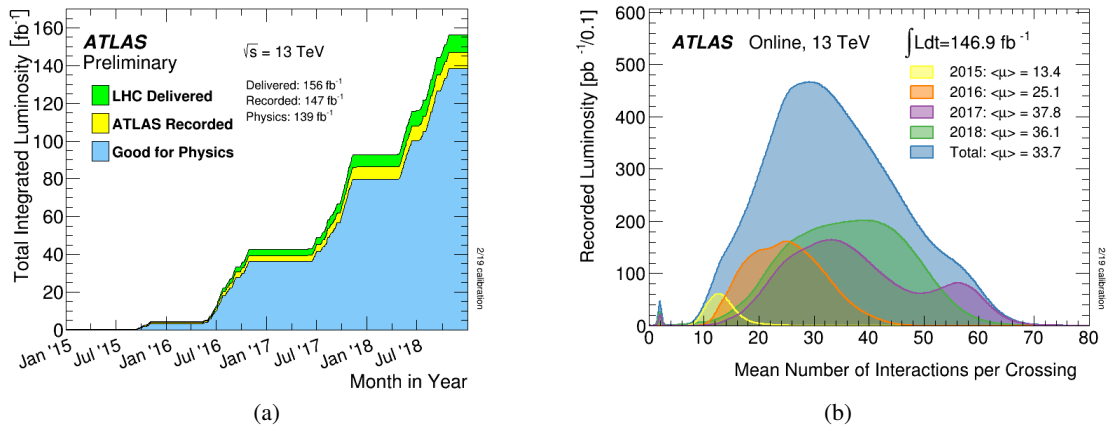


Figure 4.3: The integrated luminosity (a) and the number of interactions per crossing (pile-up) distribution (b) for the overall ATLAS 2015 to 2018 data taking in LHC run 2 [96].

4.3 Data and MC samples

The analysis of proton-proton collision data requires accurate modeling of the signal and background processes. Monte Carlo (MC) generators are used for this purpose, which simulates the matrix element, parton shower and hadronization, and underlying event for the hard proton-proton scattering. The generators employed for modeling both signal and background processes are listed in Tab. 4.1.

Table 4.1: MC generators used to model the signal and background processes. Alternative generators or parton shower models used to estimate systematic uncertainties are shown in parenthesis. In the last column, the prediction order (in QCD, unless specified otherwise) for the total cross-section is shown.

Process	ME (alternative)	PS/UE (alternative)	Prediction order for total cross-section
$q\bar{q} \rightarrow WH$	POWHEG Box v2 MiNLO	PYTHIA 8 (HERWIG 7 [102, 103])	NNLO QCD + NLO EW [97–101]
$q\bar{q} \rightarrow ZH$	POWHEG Box v2 MiNLO	PYTHIA 8 (HERWIG 7)	NNLO QCD + NLO EW [97–101]
$gg \rightarrow ZH$	POWHEG Box v2	PYTHIA 8 (HERWIG 7)	NLO + NLL [104, 105]
ggF H	POWHEG Box v2 NNLOPS	PYTHIA 8	N ³ LO QCD + NLO EW [106–116]
VBF H	POWHEG Box v2	PYTHIA 8	NNLO QCD + NLO EW [117–119]
$t\bar{t}H$	POWHEG Box v2	PYTHIA 8	NLO QCD + NLO EW [115]
Z/γ^*	SHERPA 2.2.1 (MADGRAPH5_aMC@NLO)	SHERPA 2.2.1 (PYTHIA 8)	NNLO [120]
$q\bar{q}/g \rightarrow WW$	SHERPA 2.2.2	SHERPA 2.2.2	NLO [121–123]
$WZ/ZZ/V\gamma^*$	SHERPA 2.2.2	SHERPA 2.2.2	NLO [124]
$V+\gamma$	SHERPA 2.2.8	SHERPA 2.2.8	NLO [124]
$gg \rightarrow WW/ZZ$	SHERPA 2.2.2	SHERPA 2.2.2	NLO [125, 126]
VVV	SHERPA 2.2.2 (MADGRAPH5_aMC@NLO)	SHERPA 2.2.2 (PYTHIA 8)	NLO [127]
$qq \rightarrow WWqq$	MADGRAPH5_aMC@NLO	PYTHIA 8	LO
$t\bar{t}$	POWHEG Box v2 (MADGRAPH5_aMC@NLO)	PYTHIA 8 (HERWIG 7)	NNLO + NNLL [128–134]
Wt	POWHEG Box v2	PYTHIA 8	NLO [135, 136]
$t\bar{t}V$	MADGRAPH5_aMC@NLO	PYTHIA 8	NLO [137]
tZ	MADGRAPH5_aMC@NLO	PYTHIA 8	NLO [138]
tWZ	MADGRAPH5_aMC@NLO	PYTHIA 8	NLO [139]

In this analysis, Higgs boson signal samples are created through the decay of $H \rightarrow WW^*$ across four primary production channels: ggF , VBF , VH , $t\bar{t}H$. In order to keep the consistency, these samples are generated using a 125 GeV Higgs boson mass and are subsequently normalized to the cross-sections calculated for a mass of 125.09 GeV [140]. The PDF4LHC15 [141] is used as the parton distribution function (PDF) when producing the samples, and parton showering and hadronization is simulated by PYTHIA 8 [142]. The configurations are established based on the AZNLO [143] (for VH , ggF , and

4 Measurement of the Vector Boson Associated Production with the $H \rightarrow WW^*$ Decay

VBF) or A14 [144] (for $t\bar{t}H$) tunes, which guarantees the precision and robustness of the measurement acquired.

The WH and ZH events investigated in this research are generated using POWHEG BOX v2 MINLO [145–148] at the next-to-leading order (NLO) in perturbative quantum chromodynamics (QCD), including up to one extra jet. Each sample is normalized to a computed cross-section at the next-to-next-to-leading order (NNLO) in QCD, and at the NLO in electroweak theory (EW) [97–101]. The less significant process of $gg \rightarrow ZH$ is produced at the leading order (LO) in QCD utilizing POWHEG BOX v2, followed by normalization to a cross-section determined at the NLO in QCD with next-to-leading logarithmic (NLL) adjustments [104, 105].

The ggF samples are produced with POWHEG BOX v2 NNLOPS [145–147, 149]. This process is simulated at NNLO in QCD for events without jets, at NLO in QCD for events featuring one jet, and at LO for events containing two jets. The sample is normalized to a cross-section calculated at the next-to-next-to-next-to-leading order (N^3 LO) in QCD with NLO EW adjustments [106–116]. The VBF samples are produced with POWHEG BOX v2 [145–147, 150] and normalized to a cross-section determined at NLO in QCD and EW [117, 118], with approximate NNLO in QCD corrections applied [63]. The $t\bar{t}H$ samples are produced with POWHEG BOX v2 [145–147, 151, 152] with NLO precision in QCD. The samples are scaled to the cross-section at NLO precision in QCD and NLO EW adjustments [115].

The primary background in the target signal regions are single boson, diboson, triboson, single top quark, and $t\bar{t}$ processes, and the corresponding generator for the sample generation is listed in the Tab. 4.1. Every sample undergoes processing through the GEANT4-based [153] ATLAS detector simulation and the standard ATLAS reconstruction software [154]. Pile-up effects are simulated by combining the hard-scattering event with simulated inelastic proton-proton events produced by PYTHIA 8 using the NNPDF2.3 [155] PDF set and the A3 [156] tune.

4.4 Reconstruction of objects and events

Potential signal events are identified using triggers that require a single isolated lepton with minimum p_T thresholds varying between 24 GeV and 26 GeV for electrons and between 20 GeV and 26 GeV for muons, depending on the period of data-taking. At least one lepton reconstructed offline is required to match the trigger requirement. Furthermore, the p_T of the lepton reconstructed offline must exceed the trigger p_T threshold by at least 1 GeV.

Electron

The reconstruction of *electrons* is achieved by associating clusters of energy deposits in the EM calorimeter with ID tracks, and their identification relies on criteria involving calorimeter shower patterns, the track-cluster matching quality, and the emitted transition radiation in the ID, as explained in [158]. Electrons must fulfill $|\eta| < 2.47$, excluding the transitional area $1.37 < |\eta| < 1.52$ between the barrel and endcap EM calorimeters.

4.4 Reconstruction of objects and events

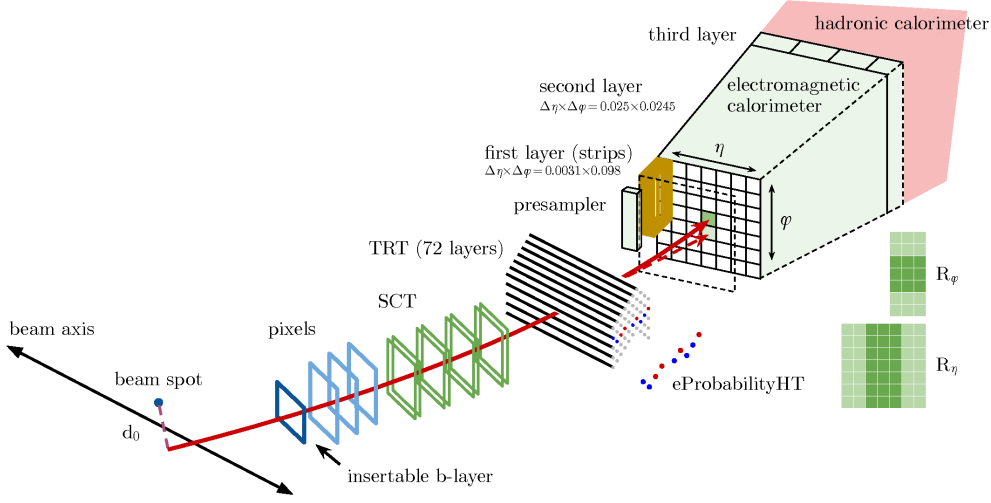


Figure 4.4: The illustration of the detector and algorithm for reconstruction and identification of the electrons in ATLAS detector [157].

Muon

The reconstruction of *muons* is achieved by merging ID and MS tracks that exhibit coherent trajectories and curvatures. A comprehensive fit incorporating hits from the ID track, energy loss in the calorimeter, and the hits of the track in the muon system forms muon candidates, as outlined in [159]. Muons must adhere to the condition $|\eta| < 2.5$.

Jet

The reconstruction of *jets* is achieved by employing the anti- k_t algorithm with a radius parameter $R = 0.4$ [160, 161] and incorporating both calorimeter and track data as input [162]. Jet four-momenta undergo corrections to account for calorimeter non-compensation, energy loss in non-instrumented areas, and pile-up contributions [163]. Jets must meet the requirements of $|\eta| < 4.5$ and $p_T > 20$ GeV. For jet counting purposes, only jets with $p_T > 30$ GeV are taken into account.

Jets containing *b*-hadrons are identified using a deep neural network tagger [164, 165]. The *b*-jets are required to satisfy the requirements of the 85% efficiency working point determined using $t\bar{t}$ simulated events. The jets originating from *b*-hadron decays with $p_T > 20$ GeV and $|\eta| < 2.5$ are referred to as *b*-jets in this analysis. The DL1r algorithm is used with the discriminant defined to be:

$$D_{\text{DL1r}} = \ln \left(\frac{p_b}{f_c \cdot p_c + (1 - f_c) \cdot p_{\text{light}}} \right). \quad (4.1)$$

where p_b , p_c , p_{light} refer to the probabilities for an input jet originating from a *b*, *c* or a light-flavor hadron, which corresponds to the three output nodes of the DNN output. f_c is the fraction of the effective *c*-jet in the background hypothesis which is optimized to be 0.018. The algorithm in such

4 Measurement of the Vector Boson Associated Production with the $H \rightarrow WW^*$ Decay

configuration provides a rejection factor of 29 against the jets originating from the light quark or gluon and of 2.6 against the jets containing the c -hadrons.

$$E_T^{\text{miss}}$$

The reconstruction of E_T^{miss} is achieved by determining the magnitude from the negative vector sum of the transverse momenta of all identified and calibrated objects, in addition to reconstructed tracks not linked to these objects but consistent with originating from the primary vertex [166]. An object-based E_T^{miss} significance [167], S_{miss} , is employed to discard events in which the E_T^{miss} results from the mis-reconstruction of physics objects contributing to the calculation.

In the end, the events passed the selection must contain at least one primary vertex reconstructed using at least two related tracks, with each track having transverse momentum $p_T > 500$ MeV, as detailed in Ref. [168]. In cases where multiple primary vertices are reconstructed in an event, the vertex with the highest track $\sum p_T^2$ is selected for analysis.

4.5 Event selection

4.5.1 Definition of the channels

Based on the leptons' multiplicity and summed charge in the event, the specific selection criteria are defined for each channel. For improving the sensitivity, the data samples are divided into several signal regions (SRs) and dedicated control regions (CRs) with orthogonal selection criteria (Tab. 4.2). The CRs are used to determine the normalization factors of the major backgrounds in each SR.

In order to handle the final state with a bunch of particles and invisible neutrinos and identify the signal from the sophisticated background with similar features, the multi-variable analysis (MVA) technique is employed in all channels to enhance the separation of signals from backgrounds. The choice of multivariate analysis architecture, algorithm, configuration, and input variables are optimized for each channel to chase the best performance. The ANN is applied for 2ℓ and 3ℓ channels, which are built up on the backend of Keras [169] and TensorFlow [170], while the BDT [171] is applied for the 4ℓ channel.

The final results are obtained through a simultaneous fit of all SRs and CRs. The 3ℓ and 4ℓ channels are the most sensitive for the WH and ZH production measurements, respectively, and also for the combined measurement of the VH production.

4.5 Event selection

Table 4.2: The event categories definition before the multivariate analysis treatment applied.

Category	2ℓ		3ℓ		4ℓ	
	OS	SS	Z-dominated	Z-depleted	1-SFOS	2-SFOS
Minimum lepton p_T [GeV]	15	15	15	15	10	10
Number of leptons	2	2	3	3	4	4
Total lepton charge	0	± 2	± 1	± 1	0	0
Number of SFOS pairs	0	0	1 or 2	0	1	2
Minimum $\Delta R_{\ell\ell}$	0.1	0.4	0.1	0.1	0.2 ($\ell_0\ell_1$)	
Minimum $m_{\ell\ell}$ [GeV]	10	–	12 (smallest SFOS)	–	12 (all SFOS) or 10 (all DFOS)	
Number of jets	≥ 2	≥ 1	–	–	–	–
Number of b -tagged jets	0	0	0	0	0	0
$ m_{\ell,\ell} - m_Z $ [GeV]	–	$> 20 (e^\pm e^\pm)$	> 25 (all SFOS)	–	–	–
$m_{\ell\ell}$ [GeV]	–	–	–	–	–	$< 50 (\ell_0\ell_1)$
E_T^{miss} [GeV]	–	–	> 30	–	–	–

4.5.2 Opposite-sign 2ℓ channel

The opposite-sign 2ℓ channel requires two different-flavor, opposite-sign (DFOS) leptons from the decay of the Higgs boson and two or more jets from the decay of the associated vector boson, which can be either a W or a Z . The leading and subleading leptons must exceed p_T thresholds of 22 GeV and 15 GeV, respectively, and are required to pass the common lepton selections. The invariant mass of the leptons must satisfy $m_{\ell\ell} > 10$ GeV to remove low-mass resonances, and the angular separation between the leptons must satisfy $\Delta R_{\ell\ell} > 0.1$ to remove overlapping leptons. In order to reject top quark production processes, events with one or more b -jet are vetoed. To ensure orthogonality with the ATLAS ggF and VBF production measurements [172], the leading and subleading jets are required to have an invariant mass of $|m_{jj} - 85| < 15$ GeV and a rapidity separation of $\Delta Y_{jj} < 1.2$. For increasing the sensitivity, the two and three lepton channels employ ANN based on Keras [173] with the TensorFlow [170] backend.

The ANN is trained to simultaneously classify VH , ggF , VBF , top, Z +jets, and WW processes. The output consists of six distinct output nodes, $\text{ANN}_{\text{VHOS}}^i$, each describing the likeliness of the input event to stem from process i ($i = VH, ggF, VBF, \text{top}, Z\text{-jets}, \text{and } WW$) with the condition that $\sum_i \text{ANN}_{\text{VHOS}}^i = 1$. Different nodes are needed to build dedicated control regions to normalize the relevant background processes, as explained in Sec. 4.17. In total, 19 variables are used as input:

$p_T^{\ell_0}$ and $p_T^{\ell_1}$, which represent the transverse momenta of the leading and subleading leptons, respectively; $\Delta\phi_{\ell\ell}$, which stands for the azimuthal separation between the two leptons; $\Delta Y_{\ell\ell}$, which stands for the rapidity separation between the two leptons; $m_{\ell\ell}$, which represents the invariant mass of the dilepton system.

Apart from the lepton-based variables, the following variables based on the jets and the missing transverse energy are also employed: $p_T^{j_0}$ and $p_T^{j_1}$, which represent the transverse momenta of the

4 Measurement of the Vector Boson Associated Production with the $H \rightarrow WW^*$ Decay

Table 4.3: ANN input variables used in the opposite-sign 2ℓ channel.

ANN input variables for opposite-sign 2ℓ channel

$p_T^{\ell_0}$	$p_T^{\ell_1}$	$\Delta\phi_{\ell\ell}$	$\Delta Y_{\ell\ell}$	$m_{\ell\ell}$
$p_T^{j_0}$	$p_T^{j_1}$	$\Delta\phi_{jj}$	ΔY_{jj}	m_{jj}
m_T	$m_{\tau\tau}$	$m_{\ell_0 j_0}$	$m_{\ell_0 j_1}$	$m_{\ell_1 j_0}$
$m_{\ell_1 j_1}$	H_T	E_T^{miss}	S_{miss}	

leading and subleading jets, respectively; m_{jj} , which stands for the invariant mass of the dijet system; $\Delta\phi_{jj}$, which stands for the azimuthal separation between the two jets; ΔY_{jj} , which stands for the rapidity separation between the two jets; $m_{\tau\tau}$, which is the $\tau\tau$ invariant mass computed using the collinear approximation [174]; $m_{\ell_0 j_0}$, $m_{\ell_0 j_1}$, $m_{\ell_1 j_0}$, $m_{\ell_1 j_1}$, which represent the invariant masses of the lepton-jet pairs; H_T , which stands for the transverse energy sum of all leptons and jets; E_T^{miss} , which represents the missing transverse energy; S_{miss} , which stands for the E_T^{miss} significance.

Moreover, the input feature m_T is used, which is the transverse mass of the $H \rightarrow WW^*$ system, defined as:

$$m_T = \sqrt{2p_T^{\ell\ell} E_T^{\text{miss}} (1 - \cos \Delta\phi_{\ell\ell, \text{miss}})}, \quad (4.2)$$

where $p_T^{\ell\ell}$ is the transverse momentum of the dilepton system and $\Delta\phi_{\ell\ell, \text{miss}}$ is the azimuthal separation between the dilepton system and the E_T^{miss} . The list of all input variables for opposite-sign 2ℓ is shown in Tab. 4.3.

In the analysis, The $\text{ANN}_{\text{VHOS}}^{VH}$ is used for the signal region definition and the final discriminant to extract the signal in the statistical fit. The $\text{ANN}_{\text{VHOS}}^{\text{top}}$, $\text{ANN}_{\text{VHOS}}^{\text{Z+jets}}$, and $\text{ANN}_{\text{VHOS}}^{WW}$ are used for the selections in control regions. The performance of the ANN for the opposite-sign 2ℓ channel is evaluated by the distributions on the signal and background for each node. The node for the VH and dominate background top, Z+jets, WW are shown in Fig. 4.5.

The resulting distribution of the $\text{ANN}_{\text{VHOS}}^{VH}$ discriminant after the fit procedure introduced in Sec. 4.8.3 is referred to as a “post-fit” distribution. This distribution is illustrated in Fig. 4.6.

The validation of the top background model is performed in a specific control region, where the SR selections are applied, but with the additional requirement of having at least one jet that is b -tagged. In order to ensure its accuracy, the background model is also verified in a side-band region that has a very low anticipated signal rate. This is achieved by reversing the cut on the VH output node of the ANN.

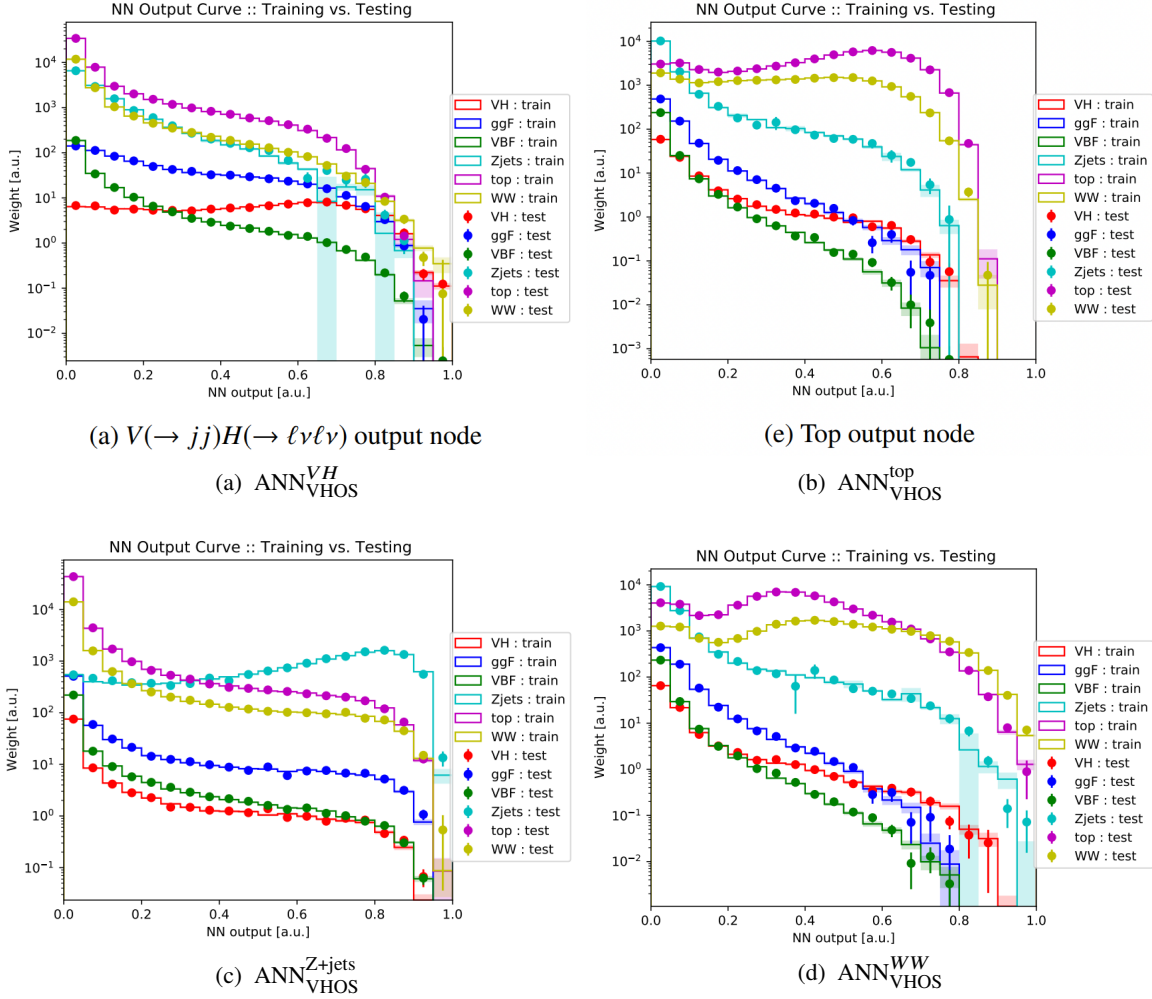


Figure 4.5: The performance of the $\text{ANN}_{\text{VHOS}}^{VH}$ used in the analysis. The distributions on the signal and background for the VH , top, Z +jets, and WW node.

4 Measurement of the Vector Boson Associated Production with the $H \rightarrow WW^*$ Decay

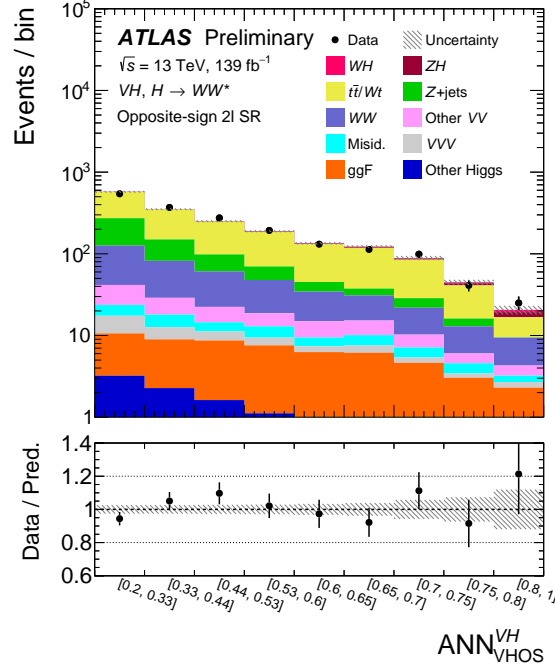


Figure 4.6: Post-fit distribution of $\text{ANN}_{\text{VHOS}}^{\text{VH}}$ in the opposite-sign 2ℓ SR. In all subsequent post-fit distributions, “Misid.” refers to the mis-identified lepton background which is primarily from the $W + \text{jets}$.

4.5.3 Same-sign 2ℓ channel

The channel for same-sign 2ℓ requires exactly two isolated leptons with the same charge. The leading lepton must have a p_T greater than 22 GeV, while the subleading lepton must have a p_T greater than 15 GeV. To minimize background noise from $W(Z/\gamma^*)$, events containing any additional reconstructed lepton with $p_T > 10$ GeV are discarded. At least one reconstructed jet is required to be present, given that 57% of expected signal events are predicted to have only one reconstructed jet. For events with two or more jets, the invariant mass of the leading and subleading jets must be below 500 GeV to suppress contributions from the same-sign WW process. Events that contain any b -tagged jets are rejected to minimize top backgrounds. For reducing the $W+\gamma$ events, the angular separation between the leptons is constrained to be $\Delta R_{\ell\ell} > 0.4$.

The signal region is divided into three categories based on the lepton flavor: $\text{SS}2e$, $\text{SS}2\mu$, and SSDF . The $\text{SS}2e$ category requires two electrons and rejects events where the invariant mass of the electron pair is within ± 20 GeV of the Z pole to reduce the impact of $Z+\text{jets}$ events where an electron has been mis-reconstructed. The $\text{SS}2\mu$ category requires two muons, while the SSDF category requires one electron and one muon. A multivariate tagger [158] is employed to further reduce events containing electrons with mis-identified charge.

The main background in the same-sign 2ℓ channel is the $W(Z/\gamma^*)$ process. A RNN is utilized to differentiate between WH and $W(Z/\gamma^*)$ across all categories. The RNN possesses the benefit of acquiring knowledge of sequential dependencies for input sequences that have varied lengths. In this

study, the basic unit of RNN employed is the Long Short-Term Memory (LSTM) [175] unit. For each input event, the LSTM collects the characteristics of the first object in the sequence and calculates the outcome. For each subsequent object, the LSTM combines the features of the current object and its previous output to determine a new output. By doing so, the LSTM, along with the final object, will consider the information of all objects in the sequence. Subsequently, a conventional feed-forward network processes the LSTM output.

The RNN is provided with sequences comprising reconstructed objects ordered according to leptons, E_T^{miss} , and jets (with a maximum of 5 jets), where leptons and jets are additionally ordered by p_T . Several ordering methods were experimented with, but none had any impact on RNN performance, as revealed through observation. Input variables for each type of object are summarised in Tab. 4.4. A variable providing information to distinguish among different particle types (leptons, missing transverse momentum, and jets) is also given as input to the RNN. The geometry of the ATLAS detector is characterized by rotational symmetry in the ϕ direction and mirror symmetry in the η direction, owing to both physics and design considerations. In order to leverage these symmetries, the input variables are pre-processed: the sequence's coordinate system is rotated such that the leading lepton has a ϕ coordinate of 0 and reflected so that the leading lepton has a positive η coordinate. This approach enhances training efficiency as the RNN does not need to learn these symmetries during the training phase.

Table 4.4: Input variables for the RNN in the same-sign 2ℓ channel.

RNN input variables for same-sign 2ℓ channel			
Object	p_T	η	ϕ
Lepton	p_T^ℓ	η^ℓ	ϕ^ℓ
Missing transverse momentum	E_T^{miss}	0	ϕ^{miss}
Jet	p_T^j	η^j	ϕ^j

For the verification of the RNN model, validation regions enriched with $W(Z/\gamma^*)$ were utilized. These validation regions were selected according to the same three sets of SR selections but with the additional requirement of having an extra reconstructed lepton with $p_T > 15$ GeV, which may not meet the standard quality criteria for selecting the two isolated leptons. To address a significant mis-modeling noticed in the $\text{SS}2\mu$ and SSDF categories featuring two or more reconstructed jets (as described in Sec. 4.7), an RNN shape uncertainty was evaluated for the $W(Z/\gamma^*)$ background process.

The performance of RNN for the same-sign 2ℓ channel is evaluated as both the distributions on the signal and background and the curves of the background rejection as a function of the signal efficiency is shown in Fig. 4.8.

4 Measurement of the Vector Boson Associated Production with the $H \rightarrow WW^*$ Decay

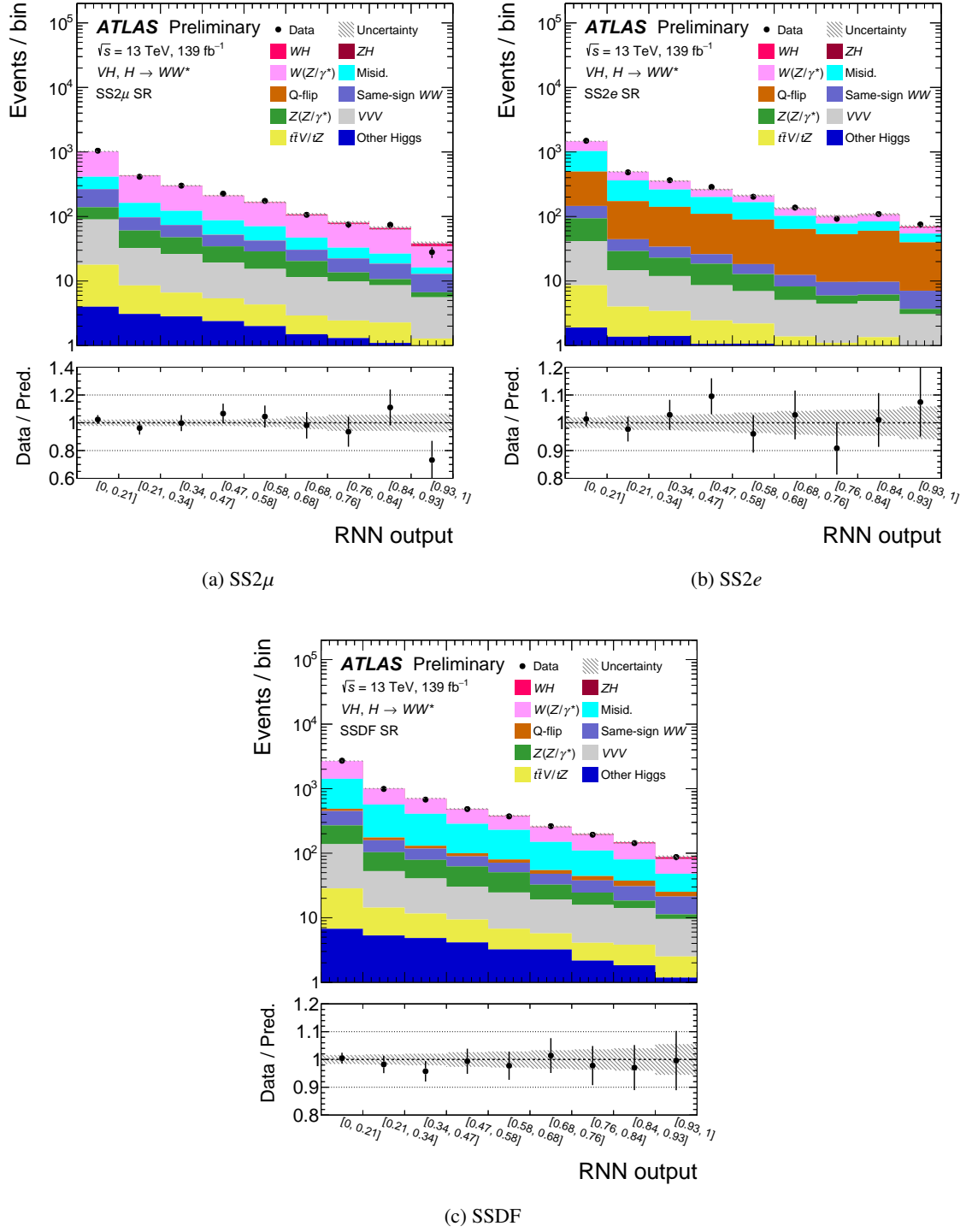


Figure 4.7: Post-fit distributions of the RNN discriminant in (a) SS2 μ , (b) SS2 e , and (c) SSDF signal region categories.

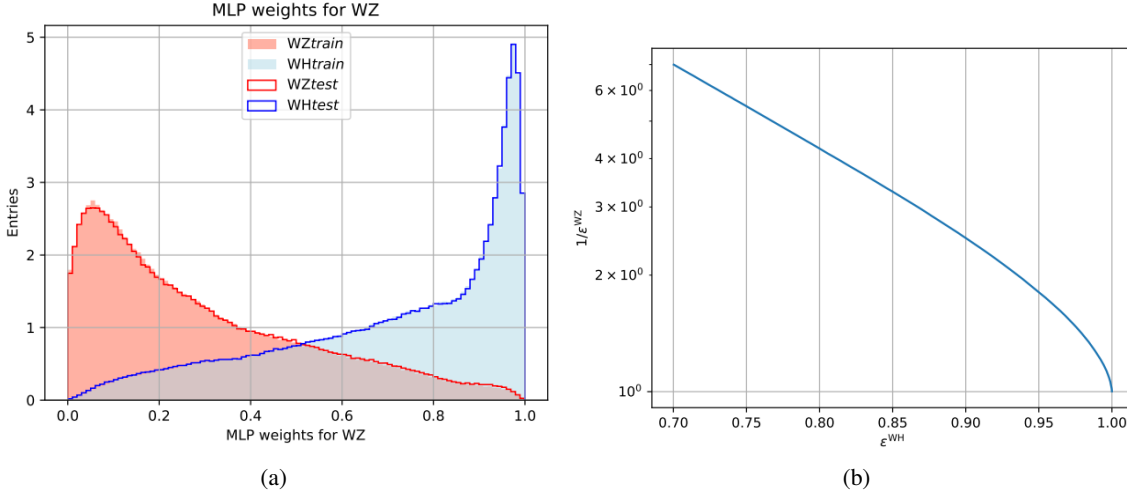


Figure 4.8: The performance of the RNN used in the same-sign 2ℓ channel analysis. (a) The distribution of the RNN output on the signal and background for the trained and tested samples is shown. (b) The background rejection as a function of the signal efficiency in the train and test samples.

4.5.4 3ℓ channel

The 3ℓ channel requires exactly three isolated leptons with $p_T > 15$ GeV and a total charge of ± 1 . To differentiate between the three leptons, the lepton with unique charge is identified as ℓ_0 , the lepton closest to ℓ_0 in angular distance ΔR is identified as ℓ_1 , and the remaining lepton is identified as ℓ_2 . In signal events, the leptons ℓ_0 and ℓ_1 are predominantly originating from the $H \rightarrow WW^*$ decay with probabilities of 99% and 85%, respectively.

The primary background processes in the 3ℓ channel are the $W(Z/\gamma^*)$ production and top-quark processes. The top-quark processes can have either three prompt leptons (e.g., $t\bar{t}V$) or two prompt leptons along with a non-prompt lepton from a b -hadron decay (e.g., $t\bar{t}$).

In the 3ℓ channel analysis, events are classified based on the presence of at least one same-flavor, opposite-sign charge (SFOS) lepton pair or zero SFOS lepton pairs, which have distinct signal-to-background ratios. The category of events with SFOS lepton pairs is referred to as the Z-dominated category because of the presence of background processes with $Z \rightarrow \ell\ell$ decays. On the other hand, the category of events with zero SFOS lepton pairs is referred to as the Z-depleted category.

The Z-dominated category is characterized by a dominant contribution of background processes involving Z bosons. In order to reduce the contribution of these backgrounds, a Z-veto selection is applied to all SFOS pairs requiring their invariant masses, $m_{\ell\ell}$, to satisfy $|m_{\ell\ell} - m_Z| > 25$ GeV. Additionally, to suppress background events from heavy-flavor quarkonia, a minimum invariant mass of 12 GeV is required for all SFOS pairs. The presence of neutrinos in the final states is identified by a minimum missing transverse energy of 30 GeV. In order to reduce the contribution from top quark processes, events with one or more b -tagged jets are rejected.

The ANN is used for both categories to distinguish between signal and background events. In the Z-dominated category, 15 variables are employed as input, including $p_T^{\ell_0}$, the magnitude of the

4 Measurement of the Vector Boson Associated Production with the $H \rightarrow WW^*$ Decay

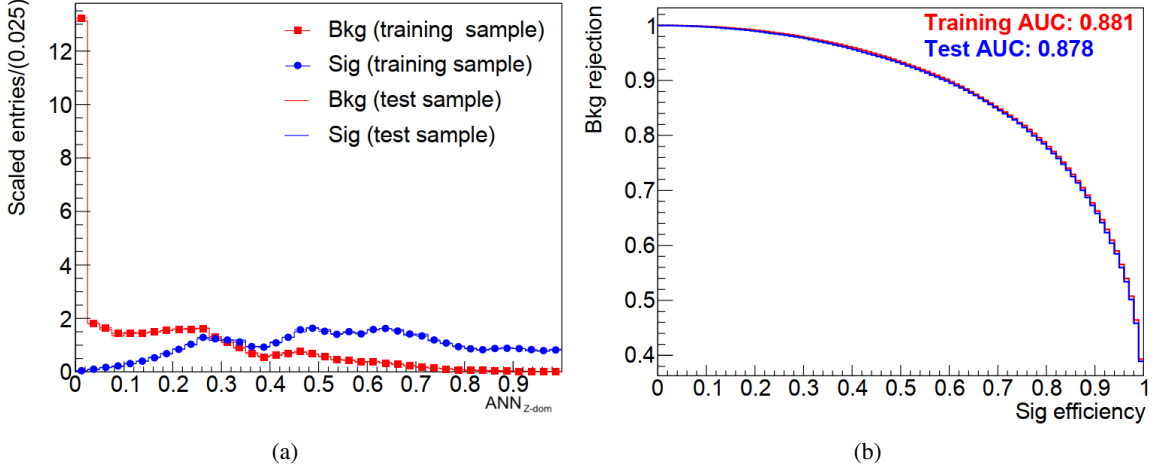


Figure 4.9: The performance of the ANN_{Zdom} used in the analysis. (a) The distribution of the ANN_{Zdom} on the signal and background for the trained and tested samples is shown. (b) The background rejection as a function of the signal efficiency in the train and test samples.

vectorial sum of lepton transverse momenta, $|\sum_{i=0}^2 \vec{p}_T^{\ell_i}|$, $\Delta\eta_{\ell_0\ell_1}$, $\Delta\eta_{\ell_1\ell_2}$, $\Delta\phi_{\ell_0\ell_2}$, $\Delta R_{\ell_0\ell_1}$, $\Delta R_{\ell_0\ell_2}$, $m_{\ell_i\ell_j}$ (for all lepton pairs), and $\Delta\phi_{\ell_i,\text{miss}}$ (the azimuthal separation between the leptons and the missing transverse momentum). Additionally, the transverse mass of the W boson, m_T^W , is calculated using the E_T^{miss} and the lepton not belonging to the SFOS pair with an invariant mass closest to that of the Z boson, either ℓ_1 or ℓ_2 , and is used as input. For the training of the single output classifier, ANN_{Zdom}, against the dominant $W(Z/\gamma^*)$ background, the output is used as the final discriminant in this channel.

The performances of ANN_{Zdom} are evaluated as both the distributions on the signal and background and the curves of the background rejection as a function of the signal efficiency are shown in Fig. 4.9.

In the Z -depleted region, the principal background contributions are $t\bar{t}$, $W(Z/\gamma^*)$, and WWW . In order to differentiate the WH signal from these backgrounds, a multiclassifier is employed, with four distinct output nodes, ANN_{Zdep} ^{i} , each quantifying the likelihood of the event originating from process i ($i = WH, t\bar{t}, WZ, WWW$), with the condition that $\sum_i \text{ANN}_{Zdep}^i = 1$ (shown in Eq. 4.3). Supplementary variables are taken into account, including the tripleton invariant mass, $m_{\ell\ell\ell}$; the number of jets, n_{jets} ; the number of b -tagged jets, $n_{b\text{-jets}}$; the transverse momentum of the leading jet, $p_T^{j_0}$; the transverse mass of each lepton pair, $m_T^{\ell_i\ell_j}$; the ratio of the E_T^{miss} significance, S_{miss} , to the E_T^{miss} , $S_{\text{miss}}/E_T^{\text{miss}}$; and the agreement of the event with the WZ hypothesis, F_α .¹ Tab. 4.5 summarizes the input variables used in both categories.

The performances of the ANNs used for the Z -depleted region are evaluated as both the distributions on the signal and background as well as the background rejection as a function of the signal efficiency

¹ Given the reconstructed charged lepton momenta and the \vec{p}_T^{miss} , the event kinematics can be calculated under the WZ with $Z \rightarrow \tau\tau$ hypothesis and using the collinear approximation for the τ decays with one remaining unknown – for example, the ratio of one τ 's energy to the energy of the lepton from the same τ 's decay. This unknown is varied, and the number of physical kinematic solutions is taken as a measure of compatibility with the WZ hypothesis.

4.5 Event selection

Table 4.5: Summary of input variables for the ANNs in the Z-dominated (left) and Z-depleted (right) categories.

(a)				(b)			
ANN input variables for $3l$ Z-dominated channel				ANN input variables for $3l$ Z-depleted channel			
$p_T^{\ell_0}$	$\left \sum_{i=0}^2 \vec{p}_T^{\ell_i} \right $	$\Delta\eta_{\ell_0\ell_1}$	$\Delta\eta_{\ell_1\ell_2}$	E_T^{miss}	$\Delta R_{\ell_0\ell_1}$	$\Delta R_{\ell_0\ell_2}$	$\Delta R_{\ell_1\ell_2}$
$\Delta\phi_{\ell_0\ell_2}$	$\Delta R_{\ell_0\ell_1}$	$\Delta R_{\ell_0\ell_2}$	$m_{\ell_0\ell_1}$	$\Delta\eta_{\ell_0\ell_1}$	$\Delta\eta_{\ell_0\ell_2}$	$\Delta\eta_{\ell_1\ell_2}$	$m_{\ell\ell\ell}$
$m_{\ell_0\ell_2}$	$m_{\ell_1\ell_2}$	$\Delta\phi_{\ell_0,\text{miss}}$	$\Delta\phi_{\ell_1,\text{miss}}$	$p_T^{\ell_0}$	$p_T^{\ell_1}$	$p_T^{\ell_2}$	$\left \sum_{i=0}^2 \vec{p}_T^{\ell_i} \right $
$\Delta\phi_{\ell_2,\text{miss}}$	E_T^{miss}	m_T^W		$p_T^{j_0}$	n_{jets}	$n_{b\text{-jets}}$	$\Delta\phi_{\ell_0,\text{miss}}$
				$m_{\ell_0\ell_1}$	$m_{\ell_0\ell_2}$	$m_{\ell_1\ell_2}$	$\Delta\phi_{\ell_1,\text{miss}}$
				$m_T^{\ell_0\ell_1}$	$m_T^{\ell_0\ell_2}$	$m_T^{\ell_1\ell_2}$	$\Delta\phi_{\ell_2,\text{miss}}$
				$S_{\text{miss}}/E_T^{\text{miss}}$	F_α		

curves in Fig. 4.10 for each background output node regarding to the node for WH . The final discriminant is defined as a linear combination of the output nodes as:

$$\text{ANN}_{\text{Zdep}}^\Delta := \text{ANN}_{\text{Zdep}}^{WH} - \text{ANN}_{\text{Zdep}}^{WZ} - \text{ANN}_{\text{Zdep}}^{WWW}. \quad (4.3)$$

4 Measurement of the Vector Boson Associated Production with the $H \rightarrow WW^*$ Decay

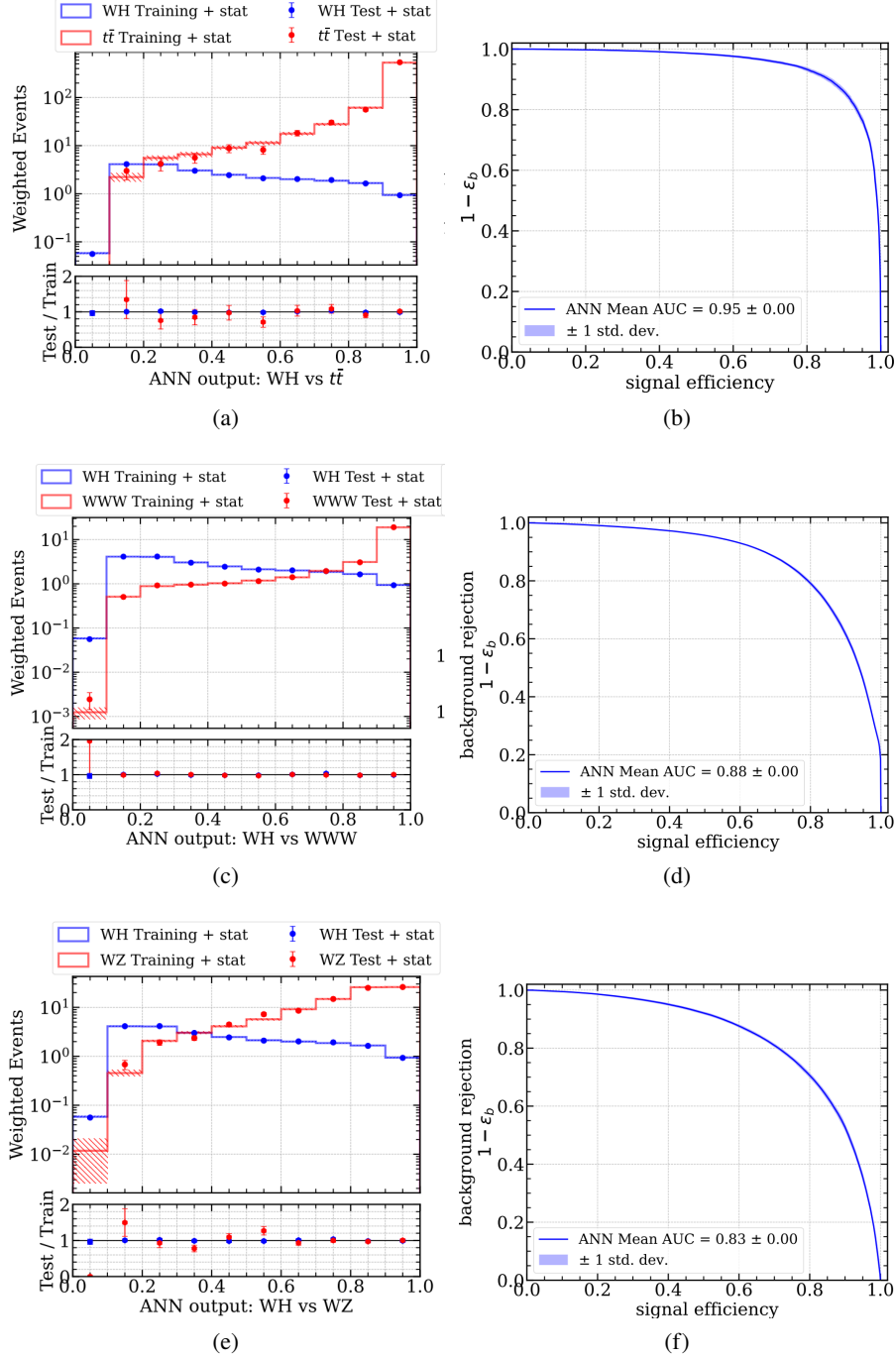


Figure 4.10: The performance of the ANN_{Zdep} used in the analysis. (a) (c) (e) The distribution of the ANN_{Zdep} on the signal and background for the trained and tested samples on the output nodes for $t\bar{t}$, WWW , WZ regarding to the WH node. (b) (d) (f) The background rejection as a function of the signal efficiency in the train and test samples on the output nodes for $t\bar{t}$, WWW , WZ regarding to the WH node.

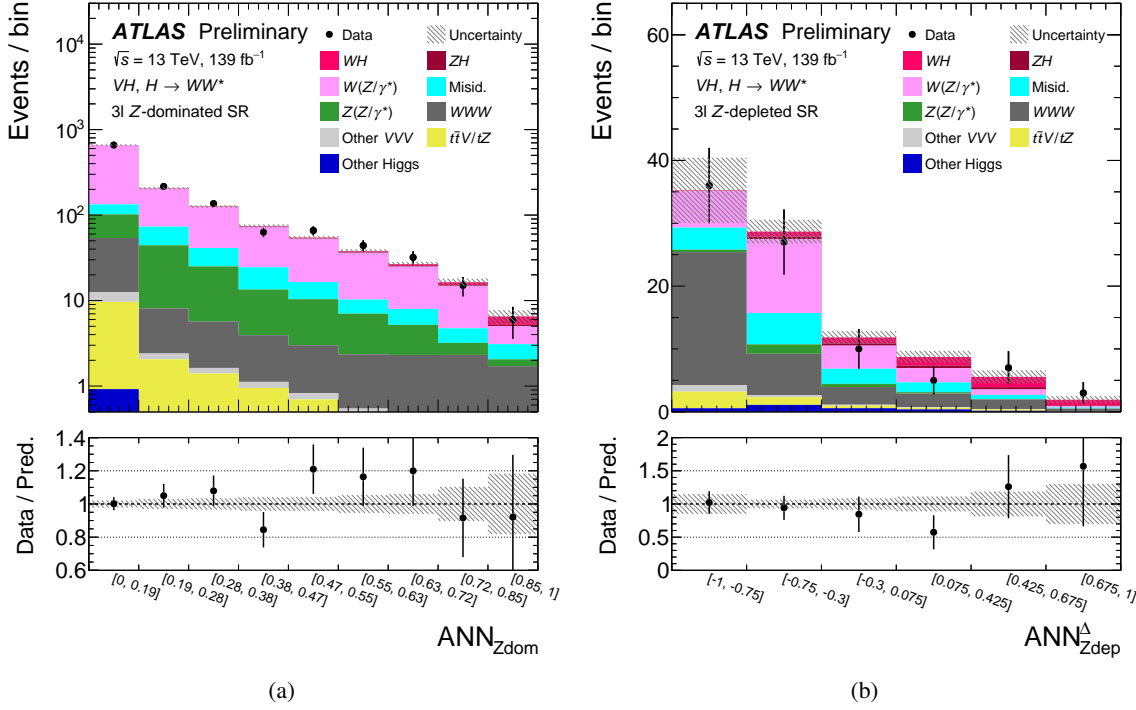


Figure 4.11: Post-fit distributions of (a) ANN_{Zdom} in the Z-dominated SR and (b) $\text{ANN}_{\text{Zdep}}^{\Delta}$ in the Z-depleted SR. The lower panel shows the ratio of the data to the sum of the fitted signal and background. The hatched band in the upper panel and the shaded band in the lower panel show the total uncertainty. The post-fit results are obtained from the combined 2 POI fit described in Sec. 4.8.3.

4.5.5 4ℓ channel

The ZH channel includes events with four isolated leptons with $p_T > 10$ GeV and a total electric charge of zero. Events containing an SFOS lepton pair with $m_{\ell\ell} < 12$ GeV or a DFOS lepton pair with $m_{\ell\ell} < 10$ GeV are rejected in order to suppress the contamination from heavy-flavour quarkonia. Selected events are classified according to the number of SFOS lepton pairs: 1-SFOS and 2-SFOS. Events with no SFOS lepton pairs are excluded.

The reconstruction of the ZH process proceeds through the identification of the leptons from the Z boson, called ℓ_2 and ℓ_3 , as the SFOS lepton pair with invariant mass closest to the mass of the Z boson. The remaining two leptons, labeled as ℓ_0 and ℓ_1 , are candidates for originating from the Higgs boson decay. In order to suppress the $t\bar{t}Z$ process, events containing b -tagged jets are rejected. To reduce the ZZ background process in 2-SFOS events, the invariant mass of ℓ_0 and ℓ_1 , $m_{\ell_0\ell_1}$, is required to be below 50 GeV; to ensure orthogonality with the ATLAS $H \rightarrow ZZ^* \rightarrow 4\ell$ measurement [83], the 4-lepton invariant mass is required to be below 115 GeV or above 130 GeV. Moreover, the $\tau\tau$ invariant mass, $m_{\tau\tau}$, is required to be below 5 TeV, where $m_{\tau\tau}$ is computed using the collinear approximation [174] using ℓ_0 and ℓ_1 . This cut is used to remove events with unphysical $m_{\tau\tau}$ values. Finally, the angular separation between ℓ_0 and ℓ_1 , $\Delta R_{\ell_0\ell_1}$, is required to be larger than 0.2 to remove

4 Measurement of the Vector Boson Associated Production with the $H \rightarrow WW^*$ Decay

Table 4.6: Summary of input variables for the BDTs in the 4ℓ channel.

BDT input variables for 4ℓ channel			
n_{jets}	$p_{\text{T}}^{\ell_0}$	$p_{\text{T}}^{\ell_1}$	$p_{\text{T}}^{\ell_2}$
$p_{\text{T}}^{\ell_3}$	$E_{\text{T}}^{\text{miss}}$	$p_{\text{T}}^{4\ell}$	$m_{\ell_2\ell_3}$
$m_{\ell_0\ell_1}$	$m_{4\ell}$	$m_{\tau\tau}$	$\Delta\phi_{\ell_0\ell_1,\text{miss}}$
$\Delta\phi_{\ell_0\ell_1}^{\text{boost}}$			

overlapping leptons.

For each of the 1-SFOS and 2-SFOS categories, a discriminant based on a boosted decision tree (BDT) [171] is used to achieve a further separation between the ZH and ZZ processes. Independent BDTs are trained for each category but share a common set of input variables, including: the number of jets, n_{jets} ; the transverse momenta of the leptons, $p_{\text{T}}^{\ell_i}$; the missing transverse energy, $E_{\text{T}}^{\text{miss}}$; the four-lepton transverse momentum, $p_{\text{T}}^{4\ell}$; the invariant mass of the Z candidate, $m_{\ell_2\ell_3}$; the invariant mass of the Higgs candidate, $m_{\ell_0\ell_1}$; the four-lepton invariant mass, $m_{4\ell}$; the $\tau\tau$ invariant mass, $m_{\tau\tau}$; and the azimuthal separation between the Higgs-candidate lepton pair and the $E_{\text{T}}^{\text{miss}}$, $\Delta\phi_{\ell_0\ell_1,\text{miss}}$. The final variable is the azimuthal separation between the leptons from the Higgs candidate in the frame where the Higgs boson p_{T} is zero, $\Delta\phi_{\ell_0\ell_1}^{\text{boost}}$. The Higgs boson transverse momentum is approximated with $\vec{p}_{\text{T}}^H \approx -\vec{p}_{\text{T}}^Z$ or $\vec{p}_{\text{T}}^H \approx -\vec{p}_{\text{T}}^Z - \sum \vec{p}_{\text{T}}^{\text{jet}}$, if at least one jet is present in the event.

Tab. 4.6 summarises the input variables used in both categories and Fig. 4.12 shows the post-fit distributions of the BDT discriminant in the two 4ℓ categories.

The $t\bar{t}Z$ background modeling is validated in a region built from the SR but with at least two jets and at least one b -tagged jet. At least one SFOS lepton pair is required to be within 10 GeV of the Z boson mass. In order to increase the purity in the events with a second SFOS lepton pair, the ZZ process is suppressed by requiring the invariant mass of the $\ell_0\ell_1$ pair to be outside a window of 20 GeV around the Z boson mass and greater than 40 GeV. A second validation region with a small amount of expected signal is defined in the least sensitive regions of the BDT distributions, namely the regions with $\text{BDT} < 0.12$ and $\text{BDT} < 0.16$ for the 1-SFOS and 2-SFOS categories, respectively. The modeling of the background processes in these regions is found to be satisfactory.

The performance of the BDT used for the 4ℓ channel is evaluated as both the distributions on the signal and background and be shown in Fig. 4.13.

4.5 Event selection

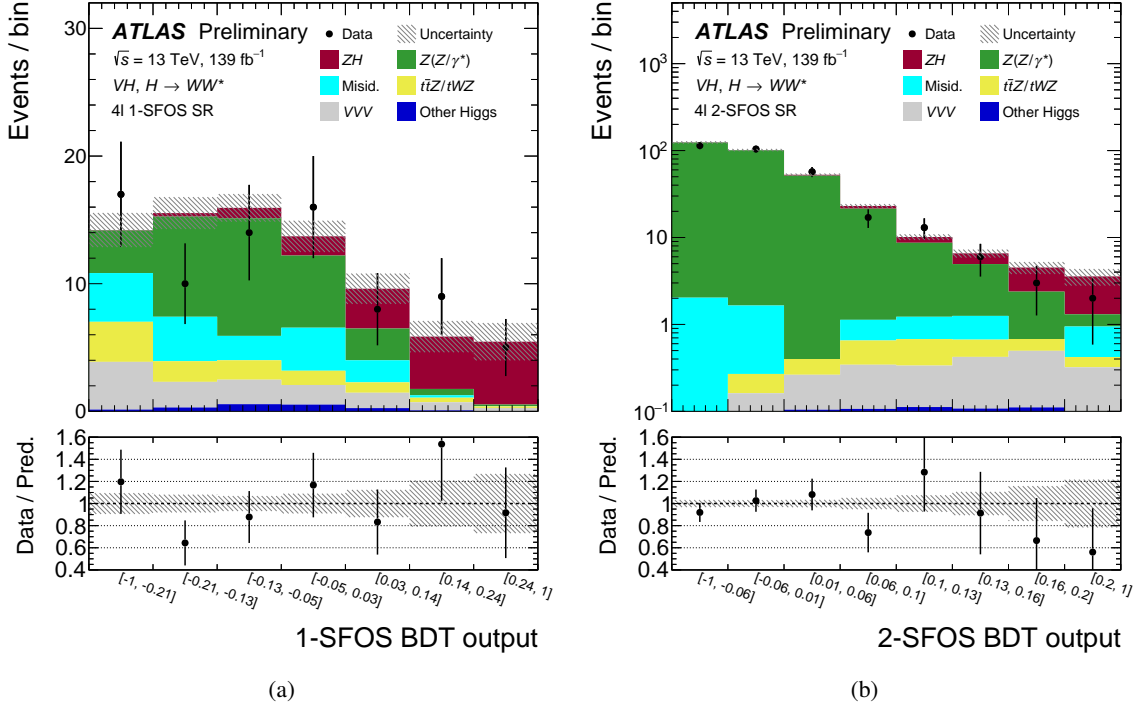


Figure 4.12: Post-fit distributions of the BDT in (a) the 1-SFOS category and (b) the 2-SFOS category. The lower panel shows the ratio of the data to the sum of the fitted signal and background. The hatched band in the upper panel and the shaded band in the lower panel show the total uncertainty. The post-fit results are obtained from the combined 2 POI fit described in Sec. 4.8.3.

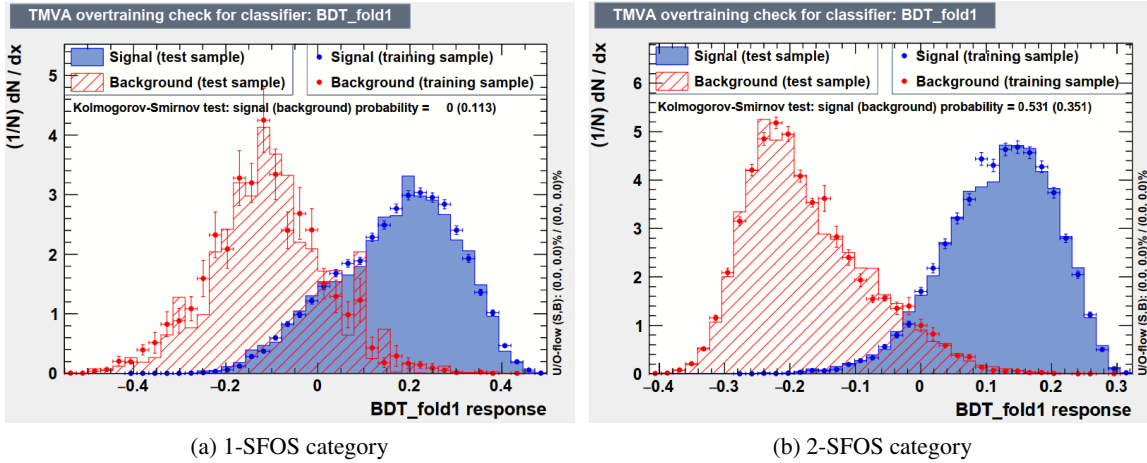


Figure 4.13: The performances of the BDTs used in the analysis are shown by the distribution of the signal and background for the trained and tested samples. The BDT is trained and applied individually for (a) 1-SFOS and (b) 2-SFOS categories.

4.6 Background estimation

The SRs contain background contamination resulting from various physics processes, which are modeled using one of three methods: the pure Monte Carlo (MC) prediction, the MC prediction, which is further normalized to data, or the pure data-driven prediction. With the first method, rates and differential distributions (shapes) are obtained from simulation and then normalized to the predicted cross-sections. In the second method, rates are constrained to data in dedicated control regions (CRs) that are either orthogonal to the SRs or within the SRs themselves, while the shapes are extracted from the simulation. To estimate the background with misidentified leptons, pure data-driven prediction is used, wherein rates and shapes are extracted from data using the fake-factor method. The method adopted for each background process in each signal region is summarized in Tab. 4.7.

Table 4.7: The background modeling of each channel. At least one reconstructed misidentified lepton in the data-driven background processes.

Channel	Normalised in the fit	Control Region	Data-driven
Opposite-sign 2ℓ	–	$t\bar{t}/Wt$, Z +jets, WW	$W+\gamma$, W +jets
Same-sign 2ℓ	$W(Z/\gamma^*)$	–	$V+\gamma$, V +jets
3ℓ	WWW	$W(Z/\gamma^*)$	$Z+\gamma$, Z +jets, $t\bar{t}/Wt$, WW +jets
4ℓ	–	ZZ	$W(Z/\gamma^*)$ +jets, $t\bar{t}W/tZ$, Z +jets, $t\bar{t}/Wt$

4.6.1 Opposite-sign 2ℓ channel

For the opposite-sign 2ℓ channel, in order to normalize the top, Z +jets, and WW background processes, distinct CRs are established. The definition of these CRs involves setting a requirement that the VH output node of the ANN is less than 0.2, which establishes a region that is orthogonal to the SR. Additionally, dedicated cuts are applied to each of the ANN’s background nodes to define the three CRs. The top CR serves as the normalization factor for both the $t\bar{t}$ and Wt background processes. The purity is 72%, 77%, and 58% for the top, Z +jets, and WW CRs, respectively. The distributions of the multivariate discriminant are shown in Fig. 4.14.

4.6.2 Same-sign 2ℓ channel

The normalisation of the $W(Z/\gamma^*)$ background in the SR is achieved by fitting a free parameter in the same-sign 2ℓ channel. Whenever one lepton’s charge is incorrectly assigned, the background processes $t\bar{t}$ and Z +jets become relevant. The probability of charge mis-identification is considerably high for an electron with hard bremsstrahlung or a track curvature that is mis-measured. For measuring this probability, a control sample of electrons from Z boson decays is employed in the data-driven procedure, from which the mis-identified lepton background is obtained, and the $W(Z/\gamma^*)$ background is obtained from MC. Using four bins of electron p_T and six bins of $|\eta|$, the charge mis-identification

4.6 Background estimation

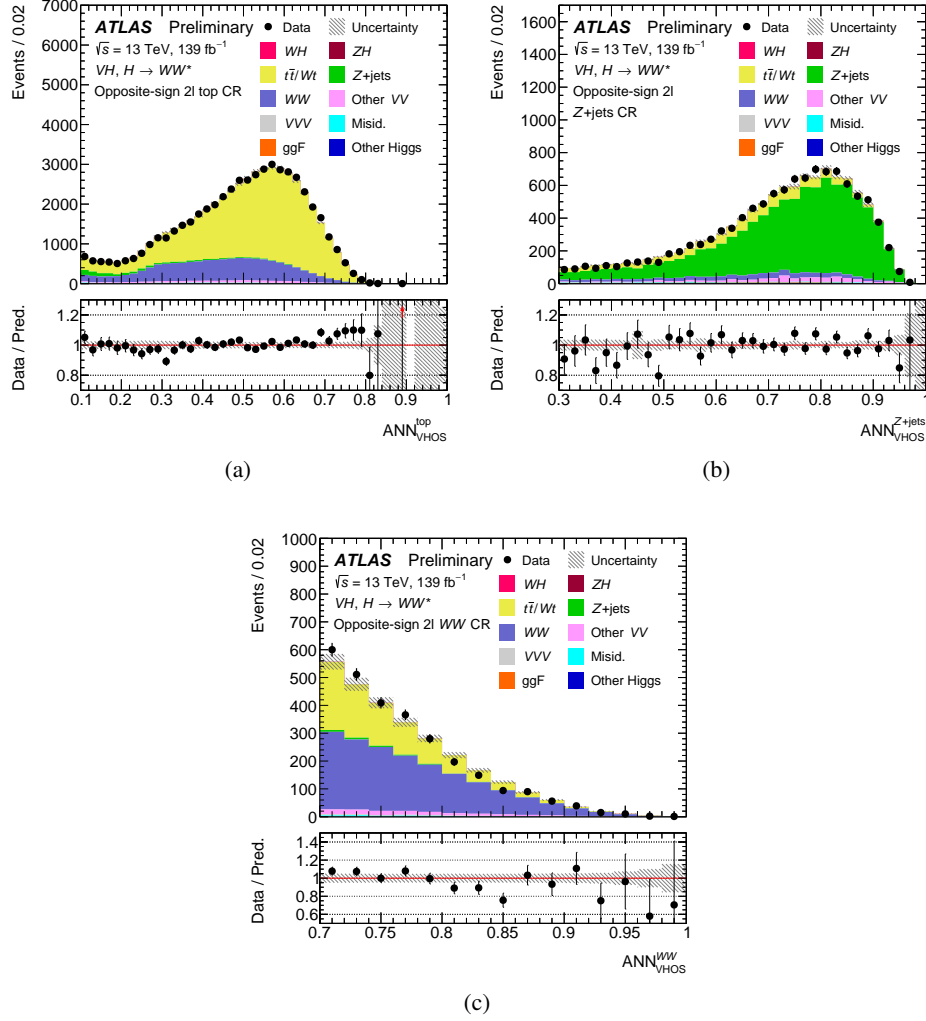


Figure 4.14: Post-fit distributions of (a) ANN_{VHOS}^{top} in the top CR, (b) ANN_{VHOS}^{Z+jets} in the Z+jets CR, and (c) ANN_{VHOS}^{WW} in the WW CR of the opposite-sign 2ℓ channel. The lower panel shows the ratio of the data to the sum of the fitted signal and background. The hatched band in the upper panel and the shaded band in the lower panel show the total uncertainty. The post-fit results are obtained from the combined 2 POI fit described in Sec. 4.8.3.

4 Measurement of the Vector Boson Associated Production with the $H \rightarrow WW^*$ Decay

probability is parameterized as a function of these variables. The bin size was determined based on the size of the event sample and the detector geometry. For electrons with $15 < p_T < 60$ GeV and $|\eta| < 0.6$, the charge mis-identification probability ranges from $\mathcal{O}(10^{-5})$, while for electrons with $p_T > 130$ GeV and $|\eta| > 2.3$, it can be as high as $\mathcal{O}(10^{-2})$. By utilizing the measured probabilities of mis-identifying charges, an estimation of the background caused by charge mis-identification is made for the sample of opposite-sign leptons, which meets the criteria of the same-sign 2ℓ groups. The charge mis-identification background is evaluated for each category. The SS2e SR contains a charge mis-identification background fraction of 26%, whereas the SSDF SR has a fraction of 1.6%. The probability of muon charge mis-identification is considered negligible in the relevant p_T range for this analysis.

4.6.3 3ℓ channel

In the 3ℓ channel, the $W(Z/\gamma^*)$ control regions (CRs) are established by enforcing the presence of a minimum of one pair of same-flavor opposite-sign (SFOS) leptons and reversing the Z-veto criterion that applies in the signal region (SR). It has been determined that the magnitude of the $W(Z/\gamma^*)$ background is linked to the number of jets in the events. Thus the CR is separated into two categories: one that comprises events with no identified jets and another that encompasses events with at least one identified jet. The rate of purity for the jet-free regions is 93%, while the rate of purity for the region with one or more jets is 88%. The distributions of the multivariate discriminant are shown in Fig. 4.15.

Following the detection of an excess in the rate of the SM $WWW + WH$ process, as documented in Ref. [176], the WWW background is normalized in the fitting process through a floating parameter. The most substantial background in the 3ℓ channel where the Z boson is depleted is the WWW process, trailed by the production of $W(Z/\gamma^*)$. The measured normalization factor, $2.18^{+0.73}_{-0.61}$, is in harmony with the signal strength of 1.61 ± 0.25 , as measured by the SM WWW analysis [176].

4.6 Background estimation

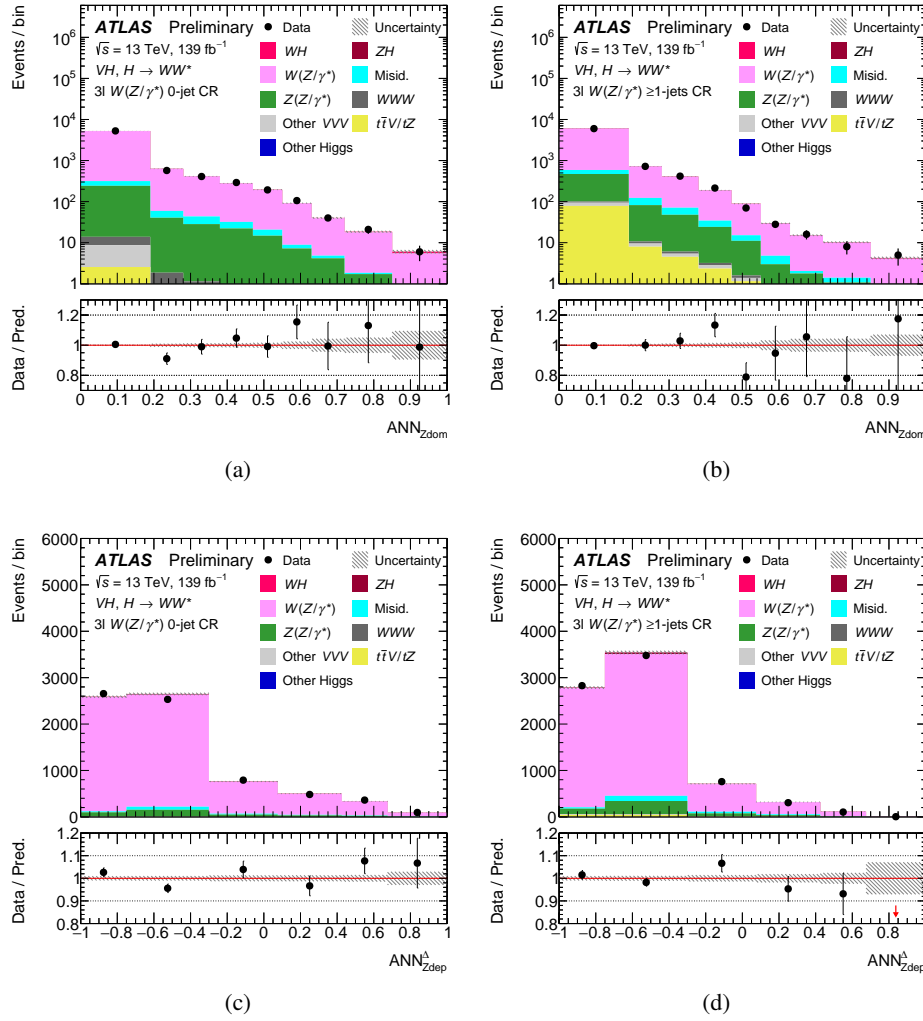


Figure 4.15: Post-fit distributions of ANN_{Zdom} in the (a) $W(Z/\gamma^*)$ CR with no jets and (b) $W(Z/\gamma^*)$ CR with at least one jet and of ANN_{Zdep}^A in the (c) $W(Z/\gamma^*)$ CR with no jets and (d) $W(Z/\gamma^*)$ CR with at least one jet. The lower panel shows the ratio of the data to the sum of the fitted signal and background. The hatched band in the upper panel and the shaded band in the lower panel show the total uncertainty. The post-fit results are obtained from the combined 2 POI fit described in Sec. 4.8.3.

4.6.4 4ℓ channel

In the 4ℓ channel, an exclusive CR is employed to evaluate the normalization factor of the ZZ process. This CR is established in the 2-SFOS category after applying b -jet veto by imposing additional requirements on the invariant mass of both the lepton pairs. To ensure that only on-shell Z boson leptonic decays are selected, $m_{\ell_2\ell_3}$ must fall within a window of ± 10 GeV around the Z boson mass. Additionally, $m_{\ell_0\ell_1}$ must exceed 50 GeV. The degree of purity in this region is roughly 97%. The distributions of the multivariate discriminant are shown in Fig. 4.16.

4 Measurement of the Vector Boson Associated Production with the $H \rightarrow WW^*$ Decay

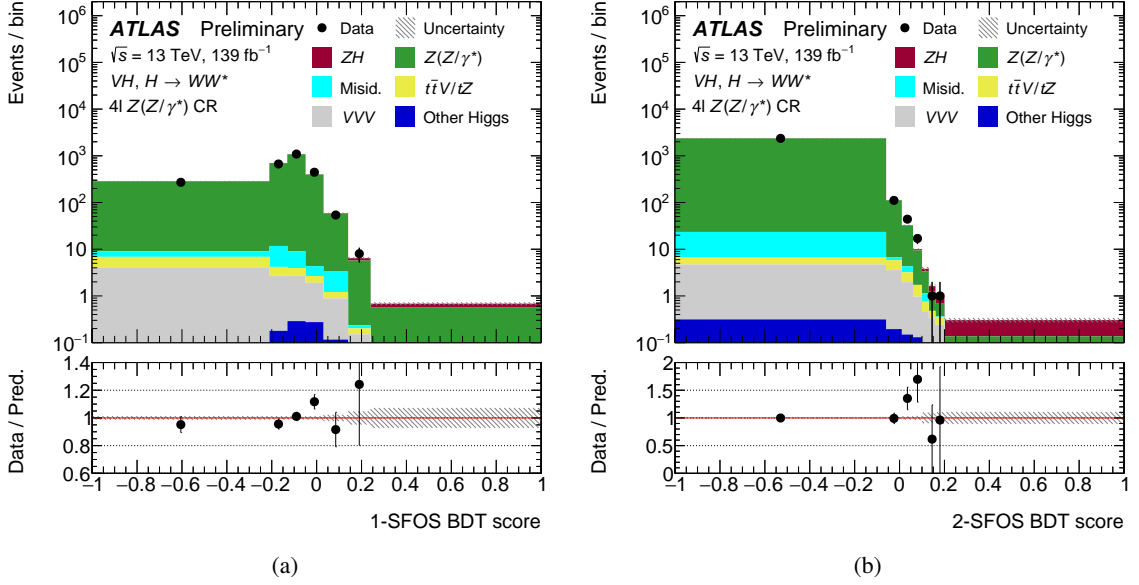


Figure 4.16: Post-fit distributions of the (a) 1-SFOS BDT output and (b) 2-SFOS BDT output in the ZZ CR. The lower panel shows the ratio of the data to the sum of the fitted signal and background. The hatched band in the upper panel and the shaded band in the lower panel show the total uncertainty. The post-fit results are obtained from the combined 2 POI fit described in Sec. 4.8.3.

The post-fit background normalization factors obtained from the fit are summarized in Tab. 4.12. The background processes which are not normalized in the fit procedure or not measured via the data-driven method are estimated via pure MC prediction and normalized to theoretical cross-sections.

4.6.5 Background from fake-leptons

$VH\ 2\ell$ DFOS, $WH\ 2\ell$ same-sign and 3ℓ channels

When a jet is misidentified as a lepton, that lepton only carries a fraction of the underlying jet's total momentum. The fake-factor method is used to estimate the fake background contribution in the SR from the dedicated fake control regions with the formula as Eq. 4.4. The id leptons are required to pass isolation cut so that they typically carry a much larger fraction of the underlying jet's p_T than the anti-id leptons (which are allowed to fail the isolation criteria). When one anti-id lepton and one id lepton fall into the same p_T bin, the anti-id lepton is supposed to originate from a jet with higher p_T than the jet that the id lepton emanates from. Since in the normal fake factor definition, events are binned in the leptons' p_T , within a given bin the underlying jet p_T spectrum can differ substantially and, more importantly, such difference will depend on the specific kinematic selections (e.g. $t\bar{t}$ versus Z +jets versus nominal signal or control regions selections). The estimated muon fake-factor in the $VH\ 2\ell$ DFOS, $WH\ 2\ell$ same-sign and 3ℓ channels are shown in Tab. 4.8 with the estimated uncertainties.

4.6 Background estimation

Table 4.8: The estimated muon fake-factor in the $VH\ 2\ell$ DFOS, $WH\ 2\ell$ same-sign and 3ℓ channels with the relative uncertainties

	FF_μ^{DD}	$\sigma_{\text{stat}}^{\text{fit}}$	$\sigma_{\text{stat}+xs}^{\text{fit}}$	$\sigma_{\text{non-closure}}$	σ_{total}
$15\text{GeV} < p_T < 30\text{GeV}$	0.012	19.1%	19.2%	71.7%	74.2%
$p_T > 30\text{GeV}$	0.017	26.6%	27.3%	23.0%	35.7%

$$FF = \frac{N_{\text{fake}}^{\text{id}, p_T}}{N_{\text{fake}}^{\text{anti-id}, p_T}} = \frac{N_{\text{data}}^{\text{id}, p_T} - N_{\text{real}}^{\text{id}, p_T}}{N_{\text{data}}^{\text{anti-id}, p_T} - N_{\text{real}}^{\text{anti-id}, p_T}}. \quad (4.4)$$

For the electrons, there are 3 sources: heavy flavor jets, light flavor jets, γ conversions. The scale factor method is used instead of the fake factor due to the difficulty to design CRs that would allow measuring separate fake factors for each source. Three electron scale factor CRs are designed for each contribution source. To measure the scale factors, a maximum likelihood fit is utilized which is defined as:

$$\mathcal{L}(\vec{SF}) = \prod_{ij} \underbrace{\text{Poisson}(N_{ij}^{\text{id data}}; N_{ij}^{\text{id estimated}}(\vec{\theta}))}_{\text{Poisson for ID CRs with scale factors } \vec{SF}} \times \prod_k \underbrace{\text{Gaussian}(\theta_k; \tilde{\theta}_k, \Delta\theta_k)}_{\text{Gauss. for prompt background norm.}}, \quad (4.5)$$

where,

- $N_{ij}^{\text{id data}}$ is the data yield in ID CR j p_T bin i ,
- $N_{ij}^{\text{id estimated}}(\vec{\theta}) = N_{ij}^{\text{id prompt}}(\vec{\theta}) + \sum_f SF_f^i \cdot N_{ij}^{\text{anti-id fake } f}$ is the sum of the prompt lepton background yield in ID CR j and the fake lepton background yield in AntiID CR j with the scale factors assigned in the p_T bin i ,
- $N_{ij}^{\text{id prompt}}(\vec{\theta}) = \sum_k N_{ij}^{\text{id prompt } k} \cdot \theta_k$, is the sum of the yield with normalization factor θ_k of each prompt process k in the ID CR j , p_T bin i and $k = WZ, ZZ, VVV, ttV, VH, ttH, tZ$,
- i is the index for 3 p_T bins, j is the index for 3 pairs of scale factor CRs and f is the index for 3 fake sources.

The estimated electron scale-factors for each contribution source, $SF_{\gamma \text{ conv}}$, SF_{heavy} and SF_{light} , are shown in the Tab. 4.9 with the estimated uncertainties.

ZH 4ℓ channel

The fake estimation in the ZH analysis relies on the two CRs enriched in processes with 3 prompt leptons and exactly one fake lepton ($3\ell + 1X$ CR), and two prompt leptons and two fake leptons ($2\ell + 2X$ CR). The fake contribution in these control regions is obtained from the data after subtracting

4 Measurement of the Vector Boson Associated Production with the $H \rightarrow WW^*$ Decay

Table 4.9: The estimated electron fake-factor in the $VH\ 2\ell$ DFOS, $WH\ 2\ell$ same-sign and 3ℓ channels with the relative uncertainties

	$SF_{\gamma\ \text{conv}}$	$\sigma_{\text{stat}}^{\text{fit}}$	$\sigma_{\text{stat+xs}}^{\text{fit}}$	$\sigma_{\text{non-closure}}$	σ_{total}
$15\ \text{GeV} < p_T < 20\ \text{GeV}$	0.091	+6.6% -6.3%	+6.5% -6.4%	79.0%	79.3%
$20\ \text{GeV} < p_T < 30\ \text{GeV}$	0.144	+6.0% -5.8%	+6.0% -5.9%	25.1%	25.8%
$p_T > 30\ \text{GeV}$	0.207	+8.6% -8.4%	+9.1% -8.7%	27.6%	29.0%
	SF_{heavy}	$\sigma_{\text{stat}}^{\text{fit}}$	$\sigma_{\text{stat+xs}}^{\text{fit}}$	$\sigma_{\text{non-closure}}$	σ_{total}
$15\ \text{GeV} < p_T < 20\ \text{GeV}$	0.064	+104.4% -83.7%	+102.1% -82.8%	61.3%	110.9%
$20\ \text{GeV} < p_T < 30\ \text{GeV}$	0.079	+100.0% -100.0%	+100.0% -100.0%	49.9%	111.8%
$p_T > 30\ \text{GeV}$	0.049	+100.0% -100.0%	+100.0% -100.0%	57.4%	115.3%
	SF_{light}	$\sigma_{\text{stat}}^{\text{fit}}$	$\sigma_{\text{stat+xs}}^{\text{fit}}$	$\sigma_{\text{non-closure}}$	σ_{total}
$15\ \text{GeV} < p_T < 20\ \text{GeV}$	0.113	+23.7% -25.3%	+24.0% -25.2%	43.9%	50.3%
$20\ \text{GeV} < p_T < 30\ \text{GeV}$	0.025	+107.5% -99.6%	+105.9% -99.6%	49.4%	114.0%
$p_T > 30\ \text{GeV}$	0.025	+100.0% -100.0%	+100.0% -100.0%	53.8%	113.6%

the 4-prompt lepton background processes from MC (ZZ , VVV ² and $t\bar{t}Z$). For each contribution the expected fake yield is estimated by:

$$\begin{aligned}
N_{4\ell}^{\text{one-fake}} &= N_{3\ell+X}^{\text{est. fakes}} \times FF, \\
N_{4\ell}^{\text{two-fakes}} &= N_{2\ell+2X}^{\text{est. fakes}} \times FF \times FF, \\
N_{4\ell}^{\text{fakes}} &= N_{3\ell+X}^{\text{est. fakes}} \times FF - N_{2\ell+2X}^{\text{est. fakes}} \times FF \times FF.
\end{aligned}$$

The estimated fake yield with their uncertainties are shown in Tab. 4.10 for electrons and in Tab. 4.11 for muons.

4.7 Systematic uncertainties

When MC samples are used, we assess the sources of systematic uncertainties, both on the theoretical and experimental side, and incorporate their impacts in the statistical analysis. For every analysis region and bin, we approximate the impact of these uncertainties on distributions. In cases where the effect is comparable across various bins for a specific distribution, we only incorporate a general

² Although triboson processes could be also a source of fake background, its estimation will be purely taken from the MC simulation due to the low expected contribution in the final signal regions.

4.7 Systematic uncertainties

Table 4.10: Expected fake-lepton event yields as predicted by MC and by data-driven (DD) method. Total background includes MC-based fake estimation. Only MC statistical uncertainties are quoted.

$\mathcal{L} = 139fb^{-1}$	WZ	Rel diff
4ℓ SR (fake electron)	3.32 ± 0.31	-
$(3\ell + e \text{ CR}) \times \text{FF}_e(\text{Sherpa})$	$(59.38 \pm 1.13) \times 0.060 = 3.56 \pm 0.07$	7%
$(3\ell + e \text{ CR}) \times \text{FF}_e(\text{Powheg})$	$(59.38 \pm 1.13) \times 0.084 = 4.99 \pm 0.07$	34%

Table 4.11: Expected fake-lepton event yields as predicted by MC and by data-driven (DD) method. Total background includes MC-based fake estimation. Only MC statistical uncertainties are quoted.

$\mathcal{L} = 139fb^{-1}$	WZ	Rel diff
4ℓ SR (fake electron)	1.08 ± 0.13	-
$(3\ell + \mu \text{ CR}) \times \text{FF}_\mu(\text{Sherpa})$	$(8.33 \pm 0.43) \times 0.202 = 1.68 \pm 0.09$	36%
$(3\ell + \mu \text{ CR}) \times \text{FF}_\mu(\text{Powheg})$	$(8.33 \pm 0.43) \times 0.254 = 2.12 \pm 0.11$	49%

Table 4.12: Post-fit normalization factors which scale the corresponding estimated yields in the signal region. The quoted uncertainties include both statistical and systematic contributions. The post-fit results are obtained from the combined 2 POI fit

Channel	Background	Normalization factor
Opposite-sign 2ℓ	Top	$0.99^{+0.31}_{-0.22}$
	Z+jets	$0.87^{+0.15}_{-0.14}$
	WW	$0.89^{+0.27}_{-0.24}$
Same-sign 2ℓ	$W(Z/\gamma^*)$	$0.91^{+0.18}_{-0.16}$
3ℓ	$W(Z/\gamma^*)$ 0-jet	1.03 ± 0.06
	$W(Z/\gamma^*) \geq 1$ -jets	$0.88^{+0.16}_{-0.15}$
	WWW	$2.18^{+0.73}_{-0.61}$
4ℓ	ZZ	$0.99^{+0.08}_{-0.07}$

normalization uncertainty. In Sec. 4.9, we present a table of the systematic uncertainty sources, along with their corresponding impact on the measurement.

4 Measurement of the Vector Boson Associated Production with the $H \rightarrow WW^*$ Decay

4.7.1 Experimental uncertainties

The uncertainties related to leptons in experiments come from various sources, such as the efficiencies of reconstruction, identification, and isolation [158, 159], and the scale, resolution on their energy or momentum [177, 178]. Uncertainties in the jets arise from different factors, such as the jet energy scale as well as resolution [163], the performance for the pile-up jet tagger, and the identification of b -jets [164]. Additionally, we estimate uncertainties coming from trigger selection [179, 180] and the soft term in the E_T^{miss} reconstruction [166]. The uncertainty in the pile-up modeling for simulated samples is estimated by changing the reweighing to the data profile within the corresponding uncertainties. We measure the uncertainty on the integrated luminosity using the LUCID-2 detector [181], which is 1.7% [182].

The theoretical predictions for both the signal and background processes are subject to the uncertainty of luminosity.

In order to estimate the backgrounds arising from misidentified leptons and electrons with misidentified charge through data-driven methods, several uncertainties are taken into account, including the availability of data and MC statistics, variations in the theoretical predictions of the backgrounds from prompt lepton, changes in the selection requirements, and data-MC non-closure.

The RNN performance in the same-sign 2ℓ channel has been assessed using $W(Z/\gamma^*)$ -enriched validation regions, which follow the three sets of SR selections but mandate the presence of a reconstructed lepton with $p_T > 15$ GeV that may not meet the standard quality criteria for selecting the two leading isolated leptons. In this region, the RNN distribution can detect inaccuracies in simulating real leptons from $W(Z/\gamma^*)$, which are often poorly reconstructed and resemble those missing in $W(Z/\gamma^*)$ events that have only two reconstructed leptons. The RNN shape is found to be poorly modeled for $W(Z/\gamma^*)$ events, mainly in the $\text{SS}2\mu$ and SSDF categories, resulting in a mis-modeling that varies from -4% to 18% depending on the RNN values and event categories. This mis-modeling is treated as a shape uncertainty with full size for the same-sign 2ℓ channels, and it reduces the expected sensitivity of this channel by 30% compared to the scenario where it is not considered. The modeling of events with three reconstructed leptons that must satisfy additional quality criteria is found to be satisfactory, and hence, no further uncertainty is deemed necessary for the 3ℓ channels.

In order to account for the normalization extrapolation from control to signal regions, the experimental uncertainties are simultaneously varied for all MC processes across all signal and control region bins.

The dominant experimental uncertainties are related to several sources, including the jet energy scale and resolution for the opposite-sign 2ℓ channel, the RNN shape and the backgrounds with mis-identified leptons and electrons for the same-sign 2ℓ channel, and the lepton background estimation and isolation for the 3ℓ and 4ℓ channels.

4.7.2 Theoretical uncertainties

The different sources of the theoretical uncertainties impacts are evaluated by either the alternative MC samples or by reweighting the MC events. The difference between the two samples is symmetrized and defined as the corresponding uncertainties.

The uncertainty of the missing higher-order corrections for all processes is calculated by the enveloped maximum variation from the coherent and incoherent variations on the renormalization and factorization scales. The PDF center value uncertainty is calculated by the difference between nominal weight and alternative weights. The strong coupling constant ($\alpha_s = 0.1180 \pm 0.0015$) center value uncertainties is calculated by the up and down variation following its uncertainty. The symmetrization is applied on the midpoint between those variations and assigned correspondingly.

The difference between the nominal sample showered by PYTHIA 8 and by HERWIG 7 is assigned as the Higgs process PS modeling uncertainty.

The MEPS@NLO method [183] is used to merge the NLO and LO matrix elements for the VV processes (modeled by SHERPA 2.2.2). The up and down variations in the threshold separating the ME and the PS are used to be assigned as a jet merging uncertainty. The up and down variations in the resummation scale are used to be assigned as a PS resummation uncertainty. The difference between the nominal sample using the recoil scheme described in Ref. [184], to an alternative sample using the recoil scheme described in Ref. [185] is assigned as a PS momentum recoil scheme choice uncertainty.

The difference between the nominal SHERPA samples and MADGRAPH5_aMC@NLO samples showered with PYTHIA 8 is used to assign a ME and PS modeling uncertainty for the VVV and Z+jets processes.

The difference between the PYTHIA 8 showered nominal sample and HERWIG 7 showered alternative sample is used to assign a hadronization and fragmentation modeling uncertainty. The difference between the POWHEG generated nominal sample and the MADGRAPH5_aMC@NLO generated alternative sample is used to assign a generator and matching algorithm choicing uncertainty. The varying scale, resummation, and showering parameters is used to assign the initial- and final-state radiation modeling uncertainties.

The dominant theoretical uncertainties sources are: uncertainties on the hadronisation/fragmentation modeling of $t\bar{t}$ production and on the ME/PS modeling of Z+jets production for the opposite-sign 2ℓ channel; uncertainties on the K-factor for same-sign WW production for the same-sign 2ℓ channel; uncertainties relating to the choice of PS recoil scheme for $W(Z/\gamma^*)$ production and on the modeling of WWW production for the 3ℓ channel; and uncertainties relating to the missing higher-order corrections to ZH production and on the $H \rightarrow WW^*$ branching ratio for the 4ℓ channel.

4.8 Statistical Treatment

4.8.1 Statistical Framework

Maximum likelihood estimation

The extraction of cross sections and signal strengths are performed with maximum likelihood method. The signal significances are calculated using the Log-Likelihood Ratio test. The likelihood function is constructed with Poisson statistics, with the systematics implemented as nuisance parameters, which are constrained with control regions or Gaussian probability distribution functions based on dedicated evaluations. Namely, the form of the likelihood function is

$$\mathcal{L}(\mu, \mu_b) = P(N|\mu s + \mu_b b_{\text{SR}}^{\text{exp}}) \times P(M|\mu_b b_{\text{CR}}^{\text{exp}}), \quad (4.6)$$

where $b_{\text{SR}}^{\text{exp}}$ and $b_{\text{CR}}^{\text{exp}}$ are expected background yields in the signal and control regions determined using MC, μ is the signal strength parameter, and μ_b is the background strength parameter.

Upon incorporating the nuisance parameters θ , it is possible to take into account a constraint $N(\tilde{\theta}|\theta)$, which serves as an additional measurement $\tilde{\theta}$ associated with the nuisance parameter θ . The two prevalent instances utilized in this examination involve a standard Gaussian function, $G(\tilde{\theta}|\theta, 1) = \frac{1}{\sqrt{2\pi}} e^{-\frac{(\tilde{\theta}-\theta)^2}{2}}$, or a Poisson function, $P(\tilde{\theta}|\theta\lambda) = \frac{(\theta\lambda)^{\tilde{\theta}} e^{-\theta\lambda}}{\tilde{\theta}!}$, where λ is a constant generally considered as the nominal value of $\tilde{\theta}$.

Nuisance parameters θ determine the anticipated signal and background functions. These functions are parameterized to ensure that the response of s and b to each θ is separated from the expected rate's nominal value. In other words, $s = s_0 \times \prod \nu(\theta)$, with the structure of $\nu(\theta)$ relying on the systematic source. We have four cases in general:

1. Flat systematic uncertainties (those that don't alter the shape of the discriminating variable) adopt the form $\nu_{\text{flat}}(\theta) = \kappa^\theta$, where κ is ascertained by evaluating ν_{flat} at $\theta = \pm 1$. In this situation, the likelihood contains a constraint term on θ as a unit Gaussian, resulting in a logarithm distribution for κ^θ .
2. When a systematic uncertainty can impact the shape, the shape variation is initially divided into a flat component and a pure shape component. The pure shape component variation of s or b does not affect the expected rate, and the flat component is processed as previously mentioned. The pure shape component employs vertical linear interpolation to approximate the variation and follows a truncated Gaussian distribution. Specifically, $\nu_{\text{shape}}(\theta) = 1 + \epsilon\theta$, with ϵ determined by measuring ν_{shape} at $\theta = \pm 1$ and the constraint being a unit Gaussian. The truncation is applied such that $\nu_{\text{shape}}(\theta < \frac{-1}{\epsilon}) = 0$. It is worth noting that systematic sources can possess both a normalization (e.g., Case 1) and a shape component, in which case the same θ is shared between functions $\nu_{\text{flat}}(\theta)$ and $\nu_{\text{shape}}(\theta)$.

3. The third scenario pertains to the management of purely statistical uncertainties, such as those arising from Monte Carlo (MC) statistics or data-driven techniques. In this case, the constraint symbolizes an auxiliary measured number of events $\tilde{\theta}$ with an expected number $\theta\lambda$. This translates to the Poisson probability $P(\tilde{\theta}|\theta\lambda) = \frac{(\theta\lambda)^{\tilde{\theta}} e^{-\theta\lambda}}{\tilde{\theta}!}$. Given an uncertainty σ_b on an expectation b_0 , $\tilde{\theta} = \lambda = \frac{b_0^2}{\sigma_{b_0}^2}$, and $\nu_{\text{stat}}(\theta) = \theta$.
4. The final case involves employing a high statistics control region to constrain the normalization of a background. This resembles the third case, with the constraint being the Poisson probability $P(\tilde{\theta}|\lambda(\theta)) = \frac{(\theta\lambda(\theta))^{\tilde{\theta}} e^{-\lambda(\theta)}}{\tilde{\theta}!}$, where $\tilde{\theta}$ signifies the observed events in the control region. The expected number of events is $\lambda = \mu s + \theta b_{\text{target}} + \sum_i^{N_{\text{bkg}}-1} b_i$, where b_{target} represents the background targeted by the control region. This method properly accounts for contamination due to the signal and other backgrounds. In complete likelihood, numerous nuisance parameters denote the strengths of almost all backgrounds. Additionally, the strength parameters multiply the expected background wherever that background is present, ensuring that contaminations among various control regions are addressed appropriately.

Test statistic and p -values

The statistical computation methodology utilizes the profile likelihood ratio test statistic q . The profile likelihood ratio is initially constructed as follows:

$$\tilde{\lambda}(\mu) = \begin{cases} \frac{L(\mu, \hat{\hat{\theta}}(\mu))}{L(\hat{\mu}, \hat{\hat{\theta}})} & \hat{\mu} \geq 0, \\ \frac{L(\mu, \hat{\hat{\theta}}(\mu))}{L(0, \hat{\hat{\theta}}(0))} & \hat{\mu} < 0. \end{cases} \quad (4.7)$$

In this equation, $\hat{\hat{\theta}}(0)$ and $\hat{\hat{\theta}}(\mu)$ denote the conditional maximum likelihood (ML) estimators of $\vec{\theta}$, given a strength parameter of 0 or μ , respectively. The test statistic \tilde{q}_μ is defined as:

$$\tilde{q}_\mu = \begin{cases} -2 \ln \tilde{\lambda}(\mu) & \hat{\mu} \leq \mu \\ 0 & \hat{\mu} > \mu \end{cases} = \begin{cases} -2 \ln \frac{L(\mu, \hat{\hat{\theta}}(\mu))}{L(0, \hat{\hat{\theta}}(0))} & \hat{\mu} < 0, \\ -2 \ln \frac{L(\mu, \hat{\hat{\theta}}(\mu))}{L(\hat{\mu}, \hat{\hat{\theta}})} & 0 \leq \hat{\mu} \leq \mu, \\ 0 & \hat{\mu} > \mu. \end{cases} \quad (4.8)$$

The modified frequentist method CLs is employed to calculate 95% confidence intervals for the signal strength parameter μ . In this situation, the test statistic is one-sided, with the constraint $0 < \hat{\mu} < \mu$. The p -values p_μ and p_b are derived from the sampling distributions $f(q|\mu, \hat{\theta}_\mu)$ and $f(q|0, \hat{\theta}_0)$, respectively:

4 Measurement of the Vector Boson Associated Production with the $H \rightarrow WW^*$ Decay

$$p_\mu = \int_{\tilde{q}_{\mu,\text{obs}}}^{\infty} f(q|\mu, \hat{\theta}_\mu) dq, \quad (4.9)$$

$$p_b = \int_{\infty}^{\tilde{q}_{\mu,\text{obs}}} f(q|0, \hat{\theta}_0) dq. \quad (4.10)$$

The CLs is subsequently constructed as the ratio of p -values:

$$\text{CLs} = \frac{p_\mu}{1 - p_b}. \quad (4.11)$$

The 95% CL upper limit on μ is the solution to $\text{CLs} = 0.05$. To compute statistical significance, the background-only p -value is determined from the test statistic q_0 , with an alternative constraint $\hat{\mu} > 0$:

$$p_0 = \int_{q_{0,\text{obs}}}^{\infty} f(q_0|0, \hat{\theta}_0) dq_0. \quad (4.12)$$

The statistical significance Z can be extracted from p_0 by converting from the Gaussian tail probability:

$$Z = \Phi^{-1}(1 - p_0), \quad (4.13)$$

where Φ^{-1} represents the quantile of the standard Gaussian. Asymptotic formulae are utilized to approximate the sampling distributions, as described in [186].

4.8.2 Binning

The binning method for the MVA outputs is same as the one used in the previous $VH, H \rightarrow b\bar{b}$ analysis ([187]). To achieve a good significance while preventing the statistic fluctuation, a function Eq. 4.14 is defined to judge the quality of each bin during the re-binning:

$$Z(I[k, l]) = Z(z_s, n_s(I[k, l]), N_s, z_b, n_b(I[k, l]), N_b), \quad (4.14)$$

where

1. $I[k, l]$ is an interval of the histograms, containing the bins between bin k and bin l ,
2. N_s is the total number of signal events in the histogram,

4.8 Statistical Treatment

3. N_b is the total number of background events in the histogram,
4. $n_s(I[k, l])$ is the total number of signal events in the interval $I[k, l]$,
5. $n_b(I[k, l])$ is the total number of background events in the interval $I[k, l]$,
6. z_s and z_b are parameters used to tune the algorithm.

Whilst several different possible Z functions exist to transform the MVA outputs, in the results below, the transformation in Eq. 4.15 found to offer a significant decrease in the number of bins, whilst comparatively increasing the expected sensitivity is considered.

$$Z = z_s n_s / N_s + z_b n_b / N_b, \quad (4.15)$$

where, z_s and z_b are parameters used to tune the algorithm and N_s (N_b) is the total number of signal (background) events in the histogram. The re-binning is then conducted using the following algorithm:

1. Starting from the last bin on the right of the original histogram, increase the range of the interval $I(k, \text{last})$ by adding one after the other, the re-binning is from the right to the left.
2. Calculate the value of Z at each step.
3. Once $Z(I[k_0, \text{last}]) > 1$, re-bin all the bins in the interval $I(k_0, \text{last})$ into a single bin.
4. Repeat steps 1-3, starting this time from the last bin on the right, not included in the previous remap (the new last is $k_0 - 1$), until k_0 in the first bin.

The z_s and z_b are optimized with MC statistical uncertainties to maximize the expected sensitivity. This re-binning method is utilised for all of the channels. The choice of z_s and z_b for each channel summarized in Tab. 4.13.

Table 4.13: Summary of the optimized MVA output binning for each channel.

Channels	(z_s, z_b) proposals	bin boundary values
WH 3ℓ Z-dominated	(8, 2)	(0.19,0.28,0.38,0.47,0.55,0.63,0.72,0.85)
WH 3ℓ Z-depleted	(5, 3)	(-0.75,-0.3,0.075,0.425,0.675,0.825,0.925)
ZH 4ℓ 1-SFOS	(3, 4)	(-0.2,-0.12,-0.04,0.04,0.15,0.25,)
ZH 4ℓ 2-SFOS	(7, 2)	(-0.05, 0.02, 0.07, 0.11, 0.14, 0.17, 0.21)
VH 2ℓ DFOS	(8, 2)	(0.33,0.44,0.53,0.6,0.65,0.7,0.75,0.8)
WH 2ℓ SS DF	(8, 2)	(0.08,0.21,0.34,0.47,0.58,0.68,0.76,0.84,0.93)
WH 2ℓ SS $\mu\mu$	(8, 2)	
WH 2ℓ SS ee	(8, 2)	

4 Measurement of the Vector Boson Associated Production with the $H \rightarrow WW^*$ Decay

Table 4.14: Regions and POIs used for each channel fitting. The fitted value and expected significance are also shown, both experimental and theoretical systematics are included in the fitting.

Channels	Regions included	POIs	Fitted value	Significance(exp)
VH 2ℓ DFOS	DFOS SR, Z+jets CR, Top CR, WW CR	μ_{VH}	$1.00^{+1.02}_{-0.98}$	1.02
WH 2ℓ SS	SS ≥ 1 jet ee SR, $\mu\mu$ SR, $e\mu + \mu e$ SR	μ_{WH}	$1.00^{+0.61}_{-0.61}$	1.65
WH 3ℓ Z-dominated	Z-dominated SR, WZ 0 jet CR, WZ ≥ 1 jet CR	μ_{WH}	$1.00^{+0.77}_{-0.71}$	1.44
WH 3ℓ Z-depleted	Z-depleted SR, WZ 0 jet CR, WZ ≥ 1 jet CR	μ_{WH}	$1.00^{+0.53}_{-0.45}$	2.54
ZH 4ℓ	1-SFOS SR, 2-SFOS SR, ZZ CR	μ_{ZH}	$1.00^{+0.47}_{-0.39}$	3.11

The left side bins in the MVA distributions are further merged for those without significant signal contribution in the background dominated bins to have a better constrain of the background in the fitting.

4.8.3 Fitting procedure

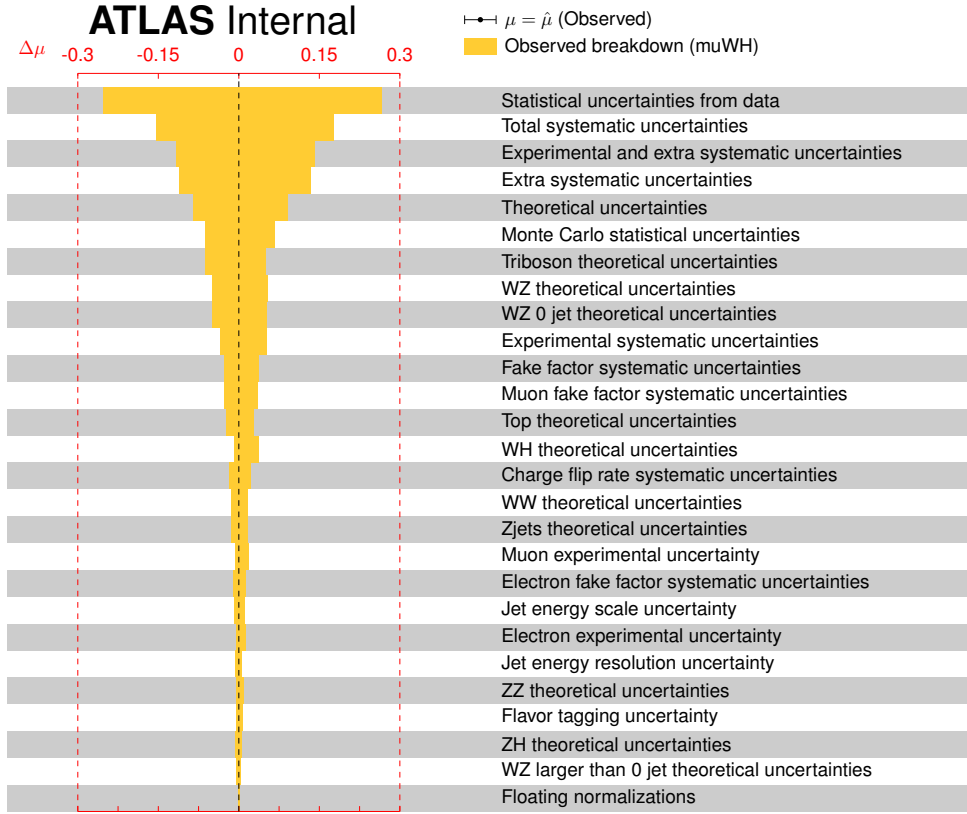
The construction of the fitting for the single channel fit. The signal and control regions, POIs, as well as the expected signal strength and significance, are shown in Tab. 4.14.

A binned likelihood function is formulated as a product of Poisson probability terms across the bins of various signal regions (SRs) detailed in Sec. 4.5. The binned likelihood function is parameterized using the signal strength, μ , which represents the ratio of the observed signal yield to the SM's prediction. The signal strength serves as the measurement's parameter-of-interest (POI). Furthermore, a Poisson probability term is incorporated for each control region (CR) to concurrently normalize its corresponding background process in the joint measurement. Systematic uncertainties are included as nuisance parameters in the likelihood function, with correlations taken into consideration. The final outcomes are derived using the profile likelihood method [186].

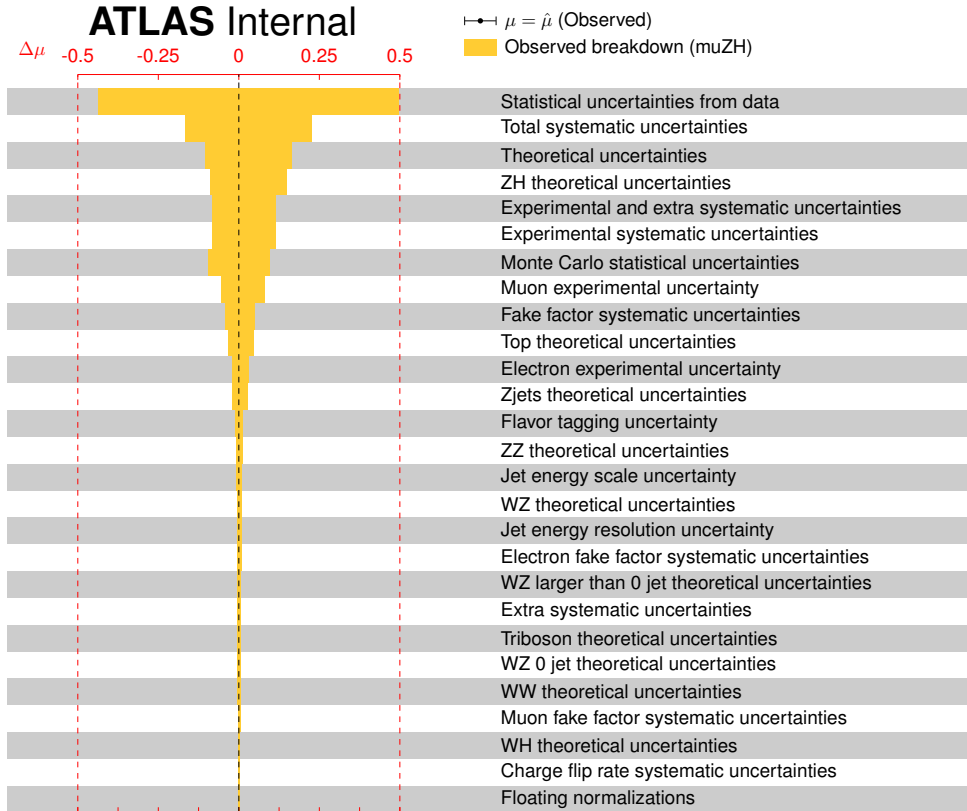
Two fit scenarios are examined: a combined 1 POI fit, where the WH and ZH yields are concurrently scaled by a single POI, μ_{VH} , and a combined 2 POI fit, where the WH and ZH yields are independently scaled by two distinct POIs, μ_{WH} and μ_{ZH} , respectively. In the case of total cross-section measurements, the signal theory uncertainties' pure normalization components are separated from the pure acceptance components, with only the latter entering the cross-section fit.

4.8.4 Asimov results and uncertainties impacts

The combined fitting procedure is executed with a comprehensive fit across all VH regions. Both single POI (μ_{VH}) and dual POIs (μ_{WH} , μ_{ZH}) are conducted. In addition to the POIs, the parameters encompass normalization factors for prevailing background processes mentioned earlier and the γ parameter accounting for the MC statistic uncertainties in the bins. The uncertainty breakdowns for each parameter are presented in Fig. 4.17 (a) and (b).



(a)



(b)

Figure 4.17: The uncertainties breakdown on (a) μ_{WH} and (b) μ_{ZH} of each contribution source with total statistical uncertainties are shown.

4 Measurement of the Vector Boson Associated Production with the $H \rightarrow WW^*$ Decay

Table 4.15: Results from VH combined asimov fit. All VH regions are included in the fitting. The Asimov dataset is used in the signal regions and the observed data are used in the control regions.

μ_{VH}	$1.00^{+0.27}_{-0.25}$
μ_{ZH}	$1.00^{+0.47}_{-0.39}$
μ_{WH}	$1.00^{+0.35}_{-0.33}$
ATLAS norm WZ 0 jet 3l	$1.04^{+0.06}_{-0.06}$
ATLAS norm WZ ≥ 1 jet 3l	$0.86^{+0.16}_{-0.15}$
ATLAS norm WZ ≥ 1 jet ss 2l	$0.90^{+0.17}_{-0.16}$
ATLAS norm ZZ	$0.99^{+0.08}_{-0.07}$
ATLAS norm Z+jets	$0.87^{+0.15}_{-0.14}$
ATLAS norm Top	$0.99^{+0.31}_{-0.22}$
ATLAS norm qqWW	$0.89^{+0.27}_{-0.24}$
Significance(exp)	4.73

Notable constraints can be observed for the majority of theoretical uncertainties due to the inclusion of control regions. Some lepton misidentification or charge misidentification related variations are also constrained because the estimates of these parameters typically possess limited statistical precision. The correlation between the fitting parameters are calculated which are consistent with what was expected. The final results of the signal strength and sensitivity for the single POI case and two POIs cases are provided in Tab. 4.15. The smoothing of theoretical uncertainties is incorporated to mitigate the impact of statistical fluctuations.

Two-dimensional likelihood contours ranging 1 to 5 σ are depicted in the phase space of μ_{WH} and μ_{ZH} in Fig. 4.18 (a). The profiled likelihood curves created for each POI are displayed in Fig. 4.18 (c) and (d)

In conclusion, the VH combined fit with the Asimov dataset yields an expected significance of 4.73 σ . The fitted values of μ_{ZH} are $1.00^{+0.47}_{-0.39}$, μ_{WH} are $1.00^{+0.35}_{-0.33}$, and μ_{VH} are $1.00^{+0.27}_{-0.25}$.

4.9 Results

The VH signal strength for the combined 1 POI fit is measured to be:

$$\mu_{VH} = 0.92^{+0.21}_{-0.20}(\text{stat.})^{+0.14}_{-0.12}(\text{syst.}),$$

corresponding to a 4.6 σ significance over the background-only hypothesis. The total VH cross-section times the $H \rightarrow WW^*$ branching ratio is measured to be:

$$\sigma_{VH} \times \mathcal{B}_{H \rightarrow WW^*} = 0.44 \pm 0.10(\text{stat.})^{+0.06}_{-0.05}(\text{syst.}) \text{ pb},$$

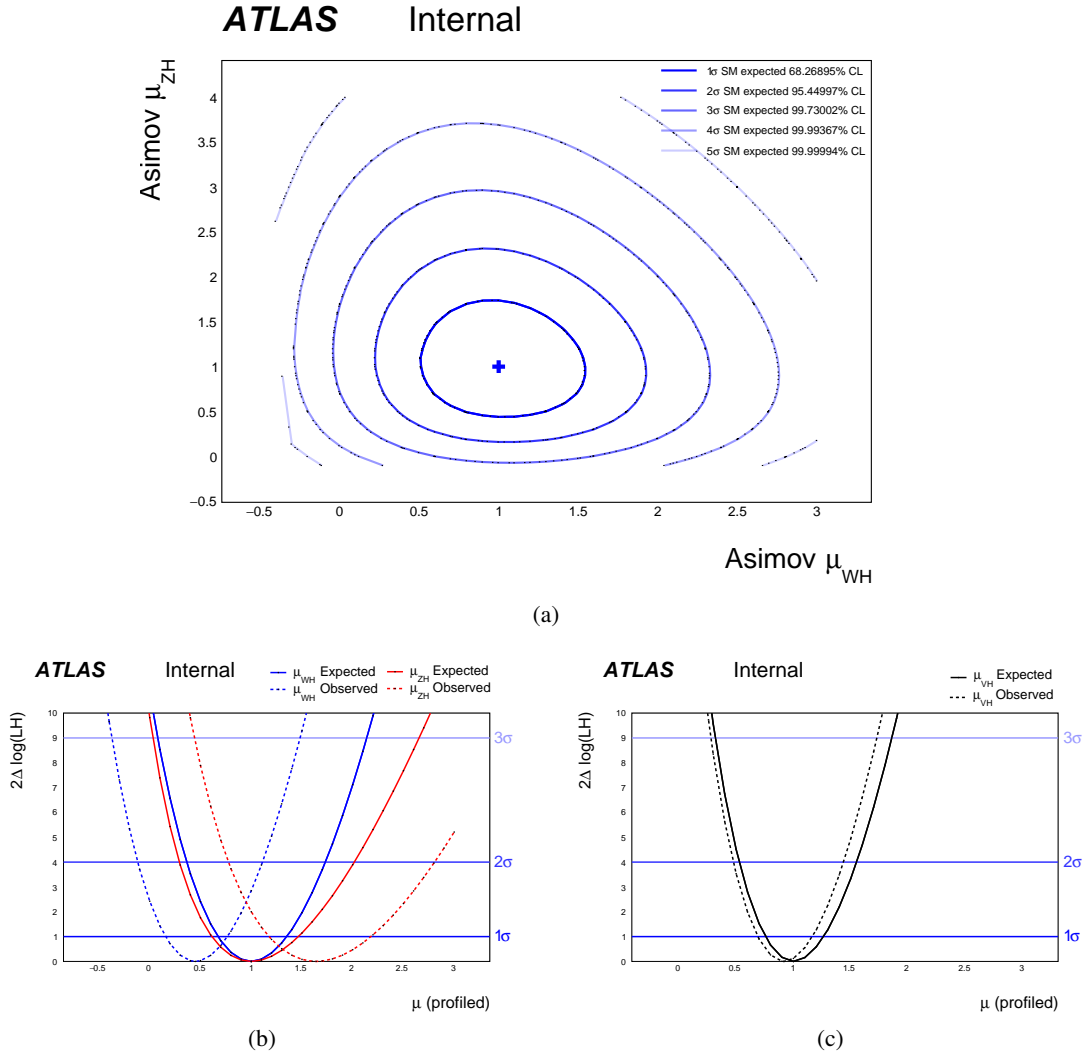


Figure 4.18: The 2D likelihood 1 to 5 sigma contours (a) of the μ_{WH} and μ_{ZH} and profile likelihood curves of μ_{WH} , μ_{ZH} (b) and of μ_{VH} (c) from the VH combined fit.

4 Measurement of the Vector Boson Associated Production with the $H \rightarrow WW^*$ Decay

in agreement with the SM expectation of 0.48 ± 0.01 pb [115].

For the signal strength of the VH and WH from 2 POI fit, the results are measured to be:

$$\begin{aligned}\mu_{WH} &= 0.45^{+0.27}_{-0.25}(\text{stat.})^{+0.18}_{-0.15}(\text{syst.}), \\ \mu_{ZH} &= 1.64^{+0.50}_{-0.44}(\text{stat.})^{+0.23}_{-0.17}(\text{syst.}),\end{aligned}\tag{4.16}$$

which corresponds to a 1.5σ and 4.6σ excess over a scenario where the respective production mode is considered absent, with the other one treated as background normalized from data. The measured values of production cross section times branch ratio for WH and VH processes are:

$$\begin{aligned}\sigma_{WH} \times \mathcal{B}_{H \rightarrow WW^*} &= 0.13^{+0.08}_{-0.07}(\text{stat.})^{+0.05}_{-0.04}(\text{syst.}) \text{ pb}, \\ \sigma_{ZH} \times \mathcal{B}_{H \rightarrow WW^*} &= 0.31^{+0.09}_{-0.08}(\text{stat.}) \pm 0.03(\text{syst.}) \text{ pb}.\end{aligned}\tag{4.17}$$

The measured values of the signal strengths and the corresponding sensitivities, Z_0 , for the single-channel fits as well as the combined 1- and 2 POI fits, are performed and summarized in Tab. 4.16. The post-fit yields of both signal and background from observed data are summarized in Tab. 4.17. The uncertainties contribution to the measurement of the cross-section times branch ratio are summarized in Tab. 4.18. The observed profile likelihood as a function of $\sigma \times \mathcal{B}_{H \rightarrow WW^*}$ normalized by the SM expectation are summarized in Fig. 4.20, and the two-dimensional likelihood contours of the measured values of $\sigma_{ZH} \times \mathcal{B}_{H \rightarrow WW^*}$ vs. $\sigma_{WH} \times \mathcal{B}_{H \rightarrow WW^*}$ for 68% and 95% confidence levels (CLs) compared with the predictions from the SM is shown in Fig. 4.21.

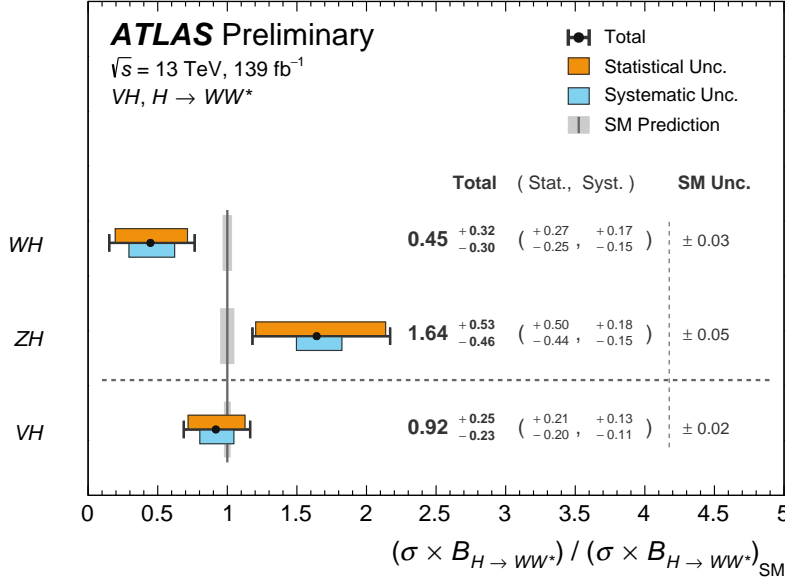


Figure 4.19: Best-fit values of the total WH , ZH , and VH cross-sections times the $H \rightarrow WW^*$ branching ratio. Each measurement is normalized to its SM prediction. The black error bars, orange boxes, and blue boxes show the total, statistical, and systematic uncertainties in the measurements, respectively. The gray bands represent the theory uncertainty of the corresponding Higgs production mode.

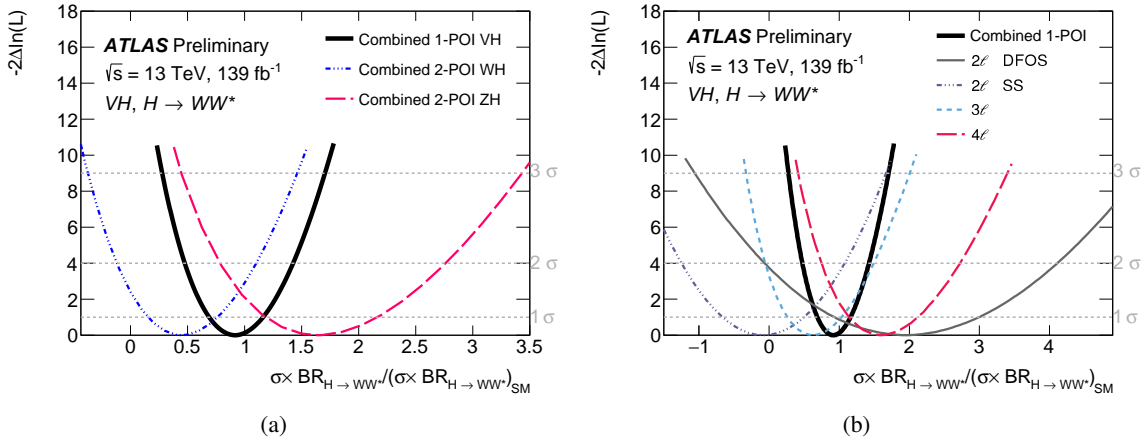


Figure 4.20: Observed profile likelihood as a function of $\sigma \times \mathcal{B}_{H \rightarrow WW^*}$ normalized by the SM expectation for (a) the VH and WH/ZH measurements from the combined 1- and 2 POI fits, respectively, and (b) the single-channel measurements.

4 Measurement of the Vector Boson Associated Production with the $H \rightarrow WW^*$ Decay

Table 4.16: The measured values of the signal strengths and the corresponding sensitivities, Z_0 , for the single-channel fits as well as the combined 1- and 2 POI fits. For each fit, both the expected and measured results are shown. The uncertainties correspond to the total of all statistical and systematic sources.

Channel	POI / Z_0	Expected	Observed
Opposite-sign 2ℓ	μ_{VH}	$1.00^{+1.02}_{-0.98}$	$1.94^{+1.07}_{-1.02}$
	Z_0	1.0	1.9
Same-sign 2ℓ	μ_{WH}	$1.00^{+0.61}_{-0.60}$	-0.08 ± 0.58
	Z_0	1.6	0.0
3ℓ	μ_{WH}	$1.00^{+0.44}_{-0.40}$	$0.64^{+0.42}_{-0.37}$
	Z_0	2.8	1.8
4ℓ	μ_{ZH}	$1.00^{+0.47}_{-0.39}$	$1.59^{+0.54}_{-0.47}$
	Z_0	3.1	4.5
Combined 1-POI	μ_{VH}	$1.00^{+0.27}_{-0.25}$	$0.92^{+0.25}_{-0.23}$
	Z_0	4.7	4.6
Combined 2-POI	μ_{WH}	$1.00^{+0.35}_{-0.33}$	$0.45^{+0.32}_{-0.30}$
	μ_{ZH}	$1.00^{+0.47}_{-0.39}$	$1.64^{+0.55}_{-0.47}$
	Z_0^{WH}	3.3	1.5
	Z_0^{ZH}	3.1	4.6

4.9 Results

Table 4.17: Post-fit MC and observed data yields in each SR as measured by the 2-POI fit. The top and Z+jets processes for a given channel correspond to those with only prompt leptons, as described in Sec . The uncertainties correspond to the total of all statistical and systematic sources. The quadrature sum of the individual sources may differ from the total uncertainty due to correlations.

	OS 2ℓ						SS 2ℓ					
Process	SS2 μ						SS2 e			SSDF		
WH	10.1	\pm	6.9	31	\pm	21	11.2	\pm	7.6	44	\pm	30
ZH	20.4	\pm	6.2	7.3	\pm	2.3	4.1	\pm	1.3	13.9	\pm	4.2
Other Higgs	58.2	\pm	7.3	19.0	\pm	2.2	9.3	\pm	1.1	32.7	\pm	3.8
WW	264	\pm	47	252	\pm	35	106	\pm	15	374	\pm	51
$W(Z/\gamma^*)$	41.2	\pm	3.1	1400	\pm	150	839	\pm	94	2600	\pm	270
$Z(Z/\gamma^*)$	7.7	\pm	0.8	143	\pm	18	100.2	\pm	8.2	307	\pm	28
$V+\gamma$	9.9	\pm	6.6	—			—			—		
VVV	18.9	\pm	6.4	167	\pm	47	75	\pm	21	258	\pm	72
Z +jets	301	\pm	27	—			—			—		
Top	1018	\pm	64	32.8	\pm	2.7	16.1	\pm	1.4	54.1	\pm	4.6
Misidentified leptons	26.5	\pm	6.3	360	\pm	140	1110	\pm	100	2170	\pm	270
Charge-flip electrons	—			—			922	\pm	67	110.2	\pm	8.5
Total	1776	\pm	39	2419	\pm	46	3197	\pm	51	5958	\pm	70
Observed	1788	\pm	42	2438	\pm	49	3233	\pm	57	5906	\pm	77

	3ℓ						4ℓ					
Process	Z-dominated			Z-depleted			1-SFOS			2-SFOS		
WH	10.9	\pm	7.5	5.7	\pm	3.9	—			—		
ZH	4.5	\pm	1.4	1.73	\pm	0.52	14.8	\pm	4.4	10.8	\pm	3.2
Other Higgs	1.78	\pm	0.17	2.81	\pm	0.31	1.87	\pm	0.22	0.68	\pm	0.08
$W(Z/\gamma^*)$	876	\pm	20	24.6	\pm	1.6	—			—		
$Z(Z/\gamma^*)$	129	\pm	17	2.63	\pm	0.28	29.2	\pm	1.5	305.7	\pm	9.1
WWW	63	\pm	16	34.7	\pm	8.9	—			—		
WWZ	3.78	\pm	0.11	1.63	\pm	0.05	10.81	\pm	0.97	1.57	\pm	0.14
WZZ	0.31	\pm	0.01	< 0.1			0.44	\pm	0.03	< 0.1		
Top	14.4	\pm	1.3	4.80	\pm	0.44	8.70	\pm	0.95	1.43	\pm	0.14
Misidentified leptons	103	\pm	14	13.3	\pm	3.0	14.5	\pm	3.2	5.5	\pm	1.2
Total	1206	\pm	23	91.9	\pm	8.0	80.3	\pm	5.5	325.8	\pm	9.5
Observed	1237	\pm	35	88	\pm	9	79	\pm	9	316	\pm	18

4 Measurement of the Vector Boson Associated Production with the $H \rightarrow WW^*$ Decay

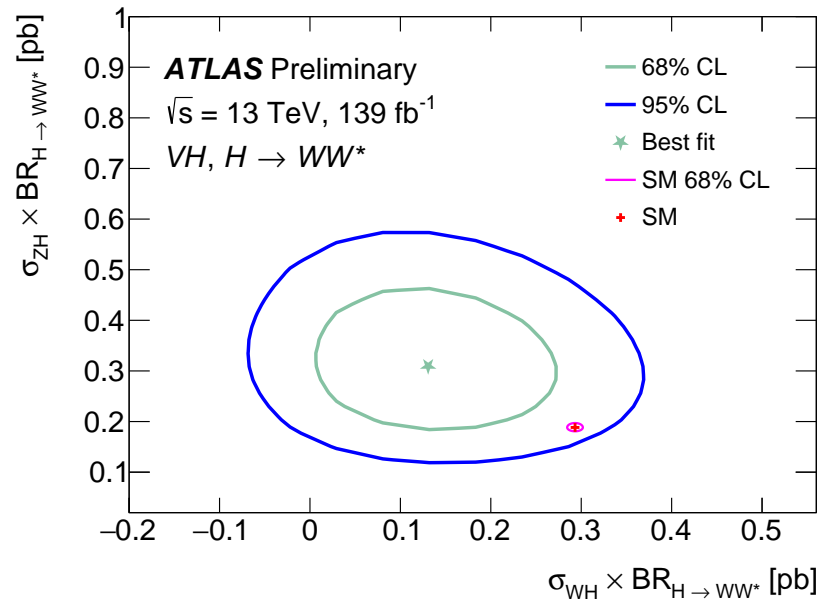


Figure 4.21: Two-dimensional likelihood contours of the measured values of $\sigma_{ZH} \times \mathcal{B}_{H \rightarrow WW^*}$ vs. $\sigma_{WH} \times \mathcal{B}_{H \rightarrow WW^*}$, for 68% and 95% confidence levels (CLs) compared with the predictions from the SM. The 68% confidence level on the SM predictions for the ZH and WH cross-sections times branching fraction is indicated by the magenta ellipse.

4.9 Results

Table 4.18: Breakdown of the average contributions to the total uncertainties in percentage on the observed values of the signal strengths for the combined 1 POI ($\sigma_{VH} \times \mathcal{B}_{H \rightarrow WW^*}$) and 2 POI ($\sigma_{WH} \times \mathcal{B}_{H \rightarrow WW^*}$ and $\sigma_{ZH} \times \mathcal{B}_{H \rightarrow WW^*}$) fits. Indentation is used to denote subcategories. “Floating normalization” refers to the uncertainties on the normalization factors obtained using control regions. The quadrature sum of the individual sources may differ from the total uncertainty due to correlations.

Source	$\frac{\Delta(\sigma_{VH} \times \mathcal{B}_{H \rightarrow WW^*})}{\sigma_{VH} \times \mathcal{B}_{H \rightarrow WW^*}} [\%]$	$\frac{\Delta(\sigma_{WH} \times \mathcal{B}_{H \rightarrow WW^*})}{\sigma_{WH} \times \mathcal{B}_{H \rightarrow WW^*}} [\%]$	$\frac{\Delta(\sigma_{ZH} \times \mathcal{B}_{H \rightarrow WW^*})}{\sigma_{ZH} \times \mathcal{B}_{H \rightarrow WW^*}} [\%]$
Statistical uncertainties in data	22.3	57.9	28.4
Systematic uncertainties	13.3	36.6	9.9
Statistical uncertainties in simulation	6.4	14.4	5.9
Experimental systematic uncertainties	5.2	9.8	6.0
Electrons	1.2	1.8	1.6
Muons	2.5	2.8	4.1
Jet energy scale	0.7	2.3	0.5
Jet energy resolution	0.6	2.8	0.6
Flavour tagging	0.9	1.4	0.8
Missing transverse momentum	0.6	0.4	0.9
Pile-up	1.1	1.5	0.8
Luminosity	2.3	2.4	2.1
Mis-identified leptons	2.9	7.1	2.7
Charge-flip electrons	1.5	4.5	0.1
Theoretical uncertainties	6.0	18.6	4.7
WH	2.3	2.8	0.1
ZH	0.7	0.7	3.4
WW	1.0	3.3	0.3
$W(Z/\gamma^*)$ 0-jet	3.2	11.3	0.3
$W(Z/\gamma^*) \geq 1$ -jets	0.2	0.8	0.4
$Z(Z/\gamma^*)$	0.8	1.5	0.6
VVV	2.4	12.7	0.3
Top	2.9	5.5	2.5
Z+jets	1.8	3.4	1.5
RNN shape uncertainty for $W(Z/\gamma^*)$	8.8	27.3	0.3
Floating normalization	0.1	0.2	0.1
Total	26.0	71.0	30.1

Part II

Low-Gain Avalanche Detector Development at USTC for the HGTD and Future Experiments

5 Working Principles of a Silicon Detector

This chapter provides a brief review of the *silicon*, from its fundamental properties as a semiconductor material to its advantages as the substrate material for particle detection applications. Specifically, it aims to elucidate the operational principles of these sensors in detecting particles and the considerations involved in designing and producing them. More comprehensive information can be found at [188–190], and the main conclusions and derived formulas will be shown here.

5.1 Properties of the silicon material

Silicon is the most abundant solid element on earth, second only to oxygen and makes up more than 25% of the earth's crust, dominantly existing in the form of compounds. It has brought up modern electronics and revolutionized our world and daily life. More and more particle physics experiments are using silicon detectors. The reason that the group IV member, silicon, can be outstanding from other elements is due to:

- Its overwhelming existence on the earth, make it easily available at relatively low costs.
- The proper energy band gap energy (1.12 eV) with the diamond crystal structure.
- Its electric properties can be adjusted according to our demands by introducing impurities.
- The silicon oxide compound, widely existing in nature, has good properties for electric isolation and passivation.

The impurities can be group V atoms (e.g., phosphorus) that have five valence electrons (one more than silicon) and serve as “donors” to transfer the crystal into electron-enriched (n-type) material and act as free electrons. Also, it can be group III atoms (e.g., boron) that have three valence electrons (one less than silicon) and serves as “acceptors” to transfer the intrinsic silicon into electron-diminished (p-type) material and act as free positive charge (holes).

The density of the free electron n in the conduction band and density of holes p holds the thermal equilibrium law following Fermi-Dirac statistics, based on which:

$$n_i^2 = n \cdot p = N_V \cdot N_C \cdot e^{\frac{-E_g}{kT}}$$

where n_i is the density of both electron and holes in the intrinsic silicon, N_V and N_C is the density of the effective state at the valance band and conduction band, the E_g is the energy gap, which is 1.12 eV. It is worth mentioning that more energies are needed due to the phonon absorption for the momentum

5 Working Principles of a Silicon Detector

conservation of the lattice as its indirect band gap. Here for silicon, the energy is 3.6 eV in average to produce an electron-hole pair.

5.1.1 Drift of charge carrier and material resistivity

The velocity of drift ($v_{e,h}$) of the charge carriers (free electron or holes) under the electric field E follow the rule:

$$v_{e,h} = \mu_{e,h} E$$

where the $\mu_{e,h}$ is the mobility which is nearly constant when the $E < 2 \times 10^4 \text{ V cm}^{-1}$ and gets smaller as the electric field increases. The $\mu_{e,h}$ gets saturated at $E \approx 1 \times 10^7 \text{ V cm}^{-1}$ in the room temperature.

With this relation in the doped material, we can get the resistivity of silicon $\rho = 1/(e(\mu_e N_e + \mu_h N_h))$. Taking into account the electron is dominated in n-type silicon, we have $\rho = 1/e\mu_e N_d$ for n-type silicon with donor concentration N_d and similarly $\rho = 1/e\mu_h N_a$ for p-type silicon with acceptor concentration N_a .

5.1.2 P-N junction

When free electron enriched silicon is contacted with hole-enriched silicon, the diffusion of the free electrons towards the p side will happen. Such contact will create a region with neither free electrons nor holes, and a p-n junction is formed. The electrons are depleted in this region (depletion region), leaving the region filled with space charge (positive at the donor side and negative at the acceptor side), which can not move, thus also called the space charge region (SCR). The electric field would be built up by the space charge in the depleted region, which is called the depletion field with a built-in voltage drop (V_{bi}).

This diffusion can either be enhanced by applying an electric field when applying the external bias that has the same direction (reverse bias), resulting in an expansion of the depletion region, or with an opposite direction (forward bias), resulting in a diminished depletion region.

The application of forward bias will lead to a large current with a reduced depletion region, and the application of reversed bias will lead to a larger depletion region with high resistivity and low leakage current. The depletion region, without free charge carriers, would be sensitive to the charged particle or photon pass through it, which can ionize the silicon and produce the electron-hole pairs. Thus, for particle detection, the silicon p-n junction with reversed bias is usually preferred.

Consider when a reverse bias, V_b , is applied on a p-n junction in the depleted region, we have the Poisson equation with V as potential, x as the position, N as the density of the space charge (positive for donor and negative for acceptor), we have :

5.1 Properties of the silicon material

$$\frac{d^2V}{dx^2} + \frac{Nq}{\epsilon} = 0.$$

With this equation, we can get the electric field and potential distribution for a silicon detector with a given doping profile.

By applying the boundary condition and making integration twice, and taking into account the global charge neutral condition, we can get the width w of the depletion region under a certain reverse bias:

$$w = x_n + x_p = \sqrt{\frac{2\epsilon V_b}{q} \frac{N_a + N_d}{N_a N_d}},$$

and with the assumption of the p-in-n or n-in-p type abrupt junction, where $N_{a,d} \gg N_{d,a}$, $x_{n,p} \gg x_{p,n}$ we have:

$$w = \sqrt{\frac{2\epsilon V_b}{q N_{a,d}}} = \sqrt{2\epsilon \mu_{p,n} \rho_{n,p} V_b}.$$

With this, we can estimate the active thickness at a given bias for a silicon detector with given doping.

5.1.3 Avalanche and breakdown

As mentioned above, an extremely high electric field ($3 \times 10^5 \text{ V cm}^{-1}$) will result in the avalanche or multiplication of the charge carriers. If it happens in an uncontrolled way, it can irreversibly damage the diodes. Thus, we must pay special attention to the avalanche effect and try to mitigate it, especially in the power semiconductor industry [191].

However, if the avalanche can be realized in a controlled way, it can be utilized for the detection of the particles with a good signal-to-noise ratio. Such devices include the avalanche photodiode (APD) or silicon photomultiplier (SiPM) when made as an array of pixels and are widely used in many areas [192]. The most recent development for its utilization is the Low-gain avalanche diode, which will be introduced in Chapter 6. Different models have been developed to model the avalanche process in silicon and introduced in Sec. 7.2.

5.1.4 Leakage current

As important as the transient character, the leakage current is the basic and important character for a p-n junction to work as a detector. The I-V curve based on this is the most widely used method. That much basic information can be extracted from it including the impurities' concentration, the gain, the active thickness, the concentration and type of the radiation defects, etc.

5 Working Principles of a Silicon Detector

The leakage current I is modeled as a function of both temperature T and bias voltage V . For an ideal diode, it is expected to be:

$$I = I_s (e^{\frac{qV}{k_B T}} - 1),$$

where

$$I_s = \frac{qD_p p_{n0}}{L_p} + \frac{qD_n n_{p0}}{L_n}.$$

The $D_{p,n}$ is the diffusion coefficient of holes and electrons, $L_{p,n}$ is the diffusion length of holes and electrons which can be calculated by $L_{p,n} = \sqrt{D_{p,n} \tau_{rp, rn}}$ with the recombination time of electrons or holes $\tau_{rp, rn}$.

The free charge carriers generated by the thermal excitation will also contribute in addition to the ideal current, which is described by the Shockley-Read-Hall mode and strongly temperature dependent [191].

5.1.5 Capacitance

Since the charge can be stored in the p-n junction in the space charge region, the capacitance character is also interesting and important as a test method for silicon detector study (C-V measurement).

Based on the parallel plate capacitor formula and the depletion width, one can get the capacitance of a silicon planar diode as:

$$\frac{C^2}{A^2} = \frac{q\epsilon_0\epsilon_{Si}|N_{eff}|}{2(V_{bi} + V)}.$$

By calculating the derivative of both sides, the doping profile can be obtained with the capacitance-voltage curve for a detector with area A :

$$|N_{eff}| = \frac{2}{\frac{d1/C^2}{dV}} \frac{1}{q\epsilon_0\epsilon_{Si}A^2}.$$

5.2 Silicon for particle detection

5.2.1 Electron-hole generation

The energy deposition for the charged particle in the material follows the Bethe-Bloch formula:

$$-\left\langle \frac{dE}{dx} \right\rangle = Kz^2 \frac{Z}{A} \frac{1}{\beta^2} \left[\ln \frac{2m_e c^2 \beta^2 \gamma^2 T_{max}}{I^2} - \beta^2 - \frac{\delta(\beta\gamma)}{2} \right].$$

the $\frac{dE}{dx}$ gives the energy loss of the particle per mass thickness with:

$K = 4\pi N_A r_e^2 m_e c^2 = 0.307075 \text{ MeV cm}^2$, z is the charge of the transversing particle in units of the electron charge, Z is the atomic number of the absorbing medium (Silicon: 14), A is the atomic mass of the absorbing medium (Silicon: 28), $m_e c^2$ is the energy of the electron at rest 0.511 MeV, β is the velocity of the particle in units of the speed of light, γ is the lorentz factor $1/\sqrt{1-\beta^2}$, I is the excitation energy (Silicon: 137 eV), T_{max} is the maximum kinetic energy that can be transferred to an electron by a particle of mass M follows:

$$T_{max} = \frac{2m_e c^2 \beta^2 \gamma^2}{1 + 2\gamma m_e/M + (m_e/M)}.$$

Based on the energy deposition, one can divide it by the average electron-hole generation energy 3.6 eV and get the number of the electron-hole pair produced in the depleted region of the detector. Due to the energy deposition following the Landau distribution, the Most Probable Value (MPV) is different from the average value, which is more commonly used in the measurement and analysis since it will not be affected by the long tail of the distributions that might cause saturation effect in the readout system. For the Minimum Ionization Particles (MIPs), the most probable number of the electron-hole pairs is $76 \mu\text{m}^{-1}$ (while the mean number is $108 \mu\text{m}^{-1}$).

5.2.2 Signal induction

Charge collection

When a charged particle crosses the detector, it creates a track of electron-hole pairs (shown in Fig. 5.1) inside the depleted silicon bulk as described by Sec. 5.2. If a total amount of energy E is absorbed in the detector from incoming high-energy particles, the number of electron-hole pairs for silicon is given by:

$$N = \frac{E}{3.6 \text{ eV}}.$$

5 Working Principles of a Silicon Detector

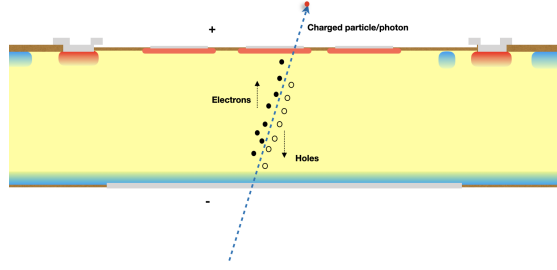


Figure 5.1: Examples of the silicon hole generation in the n-in-p silicon detector.

Ramo's theorem

The Simon Ramo [193] showed that the instantaneous current received by a given electrode due to a charge (q) motion with velocity \vec{v} could be obtained with the weight field \vec{E}_w in the weight potential ϕ_w by:

$$i = q\vec{E}_w \cdot \vec{v},$$

and the induced charge Q in the electrode is given by:

$$Q = q\Delta\phi_w,$$

where the weight potential ϕ_w is defined by the potential field when setting the readout electrode to 1 V and other electrodes to 0 V. Correspondingly, the weight field $\vec{E}_w = -\nabla\phi_w$. The ϕ_w and \vec{E}_w depends solely on the geometry of the detector. An example of the simulated weight potential and comparison with the drift potential can be found in Fig. 5.2. For the silicon detector, one must take into account the change of the depletion region and the trapping effect, which is not taken into account in this formula.

5.2.3 Layout of the detector

There are two typical layouts of the silicon detector geometry for the detector being used in the high energy particle tracking application, Strip and Pixel, depending on the relative size of its electrode dimensions.

- **Pixel detectors** are small diodes with a pixel cell of some microns shown in Fig. 5.3 (a). Normally they are assembled as a large detector by an array of pixels. It can achieve very precise position resolution due to its fine segmentation, while the challenge might exist in the inter-connection step to make the high-density readout possible. Either the micro-level bumps needed to make the hybrid of the front-end chip and sensor, or the more complex design is needed to design the front-end electronics and sensor in a monolithic way.

5.2 Silicon for particle detection

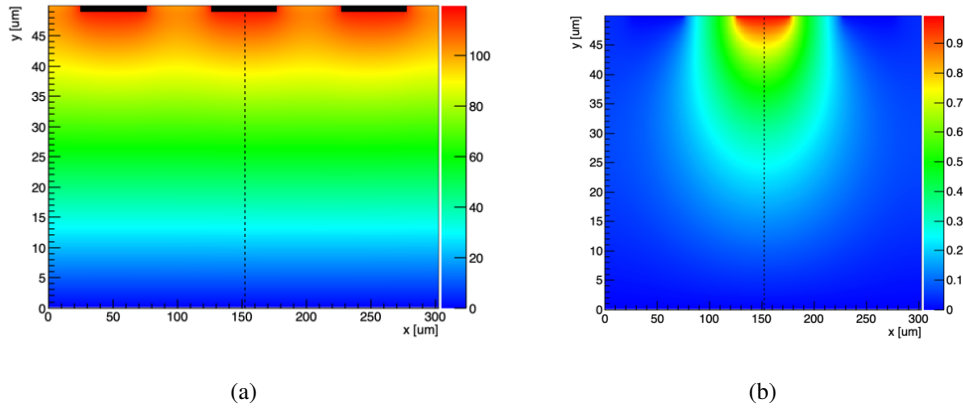


Figure 5.2: Here are examples of the drift potential (a) and weighted potential (b) generated with the *Weightfield2* simulation software [194]. The electrode have 50 μm width and 120 μm pitch with 120 V bias applied.

- **Strip detectors** are designed to be long in one dimension and thin in another dimension, shown in Fig. 5.3 (b). Thus, by positioning two of them together with a misalignment angle, a precise 2D position can be obtained. The connection can be put at the side of the detector. Since one pad can be connected with one strip, which covers a relatively large area, the assembly of the strip detector becomes relatively easy.

Both the pixel and strip detectors can be fabricated as planar detectors by making the implantation on the wafer's surface or fabricated as 3D detectors by filling the deeply etched holes with the doped polysilicon .

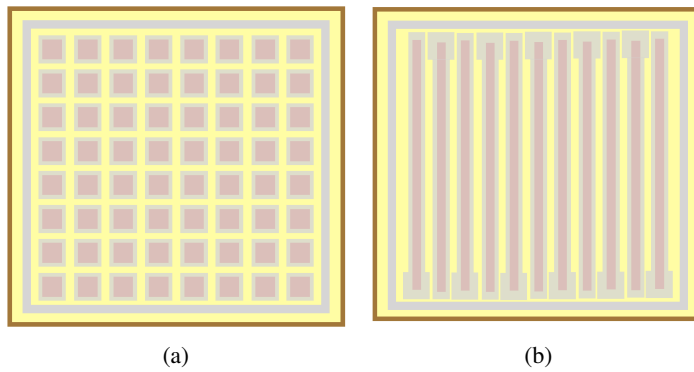


Figure 5.3: Here are examples of the detector with different layouts, the pixel detector(a) and strip detector(b).

5.2.4 Architecture of the junction

- **Planar sensors** are fabricated with two electrodes on each side of the wafer as shown in Fig. 5.4 (a). The main bulk of the wafer remains intrinsic silicon. Depending on the thickness

5 Working Principles of a Silicon Detector

of the wafer, the detector has a different volume to deplete.

- **3D sensors** are designed with the columnar implants as shown in Fig. 5.4 (b), called 3D sensors, where the electrodes are laterally separated instead of vertically. The silicon is etched with a deep reactive-ion etching (DRIE) technique, and the column is filled with doped polysilicon. The volume to deplete is the volume between columns. Since the volume between columns is typically smaller than the thickness of the wafer. Thus, 3D detectors need less bias voltage to deplete all their volume.

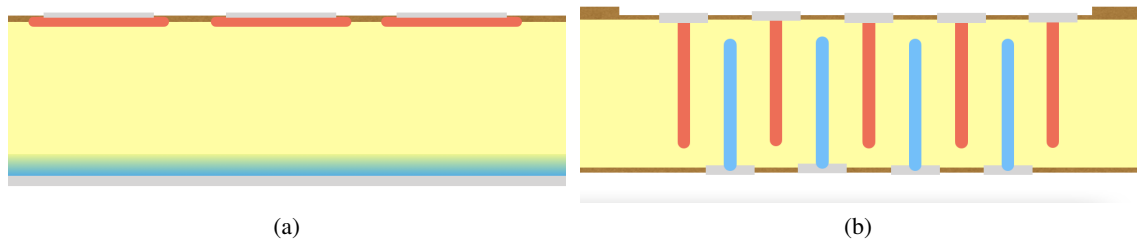


Figure 5.4: Here are examples of the different architecture in the active area. The planar sensor(a) and 3D sensor(b).

Since silicon detectors are operated as reverse-biased diodes, we can distinguish n-type and p-type detectors for detectors with n doped and p doped substrates, respectively. Since the electrode of the detector can also be n-doped or p-doped, we have four possible combinations of the substrate and electrode doping: n-in-p, p-in-n, n-in-n, p-in-p.

The p-in-p and n-in-n types typically correspond to a two-sided process of fabrication, meaning that the fabrication steps have to be performed on the front and back side of the wafer with good alignment. Two-sided fabrication processes normally are more expensive than a single-sided process (as the p-in-n and n-in-p process) since more masks are needed.

5.3 Radiation damage on the silicon detector

One major challenge for the silicon detector application is that after being exposed to the high fluences of the radiation, the original crystal lattice of silicon could be damaged in different ways. The charged particles or photons will cause the ionization of the material, which is called ionization damage. Such damage will cause the degradation of the isolation quality, which usually happens in the interface of the materials, called “Surface damage”. The hadronic particles (like neutron, proton, pion, or heavy ions), that go through the lattice, will cause large momentum transfer due to their larger masses. Such transfer can displace the silicon atoms from the crystal lattices, causing both interstitials and

vacancies. The formations called bulk damage will influence the operation condition of the detector dramatically.

In summary, damage produced by the high energy particles to the silicon detectors can be:

- Bulk damage: Displacements of the silicon atoms create vacancies, interstitials, and deep energy levels in the band gap
- Surface damage: Ionization of the isolating layers (such as SiO₂) and create fixed charges in the interface

5.3.1 Bulk damage

Charged or non-charged particles impinging into a crystallographic lattice at high energy may displace the atoms in the crystal. That effect does not depend on the type of particles but on their energy. The particles interact with the atoms via electromagnetic and strong forces. They create interstitials (I), di-interstitials (I^2), vacancies (V), di-vacancies (V^2), or even triple-vacancies. If the energy is higher than the “displacement energy” 25 eV, the single Frenkel defects would be created. Since 25 eV is the energy at which the displacement probability is one-half. The recoil atom can thus create new atom displacements if the energy is high enough. After a heavy recoil, it can create clusters of defects in the lattice, which will significantly change the lattice structure of the silicon. The approximate energy for creating a defect cluster is 5 keV according to calculation [195]. Depending on the energy and the particle, the cluster defects layout may change. The bulk damage is the main damage effect of the radiation.

In order to normalize the dependence on the type of radiation and its energy, a scaling quantity called Non-Ionizing Energy Loss is created, which quantifies the damage normalized to 1 MeV neutrons.

Particles belonging to different types with different energy might follow different mechanisms to create irradiation damages. In order to have an unified quantity to compare the effects from the different environments with different facilities and particle types and energies, a standard method described in “ASTM-722” [196] for the damage normalization was proposed and widely accepted by the community of radiation effects research. The NIEL is defined by the displacement damage function $D(E)$ for the particle with a specific type and energy E .

$$D(E) = \sum_i \sigma_i(E_{kin}) \int_0^{E_{R,max}} f_i(E_{kin}, E_R) P(E_R) dE_R,$$

$$\text{with } \kappa = \frac{\int D(E) \phi(E) dE}{95 \text{ MeV mb} \cdot \phi} = \frac{\phi_{eq}}{\phi}.$$

With this function, the hardness factor is defined for each irradiation facility to normalize their fluence in a standard way, usually to the equivalent fluence of 1 MeV neutron damage in silicon: $\phi_{eq} = \kappa \phi = \kappa \int \phi(E) dE$; $[\phi_{eq}] = n_{1\text{MeV}}/\text{cm}^2$. The measured damage functions for different types of particles are shown in Fig. 5.5.

5 Working Principles of a Silicon Detector

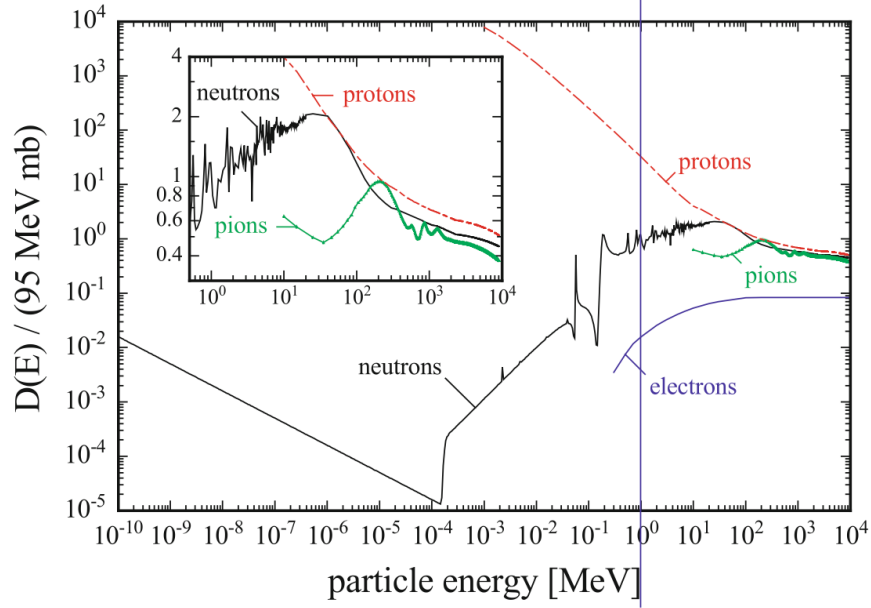


Figure 5.5: The NIEL which using the Displacement damage function $D(E)$ normalized to $95 \text{ MeV} \cdot \text{mb}$ for neutrons, protons, pions and electrons [188].

After irradiation, the defects introduce changes in the space charge region (SCR). The produced energy levels close to the conduction or valence bands create acceptor-like or donor-like effective doping. The effective doping density N_{eff} is related to the fluence Φ_{eq} , as well as the annealing temperature T and time t . These changes can be described by the “Hamburg model” [197],

$$\Delta N_{\text{eff}}(\Phi_{\text{eq}}, t, T) = N_C(\Phi_{\text{eq}}) + N_A(\Phi_{\text{eq}}, t, T) + N_Y(\Phi_{\text{eq}}, t, T), \quad (5.1)$$

which contains a stable term $N_C(\Phi_{\text{eq}})$ representing the modification to the effective doping density by the radiation damage, short-term annealing $N_A(\Phi_{\text{eq}}, t, T)$ and long term anneal $N_Y(\Phi_{\text{eq}}, t, T)$. The stable damage term contains dopant removal and creation terms,

$$N_C(\Phi_{\text{eq}}) = N_{C,0}(1 - e^{-c\Phi_{\text{eq}}}) + g_c \Phi_{\text{eq}}, \quad (5.2)$$

where c is the initial dopant removal constant, $N_{C,0} \cdot c$ is the initial removal rate and g_c is the linear induction rate dominating at fluence larger than $1 \times 10^{16} \text{ n}_{\text{eq}}/\text{cm}^2$ [188].

The defects are caused by the high-energy particles via the interaction with the silicon lattice. A complex group of different final states can be formed, creating new band gaps and new space charges. The impact will show up as an increase or decrease in the depletion voltage and the leakage current (shown in Fig. 5.6), which can be formulated by:

$$\Delta I/V = \alpha \cdot \Phi.$$

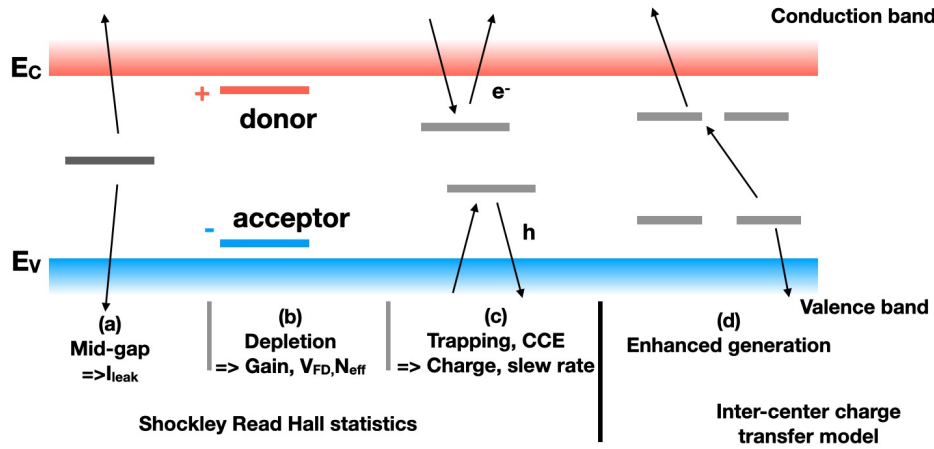


Figure 5.6: Energy level of defects caused by the displacement damage in silicon and their consequences.

5.3.2 Surface damage

Surface damage is due to electron-hole pairs created in the insulator layers, in this case, the SiO₂. The electrons are fast collected in the electrode, whereas the holes stay as a positive charge in the oxide because of their lower mobility. That leads to a flat band displacement and increases the charge in the oxide till it saturates around $Q_{ox} = 3 \times 10^{12} \text{ cm}^{-2}$. Surface damage depends on the kind of radiation since electron-hole pairs are created by charged particles or photons.

The surface damages mostly affect the device whose performance is mostly relying on the interface effect of the silicon and other oxides like MOS-based devices like field effect transistors (FET) or complementary metal oxide semiconductors devices (CMOS), which have been widely used in both electronics and high-resolution detector like DEPFETs, HV-CMOS detectors.

The bulk damages are usually caused by hadronic radiation like high energy neutrons, protons, or pions, while the surface damages are mainly caused by ionization radiation like x-ray, gamma irradiation, or electrons.

5.4 Sumamry

This chapter presents a review of the fundamental properties and operating principles of silicon-based detectors employed in particle detection applications. The section 5.1 delves into the critical properties of silicon as a material, addressing charge carrier drift and material resistivity, which are paramount for optimizing detector performance. The concept of the p-n junction, a core element of silicon detectors, is explained, and the phenomena of avalanche multiplication and breakdown are introduced. Additionally, the implications of leakage current and capacitance on the performance and efficiency of silicon detectors are investigated.

5 Working Principles of a Silicon Detector

In section 5.2, the focus is on the application of silicon for particle detection purposes. The process of electron-hole pair generation, which happens when a charged particle traverses the silicon material, is elucidated. Furthermore, signal induction, a critical mechanism for converting electron-hole pairs into quantifiable signals, is discussed. The detector's layout is delineated, offering insights into the overall structure and design considerations. Moreover, the junction architecture, an integral aspect of the silicon detector, is explained in detail.

The section 5.3 investigates the impact of radiation damage on the performance of silicon detectors. Radiation damage can significantly impair detector performance, prompting the categorization of the damage into two distinct types: bulk damage and surface damage. Bulk damage pertains to the damage inflicted within the silicon bulk material, which creates mainly by hardons. Conversely, surface damage affects the detector's surface and interfaces and is induced by photons or charged particles which are ionizing radiations. A comprehensive understanding of radiation damage is essential for the development of robust silicon detectors capable of withstanding harsh radiation environments.

6 The Low Gain Avalanche Detector History and its Principle

The LGADs are segmented planar silicon detectors with internal gain, as shown by the schematic view in Fig. 6.1. The gain is created by the strong electric field strengths above $2 \times 10^5 \text{ V cm}^{-1}$, which activate the impact ionizing multiplication. The strong electric field is located near the detector's surface (as shown by the red lines in the left of Fig. 6.1), and the strength mainly depends on the doping dose of the p-type layer. It has been proposed by the RD50 collaboration starting from the idea to utilize the multiplication mechanism in silicon-based detector with finely adjusted gain to increase the signal-to-noise ratio for a fast detection (several tens of picoseconds) of the signal [198]. The concept is first realized by CNM in Barcelona [199] and developed during the past ten years within the CERN-RD50 community, including collaboration with other LGAD vendors, HPK [200] and FBK [201], Micron [202], BNL [203], NDL [204], IHEP-IME [205] and also USTC-IME/NRFC. The development of the LGAD at USTC-IME/NRFC is documented in chapters 7, 8 and Appendix A in this thesis.

6.1 Technology motivation

The charge multiplication mechanism has been well understood in gases and solids. It is based on the avalanche process initiated by a charge moving in strong electrical fields, leading to the impact ionization with a gain defined by the average number of secondary particles created by one particle. Silicon detectors are attractive for a number of reasons. The silicon detectors are less affected by ionization radiation. With the established mature semiconductor processes that can implement novel structures, it is possible to realize a high number of detection channels in a small space, which is ideal for compact detector systems. Therefore, efforts to utilize avalanche mechanisms in solid-state detectors are also needed for applications such as future collider experiments. In the past, this mechanism is used in Avalanche Photon Detectors (APD) with a gain of about 100 and SiPM with a gain of about 10000 for single particle detection. In contrast to those applications, with more advanced front-end electronics available, a new timing detector called Low-Gain Avalanche Detectors (LGAD) was proposed with a gain of 10-20 to fully utilize the advantage of the rising edge of the fast signal induced by the gain. The target of the LGAD is to minimize the jitter contribution to the timing measurement to achieve a $\sim 10 \text{ ps}$ level timing precision. The LGAD design is based on modifying the doping profile such that an additional doping layer of *p* material (usually Boron) is introduced close to the p-n junction. The simplified drawing of the LGAD design based on a traditional n-in-p silicon detector is shown in Fig. 6.1 (a).

6 The Low Gain Avalanche Detector History and its Principle

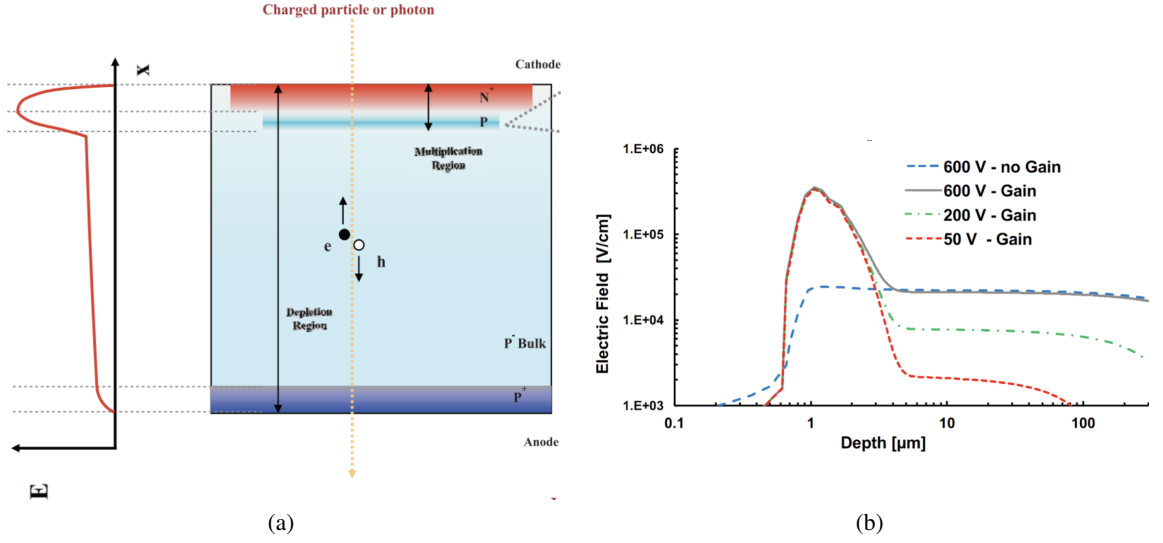


Figure 6.1: (a) The schematic view of the LGAD structure. The p-type implantation is placed near the surface, creating a strong local electric field where the electron avalanche would happen. (b) Examples of the electric-field strength in LGAD with 300 μm thickness and external bias at 50 V, 200 V, 600 V. The 300 μm in a 300 μm PIN diode without gain and biased to 600 V is also drawn for comparison. The x-axis is the depth starting from the sensor surface in a logarithm scale [206].

With this extra *p* layer, the resulting doping profile is characterized by an abrupt increase in doping concentration close to the junction, resulting in a large electric field nearby (as shown in the left side of the Fig. 6.1 (a) and zoomed in Fig. 6.1 (b)). The electric field in a 300 μm thick LGAD at three different bias voltages ($V = 50$ V, 200 V, and 600 V) and that of a PIN diode at $V = 600$ V are shown for comparison. The electric field in LGAD is, therefore, clearly divided into two distinct zones: the drift volume with relatively low electric field strength ($E \sim 30 \text{ kV cm}^{-1}$) and a thin multiplication zone located within a depth of a few micrometers with very high field ($E \sim 300 \text{ kV cm}^{-1}$). The implants need to be shaped to allow high bias-voltage operation without breakdown, and the substrate needs to have high resistivity to guarantee a full depletion and a flat drift field.

In the n-in-p LGAD design, electrons drifting toward the n^+ electrode initiate the multiplication process. In contrast, in the p-in-n design, the multiplication is initiated by the holes drifting toward the p^+ electrode. Since the multiplication mechanism starts for electrons at a lower electric field strength than what is necessary for hole multiplication (Sec. 5.1.3), the n-in-p design offers the best control over the multiplication process. It is, in fact, possible in the n-in-p design to tune the strength of the electric field in such a way that only electrons drive the multiplication process and therefore avoid operating the device in avalanche mode. Under such conditions, the gain is not very sensitive to the exact strength of the electric field, and the LGAD can be operated very reliably. This condition also minimizes the noise coming from the multiplication process, the so-called excess noise factor [207], and enhances the LGAD performance.

6.2 Timing performance of the LGAD

There are several effects that determine the time resolution: time walk from amplitude variations, jitter from electronic noise, and “Landau fluctuations” from charge deposition non-uniformities along the particle path, the bin size of timing to digital converter, the clock of electronics. The total time resolution follows below formula:

$$\sigma_{\text{Total}}^2 = \sigma_{\text{TimeWalk}}^2 + \sigma_{\text{Landau noise}}^2 + \sigma_{\text{Jitter}}^2 + \sigma_{\text{TDC}}^2 + \sigma_{\text{Clock}}^2, \quad (6.1)$$

where

$$\begin{aligned} \sigma_{\text{TimeWalk}} &= \left[\frac{V_{\text{th}}}{S} \right]_{t_{\text{rise}}}^{\text{RMS}}, \\ \sigma_{\text{Jitter}} &= \frac{N}{dV/dt} \approx \frac{t_{\text{rise}}}{S/N}, \\ \sigma_{\text{TDC}} &= \frac{\text{TDC}_{\text{bin}}}{\sqrt{12}}. \end{aligned} \quad (6.2)$$

The S refers to the signal, which is proportional to the gain, N to the noise, t_{rise} to the rise time, V_{th} to the threshold voltage and d to the detector thickness.

In the modern front-end chip technology, the σ_{TDC} and σ_{Clock} can achieve ~ 10 ps level and are negligible compared with the other terms. The three most significant effects comes from the three terms σ_{TimeWalk} , σ_{Jitter} and $\sigma_{\text{Landau noise}}$. Time walk and jitter noise depend on the type of readout electronics chosen. Both of them are inversely proportional to the signal slope dV/dt , which is the output by the front-end amplifier. From Eq. 6.2, we can find the lowest noise jitter and time walk with the sensors with a high signal-to-noise ratio (S/N) and short rise time. For an LGAD with a fixed gain, the signal shape with different detector thicknesses can be found in Fig. 6.2, where we can see that the larger signal slope can be achieved by the thin detector design. The Time-walk can also be further corrected using time reconstruction algorithms such as constant-fraction discrimination (CFD) or using the time-over-threshold (TOT) with the calibration data.

The “Landau noise” for the $\sigma_{\text{Landau noise}}$ is due to the non-uniform charge deposition along the particle trajectory leading to time-of-arrival fluctuation. However, this contribution does not have an analytic expression. Thus it needs to be evaluated by the simulation. The simulation of the timing resolutions with different detector thicknesses is performed by the “*Weightfield2*” [194]. The results shown in Fig. 6.2 indicate that the Landau noise contribution is smaller for the thinner detector. The detector with $50 \mu\text{m}$ active thickness is considered, which results in an acceptable trade-off between the collected charge and Landau noise contribution for working in the high radiation environment.

6 The Low Gain Avalanche Detector History and its Principle

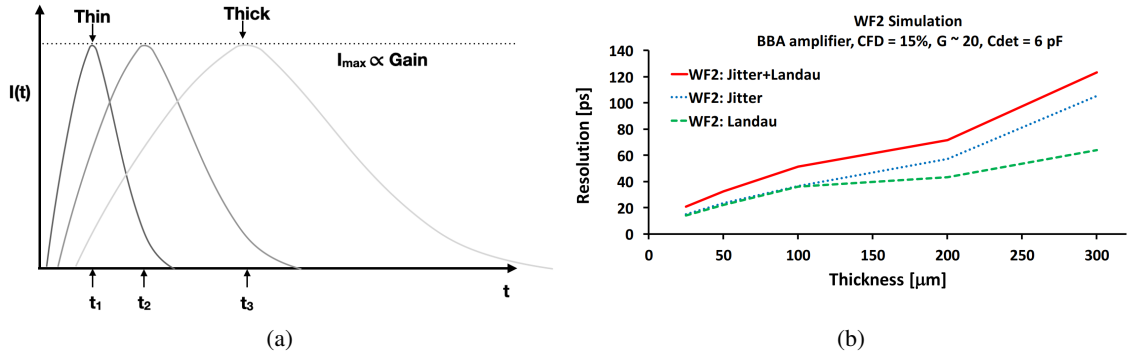


Figure 6.2: (a) The shape of the LGAD signal with fixed gain and different thickness indicates that the fast-rising edge with the highest slew rate can be achieved with the thin LGADs. (b) The simulated timing resolution by *Weightfield2* with different detector thickness. The contributions from Jitter and Landau noise are shown separately [206].

In a word, combining the contributions from these three sources in quadrature gives us the total time resolution. With the time-walk effect corrected, the dominant contribution comes from the jitter of the electric noise in the low signal-to-noise ratio case and the Landau term in the high signal-to-noise ratio case.

Fig. 6.3 shows the simulated LGAD signal with a gain of 10 with the electrons and holes from primary ionization and from multiplication are shown with different colors. Since the gain layer is close to the cathode where the electrons are collected, the dominant contribution is from the drifting of the holes that are generated associated with the electron multiplication. The Landau contribution is simulated and shown in the rising edge. The drifting time of primary electrons (\sim rising duration of the signal) is around 600 ns in this configuration. We can see that in such a slow rate, the contribution of signal noise in the rising edge can be mitigated in the timing measurement.

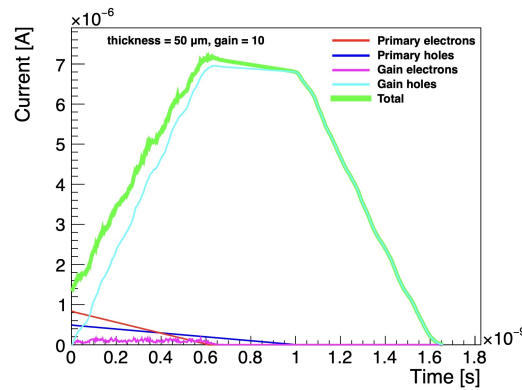


Figure 6.3: The signal composition of the LGAD with gain = 10, the simulation is done with the *Weightfield2* [194], and the thickness is set to 50 μm . The total signal and the composition from primary electrons, gain electrons, primary holes, and gain holes are shown. The MIP signal is simulated, and the Landau noise can be seen in the rising edge.

6.3 Radiation hardness of the LGAD

Due to the hadronic scattering in the forward region at increased luminosity, the environment of the HGTD detector in the HL-LHC operation is expected to have a high total NIEL radiation. The sensors placed at the innermost ring would suffer around $6 \times 10^{15} \text{ n}_{\text{eq}}/\text{cm}^2$ fluences. Thus, the radiation damage impact on the detector must be well studied and mitigated to achieve a good design that can guarantee a stable operation and the expected performance for the whole period of the operation.

The radiation damage in silicon detectors, as discussed in Chapter 5.3, mainly results in the change of the effective doping concentration, the introduction of trapping centers that reduce the mean free path of the charge carrier, and the increased of the leakage current.

Since the gain layer in the LGAD is formed by the dedicated p-type implantation, whose dose is proportional to the electric field, the change in the effective dose would result in a change of the electric field at a similar scale. However, as the avalanche model formula shown in Eq. 7.1, the multiplication (gain) will increase with the electric field strength dramatically (which is faster than the exponential relation). This means a slight change in the effective doping concentration (or dose) would significantly change the gain. The detailed calculation show that the change of the $\sim 1\%$ on the doping concentration would lead to a $\sim 10\%$ change in the V_{BD} .

When exposed to a radioactive environment, this effect causes the deterioration of the gain layer, which is a critical aspect that must be investigated. In the RD50 collaboration, a series of radiation damage and defect characterization studies have been conducted targeting to model this effect and examine the radiation hardness of LGADs. Various techniques have been employed, including the advanced I-V/ C-V, beta-scope, and TCT for performance characterization, as well as TSC and deep level transient spectroscopy (DLTS) for defect characterization, to identify and model the microscopic damage formation after radiation exposure.

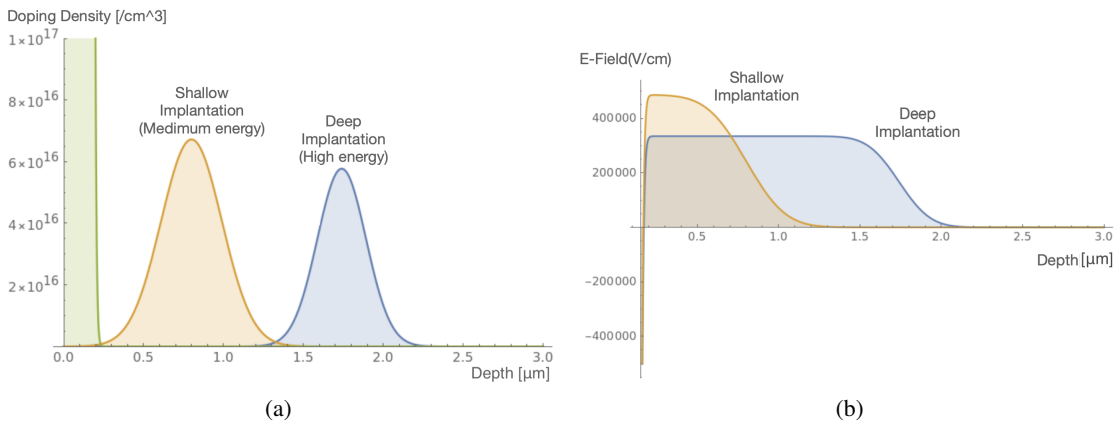


Figure 6.4: Two different approaches of the irradiation hard LGADs by selecting the different gain layer depth. (a) The two-gain layer simulated the doping profile. (b) The electric field is calculated by the corresponding doping profile.

6.3.1 Gain layer degradation – Acceptor removal

In the LGAD technology, the gain layer plays a crucial role in performance. The primary consequence of radiation exposure is the degradation of gain with fluence at a fixed voltage caused by removing initial acceptors in the multiplication layer. After several years of dedicated research, this effect, known as the “acceptor removal”, results from the inactivation of boron acceptors [208] and further reduces the effective acceptor concentration and leads to diminished gain. As a consequence, the detector’s bias voltage has to be increased after irradiation to partially compensate for the performance degradation.

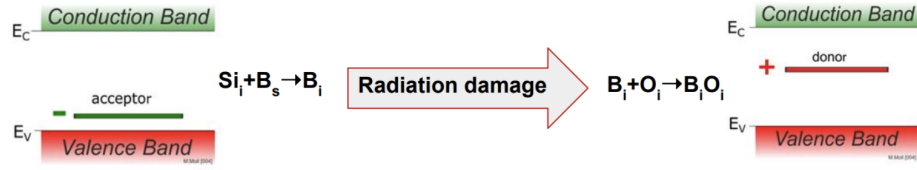


Figure 6.5: The B_iO_i formation from the B_i and O_i created by the interstitials Si_i created under the irradiation shown in the band gap.

The inactivation of the boron acceptor happens when the boron substitutions interact with the lattice defects caused by displacement damage after irradiation. Starting from the original acceptor (B_s : Boron substitution), after several intermediate steps, as shown in Fig. 6.7 (a), the B_s becomes to the interstitial state B_i , and finally formed a metastable complex B_iO_i with the oxygen interstitial B_iO_i which is a deep energy level with positive space charge appeared as Fig. 6.5. This process can be confirmed by the dedicated TSC or the DLTS measurement [208], shown in Fig. 6.7 (b). Such defects have been studied with varieties of technologies, and several theories have been proposed and verified to model it [209]. The most common one:

$$N_{A,eff}(\Phi_{eq}) = N_{A,0}e^{-c_A \cdot \Phi_{eq}} + g_A \Phi_{eq}. \quad (6.3)$$

For the model of the acceptor removal, the contributions from acceptor generation can be neglected in p-type gain layer at fluence less than $1 \times 10^{16} \text{ n}_{eq}/\text{cm}^2$ ($c_A \gg g_A$). The equation can be further simplified into

$$N_{A,eff}(\Phi_{eq}) = N_{A,0}e^{-c\Phi_{eq}}. \quad (6.4)$$

This function indicates that a simple parameter could be used to evaluate the radiation hardness of an LGAD device, the coefficient of the acceptor removal: c , also called the c -factor. As the acceptor concentration of the gain layer is proportional to the V_{GL} , the c -factor can also be measured by fitting the curves of V_{GL} vs. Φ_{eq} by

$$V_{GL}(\Phi_{eq}) = V_{GL}(0)e^{-c\Phi_{eq}}, \quad (6.5)$$

which will be applied in Chapter 8 for analysis of the data from C-V measurements.

6.3 Radiation hardness of the LGAD

The formation of B_iO_i is related to several processes as Fig. 6.7 (a), (b) shows. Thus the rate of this formation would also be influenced by the concentration of the initial and final defects' density and the temperature. Similar to the Boron, carbon atoms can also form the interstitial state defect c_i , and then form the C_iO_i in the end. These two processes are competitive with each other and can be utilized to mitigate the impact of the boron acceptors. The idea is to infuse the carbon in the gain layer region, and by the generation of the C_iO_i complex, the boron acceptors are protected. Such an idea is realized by the FBK, and the devices show promising radiation resistance [210]. The successful realization of this strategy at USTC is shown in Chapter 7 and Chapter 8.

Apart from reducing the c -factor of the acceptor removal, designing the gain layer to have a better recovery capability is also important. The model of the avalanche presents a non-linear relationship between the electric field strength and the avalanche coefficient, suggesting that the low field and high-electric field have different capabilities to recover the gain after irradiation. The gain is obtained by the integral of the coefficient (which is a function of the electric field) on the avalanche distance. Therefore, a detector with fixed gain can be realized in two ways: a lower electric field strength with a longer distance (deep gain layer) or a higher electric field strength with a shorter distance (shallow gain layer), as shown by Fig. 6.4 (a) and (b). By the numerical calculation, with a similar fraction of the gain layer acceptor concentration removed (e.g.: 30%), the electron's gain is shown as a function of bias voltage in Fig. 6.6. We can see the device with a deep gain layer and a lower electric field has better recovery capability after the same fraction of the acceptor is removed. The detailed analysis can be found in the report in Ref. [211].

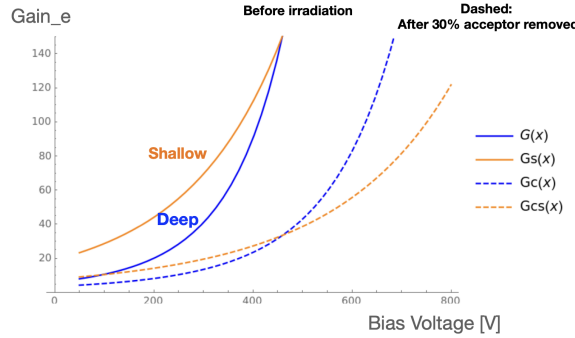


Figure 6.6: The gain of the electron is calculated by the integration of the multiplication factor derived by the Massey model with the two doping profiles. Both before and after, a fixed fraction of the acceptor removed gain layer after irradiation is plotted. The curves indicate that the loss of the gain in the deep gain layer LGAD can be compensated with less increase in the bias voltage after irradiation.

However, such calculation is based on the assumption that the c -factor is constant for the different initial boron concentrations: $N_{0,eff}$. Further measured data [210] show that the c -factor depends on the initial concentration significantly. In the fabrication process, the inducing of the deep p-type well is realized by the high energy ion implantation. The stopping range and the distribution of the ions in the silicon with the specific energy are fixed. This be simulated with the SRIM software [212] with the Monte Carlo method. Considering this effect, the depth of the gain layer and the width of the gain layer is constrained. For a deeper gain layer with the same gain, the doping profile of the gain layer is wider, and the total dose is lower, which makes the initial acceptor concentration much lower. In such a case, the acceptor removal for the deep gain layer would be quicker than the shallow gain layer. The

6 The Low Gain Avalanche Detector History and its Principle

loss due to this effect would be more significant than the benefit from the recovery capability for the deep gain layer. Later LGAD prototypes from FBK and USTC also proved this and will be shown in Chapter 8.

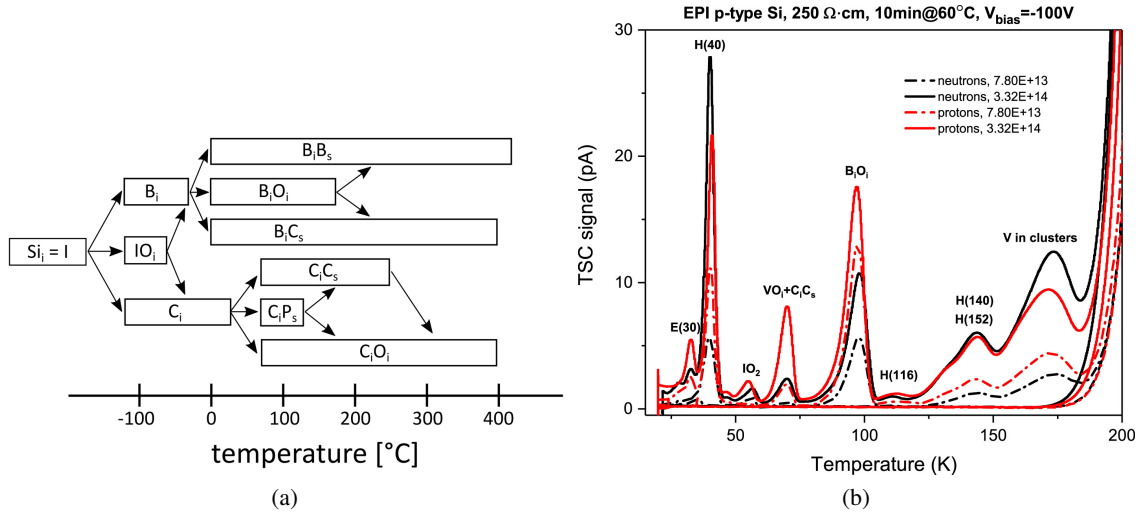


Figure 6.7: The interactions of the defects created by the displacement damage and the formation of the B_iO_i complex formation after the irradiation (a) [209]. The formation of the B_iO_i complex measured by the TSC technique with the p-type silicon samples irradiated at different fluences [208]. We can see the increments of the B_iO_i peak when the fluence gets higher.

6.3.2 High voltage operation – Single-event burnout effect

In addition to the acceptor removal, another effect also arose people's focus: the single event burnout (SEB) effect. This effect is related to the device destruction by a large amount of charge deposition from the single event on the irradiated thin LGAD. This has been observed both by the laboratory tests using the infra-red laser TCT and by the test with a highly energetic particle beam in the active volume of LGAD [213]. The large amount of charge deposition in a long operation duration is unavoidable due to the tail Landau distribution, and it leads to a high density of charge carriers. The screening effect created by such high carrier density then prevents carriers from being swept away, leading to a change in the resistivity in that part of the sensor such that it becomes conductive. The field collapses in the region of high free carrier density, leading to increased voltage drop in the region where density is lower. The increase of the field there leads to avalanche breakdown and exceeds the critical field of the silicon. Then the charge stored on the electrodes as well as on the high voltage (HV) filtering capacitor (typically 10 nF) in the front-end electronics is discharged through the sensor. The energy available in such a discharge is enough to melt the silicon, create a crater and damage the sensor (as shown by photos in Fig. 6.8 (a)). The breakdown is eventually quenched, but the sensor is permanently damaged. Such effect should be prevented in the lifetime of the detector's operation, and the systematic research has been conducted by the ATLAS HGTD collaboration with the results show the electric field should be kept below 11 V m^{-1} (as shown by Fig. 6.8 (b)). Thus, this raises the new requirement on radiation hardness besides the minimal collected charge from reduced gain. The tests

6.4 Different types of the LGAD design

with the charged particle beam in Sec. 8.4 show more detailed experimental observations for the SEB effect on LGAD.

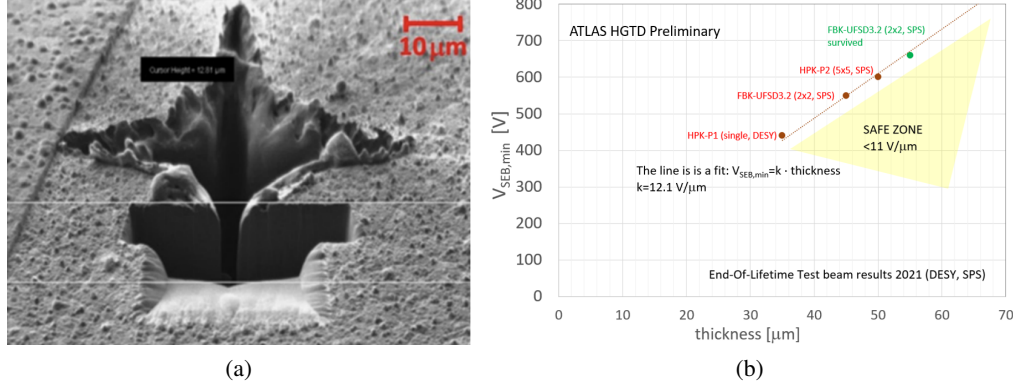


Figure 6.8: (a) Microscopic photo of a typical burn mark observed in ATLAS proton beam tests at Fermilab in 2018 in a CNM LDA35 sensor [213]. (b) Minimal SEB threshold vs. thickness of the sensor.

6.4 Different types of the LGAD design

After the LGAD was proposed and proven the promising functionality, the RD50 institutes did not stop their innovation. They continued to understand its character under the irradiation environment and explore different designs for some dedicated improvements. These state-of-arts brought us many innovative ideas with superior performance and the potential to resolve limitations of the LGADs in some aspects.

The LGAD basic structure (as shown in Fig. 6.9), due to its strong field near the junction edge, needs a larger space for the isolation of the neighbor pads. This character leads to non-negligible gap regions ($\sim 100 \mu\text{m}$) between the pixels and could be a dominating reason for the inefficiency of the detector with small pitches for the application that needs a better position resolution (more detailed in Sec. 7.3.9 for simulation and Sec. 8.5.2 for the measurement). The efforts are made both by modifying the p-n junction type, the gain layer position, the isolation method, or the readout method. In this section, four of the most developed novel LGAD design are introduced.

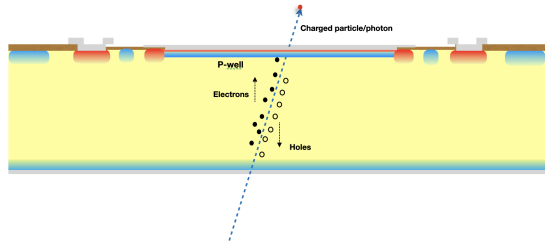


Figure 6.9: The legacy LGAD structure schematic layout.

6 The Low Gain Avalanche Detector History and its Principle

6.4.1 Inverse LGAD

Instead of reading the signal from the n-electrode, the inverse LGAD (iLGAD) uses another side of the detector for readout while keeping the isolated electrode away from the multiplication layer, thus away from the strong field region as shown in Fig. 6.10 (a). This technology is mainly developed by CNM [214] and has its advantage in X-ray detection with a thick substrate used for enough charge and good energy resolution with the double-side fabrication process.

6.4.2 Trench isolated LGAD

One of the solutions is to apply the deep trench, which is fabricated with the large aspect deep silicon etching with DRIE technology as shown in Fig. 6.10 (b). In such a way, the active region of the neighbor is realized within 10 μm of isolation regions. The efficiency (fill-factor) can be reached to almost 100%. This technology is proposed and developed by the FBK [215, 216], and several iterations have demonstrated good performances.

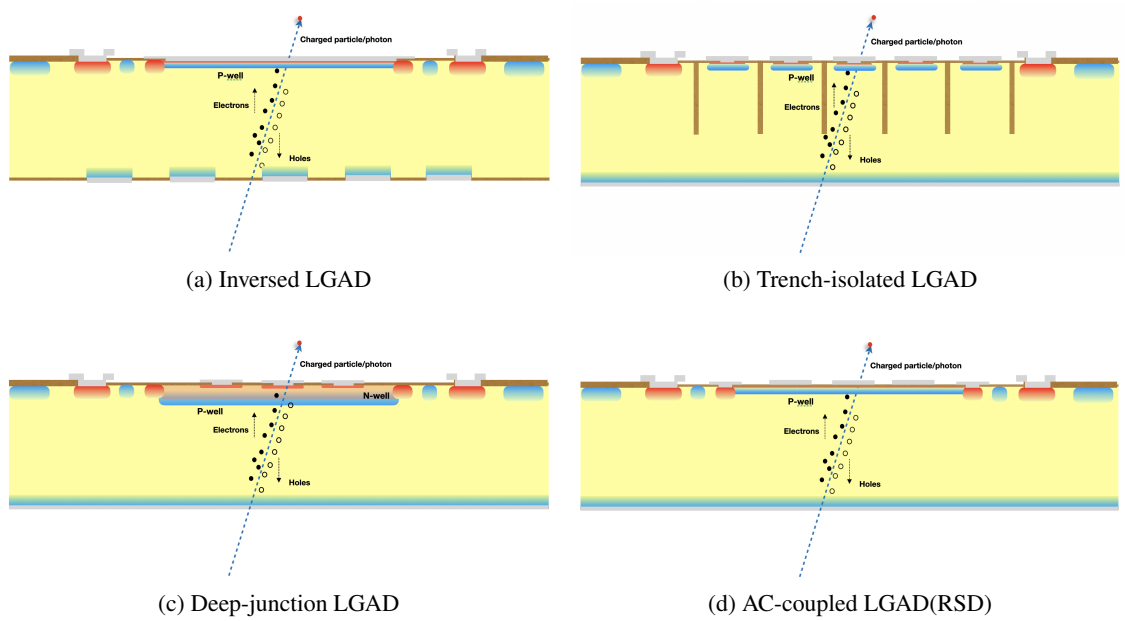


Figure 6.10: The novel LGAD structures have been developed for better performance and more wide application scenarios.

6.4.3 Deep junction LGAD

The LGAD, due to its strong field near the junction edge, needs a larger space for the isolation of the neighbor pads. Another approach to make pixel isolation easier is to reduce the electric field near the electrodes. This is achieved by moving the gain layer towards the inner of the detector. With such technology, the junction and the multiplication happen under several micrometers of the detector, and

the pixelization of the electrode can be easily made on the surface where the electric field is low. The structure is shown in Fig. 6.10 (c). This idea was originally proposed by the UC Santa Cruz group [217]. The fabrication of such devices is ongoing, and $\sim 10\ \mu\text{m}$ spatial resolution is expected.

6.4.4 AC coupled LGAD (RSD)

Another way to resolve the isolation issue and improve efficiency is to change the way of the readout circuit. In such a concept, both the gain layer and the electrode is designed to be continuous. The division of the pixels is realized on the metal layer, which is separated from the silicon by a dielectric layer. In this way, the signal is coupled to the readout via a capacitor-like layer, as shown in Fig. 6.10 (d). Such design allows the division of the pixel with quite large freedom (either shape or pitch). Moreover, both timing and spatial performance will benefit from the charge sharing with the neighboring pixels, which make precise position measurement with the method, like the center of gravity weight, possible. This design is considered to be an exceptionally beautiful idea, as it overcomes the isolation problem of legacy LGAD without introducing the complexity of the fabrication and makes the target of the high precision 4-D tracking come true. This design raises communities' interest quickly due to its simplicity in fabrication, readout, and good spatial-timing resolution. The research of the AC-LGAD has become quite a hot area in recent years. Led by FBK, several institutes have realized it and focused on its research [218] [218, 219]. This thesis will also introduce the AC-LGADs developed by USTC with the preliminary tests in Appendix A.

6.5 Summary

In this chapter, the motivation for developing LGAD technology is explored, along with a review of their timing performance and radiation hardness. The chapter also discusses the gain layer degradation due to acceptor removal and the impact of high voltage operation by the single-event burnout effect. Furthermore, various LGAD designs are introduced and analyzed, including the inverse LGAD, trench-isolated LGAD, deep junction LGAD, and AC-coupled LGAD. Both the advantage and disadvantages of them are compared. The chapter provides a comprehensive understanding of LGADs, addressing their advantages, challenges, and design variations for optimal performance in specific applications. This background information will be further demonstrated and applied in Chapter 7, 8 and Appendix A.

7 Simulation and Fabrication of the USTC-IME LGADs for the HGTD Upgrade

7.1 The structure of the LGAD sensor

After the proposal of the RD50 to consider the implementation of the multiplication with a moderate gain into the silicon diode for timing application, several institutes and companies have devoted efforts to realize and optimize it. The first fabrication technology is developed by the CNM [199]. Due to the requirement of the high voltage for the LGAD operation, the optimization of the peripheral region has become one of the most important items for LGAD design [203, 214, 220], especially when it needs to work in the harsh radiation environment. The improper peripheral region designs could lead to avalanches happening in the region outside of the multiplication layer, and the large leakage current forbids the detector from being operated with the designed gain and performance. This is called premature breakdown and should be avoided.

Several structures have been simulated and fabricated. The simulation has been validated with measurements of the fabricated devices. A subset of them have been commonly considered by the institutes that are essential for LGADs (including the JTE, guard-ring, p-stop/p-spray isolation) as shown in Fig. 7.1. However, there are different approaches for realizing the device following this idea. In this section, the process and prototypes from different fabrication technologies are reviewed and compared. The designs of the structure are discussed, including the ideas to propose them and the considerations for optimizing them.

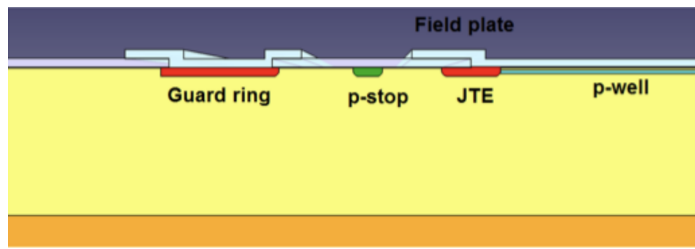


Figure 7.1: The illustration of typical LGAD structures, including the multiplication layer, n^+ layer, JTE, field-plate, p-stop, and guard ring.

7.1.1 Substrate - Where everything is based on

Based on the timing resolution analysis for LGAD in Sec. 6.2, the detector should have a thin active region to reduce the Landau noise and jitter contribution. It has been demonstrated that LGADs with

7 Simulation and Fabrication of the USTC-IME LGADs for the HGTD Upgrade

a time resolution of about 30 ps can be achieved with the substrate thickness of 50 μm [221]. However, such an active region is too thin to be handled in the fabrication directly. There are currently three main options available. The first option is the bonding of a high-resistivity wafer (usually float-zone (FZ) wafer) with a low-resistivity wafer (usually the Czochralski (Cz) wafer), followed by a mechanical thinning of the high-resistivity wafers from several hundred microns to 50 μm for producing thin LGADs, which is called Si-on-Si wafer. The second one is to use the dedicated Silicon-on-insulator (SOI) wafer, where a buried oxide layer is in the middle of two wafers. The third option is to grow a layer of high-quality p-type silicon on a low-resistivity handle wafer by the epitaxy technology, called the epitaxial wafer.

From the technical point of view, the Si-on-Si wafer raises challenges in the wafer bonding and thinning process to yield perfect Si-on-Si wafers without many defects and with good uniformity. It is difficult to produce large Si-on-Si wafers at a low price. As for SOI wafers, the devices' anode must be contacted by etching the silicon and oxide from the backside of the wafer. Thus, a double side process is needed, making the fabrication complex and expensive. For both the Si-on-Si and SOI wafers, front-side thinning is needed to achieve the 50 μm active thickness. The epitaxial wafer has advantages in simplicity and maturity in consumer electronics fabrication. It is also easy to achieve good uniformity and low defect concentration. Moreover, the low-resistivity handle layer can be used directly as the anode contact, allowing the single-side processes to be used. Therefore the epitaxial wafer has been selected by most LGAD producers to fabricate the sensors for large-scale applications. Benefiting from the rapid development of the CMOS device, the 8-inch epitaxial wafers can be obtained with both high quality and lower prices. The uniformities of this wafer on thickness and resistivity are also validated in the past application.

7.1.2 Multiplication layer (p-well) - Heart of LGAD

In a similar situation for the conventional silicon diode detector, the LGADs create the drift electric fields by the p-n junction realized with the doping of n-type (usually phosphorus) as donors and p-type (usually boron) as acceptors. For the LGAD device, an extra p-type deep implantation with a concentration higher than the substrate (p-well) is implemented to enhance the electric field near the junction. The multiplication region is then formed with a width from a fraction of a micron to a few microns, depending on the doping depth of the acceptors and donors. With a high voltage applied reversely, the p-n junction is depleted, and the space charge region (SCR) is established depending on the doping profile. Compared to the substrate region, which has much less acceptor density (usually $1 \times 10^{12} \text{ cm}^{-3}$ to $1 \times 10^{13} \text{ cm}^{-3}$), the highly doped gain layer which has several orders of magnitude higher acceptor density (usually $1 \times 10^{16} \text{ cm}^{-3}$ to $1 \times 10^{17} \text{ cm}^{-3}$) will create a much stronger electric field, which will enable the avalanche of the electrons and holes. From the Messy model, we can see that the multiplication factor strongly depends on the temperature of the device, which tell us to take the working environment of the device into account during the design of the multiplication layer. For the HGTD application, the ambient temperature is designed to be at -30°C for the detector to survive in a harsh radiation environment.

The design of the multiplication layer needs to be fine-tuned to find a proper value of the breakdown voltage and operating voltage of the LGADs. If the V_{BD} is too high (lightly doped gain layer), it would be hard to achieve enough gain with a degraded gain layer after irradiation, and the power

consumption of the LGAD would increase, leading to a risk of thermal runaway and SEB. If the V_{BD} is too low (heavily doped gain layer), it would be inefficient to achieve the saturated drift velocity for the charge carriers to drift in the substrate before the breakdown. In such cases, the signals will come out with a slower rising edge and poor time resolution, as discussed in Chapter 6.

Different configurations of the gain layer need to be simulated, and the corresponding expected performances are compared. The dedicated calibrations have been performed on the process-level simulation with the fabricated samples to eliminate the discrepancy between the simulation and the factory fabrication processes or machines. For this purpose, the splits of the wafers with different gain layer doping doses and depths have been produced in the same batch and tested with the same setup. The results will be analyzed and compared to find the most optimal multiplication layer design as a reference for the next batch.

7.1.3 n^+ layer - We got the signal? Read it out!

The heavily n-type doped (n^+) layer of LGAD is designed to be shallow and close to the cathode's surface to establish a low resistance ohmic contact with the metal layer above the silicon. It will also keep the depletion away from the surface of the silicon, where the defects and contaminations concentrate. In order to fulfill the above requirements, the n^+ layer needs to be heavily doped within a limited depth. The concentration of the doping for n^+ needs to be controlled below the solid solubility of the impurities in silicon ($\sim 1 \times 10^{20} \text{ cm}^{-2}$) and should be protected from thermal diffusion during the fabrication. The uniformity of the n^+ layer is also as crucial as the p-well for multiplication since they define the electric field for the avalanche together.

The resistivity of the n^+ layer needs to be as low as possible for the direct coupled LGAD (DC-LGAD) to prevent the distortion or delay of the signal during the transformation, which will destroy the fast edge we required for the timing measurement. It is also worth mentioning that in some cases, this layer can be adjusted to have lighter doping for the signal to be delayed. Such a signal can reflect the hit position and can be exploited to reconstruct both time and position. This is called AC-LGAD as shown in Fig. 6.10. The development of such structures at USTC is introduced in detail in Appendix A.

The high electric field will appear not only at the planar region between n^+ and p-well, but also at the edge of the n^+ layer due to the large curvature (with less than $0.1 \mu\text{m}$ radius). Without special treatment, such a localized strong electric field can lead to a premature breakdown of the device at the peripheral region. Once this happens, the operation voltage of the sensors will be limited by the peripheral region instead of the signal multiplication region, and the LGAD cannot achieve the desired gain. Moreover, new noises can be induced from the strong localized field by the thermal electrons [222] (also called Johnson–Nyquist noise) being multiplied and amplified, which further deteriorates the detector's time determination.

For the LGADs to be used in the HGTD, we need to keep increasing the operating voltage of the detector as the higher radiation fluences accumulated by the LGADs to compensate for the loss of the gain due to the radiation damage in the gain layer and substrate. The sensor, in the end, needs to be operated at ~ 500 to 600 V bias voltage, which is higher than the common silicon-based pixel detectors. Thoughtful optimization of the peripheral region has been considered for the radiation-resistant LGAD structure, similar to the multiplication layer. Several technologies developed by the industrial power

semiconductor device have been considered and proven to work well, including the JTE and field plate, which will be introduced in detail in the following sections.

7.1.4 Junction termination extension - Stop break at the edge!

The junction termination extension (JTE) is the structure widely used in the power semiconductor industry [191, 223]. By creating deeper and heavy doping at the edge of the shallow n^+ , the JTE reduced the curvature of the depletion region edge and corner. This will reduce the field strength at the edge of the electrode, making the potential drop smoother. This structure is designed to ensure that the maximum electric fields only locate in the multiplication region, which is the only reason that triggers the breakdown when the bias increases. It is critical for the JTE's effectiveness to achieve enough depth (usually several μm) and keep the curvature of the JTE's edge small and the electric field within the acceptance. The dose of the JTE layer can be controlled by the implantation directly and precisely, while the depth needs to be realized by the thermal diffusion under the high temperature for a long time. Thus, it is designed to be the first implantation to fully utilize the thermal processes in the device fabrication and avoid the impact on other implantations that need lighter diffusion. The structure of the JTE can be found in Fig. 7.1.

7.1.5 Field plate - Make the field smooth.

Apart from the doping, the shape of the electric field can also be controlled by a biased metal layer above the oxide through the field effect. If we consider a p-in-n type diode when we apply a positive bias with regard to the backside, the electrons will be attracted, which will shrink the depletion region near the sensor surface towards the edge of the sensor as shown by Fig. 7.2. After that, the edge of the depletion region gets flatter, and the electric field near the junction edge is further reduced [223]. Similarly, for the n-in-p diode like LGADs, the field plate can also smooth the field near the n-type electrodes when the bias is applied.

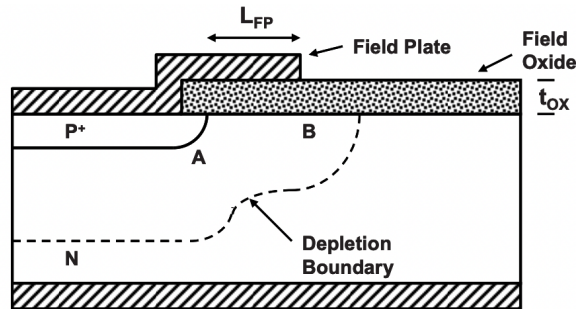


Figure 7.2: The impact of the field plate on the edge of the depletion region [191].

For such a structure, the length of the field plate (L_{FP}) and the thickness of the field oxide t_{ox} are the main parameters and to be optimized to achieve a robust design for the LGAD operation for HGTD.

7.1.6 Guard-ring - For those signals and current we don't want!

The peripheral region is introduced in order to prevent the premature breakdown of the device at the edge of the electrode, which also induces a non-negligible region (~ 300 to $500\ \mu\text{m}$ in width) where the multiplication is not covered. The shapes of the drift electric field in this region are distorted due to the non-uniform edge conditions. The signal generated in these regions would not be multiplied and drift with a lower velocity, which will show up as a delayed, distorted, and lower signal with very poor time resolution. In order to prevent these slow signals from being read out by the front-end electronics and influence the timing resolution, the guard ring (GR) is designed to surround the readout electrode to collect these slow signals directly to the ground. Besides, the collection of the lateral current from the edge of the device would result in an increment of the current in the central pad. This lateral current can cause a DC (signal baseline) shifting of signal, which will also induce short noises. The designed guard ring can collect the lateral current and prevent the central pad from the impact of the noise.

The guard ring can be realized by an overlay of the JTE and the n^+ implantation with the central pad simultaneously to fabricate the structure with both good ohmic contact and edge termination extension. The guard ring would be connected to the ground directly during the operation of the detector. The structure of the JTE can be found in Fig. 7.1.

7.1.7 Float guard ring - Lower the potential step by step.

In order to further smooth the depletion region of the detector, the float guard ring (FGR), also called the floating field ring, can be arranged outside the main guard ring. Such a structure reduced the drop of the potential near the surface of the peripheral region and improved the sensor's high voltage tolerance. With this design, the potential near the peripheral region will drop step by step, as shown in Fig. 7.3. The position and width of the FGR can be fine-optimized to prevent the detector from a premature breakdown in the region with the highest potential drops.

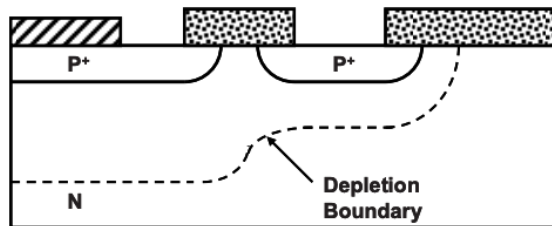


Figure 7.3: The impact of the float guard ring on the edge of the depletion region surface [191].

7.1.8 P-stop - Keep the electrodes isolated.

The unavoidable appearance of the fixed charge at the surface between the silicon oxide and the silicon could attract the electrons from the substrate. When this happens between the two neighboring n-type electrodes, it can cause an electron channel and lead to a short between the two neighboring

7 Simulation and Fabrication of the USTC-IME LGADs for the HGTD Upgrade

electrodes. The electrodes can be either the guard ring or the neighboring pixel. Such short can reduce the signal-to-noise ratio by a larger capacitance and induce the cross-talk of the neighboring pixel. This will lead to a non-negligible effect on the HGTD project since the final application requires the sensor to be as 15×15 arrays.

In order to achieve good isolation between the n-type electrodes (pixels and guard-ring), the p-stop and p-spray techniques have been considered. The p-stop is a process that induces localized p-type doping by an extra mask, which is realized in a precise and controlled way. It introduces a fixed separation with the n-type electrode without affecting the field near the junction edge. The p-spray process is a mask-less, monolithic, and cost-effective way to realize isolation, while the dose and profile of the p-spray need to be precisely adjusted. The p-spray will increase the density of the acceptor concentration near the n-type electrode, which will further increase the electric field near the junction as a side effect. Both technologies have been achieved for the LGAD fabrication. However, for the application at the HGTD, a much higher bias voltage is required after irradiation, and the acceptor removal can change the behavior of the lightly doped p-spray significantly [188]. Thus, most vendors choose either the p-stop, or a combination of both in their fabrications.

7.1.9 C-stop - Don't touch the defects!

The depletion region of the sensor needs to be carefully constrained to avoid it reaching the edge region where the contaminations, defects, and cracks are enriched [188]. After the device fabrication processes are completed, the wafers need to be diced for further assembly. Cracks and contaminations are unavoidable when dicing a wafer. Many small cracks would be formed at the edge of the device. If the depletion border touches these regions, the short of the detector will happen, show up as an abrupt rise of leakage current and limit the device to be operated at a higher bias. The channel stop (c-stop) is thus being applied with the p-type uniform doping to constrain the depletion region away from the cutting edge of the sensor and potential cracks. The comparison of the peripheral region with and without c-stop is shown in Fig. 7.4.

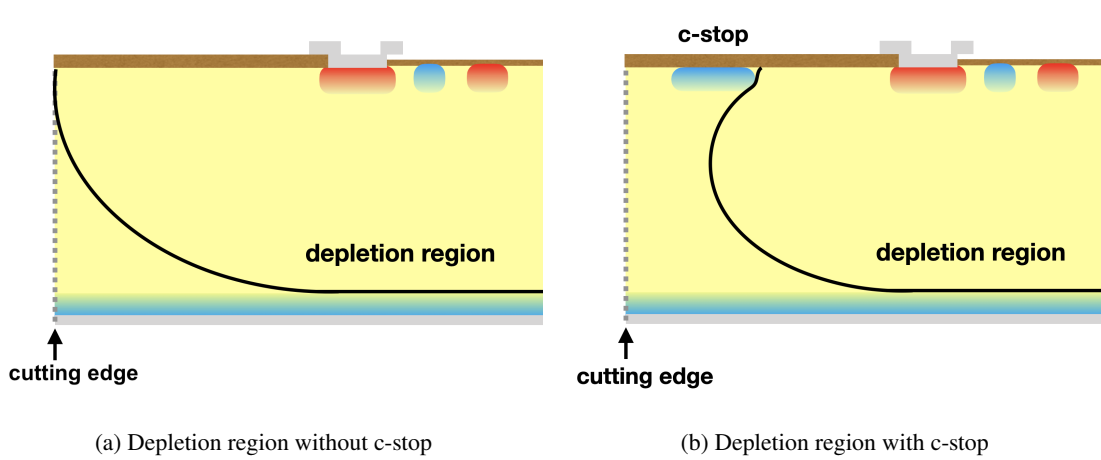


Figure 7.4: The schematic illustration of the c-stop in the peripheral region of the LGAD design. (a) The depletion region arrived at the cutting edge of the device where the defects and contaminations concentrate. This will lead to an increment in the leakage current. (b) The depletion region is constrained by the p-type c-stop implantation and kept away from the cutting edge.

7.2 TCAD simulation

One of the most powerful tools for designing silicon devices is the TCAD (Technology Computer Aided Design) software. In this thesis, the TCAD software used is Synopsys TCAD Sentaurus toolkit. The simulations use some models defined for the TCAD simulator, which adjusts better to the detectors fabricated at USTC-IME.

For the general workflow of the simulation, first, a simple single-pixel model with Sentaurus Process is created with the process parameters. Then the model is used as the input file for the Sentaurus Device with the boundary conditions, and a potential voltage is applied between the electrodes. The simulator proceeds to solve the Poisson equation in the structure to get the electric status of the device, like the field, potential and current densities.

Synopsys TCAD has several models to choose from for each physical parameter of the device being simulated, such as the mobility of the free carriers, recombination, and avalanche. Choosing the models that better describe the real system will improve the simulation precision and result in good predictions. In this section, the TCAD major models for the electric simulations used in this research will be introduced.

7.2.1 Mobility

The mobilities are combined by Matthiessen's rule [224] for the contributions from substrate, surface, and thin layers.

7 Simulation and Fabrication of the USTC-IME LGADs for the HGTD Upgrade

$$\frac{1}{\mu} = \frac{1}{\mu_1} + \frac{1}{\mu_2} + \frac{1}{\mu_3} + \dots$$

In the high-field saturation case, the final mobility is computed in two steps. First, for the low field mobility, the $\frac{1}{\mu_{low}}$ is determined according to the above equation. Second, the final mobility is computed from a model-dependent formula as a function of a driving force F_{hfs} :

$$\mu = f(\mu_{low}, F_{hfs})$$

7.2.2 Recombination

The Shockley-Read-Hall (SRH) recombination introduced in Sec. 5.3.1 takes into account the deep defect levels within the band gap. The recombination rate is described by the equation:

$$R_{net}^{SRH} = \frac{np - n_{i,eff}^2}{\tau_p(n + n_1) + \tau_n(p + p_1)},$$

with

$$n_1 = n_{i,eff} e^{\frac{E_{trap}}{kT}},$$

and

$$p_1 = n_{i,eff} e^{\frac{-E_{trap}}{kT}}.$$

The silicon value for E_{trap} is equal to 0. The lifetimes from the equation are defined as:

$$\tau_{dop}(N_{A,0} + N_{D,0}) = \frac{\tau_{max}}{1 + \frac{N_{A,0} + N_{D,0}}{N_{ref}}}$$

with the N_{ref} is equal to $1 \times 10^{16} \text{ cm}^{-3}$, τ_{max} is equal to $1 \times 10^{-5} \text{ s}$ for electrons and τ_{max} is equal to $3 \times 10^{-6} \text{ s}$ for holes.

7.2.3 Avalanche

When the electric field strength reaches a certain threshold, the electron-hole pair generation due to the avalanche (impact ionization) will happen. It shows up when the device has wide space charge regions compared to the mean free path between the two ionization impacts. It results in charge multiplication, which can cause an electrical breakdown. The reciprocal of the mean free path is called the ionization coefficient α . With these coefficients for electrons and holes, with $v_{n,p}$ as the velocity for electron and holes and n, p for electrons and holes density, the generation rate G can be expressed as [224]:

$$G = \alpha_n n v_n + \alpha_p p v_p.$$

The models based on the Chynoweth-like expression are considered to be used in the simulation of the LGAD detector performance due to the good compatibility with the data shown in the former research. The avalanche coefficient is defined to be

$$\alpha_{n,p}(E, T) = \gamma \cdot A_{n,p} \cdot \exp\left(-\gamma \frac{B_{n,p}(T)}{E}\right). \quad (7.1)$$

In the Massey model, the parameters are defined to be:

$$\begin{aligned} A_n &= 4.43 \times 10^5 \text{ cm}^{-1}, B_n = C_n + D_n \cdot T \\ \text{with } C_n &= 9.66 \times 10^5 \text{ V cm}^{-1}, D_n = 4.99 \times 10^2 \text{ V cm}^{-1} \text{ K}^{-1}, \\ A_p &= 1.13 \times 10^6 \text{ cm}^{-1}, B_p = C_p + D_p \cdot T \\ \text{with } C_p &= 1.71 \times 10^6 \text{ cm}^{-1}, D_p = 1.09 \times 10^3 \text{ V cm}^{-1} \text{ K}^{-1}. \end{aligned}$$

The recent research improved the parameterization for precise modeling of the device related to the avalanche mechanism like LGAD is achieved with a more detailed analysis of the experiment data [225].

7.3 Results from the TCAD simulation for the LGAD structures

7.3.1 Overview of the LGAD model in TCAD

This section introduced the overview of the LGAD structures and the considerations of the optimizations. The aim of the simulation is to establish a connection between the design and the performance of the device. In order to cooperate with the future fabrication better, the work uses the Sentaurus Process Simulation (*sprocess*) to build the LGAD model instead of the Sentaurus Structure Editor (*sde*). Thus, it would come out with a more straightforward way to connect the fabrication parameters and the

7 Simulation and Fabrication of the USTC-IME LGADs for the HGTD Upgrade

device performances. The device performances are simulated by using the *sprocess* produced model (shown in Fig. 7.5) as input and utilize the Sentaurus Device Simulation (*sdevice*) for the electric simulation (shown in Fig. 7.6), with the model introduced above and the boundary condition like the potential of each electrode at different bias. In the end, the electric field, the potential distribution, the depletion region, the current density, the avalanche coefficient, and the ionization integrals are obtained. Moreover, the I-V curves are obtained by integration, and C-V curves are obtained by the AC small signal simulation at each DC bias point.

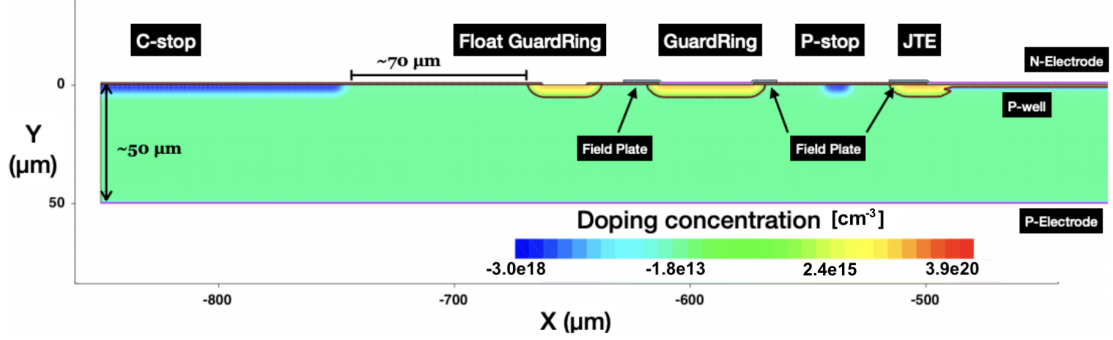


Figure 7.5: The LGAD model created by the process simulation of the TCAD for the electric properties' validation and optimization. The simulation of the single pad device is only performed on half of the device and focuses on the peripheral region since its symmetric. For the doping concentration scale, the positive value corresponds to the donor-enriched region and the negative value corresponds to the acceptor-enriched region.

For the selected candidate models that perform well in the electric simulation, the transient properties are also simulated by the ion model, in which a defined amount of charge carriers are deposited along the trajectory of the ionizing particle perpendicular to the sensor's surface. The drifting and collection of the charge carriers with the avalanche model are simulated, and the DC current signal is obtained, which is used to calculate the collected charge and gain.

In the optimization procedure, the results from the different geometry layouts and process parameters input are compared. The designs with better performance and robustness are selected. Due to the numerous input parameters, and they can be correlated with each other easily, the simulations are taken in a high dimension phase space for which the computational resource for the finite element method (FEM) cannot be afforded. Thus, a proper train of thought to guide the optimization work is crucial for efficient work.

7.3.2 Optimization of the substrate

The substrate is studied by comparing the substrate with different concentrations and its impact on the depletion voltage and the breakdown voltage. The simulations of the electric potential at the same bias are shown for different substrate concentrations ($5 \times 10^{12} \text{ cm}^{-3}$, $5 \times 10^{12} \text{ cm}^{-3}$, and $5 \times 10^{12} \text{ cm}^{-3}$) are shown in Fig. 7.7. From the results, we can find for the substrate with higher concentration $5 \times 10^{13} \text{ cm}^{-3}$ (low resist wafer), the detector is not fully depleted before the avalanche of the gain layer (shown in Fig. 7.7 (c)). For the substrate with lower concentration $1 \times 10^{13} \text{ cm}^{-3}$ and

7.3 Results from the TCAD simulation for the LGAD structures

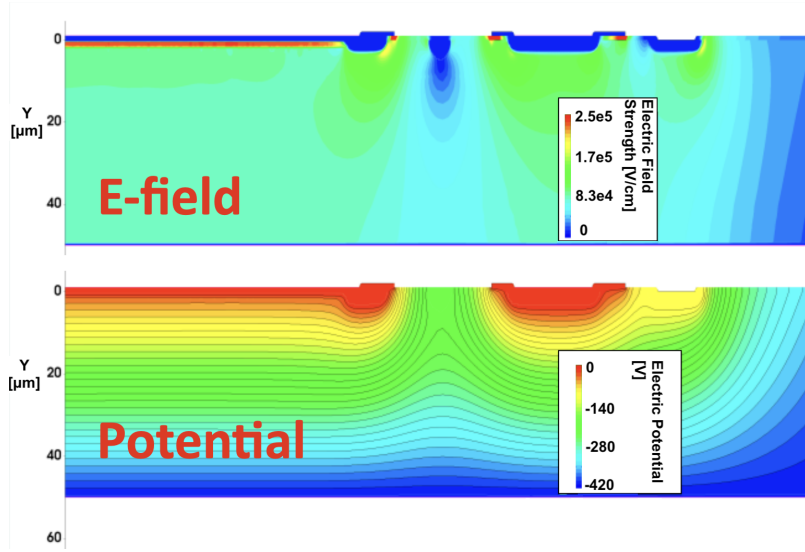


Figure 7.6: The electric simulation of the LGAD peripheral regions. The study is focused on the optimization of the electric field strength (the top figure) and the potential distribution (the bottom figure) to avoid the formation of a strong local field, which may cause premature breakdown and an increment of leakage current, especially after irradiation.

$1 \times 10^{12} \text{ cm}^{-3}$, the detector is fully depleted, which can guarantee a good charge collection (shown in Fig. 7.7 (a),(b)). The gain-layer is configured to be the same, and the thickness is $50 \mu\text{m}$.

7 Simulation and Fabrication of the USTC-IME LGADs for the HGTD Upgrade

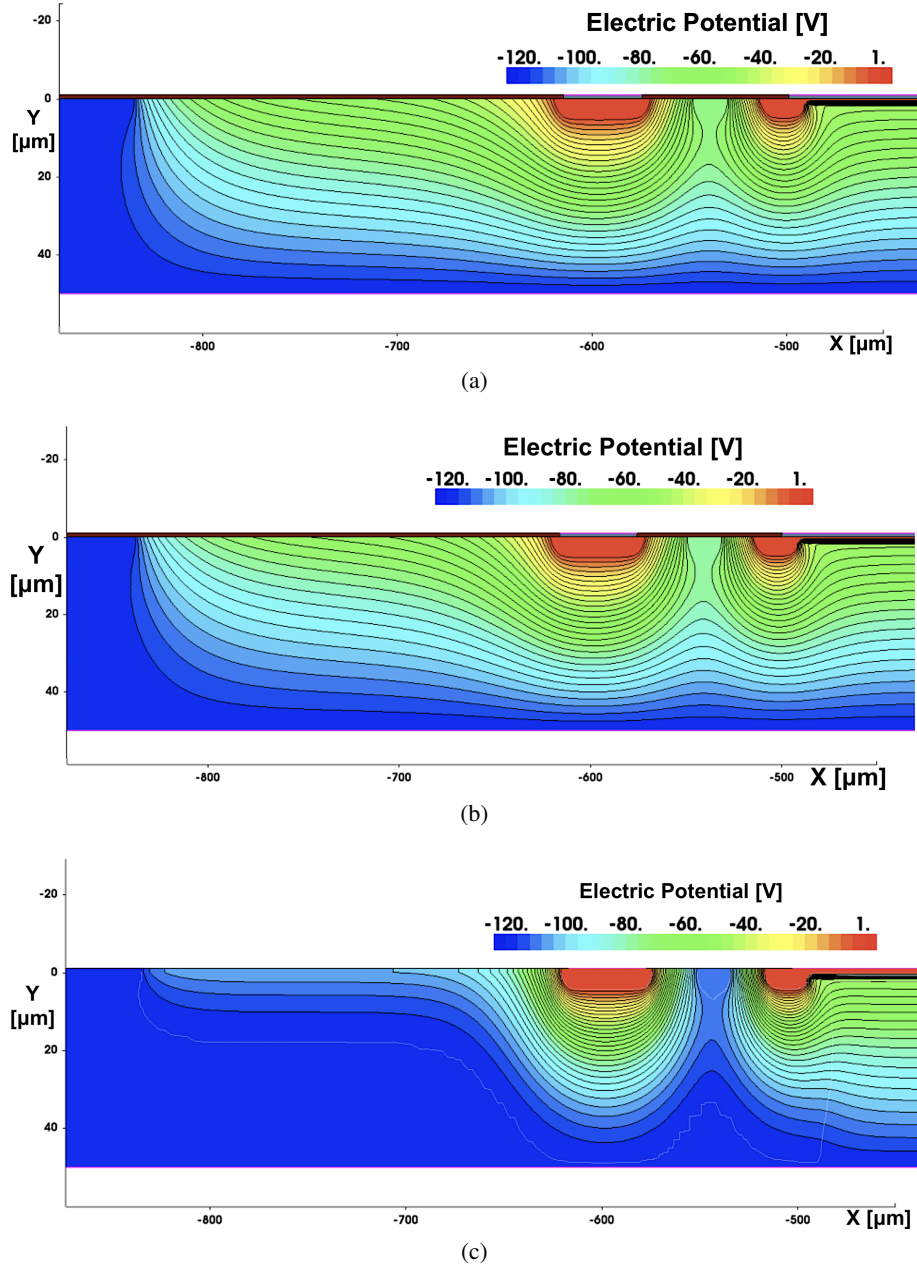


Figure 7.7: The simulated electric potential distribution at different substrate concentrations (a) $5 \times 10^{12} \text{ cm}^{-3}$, (b) $1 \times 10^{13} \text{ cm}^{-3}$, (c) $5 \times 10^{13} \text{ cm}^{-3}$. The same bias (120 V) is used for each simulation.

7.3 Results from the TCAD simulation for the LGAD structures

The V_{BD} from the different substrates is also shown as a function of the substrate concentration in Fig. 7.8 from the simulation. In conclusion, a substrate with a lower concentration is required for the LGAD to be operated at a voltage to fully deplete the sensor before the avalanche breakdown to guarantee a saturated drift velocity of the charge carriers.

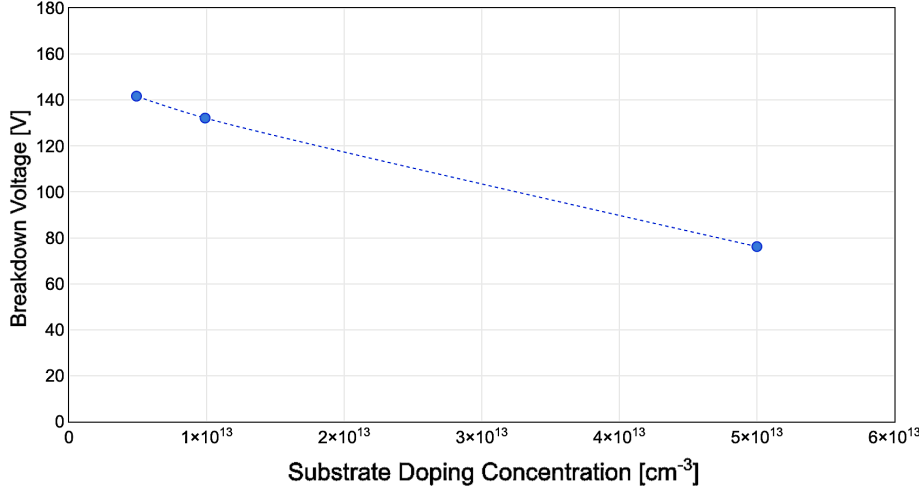


Figure 7.8: The V_{BD} dependence on the substrate concentration from the simulation shown in Fig. 7.7. The trendline is plotted for guiding eyes.

For the curves of the $1/C^2 - V$ for LGADs, there are two turning points, which divide the curves into three phrases. From the 0 V, the gain layer starts depletion at the beginning, and the $1/C^2$ is shown as a small flat value, while after the gain layer is fully depleted (V_{GL}), the $1/C^2$ increases, means the depletion of the substrate. The curves become flat again after the substrate is fully depleted (V_{FD}).

The I-V and C-V curves depend on both the gain layer and the substrate doping concentration. Therefore, they are compared together. The $1/C^2 - V$ curves of the devices with different p-well doses but the same substrate concentration is shown in Fig. 7.9 (a) and different substrate concentration but the same p-well dose is shown in Fig. 7.9 (b). We can see the p-well dose will influence the V_{GL} , and the substrate concentration will influence the V_{FD} . As discussed in Sec. 7.1.1, in order to have the LGAD operated at a possible lower bias and have the drift velocity saturated, the detector with small V_{GL} and V_{FD} is preferred. Thus the substrate with low concentration ($< 1 \times 10^{13} \text{ cm}^{-3}$) is considered for further simulation.

7.3.3 Optimization of the p-well (gain-layer)

The optimization of the gain layer is mainly done by the comparison of the C-V and I-V simulation for a relatively reasonable bias voltage for the operation. The optimization also considers the fabrication capability within the scope. Thus, the fabrication process-based simulation of the TCAD (*sprocess*) is used. The simulated devices' breakdown voltage with different p-well doses are shown in Fig. 7.10 (b). The depth of the p-well is fixed by the same implantation energy. We can see an almost linear relationship between the p-well dose and the breakdown voltage shown. The simulated relationship

7 Simulation and Fabrication of the USTC-IME LGADs for the HGTD Upgrade

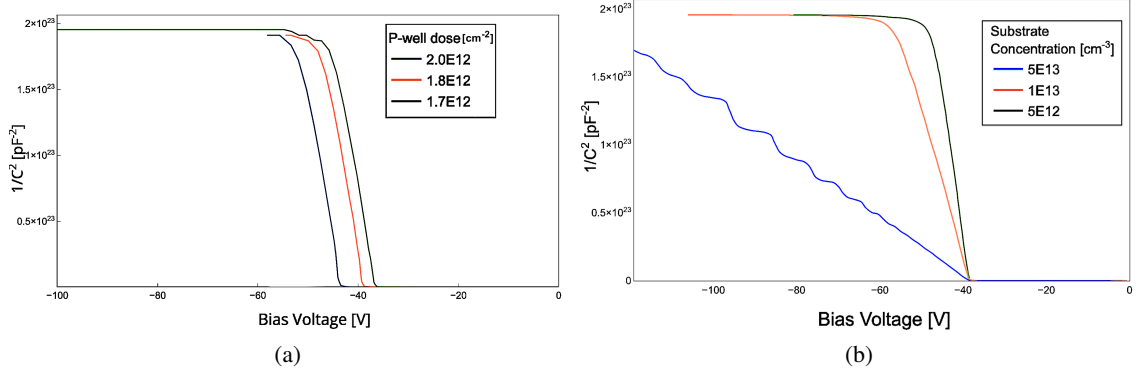


Figure 7.9: The $1/C^2 - V$ of the device with different p-well dose with the fixed substrate concentration and the $1/C^2 - V$ of the different substrate concentration but fixed p-well design.

between the gain and voltage is shown in Fig. 7.10 (a), from which we can see the moderate gain (10 to 20) is obtained with such gain layer. As discussed in Sec. 7.1.2, the LGAD needs to have a proper operating voltage both before and after the irradiation at -30°C , thus the model with the V_{BD} at 200 V is considered in the later simulation.

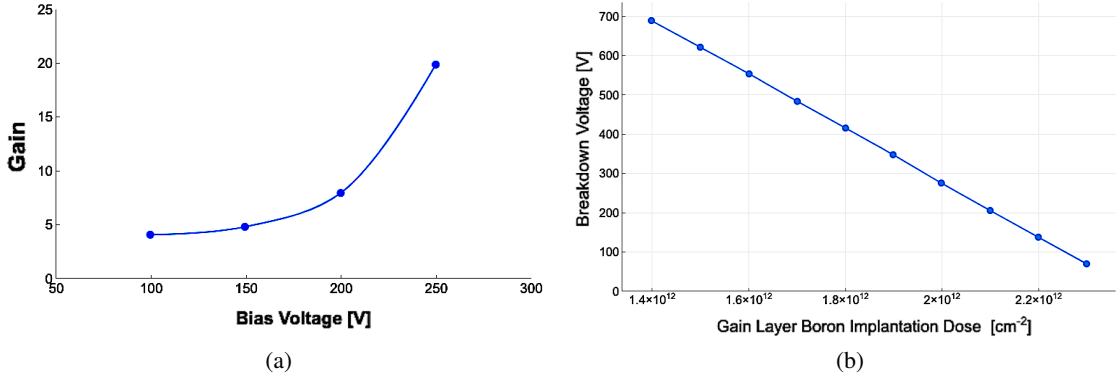


Figure 7.10: The optimization of the p-well and the gain as well as the V_{BD} dependence of the p-well doping. The 1000 keV implantation energy is used in the simulation.

7.3.4 Optimization of the guard-ring

Based on the discussions in Sec. 7.1.6, the guard ring is needed to collect the peripheral region current and signals. Its appearance could also need to be well treated due to the strong field in its n-type doing edge. The p-stop is also needed to be considered together since it needs to isolate the GR with the central pad. Thus, during the optimization of the guard ring, we also need to take the p-stop included in the equation. The simulated electric potential, electric field, and the current path with the guard ring floating are shown in Fig. 7.11 (a) and (c). The electric potential contours are also drawn.

7.3 Results from the TCAD simulation for the LGAD structures

We can see that in the peripheral region where the field is not uniform, the charge carriers are also drifted to and collected by the central pad without the grounded guard ring. After the guard ring is grounded, as shown in Fig. 7.11 (b) and (d), those charge carriers in the peripheral region are collected by the guard ring. Only the charge carrier in the central region where the electric field is uniform will be collected. The appearance of the p-stop between the guard ring and the central pad further isolated the two electrodes by creating a potential barrier between them, as expected. The detailed optimization of the p-stop will be introduced in the next section.

7 Simulation and Fabrication of the USTC-IME LGADs for the HGTD Upgrade

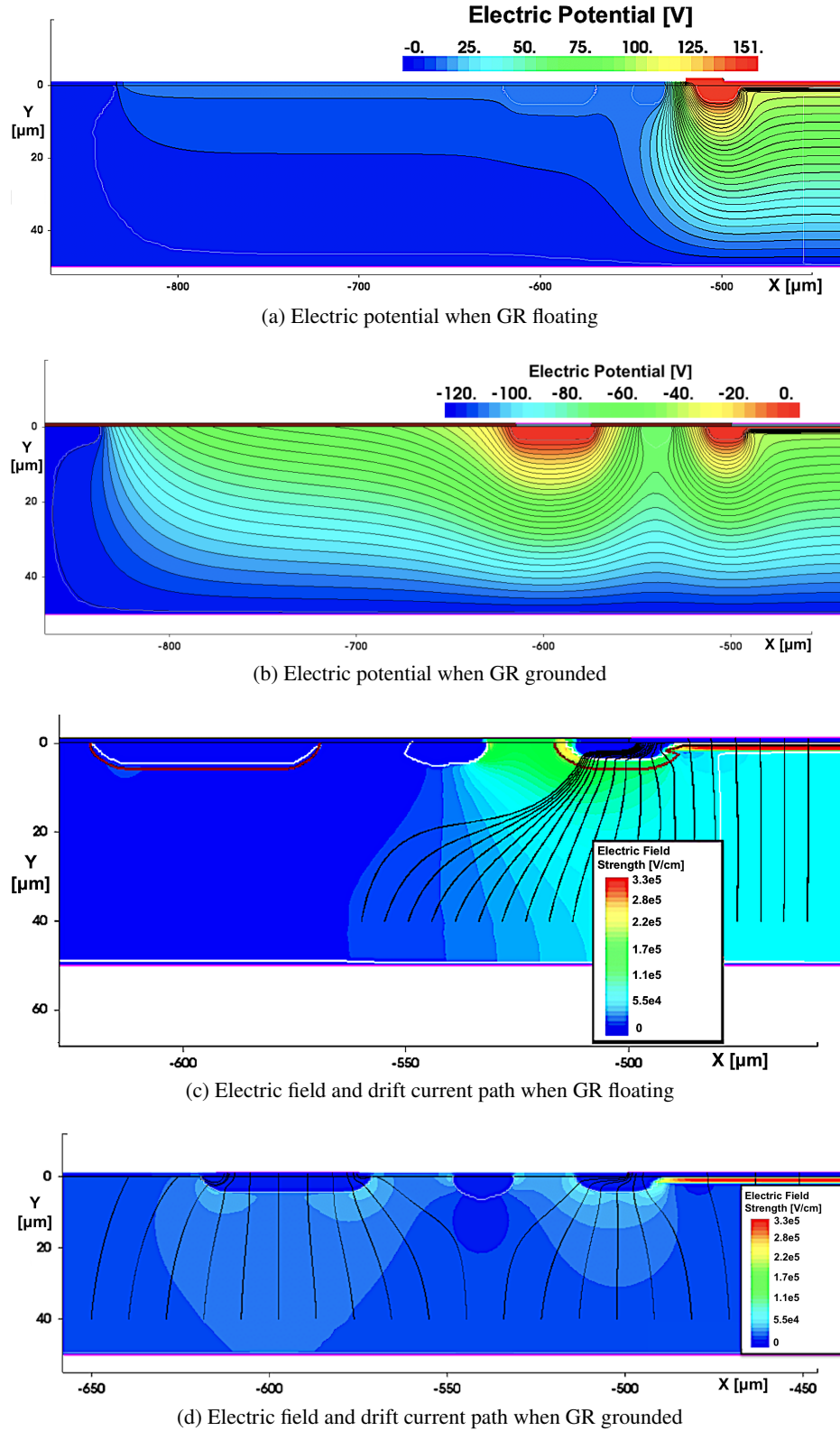


Figure 7.11: The optimization of the guard ring. The impact of floating or grounding the guard ring are shown in the figures. (a), (b) are the electric field strength distributions, and the (c), (d) are the current (charge carrier drift) paths, from which we can see without the guard ring grounded the signal and current in the peripheral region are collected by the guard ring without contributed to the central pad.

7.3.5 Optimization of the p-stop

The p-stop is designed to isolate the n-type electrodes, as discussed in Sec. 7.1.8. Thus to make sure the p-stop can isolate the two neighbor pads well, the number, the dose, and the width of the p-stop, as well as its position relative to the guard ring and the central pad edge, are studied. First, in order to guarantee the electron channel near the surface of silicon and oxide is isolated between two the guard ring and the central pad, the two p-stop design, as shown in Fig. 7.12, is simulated. The performance is evaluated and compared with the single p-stop design by the simulated electric field strength distribution and the current density distribution as shown in Fig. 7.13.

Number of the p-stops

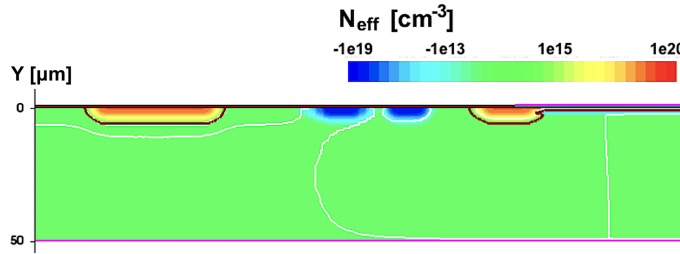


Figure 7.12: The two p-stop model is shown. Such a design can have stronger isolation for the guard ring and the central pad.

From the result, we can see that with the second p-stop added, the isolation of the peripheral region is too strong that the depletion region is constrained, and the region near the guard ring cannot be depleted. This will introduce a stronger field than the one p-stop case since the bias drops in a smaller range. Thus it recommends using the one p-stop in further optimization and design.

7 Simulation and Fabrication of the USTC-IME LGADs for the HGTD Upgrade

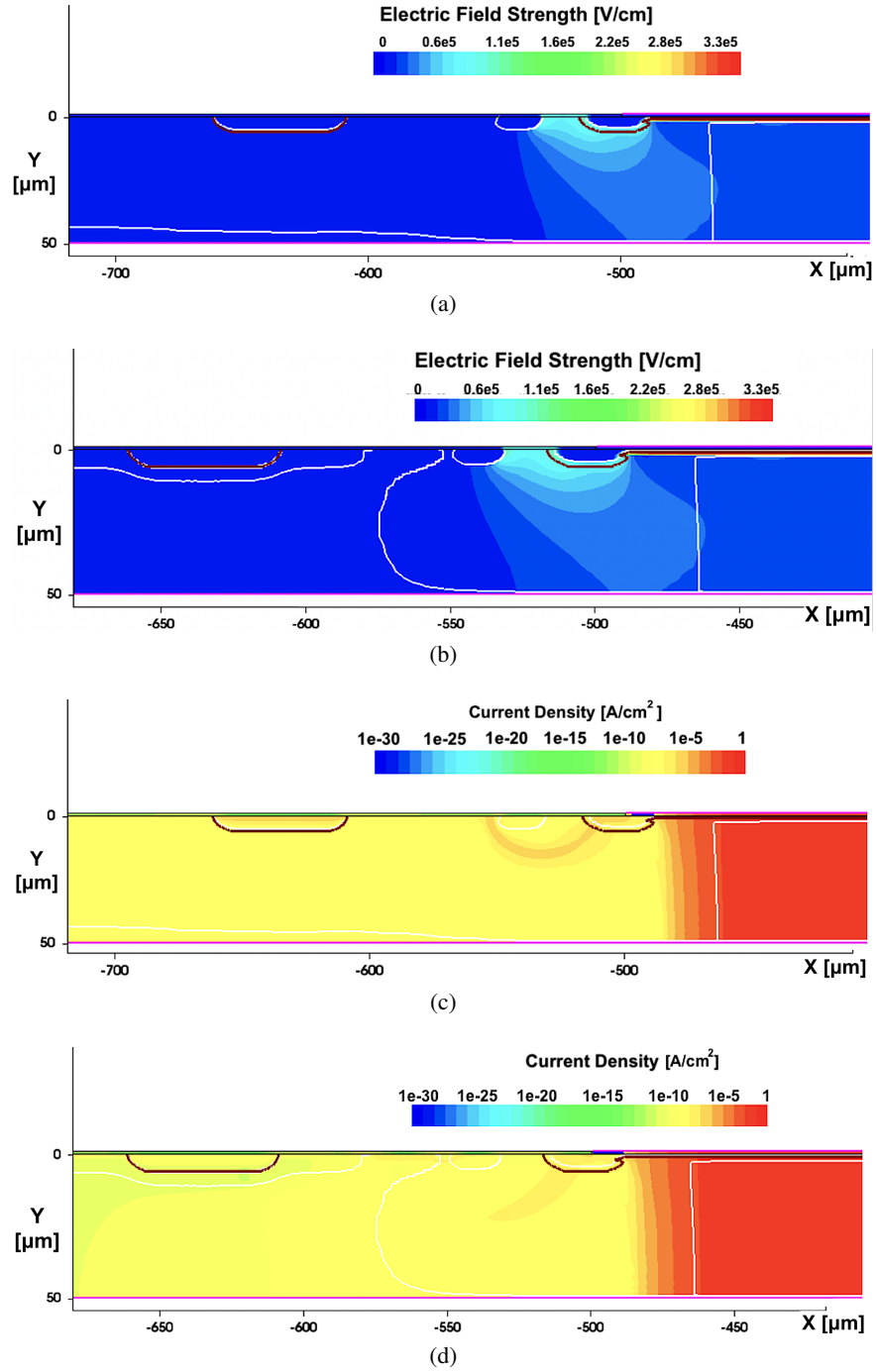


Figure 7.13: The comparison of the simulated results of the single p-stop (a), (c) and the dual p-stop (b), (d). The electric-field distributions are shown on the (a), (b), and the current density distributions are on the (c), (d).

Position of the p-stop

The position will influence the dropping rate of the potential towards the peripheral region, and the distance between the p-stop and the central pad (JTE) is studied. From the simulated electric field strength in Fig. 7.14, we can see with a longer distance between p-stop and JTE, the electric field strength is significantly smaller than the one with the shorter distance. The breakdown voltage is also compared for the two cases. In order to fulfill the 300 μm slim edge requirement, the space between the central pad and p-stop is further optimized in detail. Several layout with different p-stop, JTE distance $D_{\text{p-stop,JTE}}$ is designed and compared by the measured results.

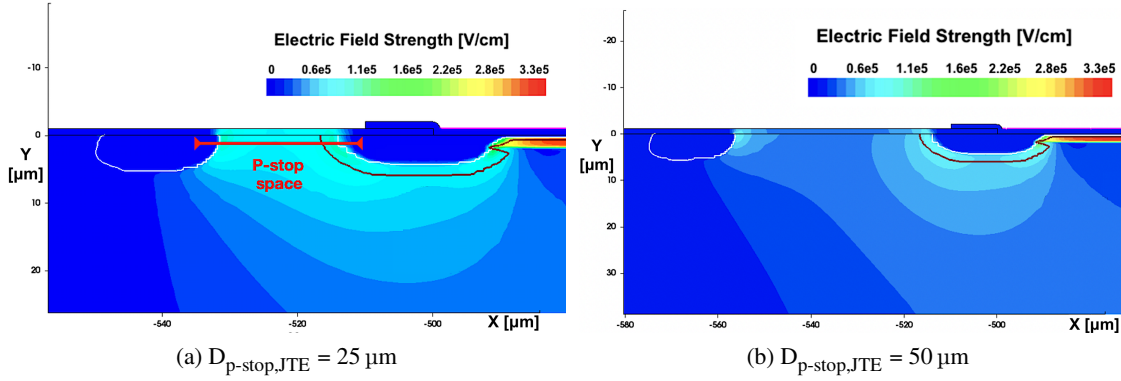


Figure 7.14: The comparison of the simulated results of the design of the p-stop with (a) 25 μm and (b) 50 μm distance to the JTE of the central pad.

7.3.6 Optimization of the field plate

The concept of the field plate is important for reducing the field strength at the edge as previous discussion in Sec. 7.1.5. It works by the field effect created together with the metal and the oxide. Thus, the length of the field plate: L_{FP} , and the thickness of the field oxide: t_{ox} are mainly considered in the optimization. The performances are evaluated by the distribution of the electric field strength. The simulated results are shown in Fig. 7.15 with L_{FP} to be 10 μm and 20 μm and the t_{ox} fixed at 0.5 μm .

7 Simulation and Fabrication of the USTC-IME LGADs for the HGTD Upgrade

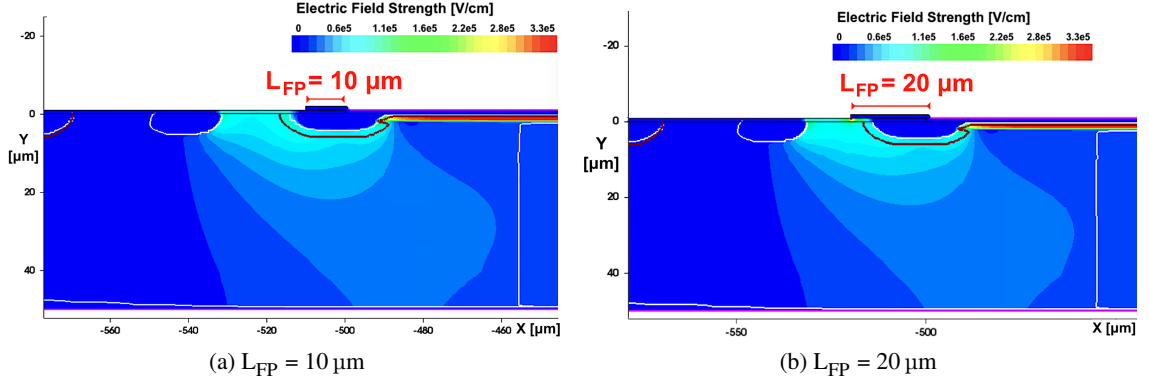


Figure 7.15: The comparison of the simulated results of the design on the field-plate with L_{FP} to be (a) $10 \mu\text{m}$ and (b) $20 \mu\text{m}$.

7.3.7 Optimization of the field plate of GR

Similar to the edge of the central pad, the grounded guard ring also needs the field plate to improve the high voltage tolerance of the field plate structure. Considering it has different n-type dose and neighbor structures, the field plate of the guard ring needs to be optimized separately. The device with the length of the guard ring field plate (L_{GRFP}) from $0 \mu\text{m}$ to $5 \mu\text{m}$, $10 \mu\text{m}$, $15 \mu\text{m}$ are simulated with bias and other structures being same. The corresponding electric field strength, as well as the electric potential contours, are shown in Fig. 7.16. With the increment of the L_{GRFP} from $0 \mu\text{m}$ to $5 \mu\text{m}$, the density of the electric potential contours gets uniform, and the distribution of the electric field strength gets flat. However, with the L_{GRFP} increasing from $5 \mu\text{m}$ to $15 \mu\text{m}$, we can clearly see that the electric potential contours are concentrated at the edges of the field plate where the electric field gets stronger. Thus there should be an optimal value of the field plate length.

7.3 Results from the TCAD simulation for the LGAD structures

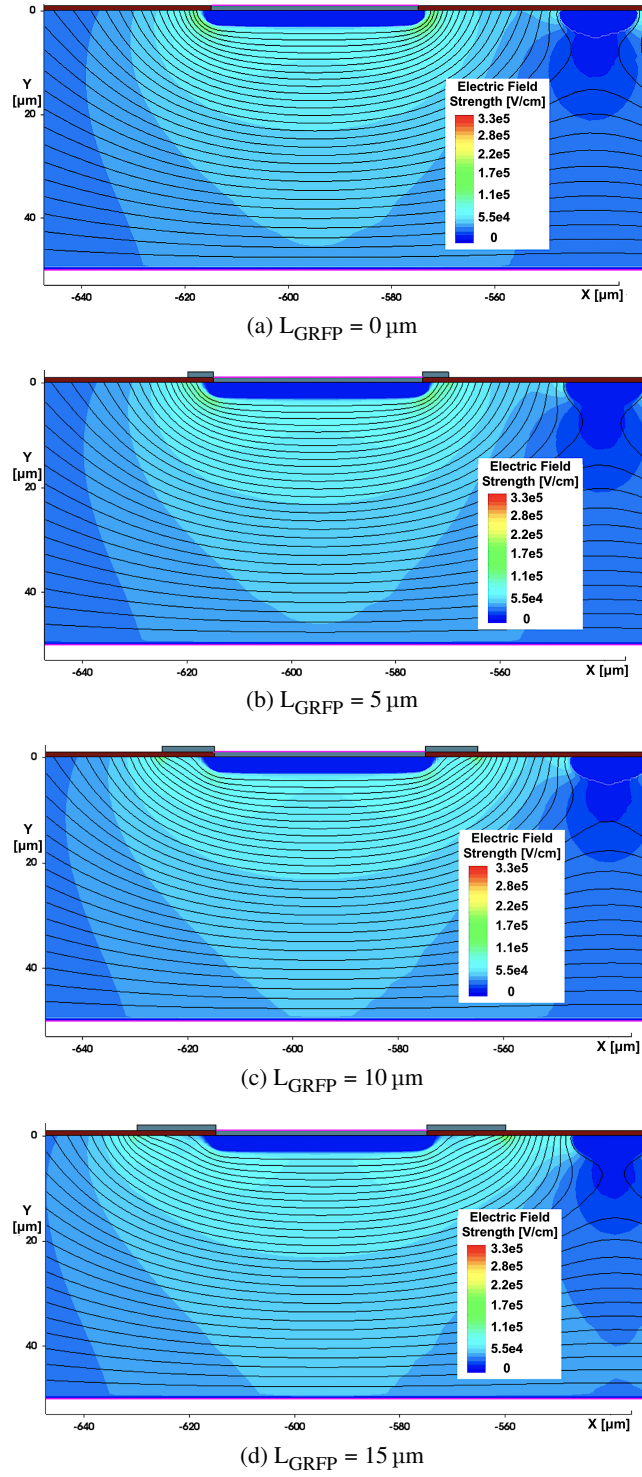


Figure 7.16: The comparison of the simulated results of the design on the field-plate for the guard ring with L_{GRFP} to be (a) 0, (b) $5 \mu\text{m}$, (c) $10 \mu\text{m}$, and (d) $15 \mu\text{m}$.

7 Simulation and Fabrication of the USTC-IME LGADs for the HGTD Upgrade

For the purpose of finding the optimal value, several scans have been performed with the L_{GRFP} varies from 0 to 30 μm and the V_{BD} are calculated and compared in order to check the HV tolerance of the peripheral region's surface, both the nominal dose ($1.8 \times 10^{12} \text{ cm}^{-2}$) and a lower dose ($1.4 \times 10^{12} \text{ cm}^{-2}$) are simulated. The total leakage current with the threshold $5 \times 10^{-8} \text{ A}$ and the ion avalanche coefficient integral are used separately to determine the breakdown for comparison.

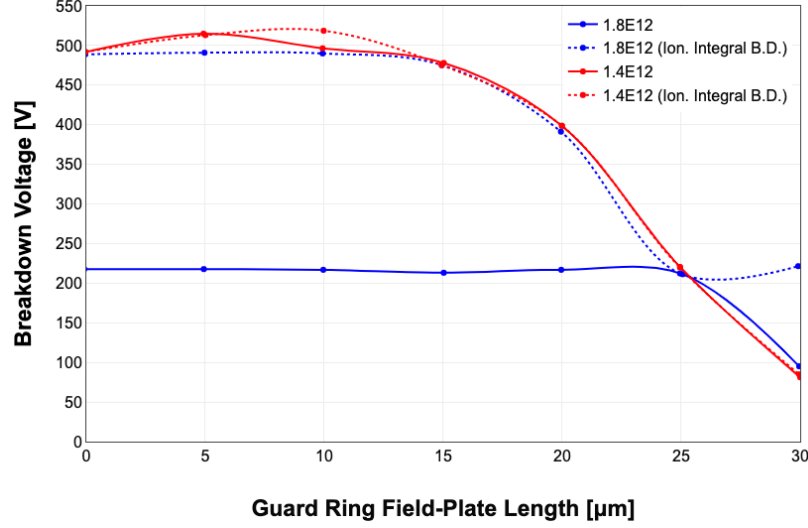


Figure 7.17: The validation of the optimized structure dimensions by a scan for the V_{BD} .

The results are shown in Fig. 7.17. For the nominal dose ($1.8 \times 10^{12} \text{ cm}^{-2}$) the V_{BD} of the leakage current remains flat when the L_{GRFP} is less than 25 μm , indicated that the breakdown is dominated by the gain layer avalanche in the central region. When the dose of the gain layer is reduced to ($1.5 \times 10^{12} \text{ cm}^{-2}$), the V_{BD} starts rising with the L_{GRFP} from 0 to around 10 μm , means the breakdown is dominated by the peripheral region. The V_{BD} drops fast in the range of 15 to 30 μm , indicating that larger L_{GRFP} would cause the strong local field as expected and shown in Fig. 7.16 (d). Both the V_{BD} by the leakage current and ion avalanche coefficient integral show that an optimal L_{GRFP} in such design is expected to be around 10 μm . Therefore, the 10 μm is considered to be the baseline design, and the layouts with other L_{GRFP} are also designed as a comparison and candidate in the fabrication since the simulation parameters could deviate from the fabrication quality.

The zoomed view on the edge of the guard ring field plate with $L_{\text{GRFP}} = 10 \mu\text{m}$ is shown in Fig. 7.18. The oxide layer is shown in the surface with Y from 0 to $-1 \mu\text{m}$. We can see the field near the edge is redistributed to be flatter, and no significant local strong electric field region is observed inside the silicon.

7.3 Results from the TCAD simulation for the LGAD structures

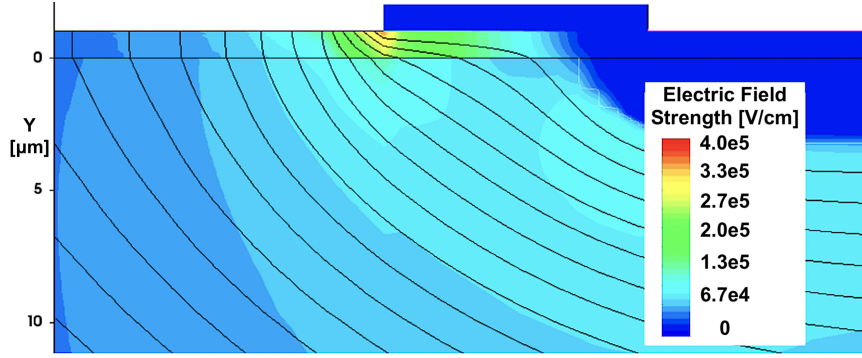


Figure 7.18: The zoomed electric field strength and potential contours for the $L_{\text{GRFP}} = 10 \mu\text{m}$ design is shown. We can see a smoother field at the edge of the guard ring with the GRFP introduced.

7.3.8 Optimization of the floating GR

The floating GR (FGR) has the capability to re-shape the depletion region at the edge and reduce the rate of the potential drop at the surface as discussed in Sec. 7.1.7 and illustrated in Fig. 7.19 (a). Therefore it is considered for the LGAD design to improve the HV tolerance after the radiation, as shown in Fig. 7.19 (b). The simulation result shows a smoother electric potential distribution in Fig. 7.20. The device with one FGR is considered the baseline design, and the devices with one, two, or zero FGRs are fabricated for comparison.

Though the FGR can make the electric field near the surface to be smoother, it introduces the non-negligible extension of the sensor edge. This conflicts with the requirement of the HGTD to have a compact slim edge design. Therefore the FGR has to be both necessary for the improvement and also be as small as possible. In the beginning, to ensure the design is robust and reduce the risk of production, the baseline includes the float GR in the layout with a larger slim edge distance, and a few layouts without float GR design is also produced. While for the later fabrication, most of the layout removed the floating GR, and details will be discussed in Chapter 8.

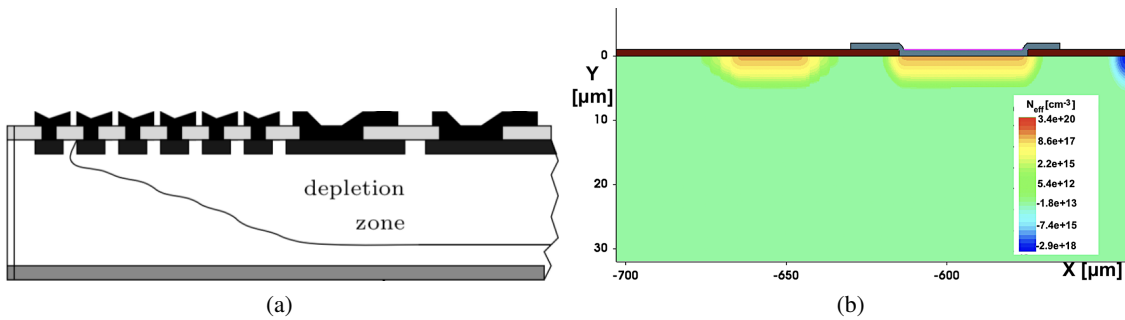


Figure 7.19: The structure of the floating guard ring for smoothing the potential drop in the peripheral region (a) [189] and the implementation for the TCAD model of the LGAD is shown in (b).

7 Simulation and Fabrication of the USTC-IME LGADs for the HGTD Upgrade

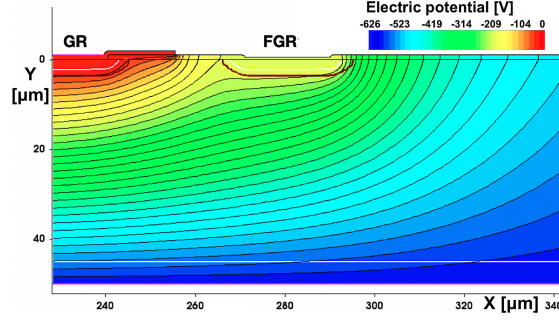


Figure 7.20: The comparison of the simulated electric potential with one float guard ring added at the outside of the guard ring. We can see that the electric-potential drop is shared by the added guard ring and mitigated the forthcoming of the local strong electric field.

7.3.9 Inter-pad gap for the 2×2 array

In the final HGTD application, the LGADs need to be placed into 15×15 arrays for each sensor. The isolation of the pads is also important. The sensor is required to both have a good isolation quality and have as small an inefficient region as possible. The requirement for the inter-pad gap isolation is to have inter-pad resistance larger above $1 \text{ G}\Omega$ and the measured inter-pad distance less than $100 \mu\text{m}$ before irradiation.

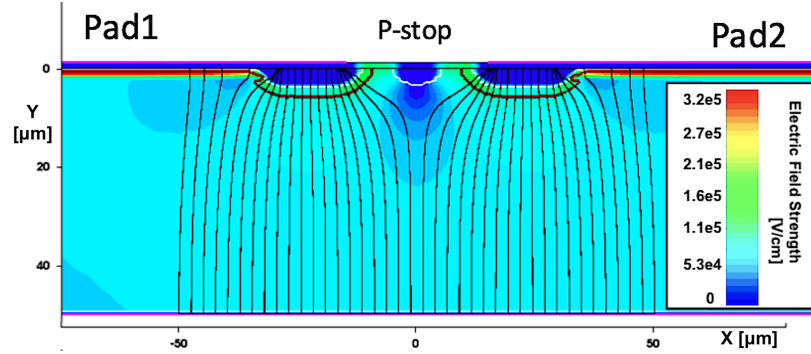


Figure 7.21: The simulated inter-pad gap design for the large array with $D_{\text{IP}} = 50 \mu\text{m}$.

Similar to the isolation used for the pad and guard ring, the p-stop is also considered in the inter-pad gap design. The isolation quality mainly relies on the dose and the width of the p-stop. The distance of the inter-pad gap is dominated by the size of the JTE. Thus a split of the inter-pad gap design with these parameters to be different is simulated and fabricated for comparison. The inter-pad design simulation proceeds on an LGAD model with two pads placed symmetric, and the full structures are simulated. Fig. 7.21 shows the simulation of the electric field strength and the electric field lines, which are roughly identical to the drift path of the charge carriers. We can see a significant amount of the field lines end at the JTE where the electrons will not be multiplied. There are four splits designed with the inter-pad gap distance: D_{IP} to be $30 \mu\text{m}$, $50 \mu\text{m}$, $70 \mu\text{m}$, $90 \mu\text{m}$. The 2×2 and 5×5 arrays with different D_{IP} is fabricated for the comparison.

7.3.10 Conclusion and design for prototype production

Based on the TCAD *sprocess* and *sdevice* EDA simulation software, the structures of the LGAD device have been modeled and simulated. The preliminary optimized design has been achieved. The finalized and converged model is shown in Fig. 7.22 (a) for production. The electric potential, electric field strength, as well as current density with this design are simulated and shown in Fig. 7.22 (b) (c) (d). The peripheral region's HV tolerance is further validated by the scan of the p-well dose (shown in Fig. 7.23), and in the lower dose, the peripheral region breakdown starts. The 500 V breakdown voltage is obtained in the low p-well dose, which guarantees a safe operating voltage of the device before and after the low fluences of radiation.

7 Simulation and Fabrication of the USTC-IME LGADs for the HGTD Upgrade

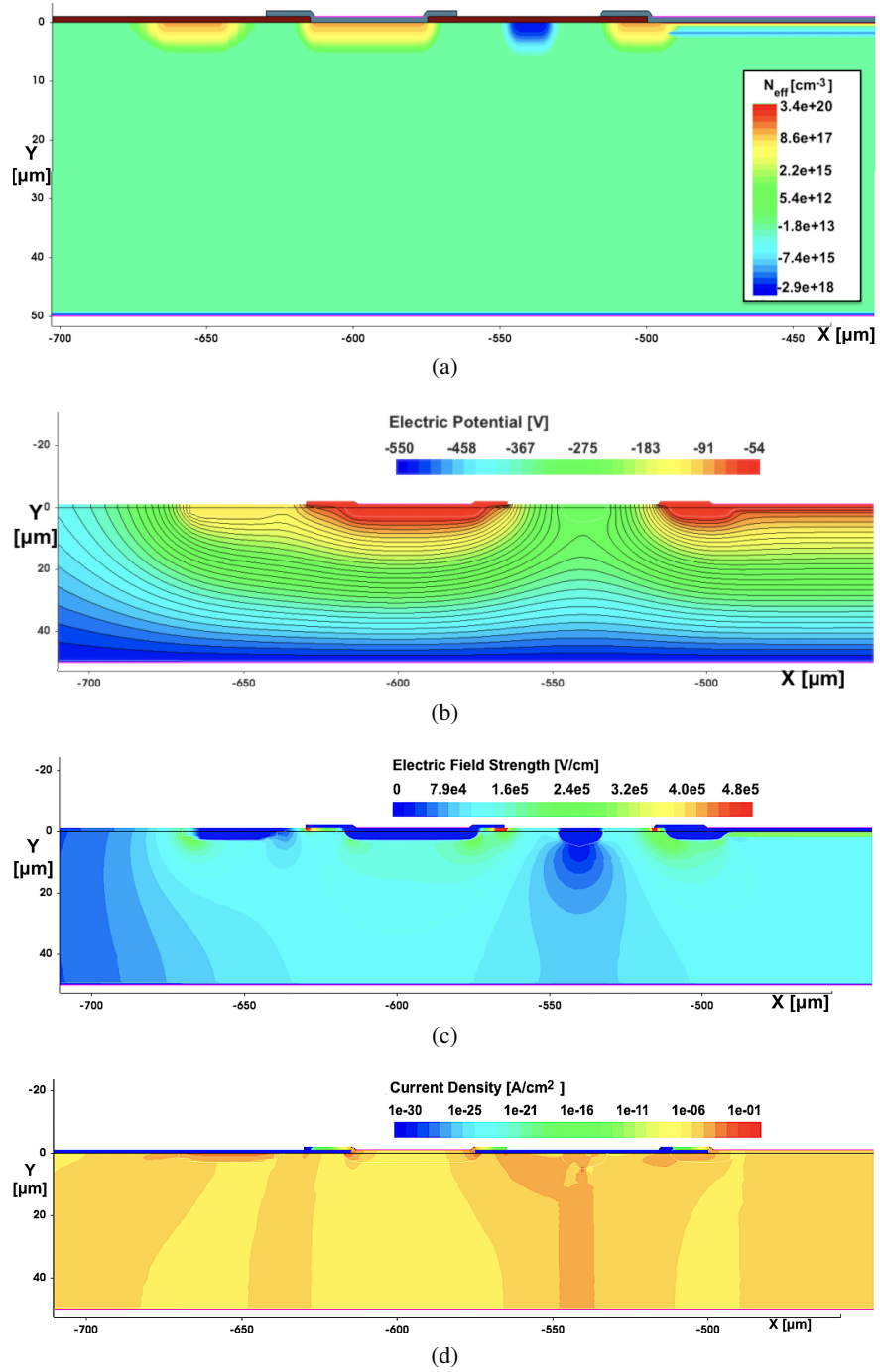


Figure 7.22: The finalized and the converged model based on the above simulation for the mask design of the fabrication.

7.3 Results from the TCAD simulation for the LGAD structures

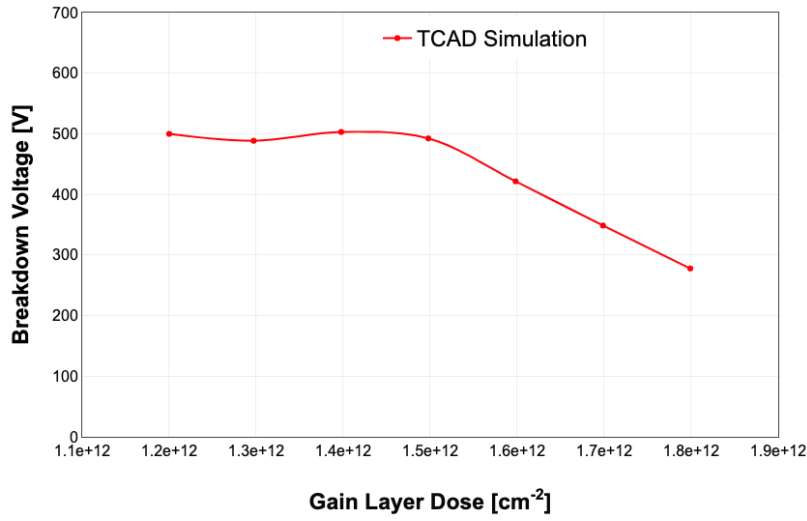


Figure 7.23: The simulated V_{BD} at different p-well dose for the validation of the peripheral design. In the region where the dose is low, the V_{BD} keeping constant means the breakdown is dominated by the peripheral region. When the dose is higher than $1.5 \times 10^{12} \text{ cm}^{-2}$, the V_{BD} gets lower, which means the breakdown is dominated by the central pads.

7 Simulation and Fabrication of the USTC-IME LGADs for the HGTD Upgrade

The I-V is shown in Fig. 7.24 (a) where the breakdown voltage in 200 to 270 V with the different gain layer design. The C-V is shown in Fig. 7.24 (b) where V_{GL} in 35 to 70 V is expected. Based on the optimized TCAD model, the eight layers' photolithographic layout is made by the *layout* software. The baseline design layout for the single pad and 2×2 devices and shown in Fig. 7.25. The detailed description of the fabrication is shown in Sec. 7.4, 7.5, and 7.6.

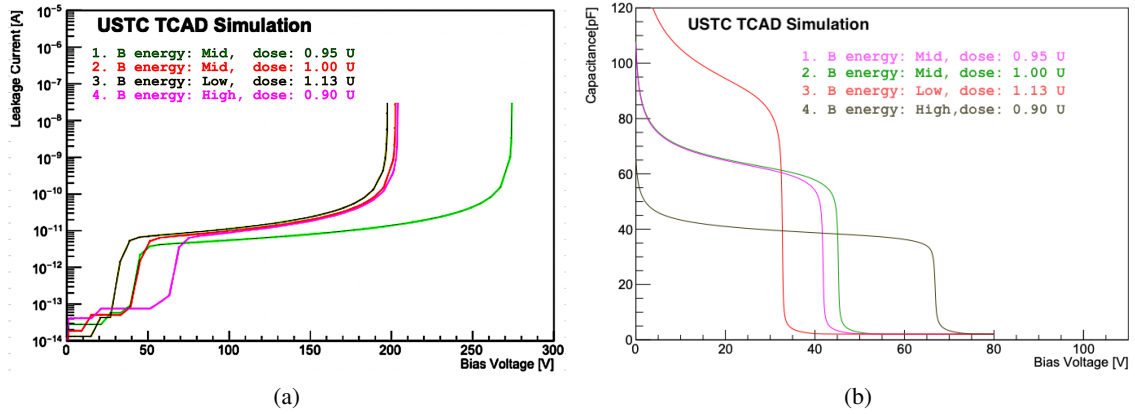


Figure 7.24: The simulated I-V and C-V curves are based on the finalized models with splits of gain layer design. The energy and the dose of the gain layer are shown in the legend of the figure. The doses are shown by the arbitrary unit with the split-2 as 1.0 U.

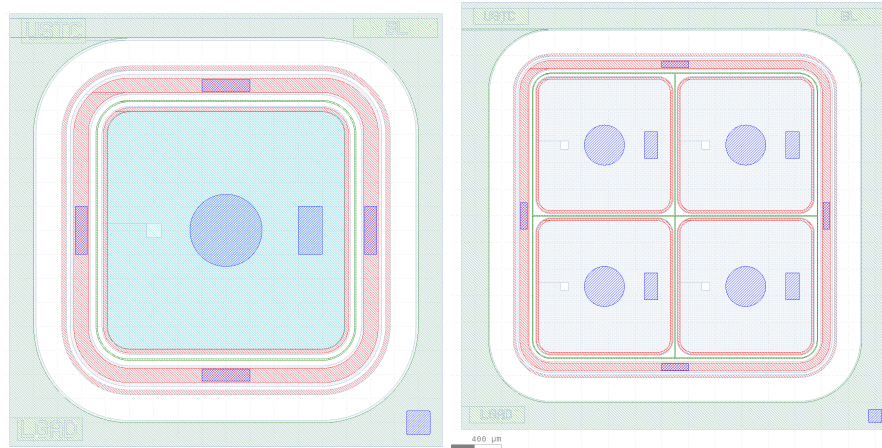


Figure 7.25: The designed layout of the 1×1 and 2×2 used in the first batch production of the USTC-IME LGADs.

7.4 USTC-IME 1st batch fabrication

The first batch of USTC-IME LGAD is fabricated with the 8-inch wafers and the reticle with the size of 40 mm \times 40 mm. The wafers are fabricated at the Institute of Microelectronics of the Chinese

Academy of Sciences (IME) [226], which possess an 8-inch fabrication line with high standard and good yield. Dedicated processes are developed for the LGAD production at IME based on the simulation results.

7.4.1 Fabrication process preparation

The fabrication process recipe (shown in Tab. 7.1) for the USTC-IME first batch consists of multiple steps. The process begins with the creation of a thin field oxide layer (Step 1) and the first photolithography step (Step 2). This is followed by an oxidation process as a screen for protection (Step 3) and a second photolithography step (Step 4). Implantations are performed with different species and energies (Steps 5, 7, and 10), with photolithography steps in between (Steps 6, 9, and 11). The device undergoes high-energy implantation (Step 12) and spike annealing at high temperatures for a short time (Step 13). A multi-layer oxidation process is carried out (Step 14), followed by a reflow step (Step 15) and another photolithography step (Step 16). Aluminum is sputtered at a thickness of 1 μm (Step 17), followed by photolithography (Step 18) and wet etching (Step 19). The pad is passivated (Step 20) before another photolithography step (Step 21) and etching (Step 22). Backside processes include aluminum sputtering (Step 23), photolithography (Step 24), and dry etching (Step 25). The schematic demonstrations of the main steps in the designed fabrication processes can be found in Fig. 7.26.

7 Simulation and Fabrication of the USTC-IME LGADs for the HGTD Upgrade

Table 7.1: The designed fabrication process recipe with the main processes based on the simulation for the USTC-IME first batch.

No.	Process Description V1 and Device Menu Group
1	Field Oxide, thin thickness
2	Photolithography 1 - FO
3	Oxidation (screen)
4	Photolithography 2 - JTE
5	Implantation - P- low energy, high dose
6	Photolithography 3 - C-STOP/P-STOP
7	Implantation - B- low energy, high dose
8	Annealing - high temperature, long time
9	Photolithography 4 - N+
10	Implantation - P-low energy, high dose
11	Photolithography 5 - P-WELL
12	Implantation - B-high energy, low dose
13	Spike Annealing - high temperature, short time
14	Oxidation few μm
15	Reflow
16	Photolithography 6 - contact
17	Sputtering Aluminum - 1 μm
18	Photolithography 7 - metal
19	Wet Etching Aluminum
20	Pad Passivation
21	Photolithography 8 - pad
22	Etching
23	Backside Sputtering Aluminum
24	Backside Photolithography 9 - back metal
25	Backside Dry Etching

7.4 USTC-IME 1st batch fabrication

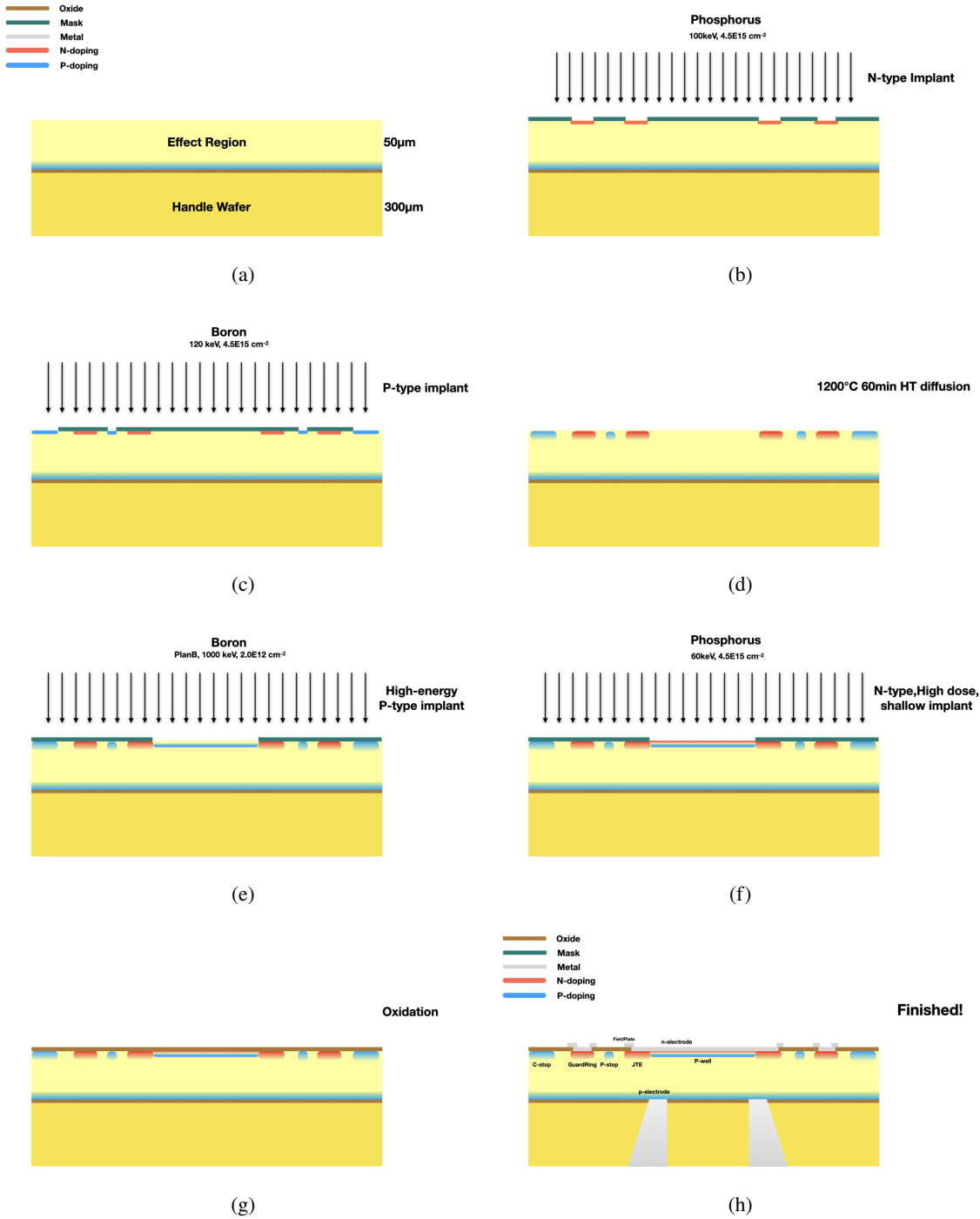


Figure 7.26: The schematic view for illustration of the processes in the LGAD fabrication with the 50 μm thickness silicon wafer.

7.4.2 Mask preparation

To carry out the fabrication process of the LGAD detectors at IME, a set of devices layout has been designed with eight photolithographic layers of masks, which allow the integration of a few different designs distributed equally in each processed wafer on a 40 mm by 40 mm size reticle, as the iteration and optimization and fully utilize the area of the wafer for studying the devices with different layouts. The process minimum line width is 2 μm , which makes this a low-risk photolithographic process in which a displacement of a few microns in the alignment of a mask does not introduce any significant variation in the functionality of the manufactured device, this is achieved by the overlay of the sensitive region towards the safe direction. All masks are applied on the same side of the wafer (epitaxial layer) to reduce the cost of fabrication.

The eight layers of photolithographic masks used in the fabrication of the USTC-IME first batch LGAD are shown in Tab. 7.2. The process starts with the “First Oxide” layer, which forms the initial oxidation layer: “FO”. The second layer, called “JTE” involves n-type implantation and high-temperature diffusion, aligning with the FO layer. The “PSTOP” layer, which is the third layer, also aligns with the First Oxide layer and consists of p-type implantation and high-temperature diffusion. The fourth layer, “NPLUS” is designed for Ohmic contact and consists of n-type high-dose shallow implantation, aligning with the FO layer as well.

Table 7.2: Description of the eight layers of photolithographic mask used to fabricate the USTC-IME first batch LGAD

Mask Name	No.	Data Area Tone	Process Description
FO	1	Clear	First oxidation layer (field oxide)
JTE	2	Clear	n-type implantation + high temperature diffusion
PSTOP	3	Clear	p-type implantation + high temperature diffusion
NPLUS	4	Clear	n-type high-dose shallow implantation for Ohmic contact
PWELL	5	Clear	High-energy p-type implantation
CONT	6	Clear	Thickening field oxide, window for electrode
METAL	7	Dark	Aluminum deposition for electric field and field plate
PASS	8	Clear	Surface passivation window

The fifth layer, “PWELL”, involves high-energy p-type implantation and aligns with the First Oxide layer. The “CONT” layer, which is the sixth layer, aligns with the First Oxide layer and serves to thicken the field oxide while providing a window for the electrode. The seventh layer, “METAL” defines the area being kept in the etching of the deposited aluminum for the electric field and field plate, aligning with the CONT layer. Lastly, the “PASS” layer serves as the surface passivation window and aligns with the METAL layer. Each of these layers contributes to the precise fabrication process of the LGAD device. The mask of the baseline single pad LGADs with these eight layers is shown in Fig. 7.27 and Fig. 7.28.

7.4 USTC-IME 1st batch fabrication

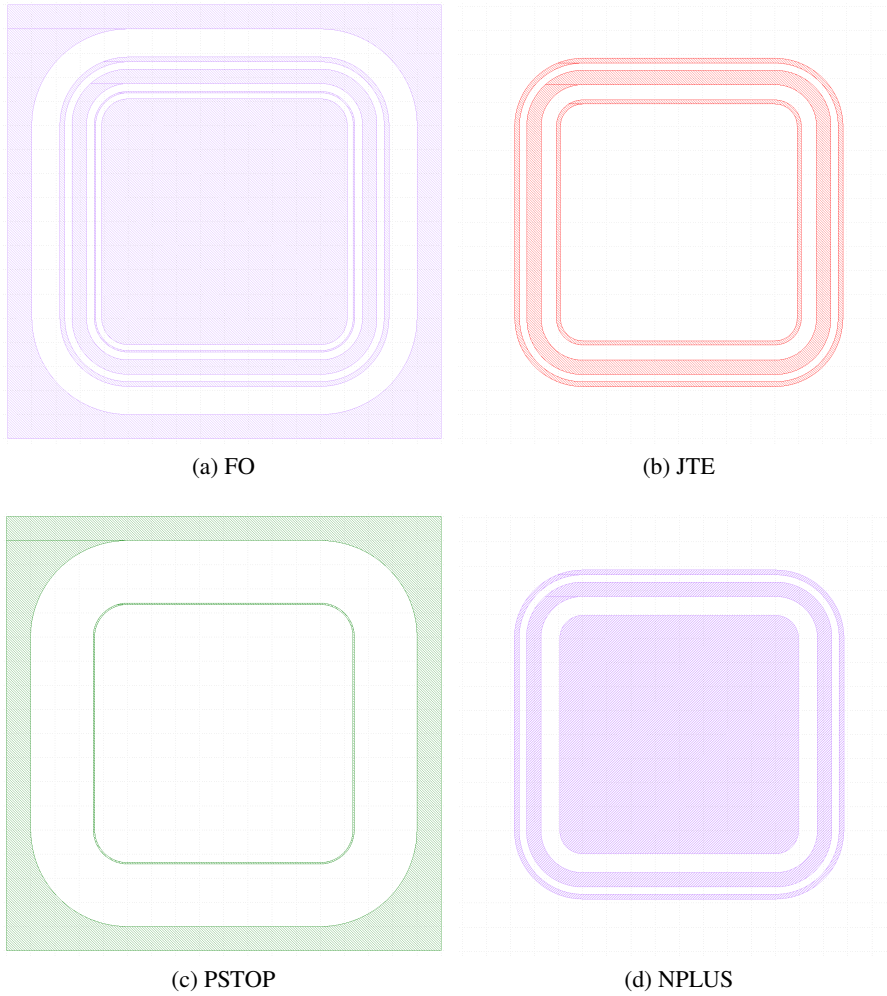


Figure 7.27: The layer 1-4 (FO, JTE, PSTOP, NPLUS) of the designed 1×1 LGAD used in the first batch production of the USTC-IME LGADs.

7 Simulation and Fabrication of the USTC-IME LGADs for the HGTD Upgrade

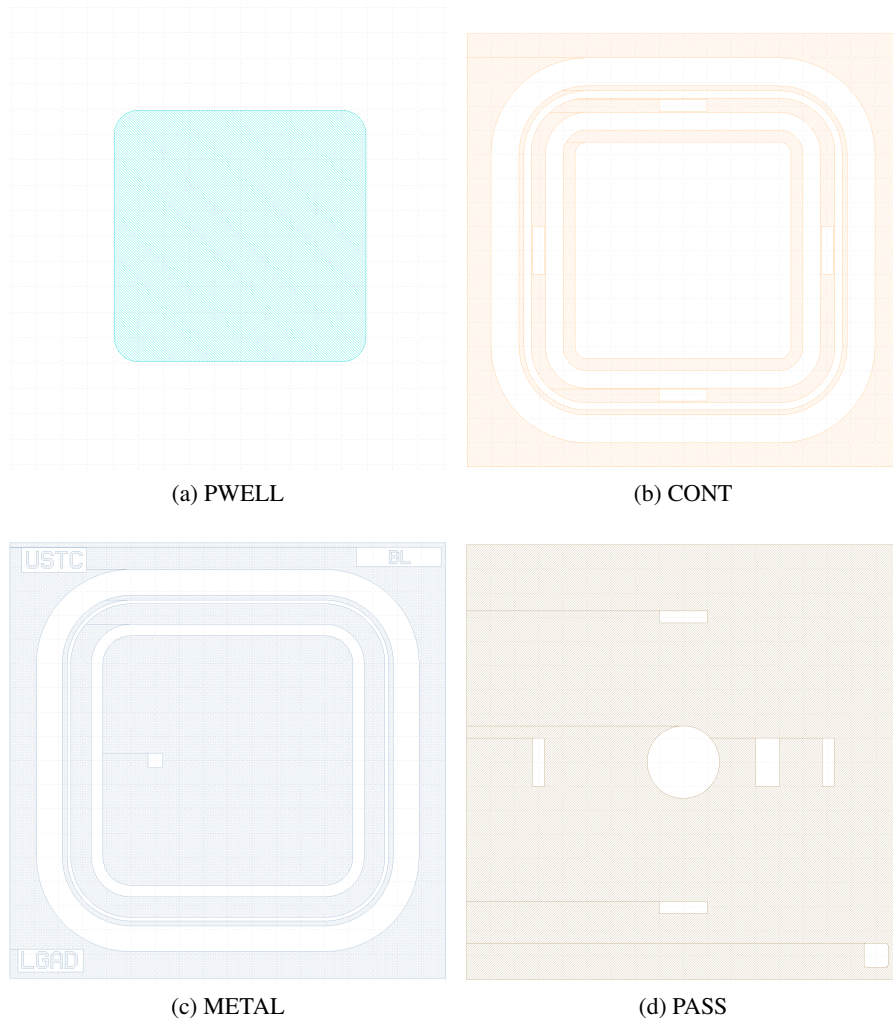


Figure 7.28: The layer 5-8 (PWELL, CONT, METAL, PASS) of the designed 1×1 LGAD used in the first batch production of the USTC-IME LGADs.

7.4 USTC-IME 1st batch fabrication

The USTC-IME first batch production reticles (as shown in Fig. 7.29) consist of 81 LGAD devices with a wide range of layouts, sizes, and designs with the array of 1×1 , 2×2 (shown in Fig. 7.30), 5×5 and 15×15 (shown in Fig. 7.31). These devices are designed to explore the impact of various parameters on LGAD performance through the following modifications:

- Field plate lengths: The batch features devices with different field plate lengths, including those with no field plate, and lengths of 3, 8, and 10 μm , allowing for the study of the impact of field plate geometry on device performance, electric field distribution, and breakdown voltage.
- Floating guard ring configurations: The devices offer a wide range of floating guard ring options, from designs without floating guard rings to those with one, two, three, or four floating guard rings. Some of these configurations also feature slim designs, which provide insights into the effect of guard ring size on edge sensitivity, charge sharing, and electric field distribution near the detector's edge.
- Slim edge variations: Devices in the batch come with different slim edge sizes, including 100, 200, and 500 μm slim edges, labeled as SE1, SE2 and SE5. The slim edge can affect the HV tolerance, the leakage current, and electric field homogeneity near the detector's boundary.
- Inter-pad gap variations: Devices in the batch come with different inter-pad gap distances, including 30, 50, and 90 μm , labeled as IP3, IP5 and IP9. The inter-pad gap distances can affect the inter-pad isolation, including cross-talk, inter-pad capacitance, and resistance.
- Guard ring width variations: Devices in the batch come with different guard ring widths, including 20, 40, 80, and 100 μm widths, which can affect the HV tolerance, the leakage current, and the noise level in the central pad.
- p-stop position variations: Devices in the batch come with different spaces between p-stop and the JTE, including 22, 30, and 35 μm , which can affect the breakdown voltage and isolation quality between the central pad and GR.
- p-stop width variations: Devices in the batch come with different p-stop widths, including 5, 6, 7, and 8 μm , which can affect the inter pad isolation quality between the central pads and between the central pad and GR.

The devices include a variety of other design features, including passivation, contact, and metalization variations. Those features provide insights into the optimization of device performance, including charge collection efficiency, noise performance, and the trade-offs between different design parameters.

Several auxiliary structures (shown in Fig. 7.32) are also implemented in case of failure analysis for the problematic wafers and control the fabrication quality. Few structures with fine pixels, strips, and AC-LGADs are placed for the novel structure research.

- Metal mesh and ring structures: The batch includes devices with metal mesh and metal ring structures, investigating various geometries to optimize performance by affecting charge collection, electric field distribution, and the impact of metal coverage on the detector's surface.

7 Simulation and Fabrication of the USTC-IME LGADs for the HGTD Upgrade

- Schottky diode designs: The batch includes Schottky diode designs with and without N doping, available in 2.5×2.5 and 0.5×0.5 mm² sizes. These designs provide insights into the role of doping and size in the performance of Schottky diodes, including leakage current, reverse bias breakdown voltage, and junction capacitance.
- PIN diodes: Several devices in the batch incorporate PIN diodes, which have no gain and may offer better radiation hardness. These designs enable the comparison of PIN diode performance with LGADs, in terms of signal response, noise characteristics, and radiation tolerance.
- AC-coupled LGADs: A subset of designs explores the use of AC-coupled LGADs with different resist and dielectric configurations, including options with n-plus or JTE resist and passivation or first oxide dielectric layers. These variations enable the study of the impact of AC coupling on the performance of LGADs, including signal shaping, charge collection efficiency, and radiation hardness.

This batch's wide variety of designs allows for a comprehensive investigation of LGAD properties and performance characteristics. The results from these devices will provide valuable insights for further optimization of LGAD designs, aiding in the development of high-performance detectors for a wide range of particle detection applications.

As for the detailed layout, we describe the device layouts with their respective device IDs. For 1×1 mm² devices, we have a variety of configurations, including different GR widths (GRW20, GRW40, GRW80, GRW100), Pstop spaces (PSSP22, PSSP30, PSSP35), Pstop widths (PSW5, PSW7, PSW8), field plate lengths (FPL3, FPL8, FPL10), floating guard ring (NFGR0, NFGR2, NFGR3), and others like MPASS, BLRD, and BL.

For 2×2 mm² devices, we have baseline (BL) designs with different inte-pad gap distances (IP3, IP5, IP9), slim edge configurations (SE1, SE2, SE5), number of floating guard rings (SE5NFGR1S, SE5NFGR2, SE5NFGR2S, SE5NFGR3, SE5NFGR3S, SE5NFGR4S), and other configurations like MMESH, MRING, PIX_AC1_NP_FO, PIX_AC2_JT_PS, and BL_LGPIN.

For 3×3 mm² devices, we have three different pixel configurations: PIX_LG, PIX_LGFL, and PIX_FLSG. Lastly, for the 3×3 mm² devices, we have a PIN design, UBM design, and a design with no metal and UBM (NM_UBM).

7.4 USTC-IME 1st batch fabrication

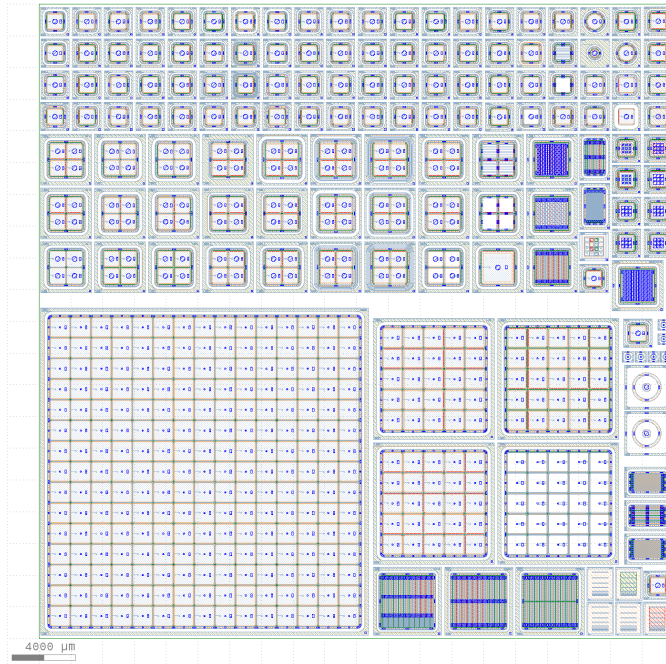


Figure 7.29: The designed layout of the reticle to be used in the first batch production of the USTC-IME LGADs.

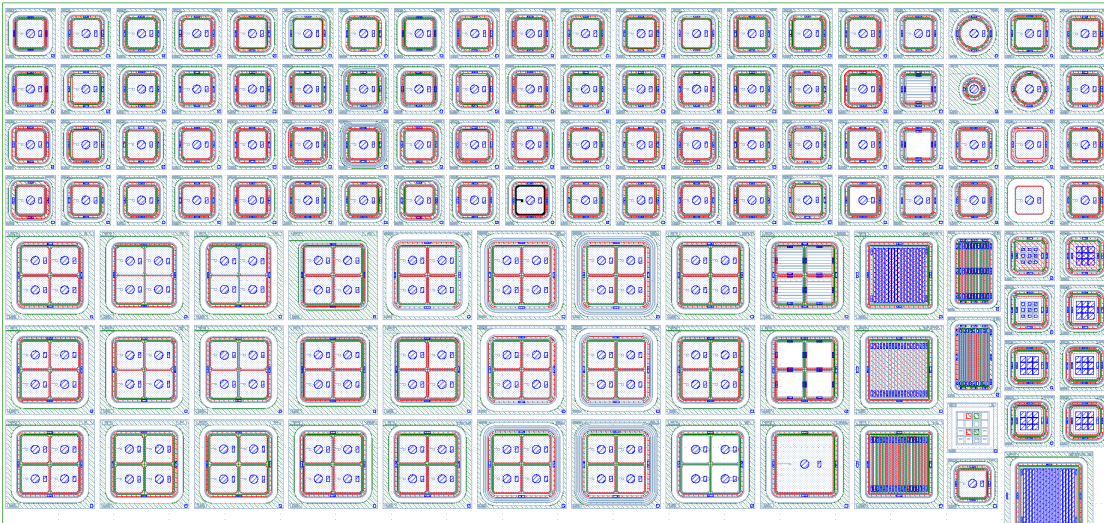


Figure 7.30: The 1×1 and 2×2 LGADs layout with different geometry parameters used in the first batch production of the USTC-IME LGADs.

7 Simulation and Fabrication of the USTC-IME LGADs for the HGTD Upgrade

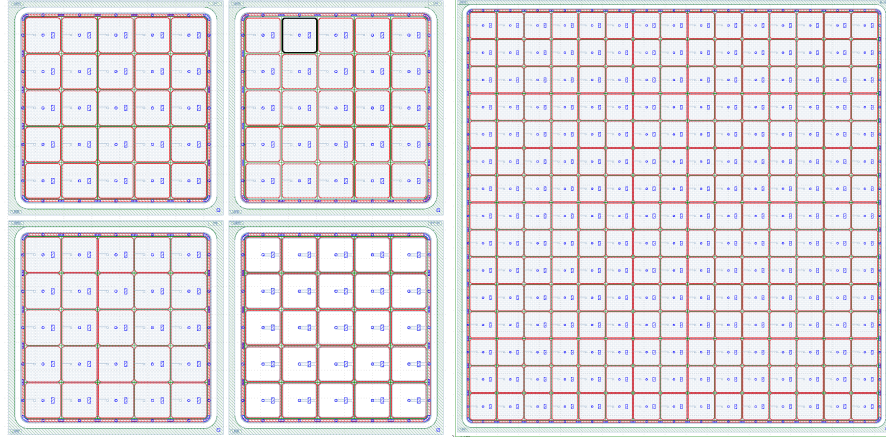


Figure 7.31: The designed layout of the 5×5 and 15×15 used in the first batch production of the USTC-IME LGADs.

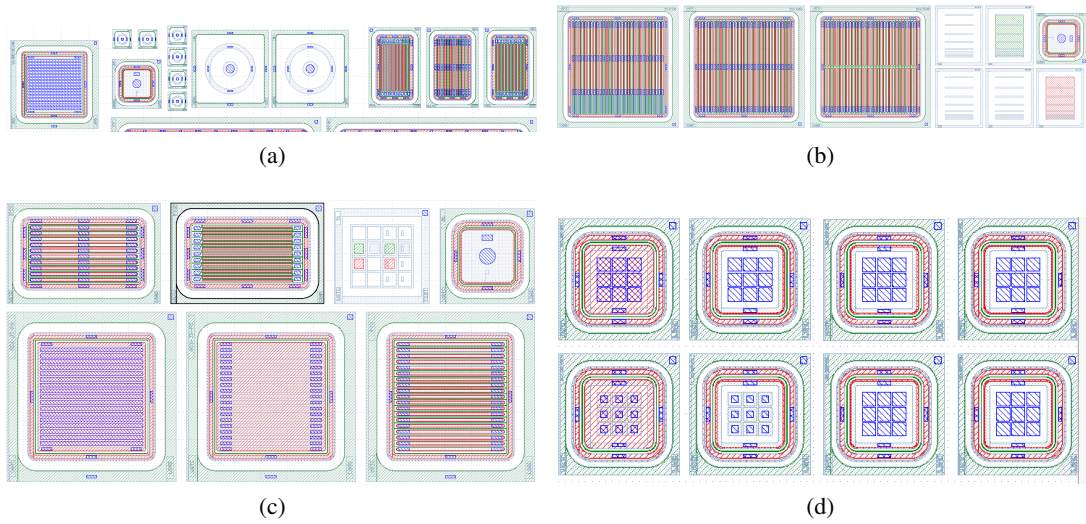


Figure 7.32: The auxiliary devices layout with different geometry parameters used in the first batch production of the USTC-IME LGADs. The candidate AC-LGADs layouts with different pixel sizes are shown in (d).

7.4.3 Wafer preparation and field oxide growing/etching

Silicon substrates must be type P of very high resistivity ($\rho > 1 \text{ k}\Omega \cdot \text{cm}$) to and with a thickness in the range of $50 \mu\text{m}$ to guarantee that the detector can operate in full depletion conditions applying relatively low voltages ($V_{\text{FD}} < 50 \text{ V}$). All the substrates used have been grown by the epitaxial technique, which minimizes the production complexity and improves the uniformity of thickness and distribution of doping. The wafers tested by the certification procedure of the manufacturer show a very good uniformity with $1\text{-}2 \text{ k}\Omega$ for resistivity and $(50 \pm 5) \mu\text{m}$ for thickness. The surface of Silicon substrates usually contains a high concentration of defects, the effect of which is especially significant in very high resistivity substrates. Thus, the wafer is cleaned and coated with a layer of oxide to serve as an insulating layer for protection and serve as the field oxide in the final structure.

The field oxide is then etched following the first mask to open the area for later implantation. The oxide etching is performed with the buffered oxide etch (BOE) solution with a well-controlled temperature and time to prevent over-etching and protect the silicon from damage.

7.4.4 JTE and p/c-stop implantation and diffusion

To form the JTE and P-stop layer, a screen oxide of around 200 nm is grown at the beginning. After the photolithography process of the JTE layer, the Phosphorous are implanted through this oxide in the corresponding region defined by the mask into a relatively shallow depth (by Low energy) with a high dose. For the P-stop layer, we re-performed a similar procedure as JTE with the new mask and Phosphorous replaced by boron. The implantation is done through a screen oxide to reduce the channeling phenomenon, which results in an uneven vertical distribution of doping, and at the same time, it minimizes the damage inflicted on the surface of the substrate.

A long-term high-temperature thermal process is carried out to drive both JTE Phosphorous and PSTOP borons into a rather deep layer. After that, the edge of the junction would be protected safely, and the P-stop has enough size to isolate the electrodes.

7.4.5 Carbon infusion

In order to protect the gain layer from the impact of the acceptor removal effect after irradiation, the carbon infusion is dedicated and designed as a process after the JTE and PSTOP layer diffusion since the carbon diffusion constant is much higher than the boron and Phosphorous in silicon at high temperatures. The carbon requires a shorter period and lower temperature for diffusion. The depth of the diffusion needs to be controlled precisely to be enough to cover the gain layer while away from the substrate. An over-diffusion of the carbon into the substrate will increase the leakage current because it introduces extra energy levels. As a consequence, it will lead to an increase in the power consumption of the device after irradiation and induce thermal noise.

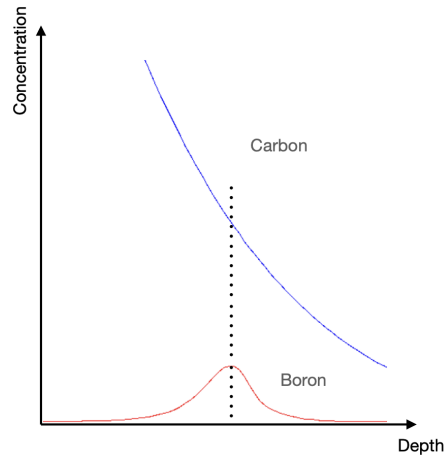


Figure 7.33: The USTC-IME design of the carbon infusion for the protection of the gain layer boron from the impact of acceptor removal.

7.4.6 n^+ and p-well implantation

The implementation of the superficial diffusions n^+ starts with the photolithography through the mask n^+ that defines the windows where the Phosphorus will be implanted to reduce the resistivity of the region and form good contact with the electrode.

The deep p-well implementation to create the multiplication layer is done after the n^+ implantation in order to avoid the contamination coming together with the boron during the high energy ion implementation being punched into the silicon by the n^+ implantation. The hard mask with a special thick photoresist which can create the 5 μm layer, is used to prevent the high-energy boron from penetrating into the region outside the multiplication region. The hard mask and the screen oxide are removed before sending the wafer into the RTA oven to perform a rapid activation of the acceptors and donors, which drive them into the expected position inside the silicon lattice quickly with minimum diffusion effect. Such a design can avoid the diffusion of the p-well, which keeps the boron's implantation peak sharp. Otherwise, a diffused gain layer with a lower boron initial concentration would have a larger c-factor and be rapidly deactivated by the radiation defects as discussed in Sec. 6.3.

7.4.7 Contact etching

After all the implantation is completed, diffused, and activated, the core structure of the p-n junction and its peripheral isolation and protect region are finalized inside the silicon. For the application, it's important to produce devices that can be read out as expected and work stably for long life without being affected by external contaminations or harsh environments. Thus, the finalization procedure is as critical as the previous parts. Besides the doped impurities inside the silicon, the wafer in the current stage only has the field oxide on the surface, which is rather thin and fragile. The growth of the field oxide in the first step by the LPCVD is very slow (can take tens of hours) and expensive to

grow thick even though the quality is the best. Thus, an extra oxide deposition would be performed cost-effectively and efficiently to achieve the thickness for the mechanical requirement.

The mask for the contact holes is then applied, and the wet etch is performed in a slight over-etch way to guarantee that no remnant oxide is left on the surface for contacting. The contact hole is designed to be as small as possible, and only the necessary area is kept. In such a way, the surface defect between the metal and the silicon, which can be formed in the thermal treatment over 200 °C after the metal deposition (known as mutual solubility [189]), will be reduced to a minimum level. The mutual solution of the metal and silicon could result in a hole near the junction, and once it punches through the junction, the device would be short and fail with an abnormally large leakage current at a very low bias voltage.

7.4.8 Metallization and passivation

The metallization procedure is finished as soon as the contact etching is completed. In order to prevent the bare silicon from oxidation in the atmosphere, the metallization is done by the deposition of a thin layer of aluminum and following a wet etching procedure with the mask to remove the metal outside the required region. The control of the etching timing with a well-optimized and stable etching rate is important, and a slight over-etch is arranged to make sure no metal residue is left, which can cause the short between the pixels and HV and increase the leakage current during the operation of the detector.

The passivation layer is done by the deposition of the silicon oxide with a relatively large thickness (around 1-2 μm). The design of the passivation layer is to protect the metal from oxygen, water vapor, and other active contamination that might be reactive with the metal and change its conductivity after a long period. It will also give mechanical protection of the surface from being scratched by the probe needle or tweezers during the test or transfer since the oxide is harder than the metal. Furthermore, with the passivation, the region between the grounded ring and HV can be well isolated, as expected, since the contamination that can cause the surface leakage will no longer be possible to be attached in the depth of the metal. The passivation opening is designed for the later test or assembling with the guard ring pad, central pad, and UBM pad in a radius of 90 μm are available for probe card contact, wire bonding, or bump bonding. The passivation opening is done with the dry etch process with the pre-defined mask.

7.4.9 Splits of the wafers

There are eleven wafers in total for the first batch, including the six pre-run wafers to determine the fab process parameters, and two sub-batches are defined by the wafer version, namely version 1.0 for the pre-run (**W1-W6**) and version 1.1 (**W7-W11**), with five wafers for each batch for a more efficient iteration and parameter optimization. There were some processes issue observed in version 1.0, leading to functionality failure for most of the LGADs and resulting in extremely low yield. The issue is further analyzed, and the improvements in both design and fabrication were realized in the later version. Thus, only version 1.1 is taken as the nominal production for the test. The summary of the wafers' general product information and the measured performance is shown in Tab. 7.3. One

7 Simulation and Fabrication of the USTC-IME LGADs for the HGTD Upgrade

carbonated wafer **W11** is also attempted to be produced with the newly designed carbon diffusion process (introduced in Sec. 7.4.5), with the expectation for an improvement in the irradiation hardness. The photo of the wafers produced in the first batch at IME is shown in Fig. 7.34. The wafer is then diced and tested with several techniques which are described in detail in Chapter 8.

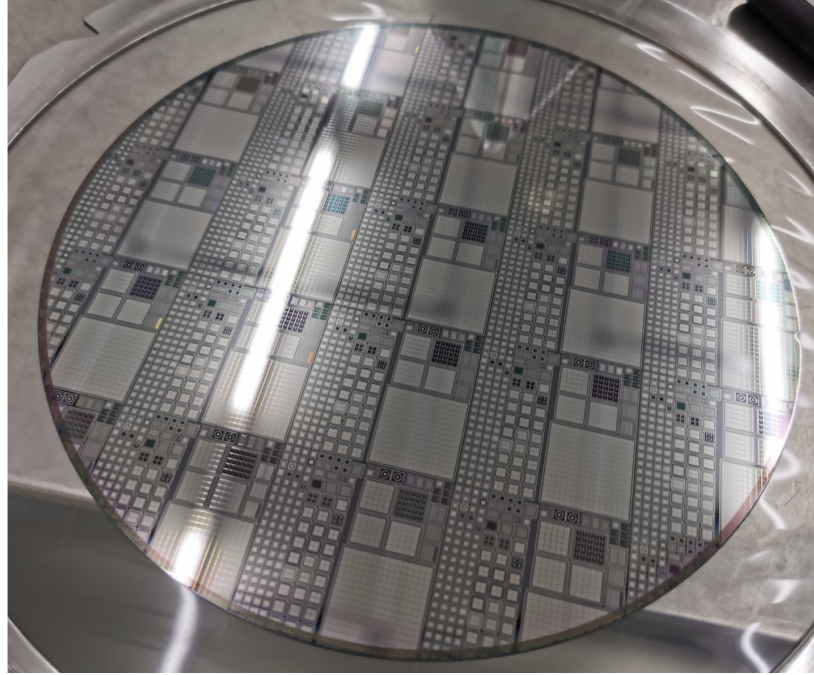


Figure 7.34: Photo of the wafer with USTC-IME version 1.1 LGADs at the first batch.

7.5 USTC-IME 2nd batch fabrication

The second batch follows most of the design and development process as batch-1 while focusing on producing the large sensors with a better yield and stable performance to fulfill the HGTD requirement. Plenty of improvements have been implemented in both the design and fabrication process to resolve the discovered issues and improve the robustness of the device for a large yield. Furthermore, the gain layer's radiation hardness has been significantly improved by a more mature design of the carbon infusion and tuning of boron doping by implantation. Some researches for this improvement are introduced in the Chapter 8 of the characterization part. These differences and new updates will be introduced in this section, and others not mentioned will be the same as the process introduced for the first batch.

7.5.1 Mask preparation

The mask for the second batch is totally new compared to the first batch for the selection of a new photolithographic machine for achieving better alignment precision and a much smaller minimal

7.5 USTC-IME 2nd batch fabrication

linewidth. The size of the reticle for each layer is $22.5 \times 22.5 \text{ mm}^2$ instead of the $40 \times 40 \text{ mm}^2$ used before. However, with the smaller size, it is impossible to place the 15×15 full-size LGAD array along with the small LGAD array in the same reticle. In order to reduce the fabrication complexity, we designed two series of masks for two sub-sets of the wafer. The first sets contain the small array LGADs (1×1 , 2×2 , 5×5) for the research and development, which are designed with different geometry for the peripheral region and inter-pixel area to further optimize the design. Besides the normal I-V C-V measurement, they can be diced for irradiation and assembled on the pre-amplifier board for the TCT test. We denote it as the **Mask A**. The second set contains only the 15×15 full-size LGAD array with the nominal LGAD design mainly for the evaluation of the uniformity and estimation of the yield. This set is denoted as the **Mask B**. The designed **Mask A** and **Mask B** are shown in Fig. 7.35.

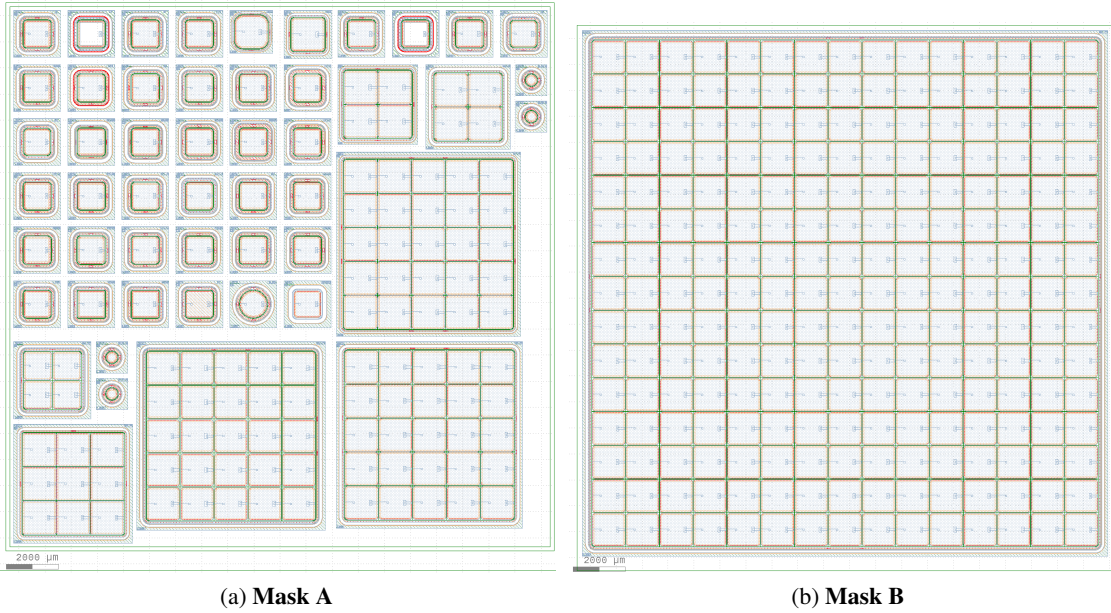


Figure 7.35: The designed reticle layout of (a) the small array devices wafer and (b) full size 15×15 array wafer (left) used in the second batch production of the USTC-IME LGADs.

Apart from the mask, the new photolithographic machine uses the zoomed exposure with a scaling ratio of 5 : 1 instead of the parallel exposure. Thus, a 6-inch reticle would be made, which can further improve the pattern precision by a factor of five for exposure. The impact of the contamination or the defects on the reticle would be much reduced and eventually negligible. This machine also uses the Nikon LSA and FIA wafer alignment system, which can achieve $0.13 \mu\text{m}$ overlay accuracy between layers with an automatic alignment system. This is much more precise than the parallel exposure machine, which has $2 \mu\text{m}$ accuracy and improvement for the overlay for the METAL/CONT, JTE/PWELL where an unexpected misalignment can cause a significant impact on the device functionality and potential failure.

7.5.2 Improvement of the contact design

The contact has been re-designed with the following considerations:

- The contact region should be fully covered by the metallization layer and have enough overlay in case of the misalignment (recommended to be more than 3 μm), in this way, the silicon surface will be protected from the over etch of the metal when using the dry etch process.
- The contact region should be designed away from the passivation opening where the probe needle and wire/bump bonding might be applied on. The external contact with this region might cause a scratch, a puncture hole, or exposure of the silicon to the environment. By re-designing the etching region of the oxide layer for contacting, such risk is minimized.
- The area of the region should be constrained as small as possible to limit the formation of the Al-Si interface. Only the necessary contact area should be applied. The Al-Si interface is unstable and can lead to a critical problem because aluminum and silicon can dissolve each other [189, 227], especially during the high-temperature treatment in a later process. When the dissolution happens, the silicon will be absorbed into the aluminum, and vacancies show up, usually as a spike. This can be a size from around tens of nanometers to a few microns, which is comparable to the depth of the surface of the depletion region in n^+ . When it touched the depletion region, a short would happen, and the device would fail, showing up as a high leakage current at low bias.

7.5.3 Improvement of the carbon infusion

The design for the infusion of the carbon has been demonstrated with a good performance in the first batch of the USTC-IME **W11**. With the confidence of the recipe of the carbon implantation and the thermal treatment, in the second batch, we produced more carbon-infused wafers. The wafers have more dose splits on the dose of carbon, and with these wafers, we are able to establish the model from the measured data to determine the most optimal for the final production. From the measured acceptor removal constant and the leakage current, it still has space for improvement with a higher carbon concentration compared with the design of other institutes. Thus, we use the splits for the carbon dose as factors of two, five, and ten based on the carbon concentration of the **W11** in the first batch.

7.5.4 Improvement of the gain layer

Upper constraint of the V_{BD}

The boron of the gain layer is adjusted to make sure the LGAD device can be operated with expected performance both before the irradiation and after irradiation. Due to the acceptor removal effect, we would like a higher initial boron concentration, which has a lower removal rate. The research of the HGTD collaboration also observed a phenomenon that the LGAD detector, after accumulating enough particles pass through the detector, would have a non-negligible possibility to burn out by a single event with high energy deposition (namely SEB effect). Such an effect can lead to permanent

damage on the detector with a burn mark left on the surface (Fig. 6.8). The later study reveals that it is mainly correlated with the operation voltage (which defines the electric-field in the bulk region) of the device after the irradiation. This shows if we operate the LGAD above a voltage (around 550 V for the 50 μm thick LGAD), it is unavoidable for the device to be burned out during the lifetime of the HGTD in HL-LHC operation. This new issue presented us with a requirement on the operation voltage limitation after the highest radiation fluence. It is a challenge not only for the fine adjustment of the carbon diffusion but also for the boron of the gain layer to make sure we have the lowest possible breakdown voltage before irradiation and then we can have the lowest possible breakdown voltage after irradiation.

Lower constraint of the V_{BD}

It leads to the question of the lowest possible voltage for the LGADs operation. This mainly depends on the depletion voltage of the gain layer and the bulk and the thickness of the detector, which the electric field strength depends on. In order to keep a good time resolution, the signal needs to be fast, which relies on the saturation of the drift velocity. For 50 μm LGADs, it needs around 70 V after the depletion to guarantee the saturation. Assume a typical depletion voltage 25 V for the gain layer and 5 V for the bulk. Considering around 60 V shifts of the V_{BD} between the room temperature and the -30°C , the 160 to 180 V is the bias for an LGAD to be operated in an ideal condition.

For the first batch of the USTC-IME LGADs, we target the 200 V as the baseline V_{BD} to design the gain layer by the simulation with TCAD. However, the final sensors turn out to have the V_{BD} of around 300 V at room temperature. Thus, in the second batch, we take this calibration into account and target the V_{BD} at 180 V with around 20 V for a safety margin.

7.5.5 Improvement of the inter-pad gap and slim-edge design

Based on the various validation structures designed and tested in the first batch, we further placed more aggressive layouts, which would further improve the acceptance (fill-factor) area by using more compact inter-pad isolation and slim edge. The design meets the final specification of the sensor for HGTD upgrade (Inter-pad gap distance: 50 μm and slim edge: 300 μm). This achievement is based on the simulation and the test result from the first batch of wafers. The design is mainly realized by the 2×2 and 5×5 LGAD array and can be found in Fig. 7.36. The performances of these designs are further characterized by the laser-TCT and test beam in Chapter 8.

7.5.6 Splits of the wafers

There are ten wafers in total for the second batch, and two sub-batches are defined by the wafer version, namely version 2.0 and version 2.1, with five wafers for each batch for a more efficient iteration and parameter optimization. Different gain layer doping is designed to compare the performance both before and after the irradiation. It includes the different gain layer depths (by the implantation energy), different gain layers doses, and different carbon doses. A summary of the wafers' general product

7 Simulation and Fabrication of the USTC-IME LGADs for the HGTD Upgrade

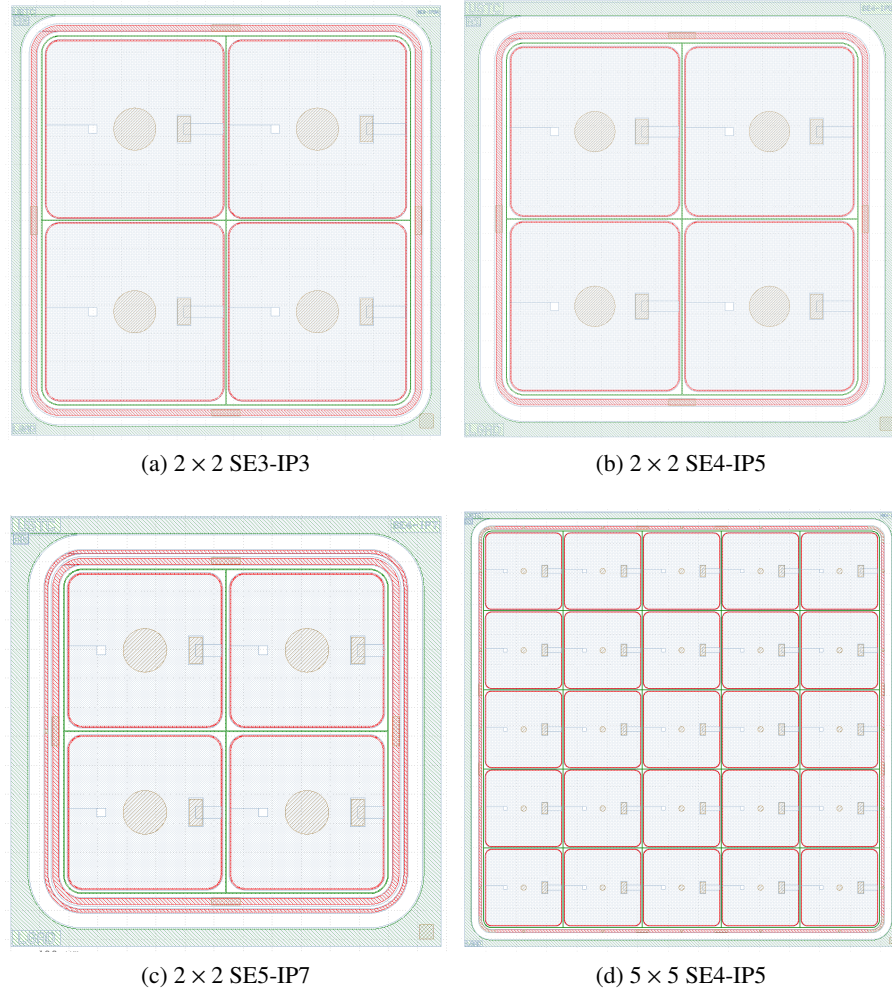
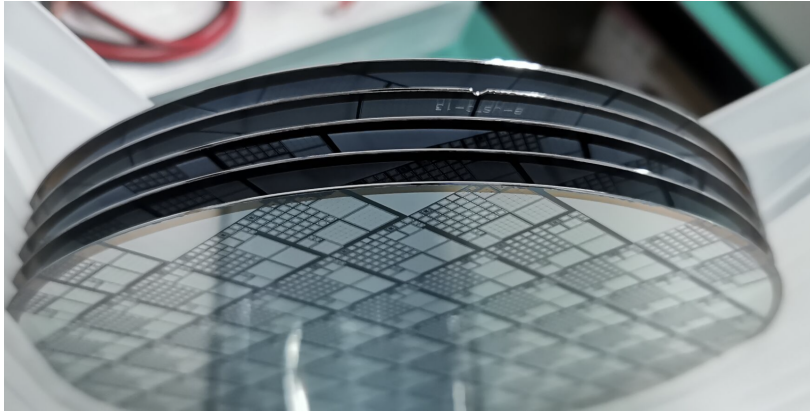


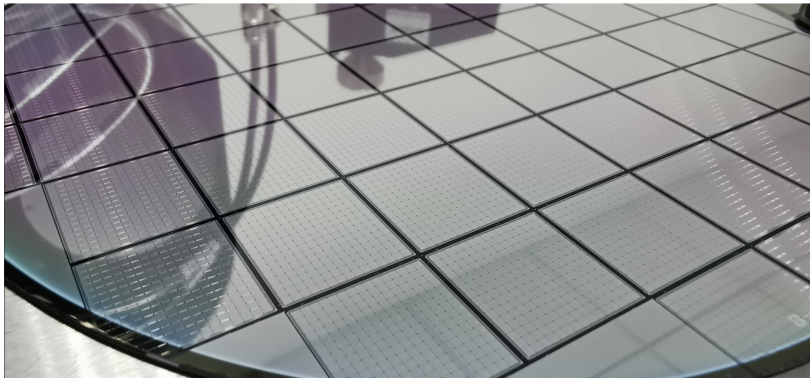
Figure 7.36: The layout of the 2×2 LGAD array with different inter-pad gap distance and slim edge used in the second batch production of the USTC-IME LGADs. (a) 2×2 IP3SE3 with 30 μm inter-pad gap and 300 μm slim edge. (b) 2×2 SE4IP5 with 50 μm inter-pad gap and 400 μm slim edge. (c) 2×2 SE5IP7 with 70 μm inter-pad gap and 500 μm slim edge. (d) 5×5 SE4IP5 with 50 μm inter-pad gap and 400 μm slim edge.

information and the measured performance is shown in Tab. 7.3. The close-up photos of the wafers from USTC-IME second batch are shown in Fig. 7.37 and Fig. 7.38.

7.5 USTC-IME 2nd batch fabrication



(a)



(b)

Figure 7.37: Photo of the wafer of the USTC-IME second batch. (a) the five wafers with different layouts and gain layer designs. (b) The wafer with 15×15 full-size LGADs arrays.

7 Simulation and Fabrication of the USTC-IME LGADs for the HGTD Upgrade

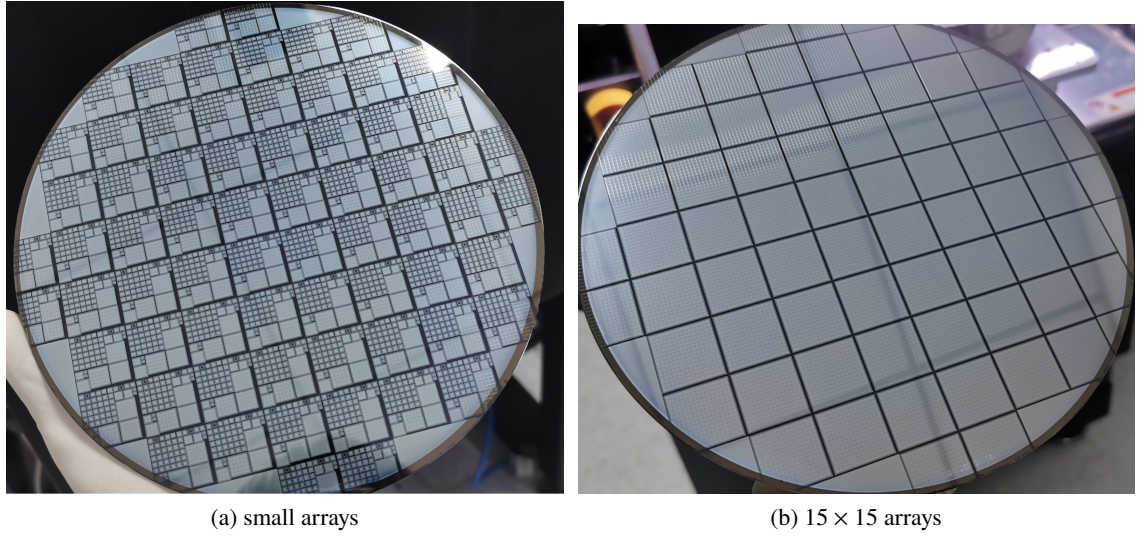


Figure 7.38: Photo of the wafers with (a) small arrays (1×1 , 2×2 , 5×5) and (b) large arrays (15×15) LGADs at the USTC-IME second batch.

Table 7.3: Summary of the USTC-IME wafers from the first batch (version 1.1) production and second batch productions (version 2.0 and 2.1). The wafer series number, the gain layer dose and energy, the type of the gain layer implantation, the layouts on the wafer, the breakdown voltage, the irradiation hardness c -factor, and the sites where the samples have been tested are listed.

Production version	Wafer No.	GL.Dose	GL.Energy	Implantation	Layout arrays	VBD [V]	c -factor [$1 \times 10^{16} \text{ cm}^{-2}$]	Tested available (irrad.)
USTC-1.1	W7	Low	High	B	Mixed	370	5.79	beta-USTC
	W8	Medium	Low	B	Mixed	295	4.12	beta-USTC
	W9	Medium	Ultra High	B	Mixed	295	7.25	beta-USTC
	W10	Medium	High	B	Mixed	320	5.72	beta-USTC
	W11	Medium	High	B+C	Mixed	300	1.85	beta-USTC/JSI, Beam-DESY
USTC-2.0	W12	Low	Low	B	Small	174	3.66	beta-USTC
	W13	Low	Low	B	15×15	172		
	W14	High	Low	B	Small	84	3.38	beta-USTC
	W15	High	Low	B	15×15	100		
	W16	High	Low	B+10C	Small	50	1.36 - 1.49	beta-USTC/JSI, Beam-DESY
USTC-2.1	W17	Medium	Low	B+1C	Small	190	1.23	beta-USTC/JSI, Beam-DESY
	W18	Medium	Low	B	15×15	190		
	W19	Medium	Low	B+2C	Small	165	1.29	beta-USTC/JSI, Beam-DESY
	W20	Medium	High	B+C	15×15	220		
	W21	Medium	High	B+C	Small	215	2.07	beta-USTC/JSI, Beam-DESY

7.6 Design for the production of the USTC-IME LGADs for HGTD

7.6.1 The 15×15 array layout

The finalized design of the LGAD sensor is 15×15 array with $300 \mu\text{m}$ slim edge in the horizontal direction and $400 \mu\text{m}$ slim edge in the vertical direction as shown in Fig. 7.39. The distance of the inter-pad gap is $50 \mu\text{m}$ and the gain layer is based on the most irradiation hard wafer, USTC-IME-v2.1 W17. The alignment markers are placed at four corners as required for the sensor flip-chip with the ALTIROC chip. The total size of the sensor is $20.1 \text{ mm} \times 20.3 \text{ mm}$ with $80 \mu\text{m}$ designed as the gap for dicing. The $90 \mu\text{m}$ radius round passivation opening is placed for the UBM and bump deposition for the bump-bonding. In the pre-production phase, around 20 wafers would be produced and evaluated in several ATLAS institutes for quality control and assurance purpose.

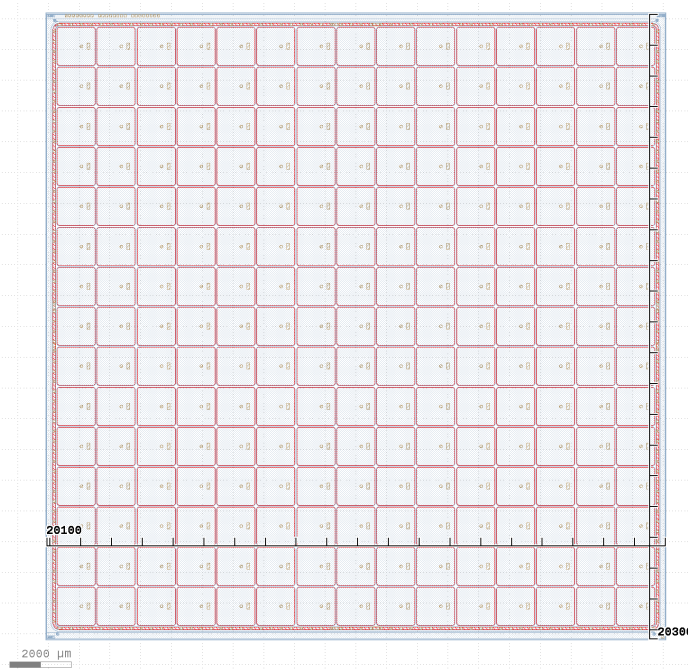


Figure 7.39: The layout of the 15×15 LGAD array with the requirement from the collaboration specification implemented.

7.6.2 QC-TS structures

The test structures are made for the fabrication process quality control purpose during the final production, as shown in Fig. 7.40. The test structures include the MOS capacitor for the purpose of the oxidation layer quality and surface charge measurement, the *van der pauw* greek cross structure for the purpose of sheet resistivity measurement for the doping layer of p-stop and JTE, gate diode for the measurement of the surface quality and the PIN, LGADs for the I-V, C-V, charge as well as the

7 Simulation and Fabrication of the USTC-IME LGADs for the HGTD Upgrade

time resolution measurement both before and after the irradiation. The reticle with both the 15×15 array and QC-TS placed is shown in Fig. 7.41.

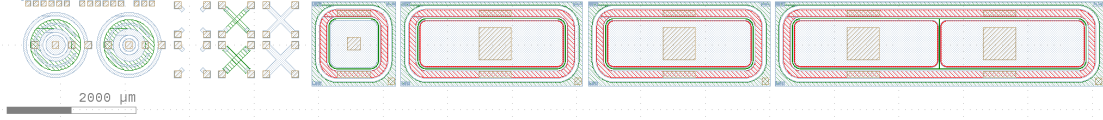


Figure 7.40: The layout of the QC test structures for the production phase.

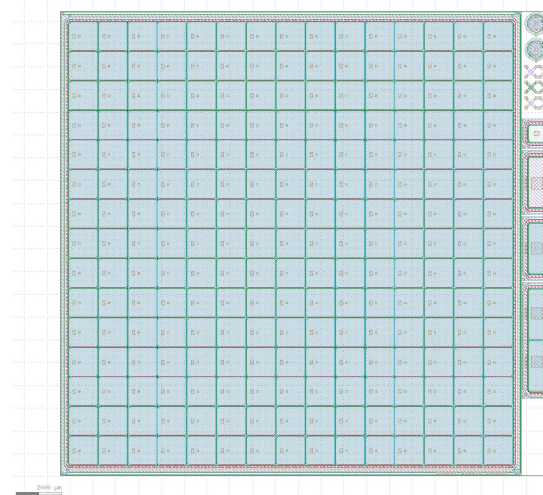


Figure 7.41: The layout of the reticle to be used in the production phase with the requirement from the collaboration specification implemented.

7.7 Summary

This chapter provided an in-depth analysis of the structure and simulation of LGADs used in the HGTD upgrade. First, it starts with an exploration of the LGAD sensor structure in Sec. 7.1, which comprises multiple layers and components. The substrate serves as the foundation for the entire sensor, followed by the multiplication layer, which is the heart of the LGAD. The n^+ layer is responsible for signal readout, and the junction termination extension prevents breakdown at the edge. The field plate ensures a smooth electric field, while the guard-ring protects against unwanted signals and currents. The p-stop and c-stop layers isolate the electrodes and shield against defects, respectively.

Next, Sec. 7.2 and 7.3 delve into TCAD simulations, which are essential for understanding the behavior of LGADs. They discussed mobility, recombination, and avalanche effects as key factors in the simulation process. The results from the TCAD simulations are used to optimize the various components of the LGAD structures, including the substrate, p-well, guard-ring, p-stop, field plate, and floating guard ring. The chapter also covers the optimization of the inter-pad gap for the 2×2 array and concludes with recommendations for prototype production.

7.7 Summary

This thesis then details the fabrication process for the USTC-IME LGADs, discussing the preparation steps for the first and second batches of fabrication in Sec. 7.4 and 7.5. The fabrication process includes mask preparation, wafer preparation, field oxide growing/etching, implantation and diffusion, carbon infusion, and metallization and passivation. It also discusses the improvements made in the second batch of fabrication, such as the contact design, carbon infusion, gain layer, and inter-pad gap and slim-edge design.

Finally, Sec. 7.6 presents the design for the final production of USTC-IME LGADs for the HGTD upgrade. It includes the 15×15 full-size array and QC-TS layout.

8 Characterization and Performance of the HPK and USTC-IME LGADs

8.1 Overview

The specification of the LGAD sensors for the HGTD upgrade is listed in Tab. 8.1 for the performances before irradiation and in Tab. 8.2 for the performances after irradiation. The sensor for the HGTD is required to be made on the substrate of p-type high-resistance silicon with resistivity higher than $1 \text{ k}\Omega$. The gain layer depletion voltage should be in the range of 24 to 55 V. The sensor should be depleted at a bias below 70 V, and the breakdown voltage should be larger than the value that the bulk's drift field is larger than $1.5 \text{ V } \mu\text{m}^{-1}$ to guarantee the saturation of the drift velocity and expected time resolution. The V_{BD} is defined by the current threshold of 200 nA per pad. In order to constrain the power consumption, the device must have the current per area within $12 \text{ } \mu\text{A cm}^{-2}$. The isolation between the electrode should be p-stop, and the pad capacitance should not exceed 4.5 pF. The inter-pad resistance should not be lower than the $1 \text{ G}\Omega$.

For the sensors after being irradiated to the highest fluences of $2.5 \times 10^{15} \text{ n}_{\text{eq}}/\text{cm}^2$. Key criteria include a hit efficiency of greater than 95% at normal incidence with discrete testing electronics in the central part of a $1 \times 1 \text{ mm}^2$ pad, a time resolution of less than 50 ps, power consumption less than 100 mW/cm^2 at the minimum operating voltage and a maximum total leakage current of less than $160 \text{ } \mu\text{A cm}^{-2}$ for a $50 \text{ } \mu\text{m}$ thickness. Additional requirements encompass a collected charge greater than 4 fC at the minimum operating voltage, pad leakage current below $5 \text{ } \mu\text{A}$, a maximum operating voltage limited by SEB at $11 \text{ V}/\mu\text{m} \cdot \text{D}$, inter-pad resistance greater than $10 \text{ M}\Omega$, leakage current stability within $\pm 5\%$ when corrected for temperature, and micro-discharge hits at the minimum operating voltage below 1 kHz. These specifications are critical in ensuring the reliable performance of HGTD sensors in highly irradiated environments.

8 Characterization and Performance of the HPK and USTC-IME LGADs

Table 8.1: HGTD electric requirements as well as timing and charge collection performance of the sensor as produced at $V_{OP} = 0.8 \cdot V_{BD}$ and $T = -30^\circ\text{C}$.

Substrate (resistivity)	p-type ($\geq 1 \text{ k}\Omega \text{ cm}$)
HV biasing	back side
Gain layer depletion (V_{GL})	$24 \text{ V} < V_{GL} < 55 \text{ V}$
Full depletion (V_{FD})	$< 70 \text{ V}$
Breakdown voltage (V_{BD}) (-30°C)	$V_{BD} > V_{FD} + D \cdot 1.5 \text{ V mm}^{-1}$
Breakdown condition (-30°C)	$> 200 \text{ nA/pad}$
Device leakage current (-30°C)	$< 12 \mu\text{A cm}^{-2}$
Inter-pad isolation	p-stop
Pad capacitance	$< 4.5 \text{ pF}$ (to the backplane and inter-pad)
Hit efficiency at normal incidence obtained with discrete testing electronics (in central part of pad) $\sim 1 \text{ mm} \times 1 \text{ mm}$	$> 97\%$
Time resolution (using discrete testing electronics)	$< 40 \text{ ps}$
Effective interpad distance:	$< 100 \mu\text{m}$
Collected charge	$> 15 \text{ fC}$

Table 8.2: HGTD sensor performance requirements after irradiated to highest fluences $2.5 \times 10^{15} \text{ n}_{eq}/\text{cm}^2$.

Hit efficiency	$> 95\%$
Time resolution (using discrete testing electronics)	$< 70 \text{ ps}$
Power consumption at $V_{OP,min}$	$< 100 \text{ mW/cm}^2$
total maximum leakage current	$< 5 \mu\text{A cm}^{-2}$
Collected charge $V_{OP,min}$	$> 4 \text{ fC}$
pad leakage current at $V_{OP,min}$	$< 5 \mu\text{A cm}^{-2}$
Maximum $V_{OP,max}$ (limited by SEB)	$11 \text{ V}/\mu\text{m}\cdot\text{D}$
Interpad-resistance at $V_{OP,min}$	$> 10 \text{ M}\Omega$
Leakage current stability	to remain stable within $+/-5\%$ when corrected for temperature exhibiting no long-term drifts (on days scale) or prompt excursions
micro-discharge (“ghost hits”) hits at $V_{OP,min}$	$< 1 \text{ kHz}$

8.2 The laboratory setup for characterization of the LGADs at USTC

8.2.1 Probe-station setup for IV/CV measurement

There are three characterization platforms used for the LGAD tests at USTC in the different stages in general for testing the different sensors:

- In stage-1, we use the probe station in the NRFC, shown in the Fig. 8.1. The probe station is located in an environment with temperature around 25 °C and humidity around 40% - 50% depending on the weather. The platform can apply up to five needles and instruments including a Keithley 2410 source measure unit (SMU) for HV bias and a Keithley dual-channel SMU 2636B for precision current measurement and a LV supply. The dedicated probe card holder is installed in order to fit the 5×5 and 15×15 probe cards made by the V-Probe company into our probe station. The digital switchboard is equipped for the probe card to select channels for measurement among 25 or 225 pads [228].

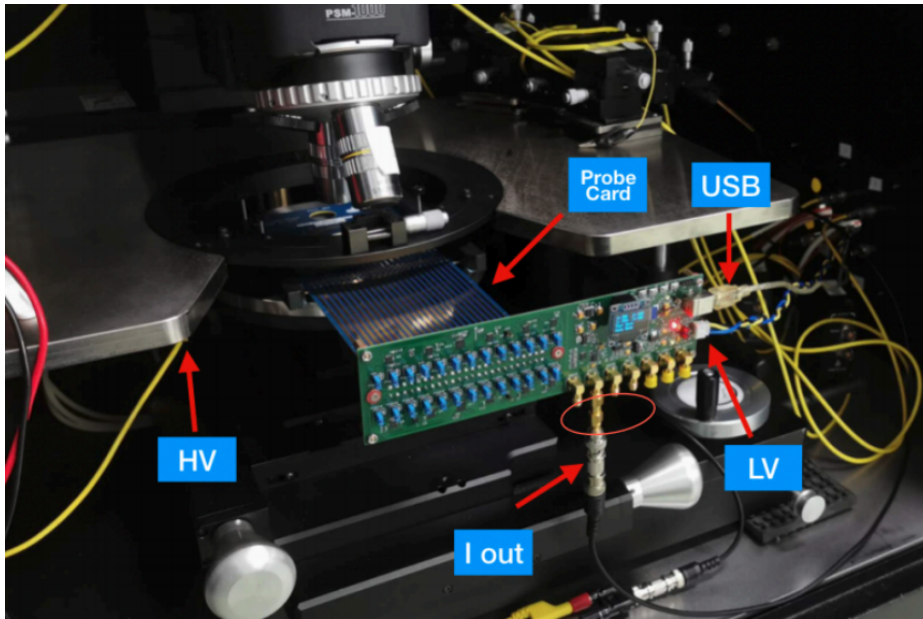


Figure 8.1: The manual probe station with an 8-inch trunk is used for the room temperature IV/CV test at stage-1.

- In stage-2, we have a new manual probe station available and dedicated to the HGTD project shown in Fig. 8.2. The probe station has a compact chamber so that the environment can be kept dry and dark and shielded from noises during the test. The low-temperature circulator and a 4-inches chuck with a built-in Peltier cooler allow us to control the temperature of the chuck in the range between -40 °C to 120 °C swiftly. Accordingly, a dehumidifier is connected between the compressor and the chamber, which can restrict the humidity within 0.1%. A Keithley 2410 SMU and a 6482 dual-channel pico-ammeter are equipped for the system. The 5×5 probe card

8 Characterization and Performance of the HPK and USTC-IME LGADs

with a ceramic blade design from Apollowave (different from the E-proxy design by V-Probe) is equipped for large array tests.

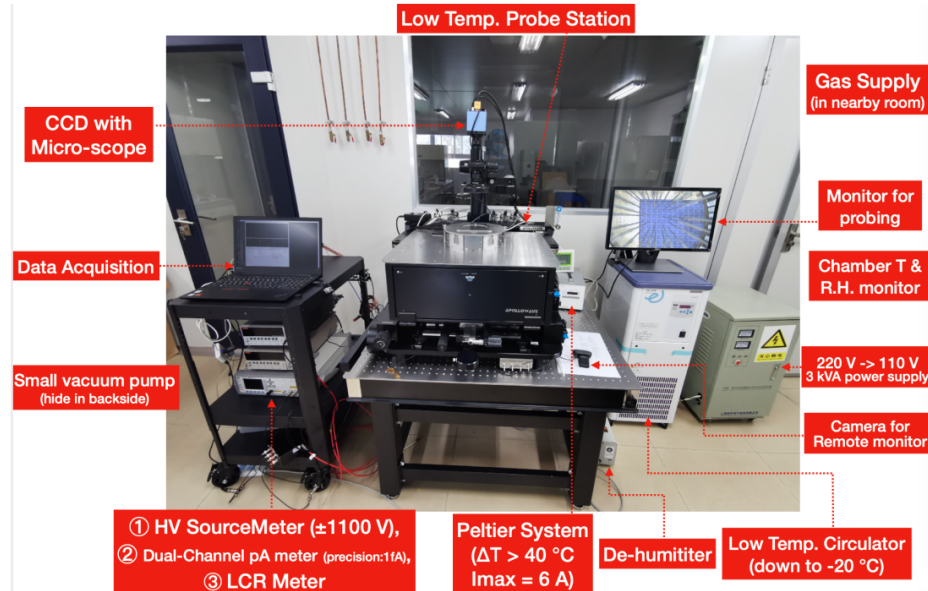


Figure 8.2: The probe station with a 4-inch trunk for the room and low-temperature IV/CV test at stage-2.

- In stage-3, we used a shared SUMMIT-200 automatic probe station for the wafer-level fast and automatic IV/CV test shown in Fig. 8.3. The probe station can do the IV/CV scan automatically with a pre-configured die map on the wafer to locate each pad. The speed is configured and optimized to measure a I-V with 2-3 seconds per pixel with 3 V per step. The data are used for quality assurance, yield analysis, and uniformity study, which are shown in Sec. 8.7. Furthermore, the data are compared with the manual probe station for a cross-check of the setup when abnormalities are spotted in the results.

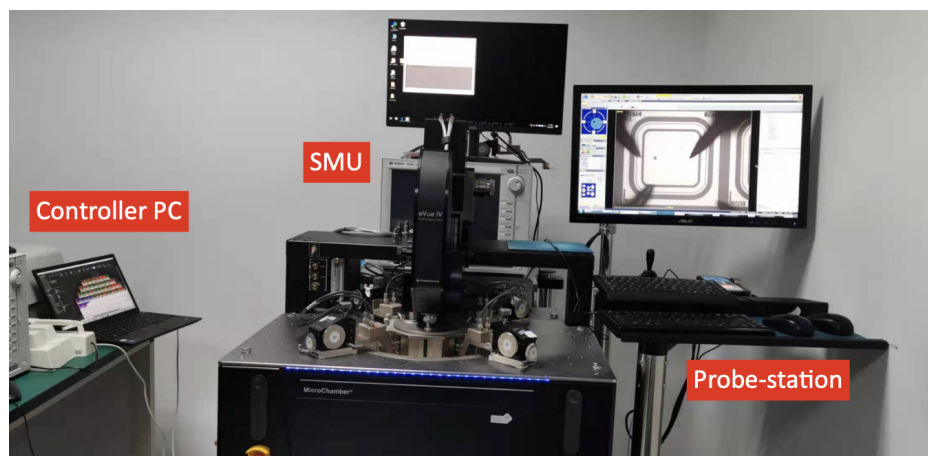


Figure 8.3: The setup of the automatic probe station at the USTC for the wafer-level IV/CV test.

8.2 The laboratory setup for characterization of the LGADs at USTC

In both manual systems (stage-1 and stage-2), we have an E4980A 20Hz-2MHz LCR meter equipped for the C-V measurement. The LCR is connected to the device through an HV bias module, which can apply bias up to 600V during the C-V measurement. A PC is used to control all instruments working together. The control and taking data acquisition are implemented with Python based software as shown in Fig. 8.4. Tab. 8.3 gives a summary of the platforms used for the I-V and C-V test in this thesis.

Table 8.3: Summary of electric characterization platforms for LGAD tests at USTC

Stage	Probe Station	Temperature	Equipments	Chuck	Samples Tested
1	PW-800, manual	25 °C	Keithley 2410 SMU, 2636B Dual-channel SMU	8-inch	HPK single pad, 2×2 , 5×5
2	ApolloWave α -200 CS, manual	-40 to 120 °C	Keithley 2410 SMU, 6482 Dual-channel pico-ammeter	4-inch	HPK single pad, 5×5 , 15×15
3	SUMMIT-200, automatic	25 °C	Keysight B1500 Semiconductor Device Analyzer (SMUs, LCR meter)	8-inch	USTC-IME batch2 8-inch wafers W12 - W21

8.2.2 I-V measurement setup

I-V of the single pads sensors

The I-V for the single pad sensor is measured with 5 μ A or higher per pad current compliance on the HV source. The step of the bias sweep is 0.5 to 5 V, and the delay time is larger than 0.5 to 1 s, depending on when the stability of the current reaches a certain level (relative change between two results is less than 0.1%). Both results with guard ring floating and grounded are obtained and compared. (shown in Sec. 8.3). The V_{BD} , V_{GL} , and I_{leak} are extracted from the I-V curve for the evaluation of the sensor's basic performances.

I-V of the 2×2 arrays

The setup is the same as the singlet's setup except for three more pads and needles. Both channels of 2636B are used to measure the current of two pads simultaneously, while the other two pads and guard ring are grounded (Fig. 8.4 (b)). All pads' current is measured by 2636B, which can provide a more precise result.

The difficulty in measuring the V_{BD} for 2×2 and 5×5 arrays is that the V_{BD} is related to the bias status of the neighboring pad. If the neighboring pad is floating, it can affect the V_{BD} of the pad under test via the punch-through effect. If we measure the pad with the neighboring pad grounded, we cannot get the V_{BD} of each pad because the pad with the lowest V_{BD} would always break down first. To solve this, a method called "semi-ground" is used. The neighbor pads during the measurement

8 Characterization and Performance of the HPK and USTC-IME LGADs

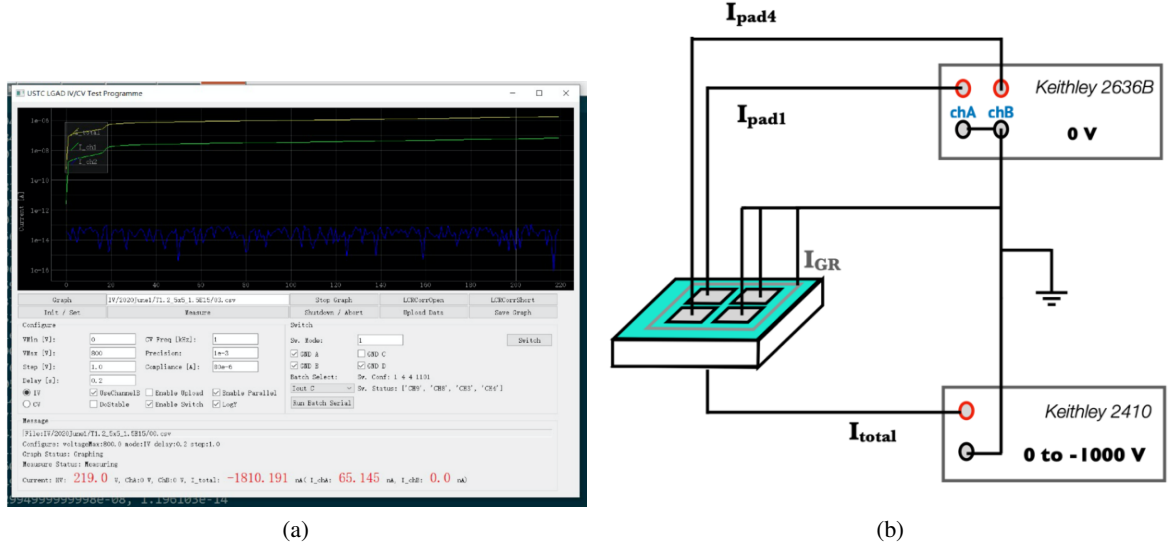


Figure 8.4: (a) The dedicated software for the I-V and C-V measurement was developed with *Qt5* and the *pymeasure* backends. (b) schematic layout of the cable connection for performing the I-V test on the 2×2 LGAD arrays, the test of the single pad and larger arrays uses similar cable connections.

are biased above the full depletion voltage and 10-20V below the expected breakdown voltage. This will guarantee the neighbor pads' currents are always lower than the pad under test and will have significant influences on the V_{BD} determination for the pad under measurement. With this method, we can measure each pad's V_{BD} with neighboring pads biased to a similar potential but away from the breakdown.

I-V of the 5×5 and 15×15 arrays

The 5×5 I-V measurements have been performed with the probes card from V-probe or Apollowave company. Several digital and manual switchboards developed by USTC with different versions of fabricated are used [228]. The measurement circuit is similar to 2×2 's except for more neighboring pads. The digital switchboard is shown in Fig. 8.5. Due to our "semi-grounded" method's need to use 2636B to give a reversed bias from the output of the digital board around the breakdown, the dynamic range of the analog switch on the board would be exceeded. This would lead to a 100 mA current leaking from the CMOS gate. Thus, although the digital version of the readout board has an excellent result of leakage current at a low voltage range, for some batches of sensor prototypes with poor uniformity, we can not obtain the V_{BD} of each pad in the whole array. For those prototypes, the manual switchboard is used instead, and a much more stable result is obtained. The I-V measured for each pad is shown in Figure I-V, and the V_{BD} distributions overall the 5×5 sensors are shown in Fig. 8.13, and Fig. 8.14.

8.2 The laboratory setup for characterization of the LGADs at USTC

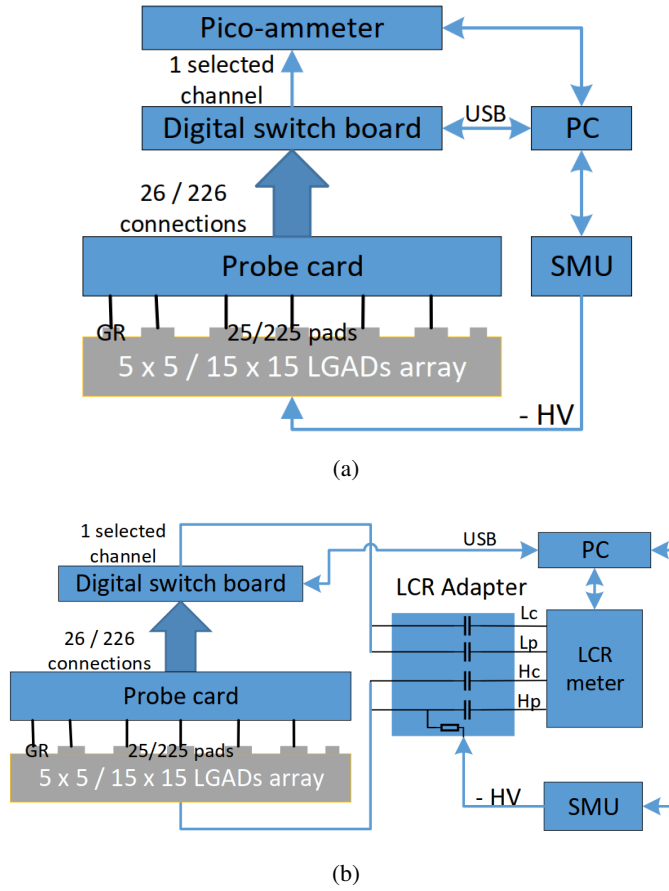


Figure 8.5: The schematic view of the circuit with the digital switch boards for (a) I-V and (b) C-V test of the 5×5 and 15×15 large array LGADs [228].

I-V of the wafer level test

The wafer level I-V and C-V test is performed with the automatic probe station for the second batch of IME 8-inch wafers. The commercial software with dedicated configuration is used for the automatic test of the wafers with USTC-IME LGADs layout. There are more than ten thousand pads that need to be tested (52×225) for the 8-inch wafers. Thus it is important to realize the automation for the test in order to obtain fast and stable results. The configure is optimized to complete each I-V sweep within 3 s (including the time to switch pads) at a step of 3 V in the range of around 0 to -150 V. The wafer is loaded manually, and the alignment is performed automatically for both the horizontal shifts and the rotation with the pattern recognition algorithms on the align marker in the wafer surface. The alignment precision with the advanced microscope is better than $10 \mu\text{m}$, which is much smaller than the width of the contact pad, $100 \mu\text{m}$. The duration of a wafer takes around 10 h if things go smoothly. The issue sometimes happens due to the stability of the SMU, which leads to a communication stuck, and the bow of the wafer can lead to an unstable contact that must be corrected manually. The measured results are displayed in the software in real time for people to monitor. In order for the postmortem check when the abnormality of some pixels is observed in later analysis, the

8 Characterization and Performance of the HPK and USTC-IME LGADs

microscope camera is also included in the program to take a photo of each pixel to check if there are visible contaminations or scratches on the surface of the device.

In the end, all the wafers from the USTC-IME second batch (**W12** to **W21**) and 6-inch wafers from NRFC are tested for the I-V and some of them have been tested with the C-V when an in-depth investigation needed. The V_{BD} , as well as I_{leak} , are extracted to analyze the uniformity and yield for improvement of the process and control of the quality as shown in Sec. 8.7.1.

8.2.3 C-V measurement setup

For C-V measurements, we use the Agilent E4980A inductance, capacitance, resistance (LCR) meter with a dedicated DC bias adapter designed by USTC for HV. The frequency is 10 kHz for the unirradiated sensor, as recommended by RD50 [229]. The AC amplitude is 200 to 1000 mV depending on the probe station and the circuit's noise level. The DC bias step is 0.1 to 0.5 V, and the waiting time after each change of the DC bias is dynamically determined during the measurement after reaching specific stable criteria similar like I-V measurement.

The V_{GL} , V_{FD} , C_p , as well as the doping profiles, are extracted from the C-V curves. The V_{GL} and V_{FD} are determined by the cross-point of the extrapolated lines in the $1/C^2 - V$ curves, detailed in [188]. The doping profile of each sensor type is extracted by $1/C^2$ with the Eq. 8.1 and 8.2. In order to reduce the fluctuation caused by the noise on the curve, 1-2 times “slide window” smoothing is applied in the C-V and doping profile. The detector's pad capacitance (C_p) is determined by the value after the sensor is fully depleted. The C-V test is performed at room temperature both for the device before and after the irradiation, while for the irradiated sensors, the lower AC frequency is usually chosen (usually 1 kHz or lower) to mitigate the impact of the defects' lifetime.

$$N(w) = \frac{2}{e \cdot \epsilon A^2} \left[\frac{d(C^{-2})}{dV} \right]^{-1} \quad (8.1)$$

$$w = A \cdot \epsilon \cdot \frac{1}{C} \quad (8.2)$$

8.2.4 TCT and β -scope setup

After the sensor is proved to be operable by the electric I-V, C-V test, another important step is to evaluate the transient performances of the device. To test the detector's response to extract the charge collection and time resolution performances for MIP, we need to inject a signal into the biased detector. This can be done by the charged particle beam at some dedicated accelerator infrastructures (usually called a test beam station), which is usually complex, and the time slot is limited. The two ways are recommended for the silicon detector to perform the charge collection and timing resolution test at the institute's laboratory, either by the β -source or the infra-red laser.

8.2 The laboratory setup for characterization of the LGADs at USTC

β -scope

First, the beta source. The ^{90}Sr is usually used due to its almost pure beta source without the associated gamma emission as others, and the radiation protection is more easily to be done with a thin shield. The ^{90}Sr will decay into the ^{90}Y with the 0.546 MeV decay energy, which is distributed to the electron, antineutrino, and the ^{90}Y . The ^{90}Y will further undergo a beta-decay with the energy of 2.28 MeV with another electron, antineutrino, and a relatively stable atom ^{90}Zr . Due to both of the decay having tree bodies in the final state, the energy of the electron follows a distribution function (namely the β -spectrum), and the energy deposition is not fixed. For such test, the source needs to be as close as possible to the detector's active area in order to get a high rate. Due to the MeV level energy and the thickness of the silicon, a maximum of three detectors can be placed in an aligned way for electrons to penetrate through. The schematic plot of the β -scope setup used at USTC can be found in Fig. 8.6 (a), and a photo of the setup can be found in Fig. 8.6 (b). Two amplifier boards are mounted for the testing.

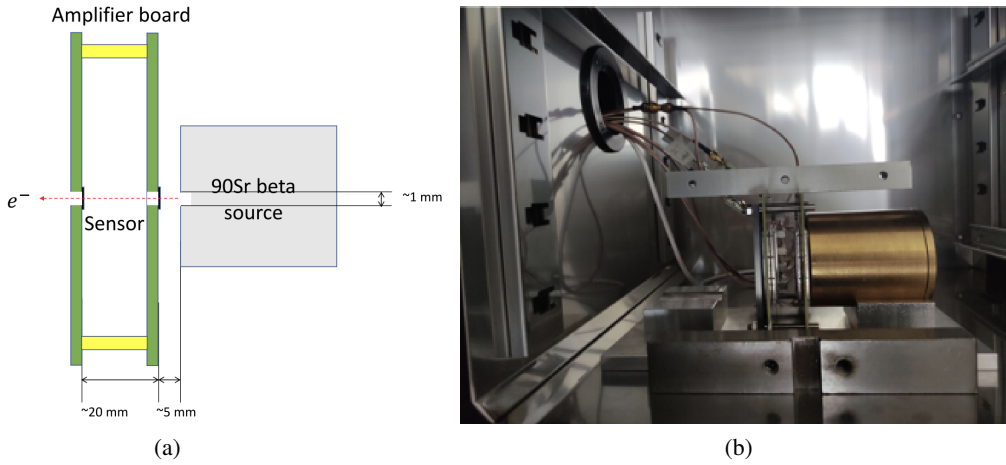


Figure 8.6: The setup of the β -scope system for the charge collection and timing performance test of LGAD with ^{90}Sr beta source. The schematic view (a) and a photo of the setup (b) are shown.

laser-TCT

Second, the Transient-Current Technique (TCT) utilizes the focused laser beam to realize the deposition of the charge via excitation. The 1064 nm laser is usually chosen to inject a uniform distributed charge into the silicon device since its absorption depth is 1 mm. The laser can be focused with a spot size smaller than 10 mm, allowing it to perform a scan of the detector with a good resolution. The advantage of using laser are listed below:

- It can inject the charge at a known position, thus allowing us to do the scan can be performed to study the devices' uniformity.
- The rate of injection can be adjusted, which allows us to accumulate the statistics within a relatively short time, which is extremely helpful in the 1D or 2D scan.

8 Characterization and Performance of the HPK and USTC-IME LGADs

- The amount of deposited charge can also be adjusted by tuning the strength of the laser, allowing us to mimic the charge deposition of MIP or heavy ions.
- There is no contribution from the Landau fluctuating for the time resolution measurement. Thus, we can measure the pure jitter contribution to break down the time resolution.

The setup of the TCT system is shown in Fig. 8.7 where the LGAD under test with the pre-amplifier board is mounted on a movable stage, allowing the fine scan of the sensors' surface with the focused laser. In this way, the uniformity and inter-pad gap can be measured.

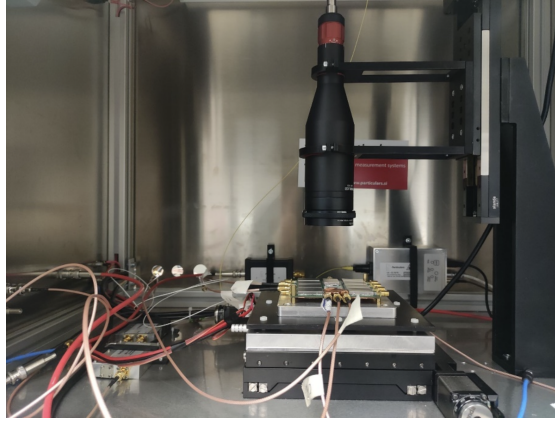


Figure 8.7: The setup of the laser TCT system for the inter-pad gap and jitter measurement at fixed position charge deposition, frequency under high rate. The 1064 nm infra-red laser is equipped for the silicon device test.

Data readout for transient test

The device under test is mounted on the pre-amplifier PCB board (shown in Fig. 8.8), where the front-end amplifier is designed. The signal induced by the charge deposition from the sensor and being amplified by the 2-stage amplifiers to get a voltage signal without adding any distortion or noise. The board was originally designed by UCSC, and further improved by the USTC to achieve a lower noise with a different PCB design and new amplifier components [230]. The total charge gain of the pre-amplifier board is $20.58 \text{ mV} \times \text{ns/fC}$ with 870 MHz at -3 dB. The circuit of the USTC pre-amplifier board is shown by a schematic plot in Fig. 8.9.

After being amplified, the signal from DUT is then read out by the oscilloscope at the sample rate of 10 GS/s and bandwidth of 1 GHz. The full waveforms of the signals are recorded for offline analysis. The reference LGAD or the scintillator is used as the trigger.

8.2.5 Data analysis for the transient test

The dataset contains full waveforms recorded by an oscilloscope for each event. The variables includes A_{max} , T_{max} , integral of the waveform around the peak (Pulse integral), RMS of the initial part of the waveform ($\text{Noise}_{\text{RMS}}$), time of arrival (TOA) are extracted from each waveform (as shown in Fig. 8.10

8.2 The laboratory setup for characterization of the LGADs at USTC

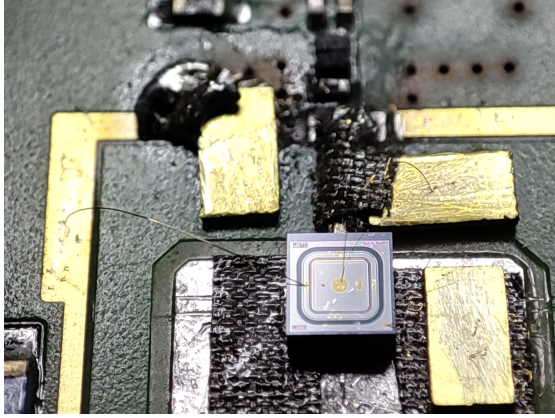


Figure 8.8: The USTC-IME LGAD sensor on the pre-amplifier board for the charge collection and timing resolution test.

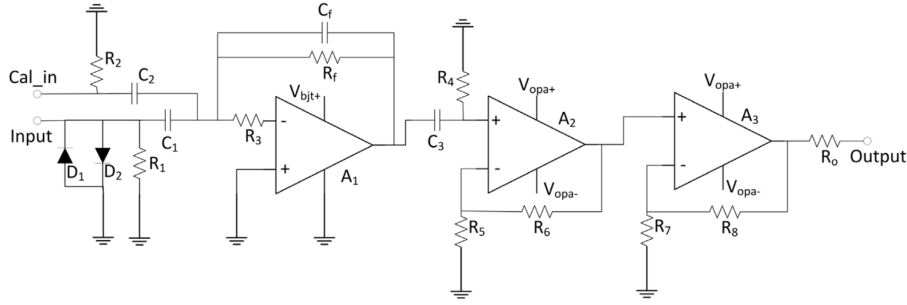


Figure 8.9: The simplified schematic of the LGAD pre-amplifier.

(a)). During data taking, a threshold of 50 mV is applied to the amplitude of the trigger sensor, but no threshold is applied to the DUT. The 2D distribution of the A_{\max} and T_{\max} of the waveforms from the DUT is shown in Fig. 8.10 (b), with visible background contribution. In order to reject background events, a threshold on the A_{\max} of the DUT is set, determined from a background-enriched control sample to ensure that less than 0.3% of background is left in the signal sample.

To determine an optimized A_{\max} threshold, the analysis of the un-irradiated sensor biased at 220 V is used as an example. The signal peak is located in the SR, a time window of -5 ns to 5 ns. The CR, a time window of -25 ns to -15 ns, is defined to study the background. Assuming that the out-of-time CR window is independent of the signal pulse, the waveform data in the CR represent the background in the SR. The noise A_{\max} distribution is extracted in the CR, and a threshold of 8.5 mV is selected to reject 99.8% of waveforms in the CR.

With $A_{\max} > 8.5$ mV in the SR, the 2D distribution of A_{\max} versus T_{\max} after selection is shown. To remove events outside the possible time window, the difference of T_{\max} between DUT and the trigger is required to fall into a time window of 1 ns, as indicated by the two red lines shown in the Fig. 8.10. The selected events are used to extract the charge collection and time resolutions.

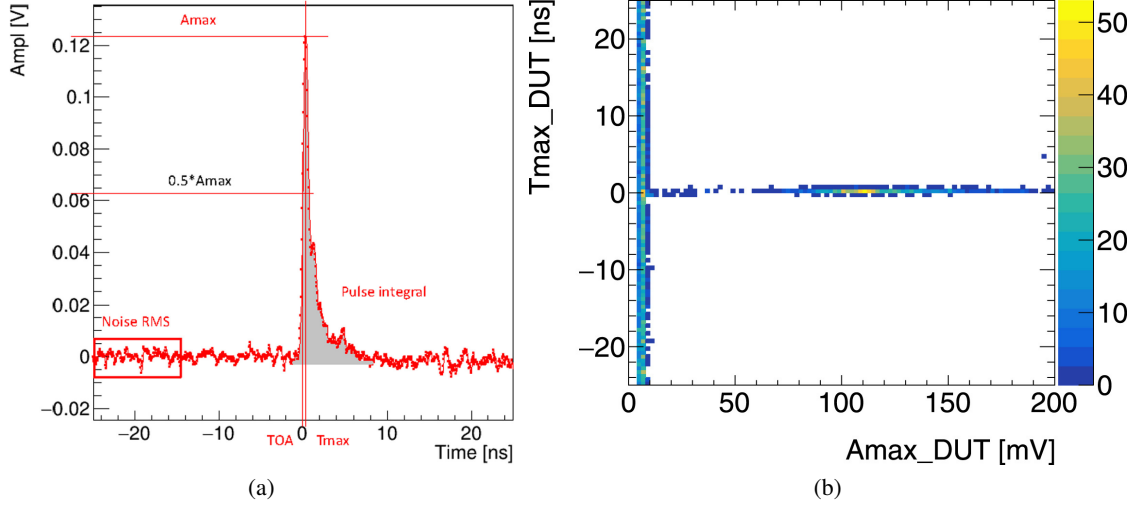


Figure 8.10: (a) The illustration of the variables being extracted from the waveforms. (b) The 2D distribution of the T_{\max} and A_{\max} for all events recorded and before the selection applied.

Collected charge

The charge collected in each event is determined by dividing the pulse integral by the calibration constant (κ) of the amplifiers. To obtain the calibration constant, signals of different pre-defined charges are generated using a fast square pulse (typical rise/fall time < 500 ps) from a signal generator that passes through a 1 pF calibration capacitor. These signals are then injected into the amplifiers, and a linear fit is used to determine the slope of the pulse integral versus the injected charge. The fit yields a calibration constant of $\kappa = 4.72 \pm 0.08$ mV ns/fC. To extract the most probable value (MPV) of the charge distribution, a Landau function convoluted with a Gaussian function is fitted to the charge distribution. The uncertainty of the MPV is estimated from the fit, and the uncertainty of the calibration constant is propagated to determine the total uncertainty of the collected charge Q .

Time resolution

To determine the time resolution, a Gaussian function is fitted to the distribution of TOA differences (ΔTOA) between the DUT and trigger, from which the standard deviation is extracted and denoted as $\sigma_{\Delta\text{TOA}}$. The time resolution of the DUT can be calculated using the following equation:

$$\sigma_t = \sqrt{\sigma_{\Delta\text{TOA}}^2 - \sigma_{\text{trigger}}^2}. \quad (8.3)$$

Here, σ_{trigger} represents the time resolution of the trigger, which is measured using two identical trigger sensors at the same bias voltage (165 V) and temperature (-30°C). The reference used is the 30 μm thick HPK sensor with a time resolution of (33.5 ± 0.8) ps.

8.3 Results from laboratory test

8.3.1 I-V/ C-V results of the HPK LGADs

The HPK LGAD sensor prototypes being tested for I-V and C-V in the lab consist of various types, each with distinct properties. The results are shown in the Fig. 8.11. As summarized in Tab. 8.4, HPK-1.1-30 and HPK-2-30 have a thickness of 35 μm , deep and narrow doping, and a bulk resistivity of $\sim 0.07 \text{ k}\Omega \text{ cm}$. HPK-1.2-30 also has a thickness of 35 μm , deep and narrow doping, but with a bulk resistivity of $\sim 3.5 - 4.5 \text{ k}\Omega \text{ cm}$. Meanwhile, HPK-3.1-50 and HPK-3.2-50 have a thickness of 50 μm , with the former having deep doping and the latter having very deep and narrow doping. Both HPK-3.1-50 and HPK-3.2-50 have a bulk resistivity of $\sim 3.5 - 4.5 \text{ k}\Omega \text{ cm}$. These samples represent a diverse range of LGAD sensor designs to be evaluated for their performance in the laboratory.

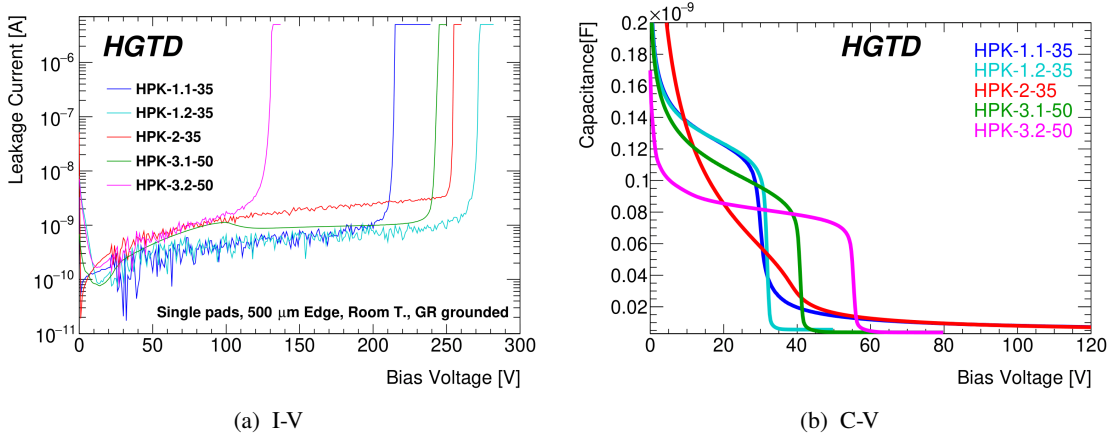


Figure 8.11: The (a) I-V and (b) C-V curves of the HPK prototype 1.1, 1.2, 2, 3.1, 3.2 LGADs.

The performances of different types of sensors are compared using single pads which have exactly the same geometry. For the 35 μm sensors, the HPK-1.1-35 sensors have breakdown voltages of 215V, while HPK-1.2-35, with the similar gain layer implantation but a higher bulk resistivity, shows a higher breakdown voltage of 270V. The HPK-2-35 sensor which has a similar bulk resistivity as HPK-1.1-35 but shallower and wider doping shows a higher breakdown voltage of 254V. For the 50 μm sensors, the major difference between HPK-3.1-50 and HPK-3.2-50 is the depth of the gain layer implantation. For HPK-3.1-50 which has a shallower implantation, the breakdown voltage is 242V. HPK-3.2-50 has a deeper implantation and its breakdown voltage is 130V, which is much lower. All measured sensors have a low leakage current level (sub-nA) before the breakdown.

The C-V measurement results for the HPK LGAD prototypes reveal insightful information about the V_{GL} and V_{FD} values for each sensor type. For the HPK-1.1-35 sensor, the V_{GL} is measured at 31 V, while the V_{FD} is observed at 195 V. In the case of HPK-1.2-35, the values are slightly higher for V_{GL} , at 33 V, and significantly lower for V_{FD} , at 36 V. The HPK-2-35 sensor shows a higher V_{GL} of 40 V and an intermediate V_{FD} of 144 V. For the thicker HPK-3.1-50 sensor, the V_{GL} is 42 V, and the V_{FD} is 49 V. Lastly, the HPK-3.2-50 sensor exhibits the highest V_{GL} of 56 V and a V_{FD} of 64 V. The measured results are summarized in the Tab. 8.5.

8 Characterization and Performance of the HPK and USTC-IME LGADs

Table 8.4: The information of the HPK sensor prototypes being tested.

Type	Thickness	Doping	Bulk Resist. [$k\Omega\text{ cm}$]
HPK-1.1-30	35 μm	Deep, Narrow	~ 0.07
HPK-1.2-30	35 μm	Deep, Narrow	$\sim 3.5 - 4.5$
HPK-2-30	35 μm	Shallow, Wide	~ 0.07
HPK-3.1-50	50 μm	Deep	$\sim 3.5 - 4.5$
HPK-3.2-50	50 μm	Very Deep, Narrow	$\sim 3.5 - 4.5$

Table 8.5: The extracted V_{GL} , V_{FD} , V_{BD} from the I-V and C-V curves, which is important for the performance of the LGAD sensor for a stable operation.

Type	V_{GL}	V_{FD}	V_{BD}
HPK-1.1-35	31	195	215
HPK-1.2-35	33	36	270
HPK-2-35	40	144	254
HPK-3.1-50	42	49	242
HPK-3.2-50	56	64	130

For each prototype measured, the $N - V$ curves are also calculated and shown in Fig. 8.12, from which we can see the depletion of the gain layer and the substrate clearly. The corresponding V_{GL} is also calculated by the minimum points shown in the curve, and this method has been proven to be more precise and sensitive compared to the legacy C-V method.

Further analysis of the sensors' uniformity on the 5×5 arrays is performed. The I-V and C-V curves are measured for each pad with the probe card (shown in Fig. 8.13). Both the breakdown and the gain layer depletion voltages are extracted.

The uniformity results are shown as the 2 dimensional maps where the V_{BD} or V_{GL} is shown by the color. The distribution of the V_{GL} by C-V measurement is shown in Fig. 8.15 (a) and by I-V measurement is shown in Fig. 8.15 (b). The distribution of the V_{BD} is shown in Fig. 8.14. A clear dependency of the V_{BD} and V_{GL} on the position of the pads in the array can be seen. For the validation of the methods, the V_{GL} from both I-V and C-V measurement and the V_{BD} are analyzed by the scattering plot where linear fits are performed (shown in Fig. 8.16). The negative correlation has been observed as expected, proving the effectiveness of the method. More detailed methods and analysis can be found in [200].

8.3 Results from laboratory test

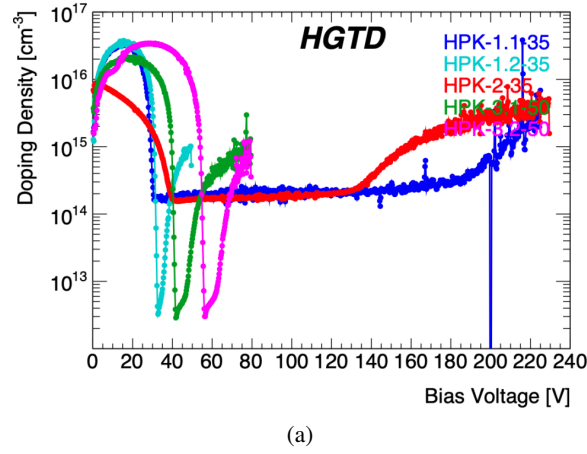


Figure 8.12: The N-V curves used for the V_{GL} determination, as we can see, for prototypes that have high bulk resistance, a dip can be clearly observed in the N-V curve.

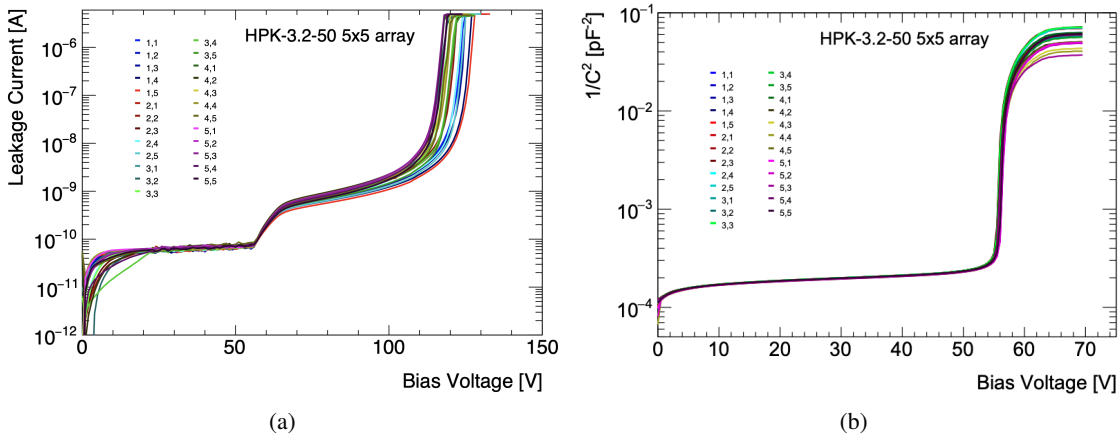


Figure 8.13: The I-V (a) and C-V (b) curves of the HPK prototype 3.2 5×5 LGADs measured with the probe card by USTC.

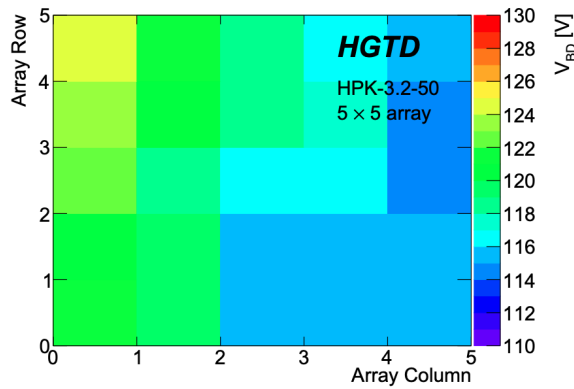


Figure 8.14: The V_{BD} distribution of the HPK prototype 3.2 5×5 LGADs measured from I-V.

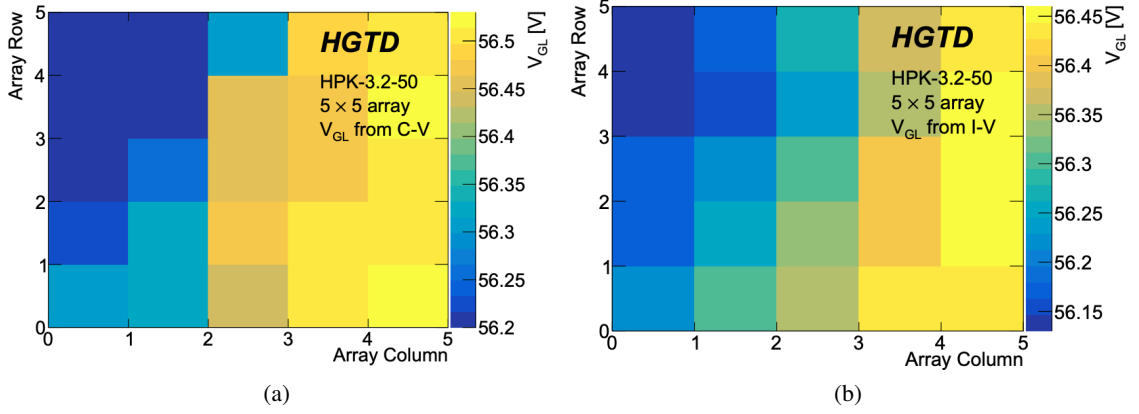


Figure 8.15: The V_{GL} distribution of the HPK prototype 3.2 5×5 LGADs measured from (a) C-V and from (b) I-V.

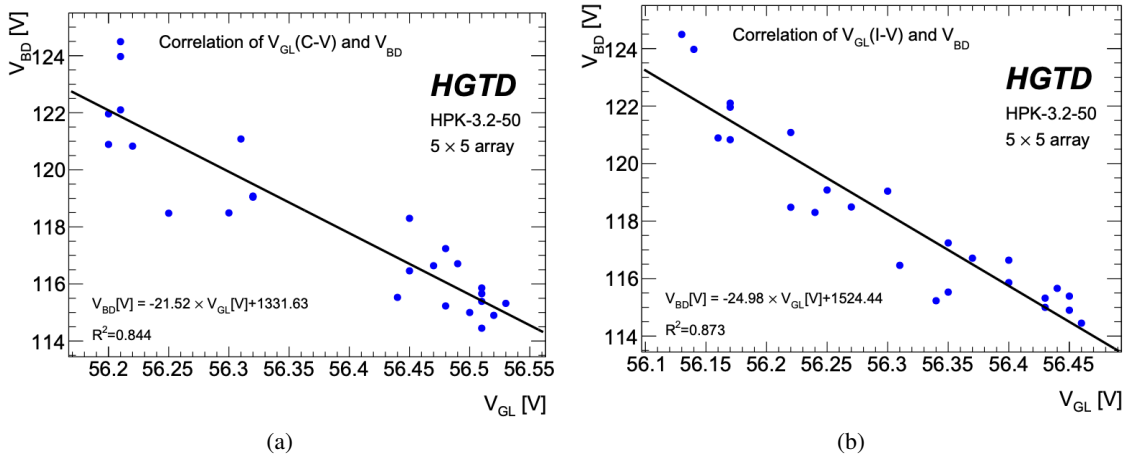


Figure 8.16: The correlation of the V_{GL} (left from C-V measurement and right from I-V measurement) and V_{BD} for the HPK prototype 3.2 5×5 LGADs.

8.3.2 Impact of the neighboring floating pads

During the operation of HL-LHC, a few pads might break down early in the large array. These pads can introduce large current to the neighbor channels and arise challenges on operating the detector safely. Thus, the impact of floating pads has to be studied. This issue also arose in the collaboration during the technique design review. The impact of the floating pads is studied with irradiated 5×5 LGAD array and probe card. We compare the nine central pads I-V change with or without central pad connected. After further analysis of the summary current of surrounding pads, we observed that the current has a sudden change at around 90 V due to the punch-through effect.

Further study indicated that disconnected pads would be biased by punch through with 90 V voltage difference, and after the punch through happens, the bias difference seems to remain around 70 V

8.3 Results from laboratory test

from the behavior of the current (shown in Fig. 8.17). The current would be separately collected by the four neighbor pads. The conclusion is that the disconnected pad would be biased by the neighbor pads, and the current is collected by neighbor pads. Meanwhile, the total current would not increase significantly.

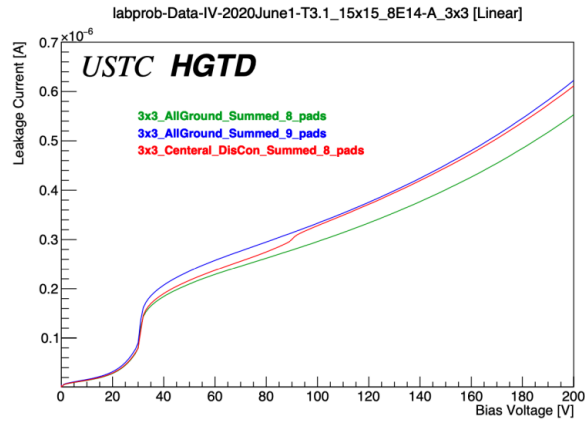


Figure 8.17: The leakage current distribution in 3 circumstances to study floating pad impact.

8.3.3 Measurements of the first batch USTC-IME LGADs

The first batch of USTC-IME LGADs consists of two production batches: pre-production (USTC-1.0) and stable version (USTC-1.1). In the pre-production batch, six wafers (**W1** to **W6**) were produced, targeting different breakdown voltages (V_{BD}) by varying the gain layer energy, dose, and implantation type. Specifically, **W1** and **W2** feature a medium gain layer energy and dose, type B implantation, and a target V_{BD} of 165V. **W3** is designed with a low gain layer energy, high dose, type B implantation, and a target V_{BD} of 150V. **W4** possesses a high gain layer energy, low dose, type B implantation, and a target V_{BD} of 180V. **W5** is characterized by a medium gain layer energy, low dose, type B implantation, and a target V_{BD} of 265V. Lastly, **W6** exhibits a medium gain layer energy, medium dose, types B and C implantation, and a target V_{BD} of 165V.

For the stable version batches, five wafers (**W7** to **W11**) are produced. **W7** has a medium gain layer energy, low dose, type B implantation, and a target V_{BD} of 270V. **W8** features a low gain layer energy, high dose, type B implantation, and a target V_{BD} of 195V. **W9** is designed with a high gain layer energy, low dose, type B implantation, and a target V_{BD} of 200V. **W10** exhibits a medium gain layer energy, medium dose, type B implantation, and a target V_{BD} of 200V. Lastly, **W11** possesses a medium gain layer energy, medium dose, types B and C implantation, and a target V_{BD} of 200V. The Tab. 8.6 also provides the measured V_{BD} , V_{GL} , and V_{FD} values for each wafer, giving a comprehensive overview of the USTC-IME LGADs' properties. The measured I-V curves can be found in Fig. 8.18 (a), and the C-V curves can be found in Fig. 8.18 (b).

Table 8.6: Overview of the information and the main test results for the first batch USTC-IME LGADs.

Production Batch	Wafer No.	$V_{BD,target}$ [V]	GL.Energy	GL.Dose	Implantation	V_{BD} [V]	V_{GL} [V]	V_{FD} [V]
USTC-1.0 (test run)	W1	165	Medium	Medium	B	154	45	65
	W2	165	Medium	Medium	B	150	46	54
	W3	150	Low	High	B	110	34	> 70
	W4	180	High	Low	B	148	75	100
	W5	265	Medium	Low	B	264	45	80
	W6	165	Medium	Medium	B + C	84	48	> 65
USTC-1.1	W7	270	Medium	Low	B	370	38	55
	W8	195	Low	High	B	295	29	40
	W9	200	High	Low	B	295	70	85
	W10	200	Medium	Medium	B	320	40	50
	W11	200	Medium	Medium	B + C	300	41	52

The samples from different wafers are also sent for irradiation at JSI by the reactor neutrons at different fluences. The I-V curves at $-30\text{ }^{\circ}\text{C}$ after different fluences are shown in Fig. 8.19 (a) and the measured V_{GL} for different wafers are shown in Fig. 8.19 (b). The c-factors are calculated with the exponential fit, and the wafer with the carbon diffused gain layer shows a c-factor of $1.85 \times 10^{-16}\text{ cm}^2$, and those without gain layer show the c-factor in the range of 4.34×10^{-16} to $7.25 \times 10^{-16}\text{ cm}^2$. The wafers

8.3 Results from laboratory test

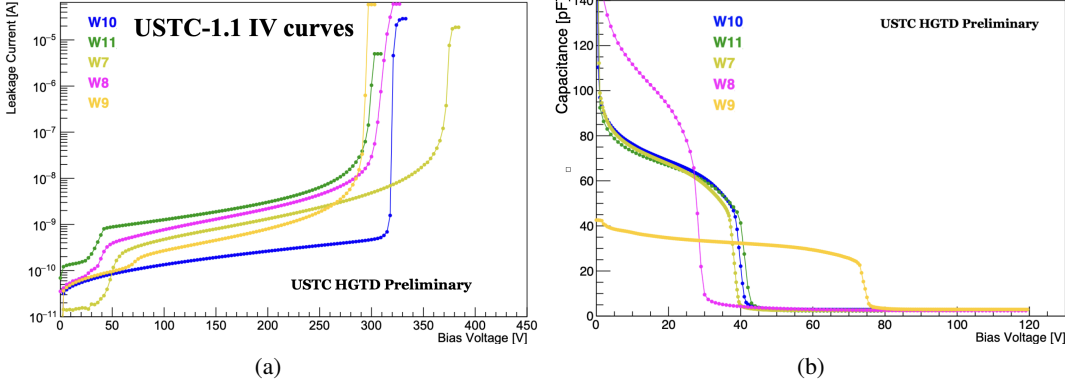


Figure 8.18: The I-V and C-V curves measured for the first batch USTC-IME wafers.

with the carbon diffused show significantly better radiation resistance, and the rate of the acceptor removal is much slower than those without carbon diffused.

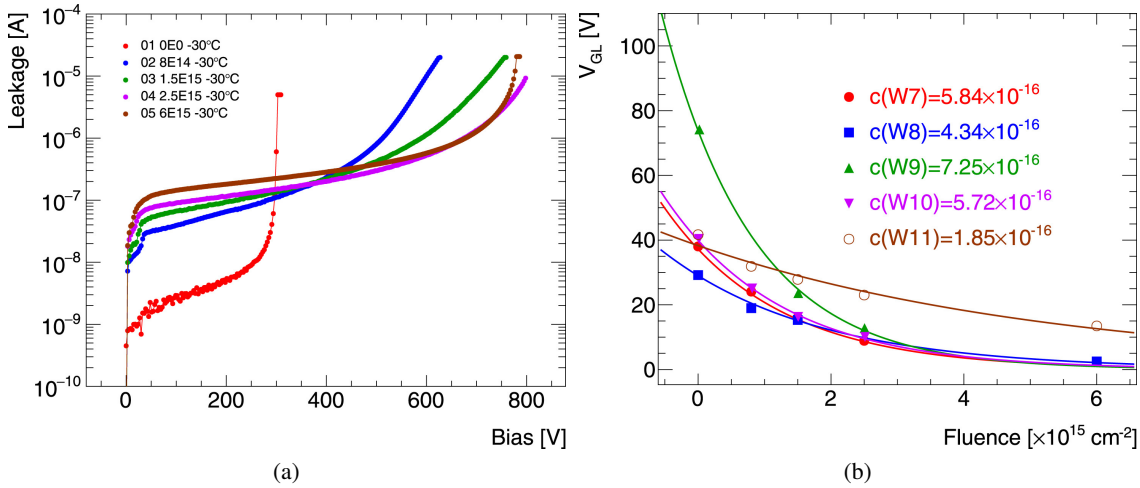


Figure 8.19: (a) The IV of the carbon enriched USTC IME LGADs after the different fluence. (b) The dependency of measured V_{GL} on the different fluence irradiated LGADs.

Timing and charge-collection

The USTC-IME **W11** sensor exhibits varying performance in terms of timing resolution and collected charge as a function of radiation fluence and the corresponding bias voltages required for a collected charge of approximately 4 fC. At a radiation fluence of 0, the timing resolution is 53.9 ± 1.9 ps, and the collected charge is 5.76 ± 0.14 fC at a bias voltage of 140 V. As the radiation fluence increases, the bias voltage also increases to maintain the collected charge. The lowest timing resolution, 43.3 ± 2.1 ps, is observed at $8 \times 10^{14} \text{ cm}^{-2}$ and a bias voltage of 330 V, while the collected charge generally decreases as the radiation fluence increases. At the highest radiation fluence of $6 \times 10^{15} \text{ cm}^{-2}$, a bias voltage of

8 Characterization and Performance of the HPK and USTC-IME LGADs

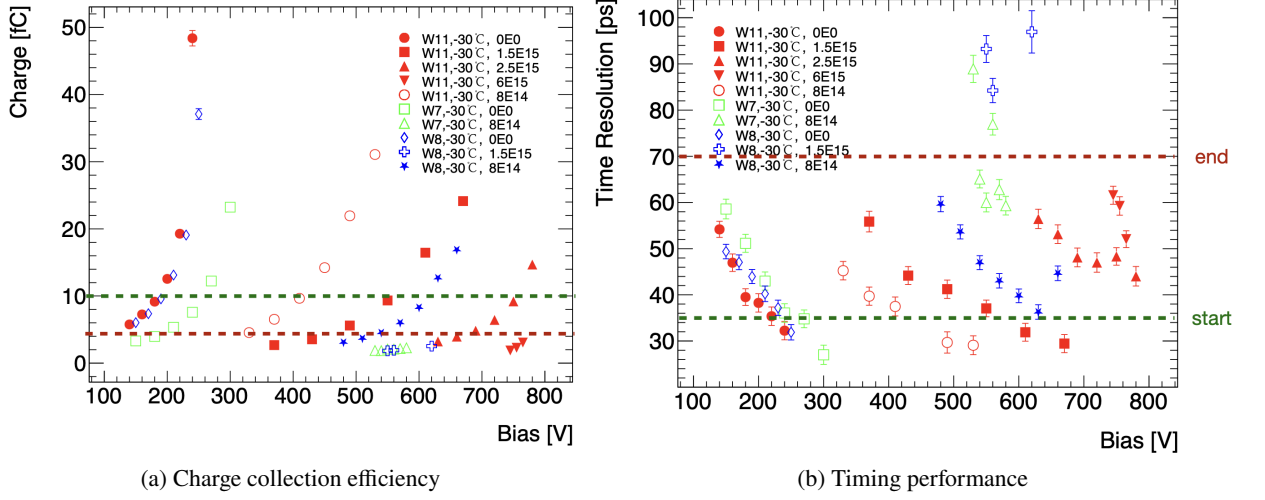


Figure 8.20: The measured result of the USTC-IME first batch LGADs with β -source.

765 V is required, the timing resolution is 50.2 ± 1.9 ps, and the collected charge is 3.07 ± 0.09 fC. These results illustrate the sensor's performance degradation with increased radiation exposure. The results are summarized in Tab. 8.7 and shown in Fig. 8.20.

Table 8.7: Charge collection efficiency and Timing performance of the irradiated USTC-IME **W11** carbonated LGADs.

Radiation fluence [cm^{-1}]	0	8e14	1.5e15	2.5e15	6e15
Bias voltage (4 ~ fC) [V]	140	330	430	660	765
Time resolution [ps]	53.9	43.3	44.1	54.0	50.2
Uncertainty [ps]	1.9	2.1	2.0	2.7	1.9
Collected charge [fC]	5.76	4.56	3.55	3.64	3.07
Uncertainty [fC]	0.14	0.11	0.09	0.12	0.09

8.3.4 Measurements of the second batch USTC-IME LGADs

I-V and C-V measurements

The results of the single pad for the second batch USTC-IME LGADs I-V curves are shown in Fig. 8.21, we can see a good V_{BD} is achieved between 160 V to 190 V at room temperature for USTC-IME **W17** and **W19**, which guaranteed a good performance both before and after the irradiation at low temperature. More tests on the large array device are performed and good uniformity is shown in the measurement which fulfills the HGTD requirements. The V_{BD} distribution from wafer level

8.3 Results from laboratory test

I-V measurement is shown in Fig. 8.29 and Fig. 8.30. The variation is observed, which is due to the fabrication process limitation. In order to estimate the uniformity and yield, the wafer level measurement is also processed for each wafer (as shown in Fig. 8.22). The analysis of the uniformity and yield at the wafer level are shown in Sec. 8.7.1.

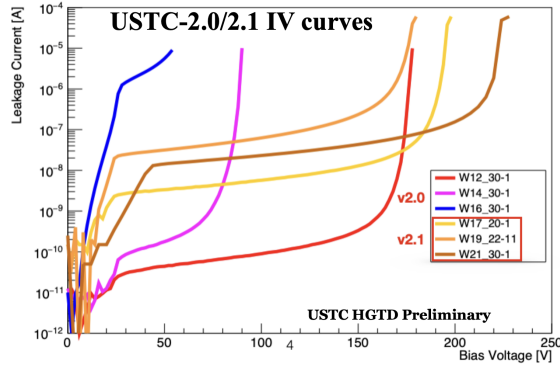


Figure 8.21: The I-V results of the USTC-IME batch 2 LGADs with different gain layer designs.

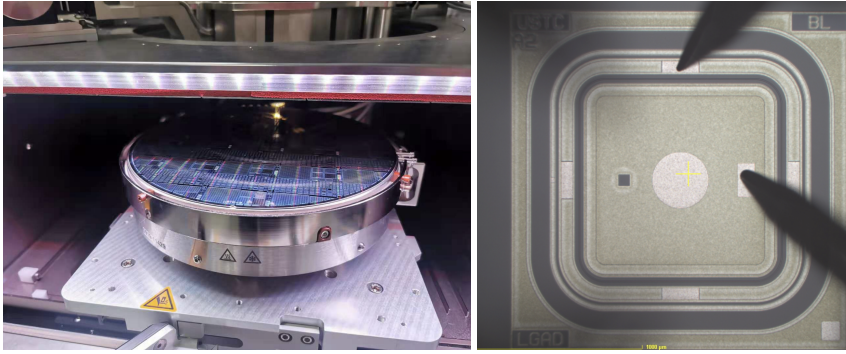
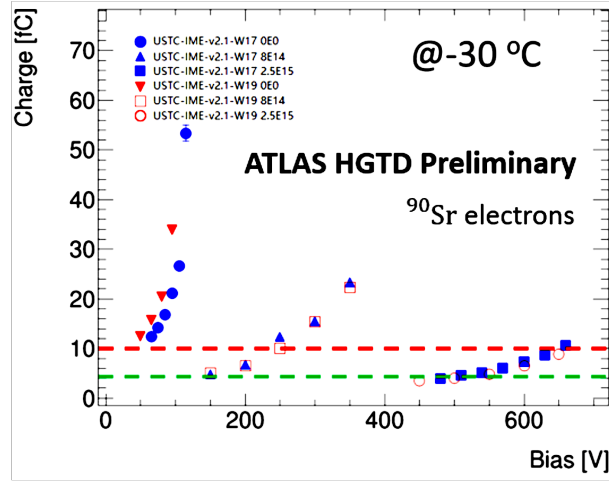


Figure 8.22: The LGAD wafers at the automatic probe station(left) and microscopic version of the LGAD wafers at the automatic probe station (right) .

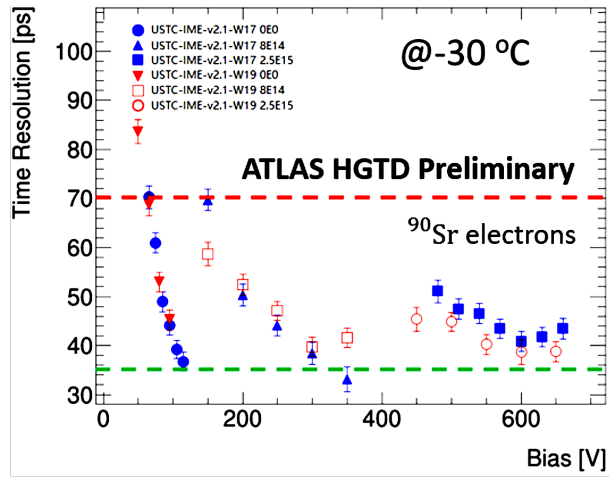
Timing and charge-collection

The results of the timing and charge collection performances are shown in Fig. 8.23. From the results, we can see a good performance is achieved by the USTC-IME **W17** and **W19**. Both of them fulfill the requirement of time resolution before and after irradiation.

8 Characterization and Performance of the HPK and USTC-IME LGADs



(a)



(b)

Figure 8.23: (a) Charge collection and (b) timing resolution of the USTC-IME version 2.1 LGADs. The measurements are performed under $-30\text{ }^{\circ}\text{C}$ with the beta source. The green and red lines specify the requirements corresponding to the initial and end-of-life performances in the specifications.

8.4 Test with charged particle beams at CERN PS/SPS and DESY

8.4.1 Setup of the test beam

Several test beam campaigns were conducted using a 120 GeV pion beam at CERN Super Proton Synchrotron (SPS) H6A line and a 5 GeV electron beam at DESY TB 22 line. The setups at both facilities were similar, with the exception that at DESY, only three DUTs could be tested to reduce multiple scattering. Fig. 8.24 shows a picture of the test beam setup at DESY TB22. The setup included a EUDET-type telescope, which consisted of two arms, each made of three MIMOSA pixel planes of $10.6 \times 21.2 \text{ mm}^2$, providing particle track information with a few-micrometer resolution [231]. The DUTs, assembled on the pre-amplifier boards, were placed between the two arms of the telescope on a movable stage. The tracking information allowed for the reconstruction of particle trajectories and the identification of the specific position where the DUT was hit. Further details on the setup and its components can be found in the plots below.

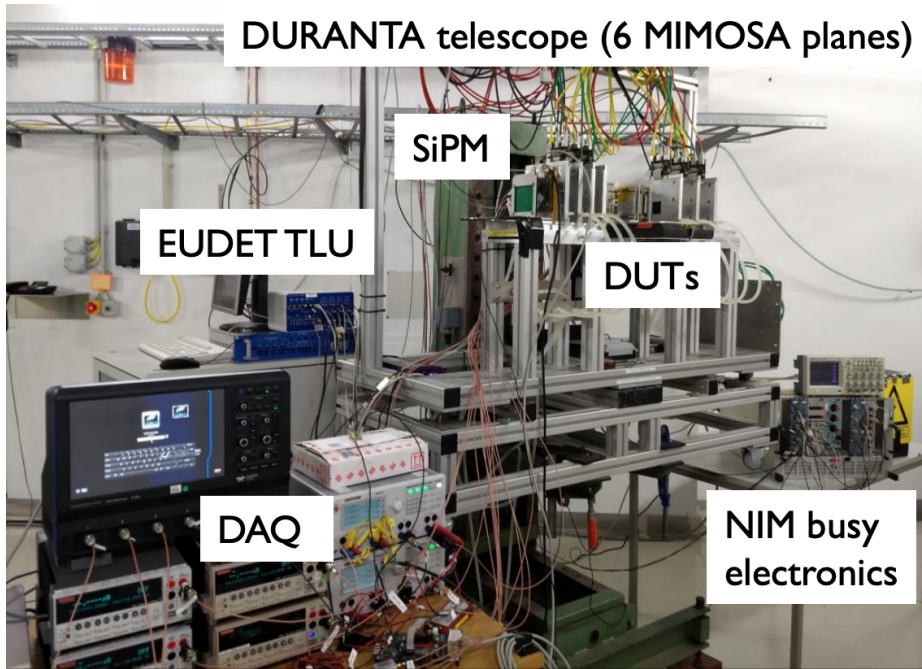


Figure 8.24: A photo of the test beam setup at DESY TB 22 beam station with 5 GeV electron for the LGAD performance test. The EUDET beam telescope with MIMOSA pixel is used for tracking. Similar hardware setup and the data acquisition system are used at CERN PS/SPS test beam for other campaigns.

8.4.2 Trigger and DAQ

The signals generated by the DUTs were digitized and recorded by a four-channel oscilloscope. The first three channels of the oscilloscope were dedicated to capturing signals from the DUTs, while the fourth channel recorded a time reference signal from a SiPM assembly. To define the ROI, an area of

approximately $3\text{ mm} \times 3\text{ mm}$ was selected on an FE-I4 plane, which covered the projected area of the LGADs and SiPM. To trigger the data acquisition process, the downstream intersecting scintillator in the oscilloscope, the HitOr signal from the FE-I4 plane, and the oscilloscope auxiliary output were used as input to the EUDET trigger logic unit (TLU). When the oscilloscope was triggered by an external signal from the TLU, it generated a TTL pulse that was sent back to the TLU module for synchronization of the telescope and FE-I4 DAQ system. Two independent data streams were recorded: one containing particle position information from the telescope and the FE-I4, and a second one containing waveform signals from the DUTs captured by the oscilloscope. These data streams were merged offline to enable a more comprehensive analysis of the experimental results.

8.4.3 Track reconstruction for data from EUDET-type telescope

The EUDET-type telescope and FE-I4 were used in combination to provide tracking information that enabled the reconstruction of particle trajectories and identification of the precise position where the DUT was hit.

To achieve tracking capability, the EUDET-type telescope utilized six MIMOSA planes, as described in the previous section. The positions of the MIMOSA, FE-I4, and DUT planes were recorded with a high precision of 1 mm in the z-direction along the beam line. The hits from each MIMOSA plane, along with their respective z-coordinate, were utilized to reconstruct particle trajectories and (x,y)-coordinates of the hits in the DUT planes.

Before clustering, “hot” pixels with occupancy greater than ten times the average were removed from the MIMOSA planes. The remaining hits were grouped into clusters, with only those with a maximum of 20 hits being utilized for tracking. The cluster coordinates were determined by the centroid of the hit coordinates in x and y. Events with exactly one cluster in the FE-I4 plane were the only ones considered.

To align the MIMOSA planes, the plane coordinates were iteratively shifted in the x and y direction with respect to a reference plane to minimize the difference between the reconstructed track position at the MIMOSA plane and the measured hit position in the same plane. The position resolution was determined as the resolution of the fit during the alignment procedure.

By utilizing the z-position of the MIMOSA planes along the beam axis and the x- and y-positions of the hits in these planes, 3D tracks were constructed. The procedure is described in the reference for data taken during test beams at CERN SPS with 120 GeV pion beam, where tracks are straightforward as there is no scattering. For data collected at DESY with a 5 GeV electron beam, the procedure was slightly different due to possible electron scattering in the equipment around the DUTs.

As shown in Fig. 8.25, 3D-proto-tracks were reconstructed from the three MIMOSA planes before the DUTs on the beam trajectory (upstream triplets), and other 3D-proto-tracks were reconstructed from the three MIMOSA planes after the DUTs (downstream triplets). The downstream triplets must coincide with a hit in the FE-I4 plane.

To identify the path of the particles passing through the six MIMOSA planes, all possible upstream and downstream triplets are reconstructed for each event. A track is considered to be complete only if a downstream triplet matches an upstream triplet in the central region, with a minimum distance of

8.4 Test with charged particle beams at CERN PS/SPS and DESY

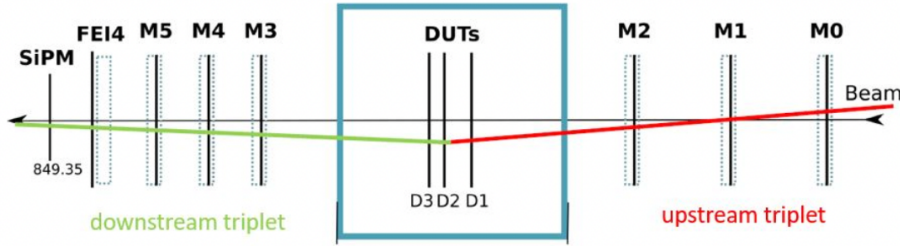


Figure 8.25: 3D-proto-tracks are reconstructed from the three MIMOSA planes before the DUTs (“upstream triplets”), and other 3D-proto-tracks are reconstructed from the three MIMOSA planes after the DUTs (“downstream triplets”). The downstream triplets must coincide with a hit in the FE-I4 plane.

approach of 150 μm . Events that have only one complete track through all six MIMOSA planes are taken into consideration for analysis.

8.4.4 Treatment of the oscilloscope waveform

The LGAD waveform processing method is thoroughly explained in Sec. 8.2.5. The procedure involves determining the start and stop points of the pulse, followed by calculating the pedestal in a region where no signal is expected. This pedestal value is then subtracted from every data point in the waveform on an event-by-event basis. After subtraction, the start and stop points are re-evaluated. Various waveform properties such as maximum pulse amplitude, charge, rise time, jitter, signal-to-noise ratio, and TOA can be extracted at this stage.

The procedure for waveform analysis involved multiple steps in extracting various properties of the pulse. The maximum amplitude of the pulse was identified by determining the sample with the highest amplitude within the signal region. The collected charge was computed as the integral of the pulse in the signal region, divided by the trans-impedance of the read-out board and the gain of the voltage amplifier. The TOA was determined using a constant fraction discriminator (CFD) method, which involves calculating the point at which the signal crosses a predefined fraction (fCFD) of its total amplitude. The SiPMs were analyzed using a TOA value of fCFD = 20%, whereas the DUTs were analyzed using a TOA value of fCFD = 50%. These values were selected based on the analysis of the DESY test beam data.

The final step involved merging the oscilloscope and telescope data to produce a single file. This process combined the information extracted from the oscilloscope waveforms with the position of the beam particle hit in the sensor plane, allowing for a unified analysis of both sets of data for each event and DUT. This ensured that all relevant information was available for a comprehensive analysis of the experimental results.

8.4.5 Data analysis

The efficiency of the detector in the LGAD sensors in the test beam is calculated by

$$\varepsilon = \frac{\text{\#Reconstructed tracks through LGAD with } Q > \text{charge threshold}}{\text{\#Total reconstructed tracks through LGAD}}. \quad (8.4)$$

Unless otherwise specified, the charge threshold is defined as 4 fC for the sensor performance evaluation in HGTD LGADs.

In the test beam, we have 2 DUT and one reference detector (either MCP or SiPM). The time resolution of the detector in the test beam is obtained by solving the below equations:

$$\begin{aligned} \sigma_{1,2}^2 &= \sigma_1^2 + \sigma_2^2, \\ \sigma_{2,3}^2 &= \sigma_2^2 + \sigma_3^2, \\ \sigma_{1,3}^2 &= \sigma_1^2 + \sigma_3^2. \end{aligned}$$

Then we can easily get the time resolution of the DUT 1 by

$$\sigma_1 = \sqrt{\frac{\sigma_{1,2}^2 + \sigma_{1,3}^2 - \sigma_{2,3}^2}{2}}.$$

Similarly, we can get σ_2 and σ_3 .

If the time resolution of one reference is a known value and performs stability during the test beam (like MCP or SiPM), the Eq. 8.3 can also be used for obtaining the time resolution. The usage of the equation to calculate the time resolution depends on the test beam setup and the behavior of the reference.

8.5 Results from the test beam

8.5.1 Time resolution and charge collection

The test beam results for carbonated LGAD sensors from IHEP-IME, USTC-IME, and FBK, as presented in Tab. 8.8, demonstrate promising performance after irradiation at different fluences. For USTC-IME-v2.1-W17 sensors, a fluence of $1.5 \times 10^{15} \text{ n}_{\text{eq}}\text{cm}^{-2}$ results in a bias voltage of 270 V required to reach 4 fC collected charge, with a time resolution of 44 ps at 350 V and an efficiency of 98.9%. At a higher fluence of $2.5 \times 10^{15} \text{ n}_{\text{eq}}\text{cm}^{-2}$, the same sensor requires a bias voltage of 470 V for a 4 fC collected charge and exhibits a time resolution of 46 ps at 550 V.

IHEP-IME-W7Q2 sensors achieve a time resolution of 39 ps at 450 V and an efficiency of 99.8% after irradiation at $1.5 \times 10^{15} \text{ n}_{\text{eq}}\text{cm}^{-2}$. When exposed to a fluence of $2.5 \times 10^{15} \text{ n}_{\text{eq}}\text{cm}^{-2}$, these sensors

8.5 Results from the test beam

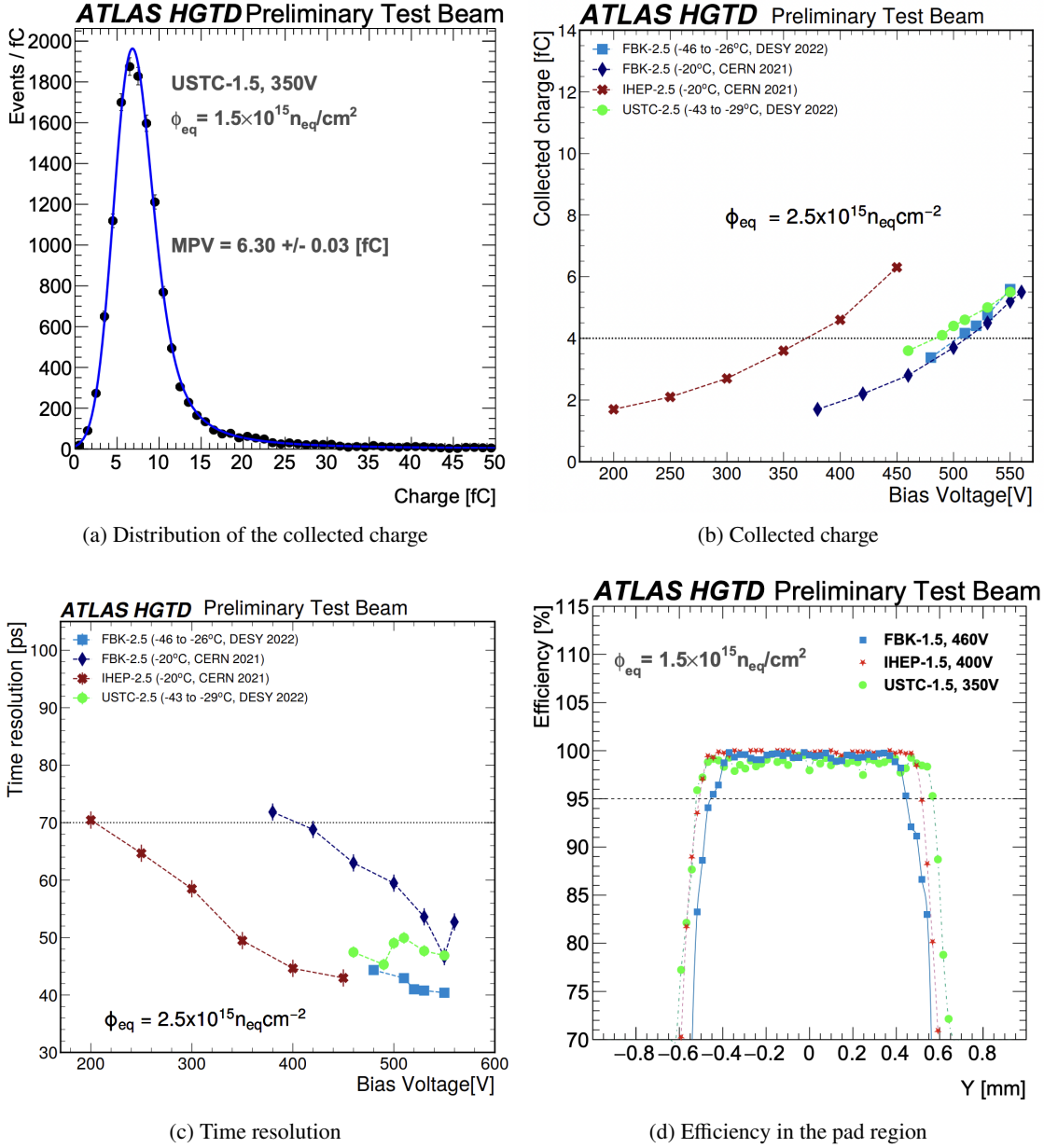


Figure 8.26: The measured results of the three carbonated LGAD prototypes from USTC-IME as well as IHEP-IME and FBK after the highest required fluence. The distribution of the collected charge under the beam is shown in (a), the collected charge at different bias voltages is shown in (b), the time resolution at different bias voltages is shown in (c), the efficiency in 1 dimension is shown in (d). The HGTD required performance is shown by the dashed line. The results demonstrated the good performance of USTC-IME LGADs that exceeded the requirement by a significant margin.

maintain a time resolution of 43 ps at 450 V. Meanwhile, FBK-UFSD3.2-W19 sensors exhibit a time resolution of 39 ps at 450 V and an efficiency of 99.4% at a fluence of $1.5 \times 10^{15} n_{eq}/cm^2$, and a time

8 Characterization and Performance of the HPK and USTC-IME LGADs

Table 8.8: The measured result of the collected charge and time resolution for carbonated LGAD sensor promising. The sensors tested are the most promising prototypes from IHEP-IME, USTC-IME and FBK.

Sensor	Fluence [$n_{eq}cm^{-2}$]	Bias at 4 fC [V]	σ_t [ps] (Bias [V])	Efficiency [%]
USTC-IME-v2.1-W17	1.5×10^{15}	270	44 (350)	98.9
IHEP-IME-W7Q2	1.5×10^{15}	270	39 (450)	99.8
FBK-UFSD3.2-W19	1.5×10^{15}	270	39 (450)	99.4
USTC-IME-v2.1-W17	2.5×10^{15}	470	46 (550)	-
IHEP-IME-W7Q2	2.5×10^{15}	370	43 (450)	-
FBK-UFSD3.2-W19	2.5×10^{15}	500	40 (550)	-

resolution of 40 ps at 550 V after irradiation at $2.5 \times 10^{15} n_{eq}cm^{-2}$.

These results indicate that USTC-IME LGAD sensors meet the HGTD specifications, achieving a time resolution of 70 ps and a hit efficiency of 95% by a significant margin after irradiated to the highest fluences. The full results are shown in Fig. 8.26.

8.5.2 Inter-pad gap distance

The measured inter-pad gap distances are shown in Fig. 8.27 (d). The occupancy map of the DUT 2x2 LGAD is shown in Fig. 8.27 (a). The sensor efficiency is calculated by the ratio between the number of the signal with a charge larger than 4 fC and the total number of the track that passes through the active area of the detector (Eq. 8.4). The efficiencies are calculated for each bin, and the 2D map is shown in Fig. 8.27 (b). A good uniformity is demonstrated, and the inter-pad gap distance is extracted by a fitting of the efficiency 1-D distribution in the gap region with the error function on both sides as shown in Fig. 8.27 (c). The final inter-pad is calculated by the distance of the region with an efficiency of less than 50%.

The test beam results for USTC-IME LGAD sensors, as presented in the Tab. 8.9, show the inter-pad distance (IP) measurements at different bias voltages for W19-2x2-IP3 and W17-2x2-IP3 sensors. For W19-2x2-IP3 sensors, the IP measured is 58.60 μm at 155 V, 63.33 μm at 145 V, and 64.61 μm at 135 V. Meanwhile, for W17-2x2-IP3 sensors, the IP measured is 60.47 μm at 170 V, 58.53 μm at 160 V, and 62.20 μm at 150 V.

In the end, an inter-pad gap distance between 63 μm to 65 μm is obtained, which consists with our expectation (around 30 μm larger than the nominal value 30 μm). These results demonstrate that USTC-IME LGAD sensors meet the HGTD specification of 100 μm inter-pad distance with an around 35 μm margin, thereby enabling a high fill factor.

8.5 Results from the test beam

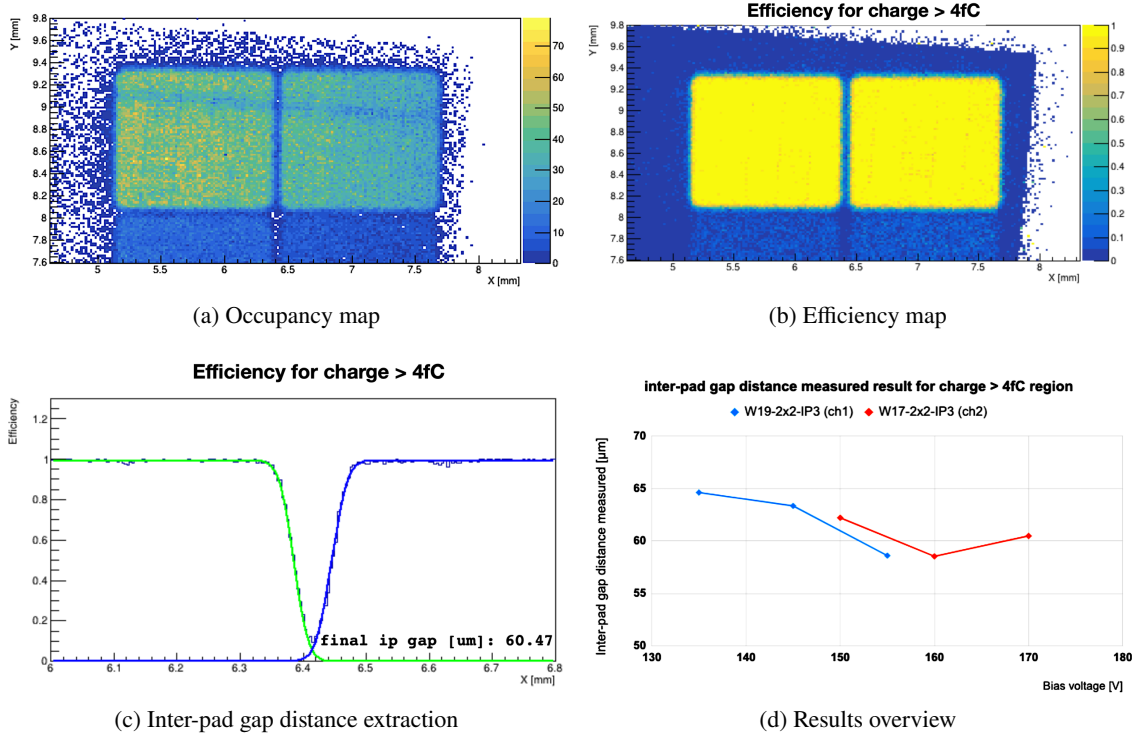


Figure 8.27: The inter-pad gap distance measured by the charged particle beam at CERN/SPS with the EUTelescope. The track is constructed with the six MIMOSA pixel detector planes placed on both downstream and upstream of the beam, and the tracks are reconstructed and extrapolated to the DUT plane for the hit position determination.

Table 8.9: The measured inter-pad distance for the USTC-IME W17 and W19 2×2 array with the nominal distance to be $30 \mu\text{m}$.

W19-2x2-IP3		W17-2x2-IP3	
Bias[V]	IP measured [μm]	Bias[V]	IP measured [μm]
155	58.60	170	60.47
145	63.33	160	58.53
135	64.61	150	62.20

8 Characterization and Performance of the HPK and USTC-IME LGADs

Table 8.10: Irradiation facilities and parameters and maximum achieved fluence and TID, as well as LGAD types irradiated.

Facility & Abbreviation	Particle Type	TID [MGy]	Max. Fluence [$10^{15}n_{eq} \text{ cm}^{-2}$]	Max. TID [MGy]	LGAD Types Irradiated
JSI Ljubljana (<i>n</i>)	$\approx 1\text{MeVn}$	0.01	6	0.06	all
CYRIC (<i>pCY</i>)	70MeVp	0.81	2.5	4.0	HPK-3.1/3.2, NDL FBK-UFSD3-C
Los Alamos (<i>pLA</i>)	800MeVp	0.43	6	0.4	early prototypes
CERN PS (<i>pPS</i>)	23GeVp	0.44	6	2.7	early prototypes

8.6 Radiation hardness of the USTC-IME LGAD

In order to characterize the USTC-IME LGAD performance after irradiation, sensors have been irradiated up to fluences of $6 \times 10^{15} \text{ cm}^{-2}$ 1-MeV neutron equivalent fluence at the nuclear reactor for the ones expected in HGTD collaboration. However, only results up to $3 \times 10^{15} \text{ cm}^{-2}$ are shown in the following sections. The Tab. 8.10 gives an overview of the facility parameters and maximum fluences, as well as the Total Ionising Dose (TID) achieved for different LGAD types irradiated. The hardness factor used throughout this document is used for the conversion of the actual particle fluence to the 1 MeV-neutron equivalent fluence. The irradiation campaign was mainly supported by JSI reactor neutrons (introduced in [190]). Since the quoted fluence at JSI has an uncertainty of roughly 10%, several sensors were irradiated, at least for the higher fluences. Then all sensors at the same fluence were tested, and the results shown in the following sections are for representative sensors. The measurements with irradiated sensors were done after the standard annealing for 80 min at 60 °C, if not noted otherwise.

The c-factor measurements of USTC-IME second batch single sensors using the C-V method at room temperature have been performed by both USTC and JSI, as shown in Tab. 8.12. The implantation designs in the gain layer include low boron (**W12**), high boron (**W14**), high boron with ten units of carbon dose (**W16**), medium boron with one unit of carbon dose (**W17**), medium boron with two units of carbon dose (**W19**), and medium boron with an unspecified number of unit of carbon dose (**W21**). The c-factor values range from $1.23 \times 10^{-16} \text{ cm}^2$ (**W17**) to $3.66 \times 10^{-16} \text{ cm}^2$ (**W12**). The measured V_{GL} for the IME second batch is shown in Tab. 8.11 after different fluences of irradiation. The formula

$$\frac{V_{GL}(\Phi_{eq})}{V_{GL}(\Phi_0)} = \frac{N(\Phi_{eq})}{N(0)} = \exp(-c\Phi_{eq}),$$

based on the Eq. 6.5, is used to extract the c-factor.

8.6 Radiation hardness of the USTC-IME LGAD

Table 8.11: The V_{GL} extracted from single sensors using CV methods.

Wafer	Implantation in gain layer	V_{GL} at different fluences [V]		
		$0.8 \times 10^{15} \text{ n}_{eq}/\text{cm}^2$	$1.5 \times 10^{15} \text{ n}_{eq}/\text{cm}^2$	$2.5 \times 10^{15} \text{ n}_{eq}/\text{cm}^2$
W12	Low Boron	18.57	15.66	11.61
W14	Low Boron	19.06	15.88	12.48
W16	High Boron + 10 Carbon	23.14	20.84	18.16
W17	Medium Boron + 1 Carbon	21.32	19.76	17.72
W19	Medium Boron + 2 Carbon	21.36	19.75	17.57
W21	Medium Boron + Carbon	34.38	29.94	24.68

Table 8.12: The c-factor extracted from USTC-IME second batch single sensors using C-V method at room temperature.

Wafer	Implantation in gain layer	c-factor [10^{-16} cm^2]	
		USTC	JSI
W12	Low Boron	2.93	3.66
W14	High Boron	2.72	3.38
W16	High Boron + 10 Carbon	1.50	1.36
W17	Medium Boron + 1 Carbon	1.23	1.23
W19	Medium Boron + 2 Carbon	1.31	1.29
W21	Medium Boron + Carbon	2.15	2.07

Among the various implantation designs, **W17**, featuring a medium boron concentration and 1 unit of carbon dose, demonstrates the most radiation-resistant LGAD gain layer design. Both USTC and JSI measurements report a c-factor of $1.23 \times 10^{-16} \text{ cm}^2$ for **W17**, which is smaller than the values obtained for the other implantation designs. Therefore, based on the c-factor measurements, we conclude that the **W17** design is the most radiation-resistant LGAD gain layer design among the tested sensors.

The measured detector capacitance and the full depletion voltage after different irradiation fluences are shown in Tab. 8.13. The capacitance below 4.5 pF and V_{FD} below 80 V are both fulfilled by all wafers in the second batch, which shows good timing performances after irradiation are expected.

8 Characterization and Performance of the HPK and USTC-IME LGADs

Table 8.13: The V_{FD} and C_p extracted from USTC-IME second batch single sensors using C-V method at room temperature.

Wafer	Fluence [$1 \times 10^{15} n_{eq}/cm^2$]	$\langle V_{FD} \rangle \pm \text{RMS(V)}$	$C_p \pm \text{RMS(pF)}$
W17	0.8	41.48 ± 0.29	2.57 ± 0.01
	1.5	55.67 ± 2.86	2.68 ± 0.08
	2.5	81.93 ± 1.51	2.79 ± 0.04
W19	0.8	41.79 ± 0.99	2.59 ± 0.03
	1.5	57.03 ± 0.34	2.68 ± 0.06
	2.5	82.08 ± 0.01	2.80 ± 0.02
W21	0.8	55.23 ± 0.40	2.51 ± 0.01
	1.5	66.08 ± 3.73	2.59 ± 0.06
	2.5	73.82 ± 0.16	2.61 ± 0.03

8.7 Postmortem analysis of the production

8.7.1 Wafer-level uniformity study evaluation

The I-V and C-V tests are done at the wafer level on the automatic probe station with the single needle probe. The I-V curves are further analyzed, and V_{BD} are extracted. The results are shown as a distribution on the wafers with colors indicated the value of the breakdown voltage to show the wafer uniformity as shown in Fig. 8.28. The similar pattern also shown up in the other wafers whose gain layer is implanted at the IME (Fig. 8.29 and W17, W19 in Fig. 8.30). Further study and analysis have confirmed that its the implantation of the gain layer that caused this variation by rotating the wafer with 45° before the gain-layer implementation in the fabrication of W18 as shown in Fig. 8.30.

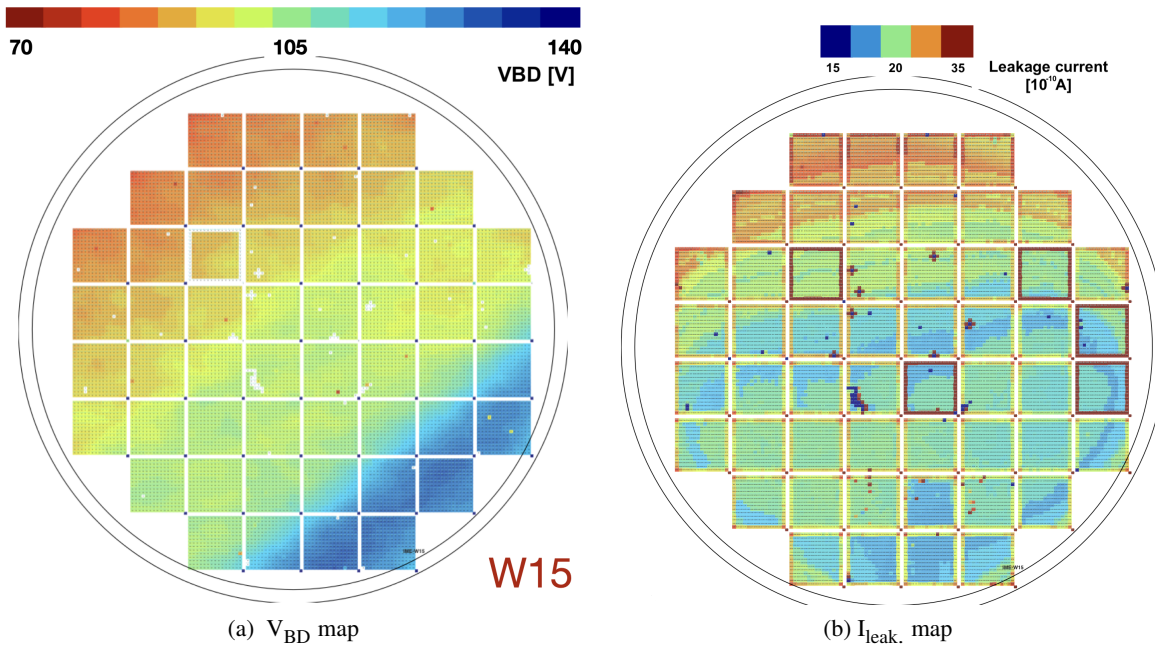


Figure 8.28: The distribution of the (a) breakdown voltage and (b) leakage current. The uniformity is observed on the wafer. Similar pattern is observed in other wafers produced by IME. Later studies have confirmed its due to the 1% level dose variation when performing the implantation of the gain layer.

8.7.2 Yield estimation of the full-size array

Based on the wafer level I-V measurements, the yield is estimated for the production with the specification by the HGTD groups. Only the sensor with all pixels without premature breakdown in the array is considered a good sensor. The yield of each wafer is calculated by the ratio between the number of good sensors and the total number of their sensors on the wafer (which is 52 for the 8-inch LGAD wafer produced by IME). A total yield of around 34% is obtained.

8 Characterization and Performance of the HPK and USTC-IME LGADs

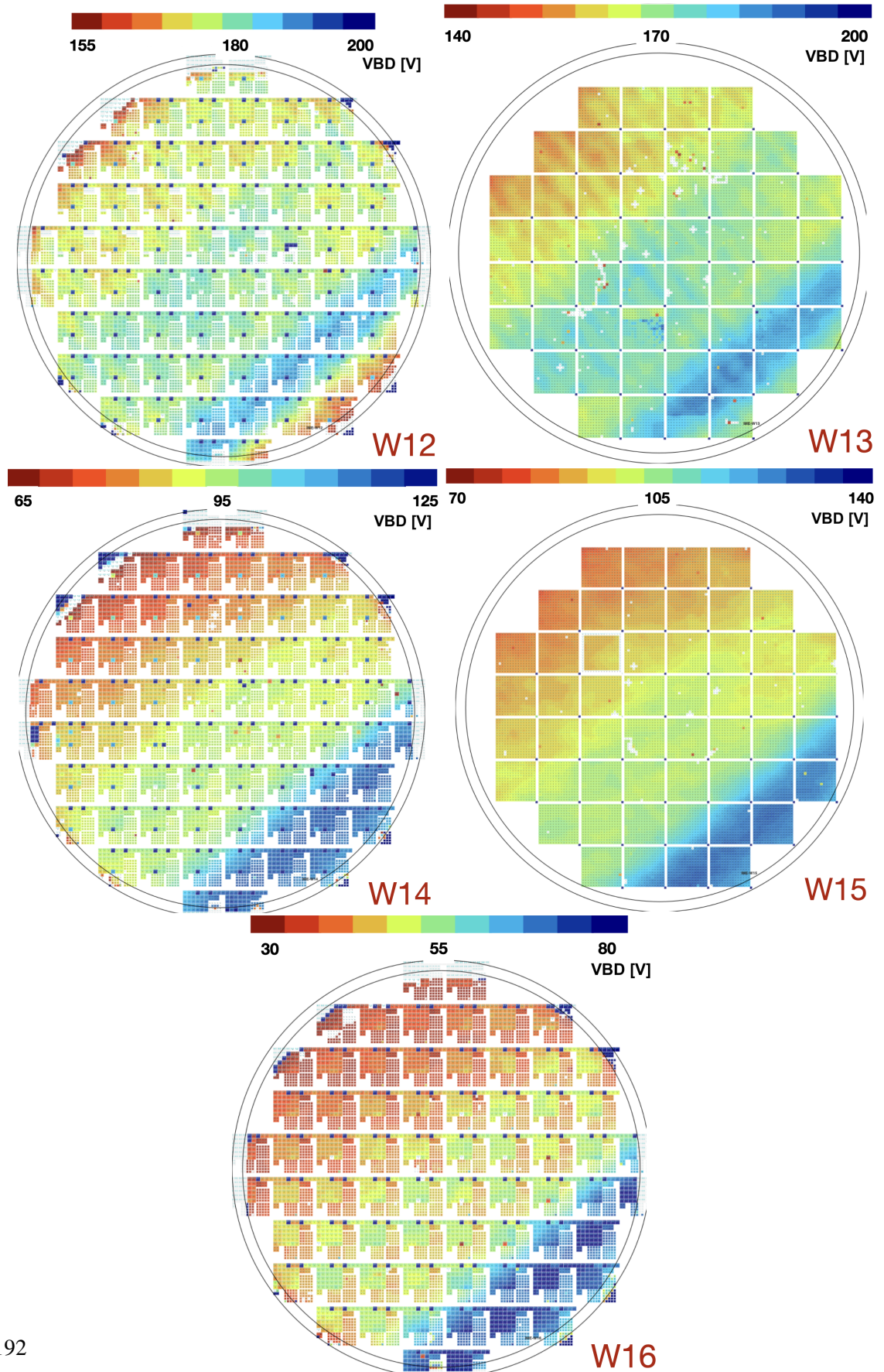


Figure 8.29: The distribution of the V_{BD} from the on-wafer I-V test for the USTC-IME second batch version 1 wafers for the uniformity evaluate and yield estimation.

8.7 Postmortem analysis of the production

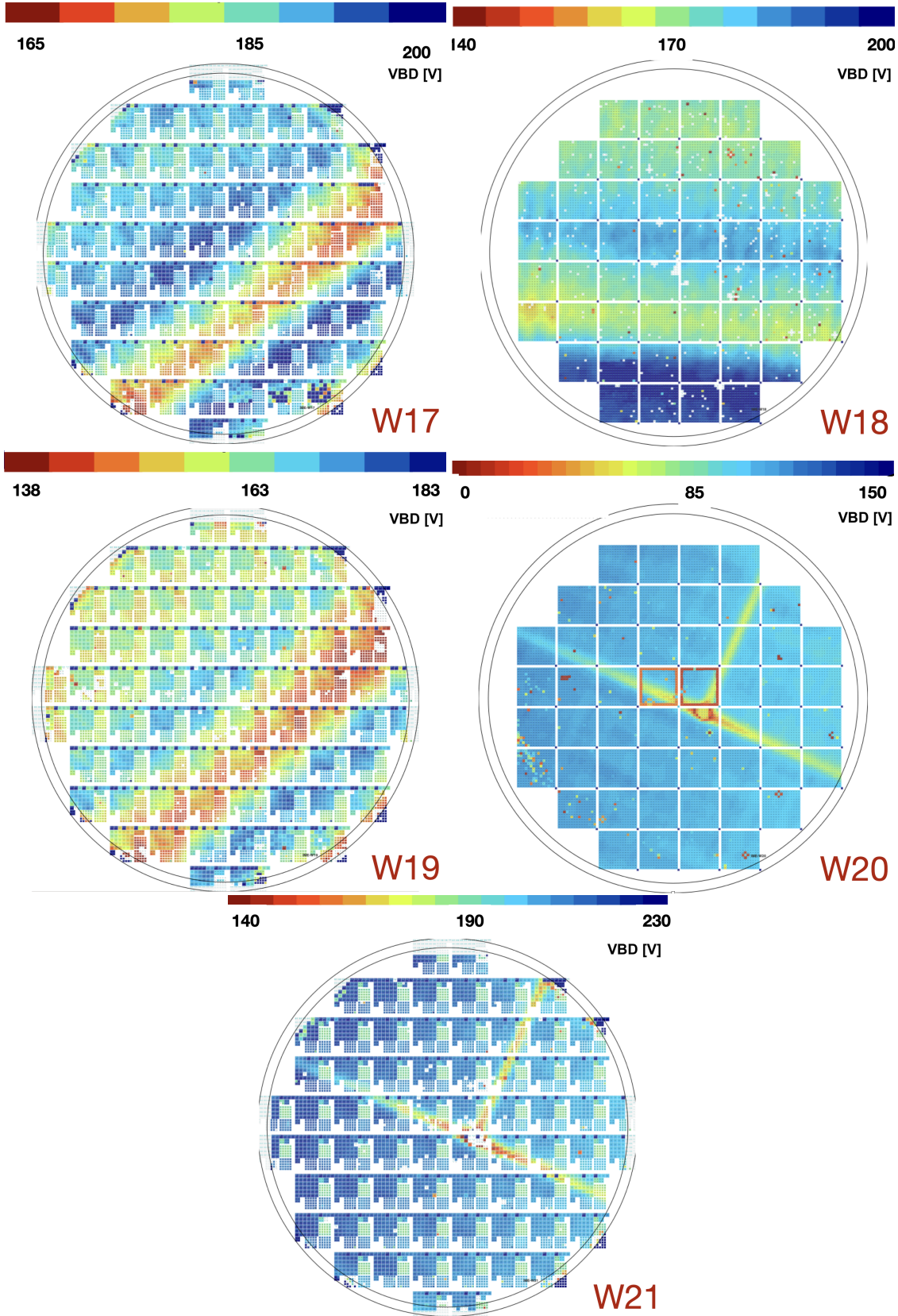


Figure 8.30: The distribution of the V_{BD} from the on-wafer I-V test for the USTC-IME second batch version 2 wafers for the uniformity evaluate and yield estimation.

8.8 Summary

In this chapter, we have presented the results of the I-V, C-V, c-factor, and test beam measurements for the HPK, USTC-IME as well as other prototype LGAD sensors for the HGTD. The results demonstrate that the USTC-IME sensors exhibit promising performance and meet the requirements for the HGTD specifications.

Measurements of I-V and C-V

The I-V measurements show that USTC-IME LGAD sensors have low leakage currents at the operational bias voltages. Furthermore, the C-V measurements indicate that these sensors have appropriate depletion voltages that increase with radiation fluence, confirming that they can operate effectively under the challenging conditions of the HL-LHC environment.

Measurements of the c-factor

The c-factor measurements reveal that the USTC-IME LGAD sensors with medium boron and carbon concentrations (W17) exhibit the highest radiation resistance, with c-factor values of $1.23 \times 10^{-16} \text{ cm}^2$. This highlights the importance of optimizing the boron and carbon concentrations in the gain layer to enhance radiation hardness. A summary of the c-factor from the most promising LGAD prototypes for HGTD of the production run by different vendors is summarized in Fig. 8.31. The advantages of carbon infusion can be observed.

Measurements with charged particles beam

The test beam measurements demonstrate that the USTC-IME LGAD sensors achieve a time resolution within the HGTD specification of 70 ps and a hit efficiency of 95% or higher after $2.5 \times 10^{15} \text{ n}_{\text{eq}} \text{ cm}^2$ irradiation. Furthermore, these sensors meet the HGTD inter-pad distance requirement of 100 μm , ensuring a high fill factor.

Overall, the results from the I-V, C-V, c-factor, and test beam measurements indicate that the USTC-IME LGAD sensors exhibit promising performance and are well-suited for the demanding conditions of the HL-LHC.

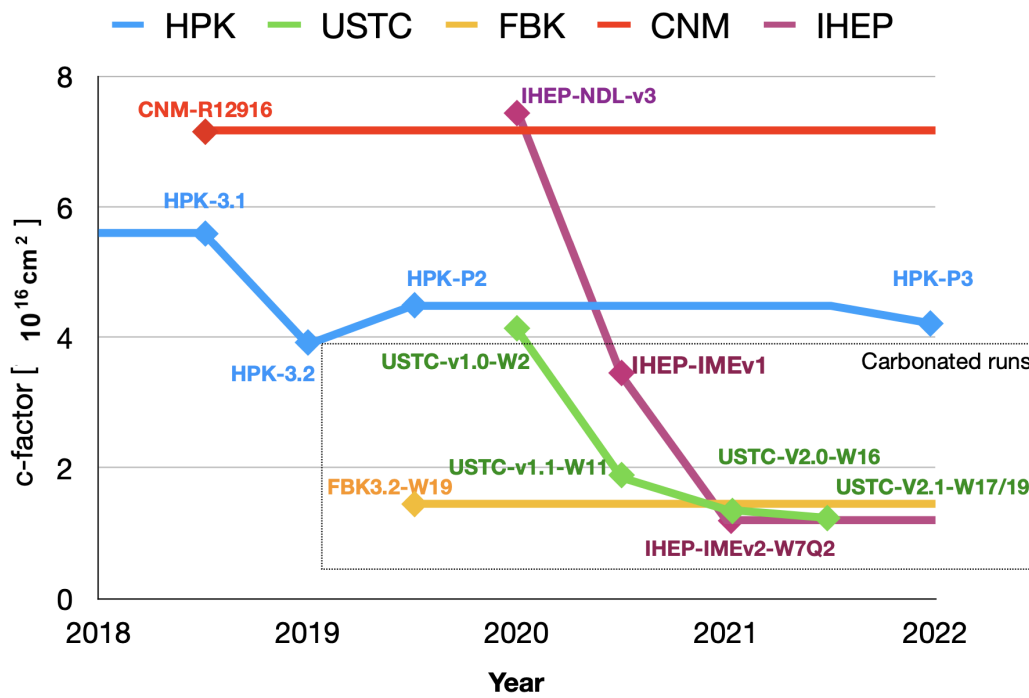


Figure 8.31: Overview of the c-factor evolution and comparison with other vendors for the radiation hard LGAD research from the most promising sample of each batch.

9 Conclusions and Future Prospective

9.1 Conclusions

This thesis has presented a comprehensive study on the measurement of the associate production of vector and Higgs bosons with the $H \rightarrow WW^*$ decay mode at the ATLAS experiment and the development of LGAD for the HGTD upgrade and future experiments.

9.1.1 The $H \rightarrow WW^*, VH$ analysis

In Part I, we focused on the Higgs boson production cross-section measurement in the $H \rightarrow WW^*, VH$ channel at the ATLAS experiment. A detailed overview of the analysis, from event selection and reconstruction to background estimation and systematic uncertainties, was provided. The thesis presented an updated and optimized analysis strategy that led to a better understanding of the Higgs boson properties and cross-section measurements. The results from this study significantly contributed to the ever-growing knowledge about the Higgs boson and its interactions within the SM of particle physics.

In the end, the measurement of the Higgs boson production cross-section via associated WH and ZH production using $H \rightarrow WW^* \rightarrow \ell\nu\ell\nu$ and $H \rightarrow WW^* \rightarrow \ell\nu jj$ decays is presented by this thesis. Results for VH , the combined WH and ZH production are also presented. This analysis uses events produced in proton-proton collisions collected with the ATLAS detector at the LHC between 2015 and 2018. The data correspond to an integrated luminosity of 139 fb^{-1} recorded at $\sqrt{s} = 13 \text{ TeV}$. The product of the $H \rightarrow WW^*$ branching fraction times the WH and ZH cross-sections are measured to be $0.13^{+0.08}_{-0.07}(\text{stat.})^{+0.05}_{-0.04}(\text{sys.}) \text{ pb}$ and $0.31^{+0.09}_{-0.08}(\text{stat.}) \pm 0.03(\text{sys.}) \text{ pb}$ respectively, in agreement with the SM predictions.

9.1.2 The LGAD development

Part II was dedicated to the development and characterization of LGAD for the High-Granularity Timing Detector in the ATLAS experiment. The thesis outlined the working principles of silicon detectors and the history of LGADs, discussing their motivation, performance, and radiation hardness.

A comprehensive study of the LGAD structures, including optimization and simulation using TCAD, was carried out. The fabrication of USTC-IME LGADs was described in detail, with improvements made in the second batch of devices. The devices' performance was characterized using laboratory setups and beam tests at CERN and DESY. Moreover, the AC-LGADs' development at the USTC

9 Conclusions and Future Prospective

Nano-Fabrication and Research Center was initiated, aiming to overcome some limitations of the current LGAD technology.

The USTC-IME LGADs, being thoughtfully optimized, come up with a time resolution better than 35 ps and charge collection better than 10 fC is shown by the measurement both with the β -source and the charged particle beams. After being irradiated by the neutrons at JSI with $2.5 \times 10^{16} \text{ n}_{\text{eq}}/\text{cm}^2$, the carbonated prototype **W17** and **W19** is measured to have the time resolution better than 50 ps and collected charge larger than 5 fC, the c-factor is measured to be $1.23 \times 10^{-16} \text{ cm}^2$, significantly outperforming the corresponding products from HPK and fully meeting the requirements of the HGTD collaboration.

The AC-LGAD developed at the USTC NRFC with a self-developed 6-inch process is proven to be functional with similar time resolution as the USTC-IME LGADs but with better spatial resolution. The laser-TCT scan is performed with the center of gravity method and the 5 μm positional resolution is obtained in the end. Such a novel structure shows us an both excellent and practical way to realize 4 dimensions tracking in the future application.

This thesis made comprehensive work to both the understanding of the Higgs boson properties in the $H \rightarrow WW^*, VH$ channel and the development of LGADs for the HGTD in the ATLAS experiment. The findings presented herein serve as a solid foundation, both on the physics analysis side and detector technique side, for further advancements in the field of particle physics and the ongoing quest to uncover the fundamental building blocks of the Universe.

9.2 Future prospective

9.2.1 The $H \rightarrow WW^*, VH$ analysis in the ATLAS run 3 and HL-LHC

The analysis presented in this thesis provided a solid foundation for future studies in the $H \rightarrow WW^*, VH$ channel. With this and the dataset to be collected in 2022 and beyond, precise measurements of the properties of the Higgs boson will become feasible. Utilizing the combined data from run 3 and run 2 with 300 fb^{-1} , we anticipate a decrease in the overall statistical uncertainty of this measurement by a factor of 1.8, making it comparable to the total systematic uncertainty. Moreover, the greater statistical power of the data set will enable the use of more advanced techniques of analysis and background estimation to better control the systematic uncertainties and facilitate precise measurements of differential cross sections in the future. For instance, it allows for the differential measurements of fake factors and scale factors for non-prompt leptons. Furthermore, incorporating additional channels targeting signals in an expanded phase space, such as the ZH 3-lepton channel, will bolster the overall sensitivity of the analysis.

9.2.2 Current limitations and possible solutions of the LGAD technology for future application

Although the LGADs developed in this thesis demonstrated promising performance, some limitations and challenges still need to be addressed to fully develop the potential advantage of this technology,

9.2 Future prospective

especially for other applications. These include the impact of radiation damage on the gain layer, the single-event burnout effect, and the influence of neighboring floating pads in large-area applications. Further research and development efforts should focus on understanding and mitigating these issues, exploring novel design concepts, and optimizing fabrication processes.

The main remained issues include

- The mortalities issue (SEB effect) which limits the sensor to be operated after high fluences irradiation,
- The yield and cost for the large active area application,
- The gain layer degradation under the ultra-high fluence ($1 \times 10^{16} \text{ n}_{\text{eq}}/\text{cm}^2$),
- The limitation to realize the fine pitch for position measurement.

There are several attempts currently ongoing to address these issues. Apart from the novel LGADs discussed in Sec. 6.4, the considerations of other materials other than silicon are also ongoing. The wide band gap like 4H-SiC or the diamond is born to be radiation resistant with low leakage current and high critical field.

Appendix

A Development of the AC-LGADs at the USTC Nano-Fabrication and Research Center

A.1 Advantages of the AC-LGAD

The AC-LGAD, also called the resistive silicon detector (RSD), are an evolution of the LGAD design aiming at eliminating the inefficient area (inter-pad gap) with a continuous gain layer, a resistive n^- implant, and a thin layer made by dielectric material for the AC coupled readout to front-end electronics. The cross-section of the AC-LGADs is shown in Fig. 6.10 (d).

The geometry of the AC metal pads determines the readout coupling strength, charge sharing, and signal delay. It can be done by re-design the masks for the metal layer and the n^- layer. The design of the resistive n^+ layer is to keep the signal localized in a confined region to reduce the capacitance seen by the array of readout pads and induce the AC signal on the nearby metal pad. Considering the continuous gain layer implant, the RSD provides 100% fill factors. The idea has been successfully validated by several vendors in the RD50 collaboration.

In order to reduce the development of the fabrication processes and have a fast iteration for the AC-LGAD study, we used the optimized baseline parameters for the DC-LGADs apart from the n^- implementation, the dielectric layer, and the metal layer pad design. The AC-LGADs are made together with the DC-LGADs design with different pixel pitch and width designs applied. Both the strip and the pixel design have been realized.

A.2 Capacity of the USTC NRFC

The USTC Center for Micro and Nanoscale Research and Fabrication (NRFC) [232] is a support platform that integrates micro- and nano-processing, manufacturing, and testing methods and can carry out innovative research and advanced manufacturing in cutting-edge and interdisciplinary fields.

The center consists of a micro-nano purification laboratory covering an area of 1000 m² and a micro-nano characterization laboratory of 200 m² and is equipped with supporting and safe factory facilities. The center has a Class 100 clean room of 500 m² and has flexible space for upgrading the purification level. The center has more than 40 sets of advanced micro-nano processing, manufacturing, and characterization devices.

The NRFC has an effective and complete process line for the semiconductor samples or wafers up to 6-inch for nanoscale research and development. The main instruments and capacities are summarized in Fig. A.1 and introduced below.

A Development of the AC-LGADs at the USTC Nano-Fabrication and Research Center



Figure A.1: Overview of the NRFC major equipments for 6-inch silicon wafers fabrication.

- For the film growth and material deposition, it has a furnace for Oxidation/Nitriding LPCVD, the PECVD and a high-temperature furnace for diffusion and annealing, an Ion implantation machine, a Rapid Thermal Processing machine, Sputters, and E-beam evaporators as well as film characterization instruments for the thickness and the profile.
- For the lithography, it has Spin Coaters, Heating Plates, and HMDS process oven for coating the photoresist. It has the Nikon 6-inch i-line stepper, the E-beam Lithography machine, an optical contact aligner with 365/405nm UV light for manual lithography, and Maskless Lithography machine for producing the mask.
- For the etching, it has the integrated platforms for standard MEMS wet etching and wet cleaning with 18.2 MΩ ultrapure water provided. It has the fume hood for both organic and inorganic processes, including PR development and removal. It has a dry etching machine including Reactive Ion Etching (RIE) for silicon or its compound, Inductively Coupled Plasma Etching (ICP) for metal, and Deep silicon etching for the high aspect ratio trench and plasma asher for the organic remnant. The Profiler is also available for probing and verification of the etched structure.
- For the packaging, it provides both the manual and 8-inch automatic dicing machine for cutting, the wire bonder for assembling the device into test PEB, and the grinding machine for thinning and polishing. For the characterization, it provides the Focused Ion Beam (FIB), Scanning electron microscope (SEM), Helium Ion Microscope, Atomic Force Microscope (AFM), X-ray CT, and automatic optical digital microscope for the structure validation and failure analysis at varieties of scales.

Plenty of the common chemical supplements are provided in the center as required by the users, including the photoresist with the thickness from a fraction of μm to tens of μm for both positive and

A.3 Design of the AC and DC coupled LGADs

negative photolithography developers, the sulfuric acid and hydrogen peroxide for organic clean with piranha solution, hydrofluoric for the oxide etching and KOH for silicon etching, the hydrochloric acid and nitric acid for the metal etching. The organic solutions include acetone, Isopropyl alcohol (isopropyl alcohol (IPA)), and N-Methyl-2-pyrrolidone (NMP) for the standard cleaning of organic contamination.

A.3 Design of the AC and DC coupled LGADs

In order to have a better understanding of the LGAD technique for the novel structure R&D and to speed up the iteration of the optimization, extensive fabrication research has been carried out at USTC NRFC. The fabrication of the LGAD at USTC NRFC has the advantage of low cost, fast turnaround, and flexibility to the “non-standard” technologies. While it is foreseeable that as a university clean room for R&D instead of production, the contamination control would not be as good, and the process procedure is not as standard and well optimized as the fab company at some large company or institute dedicated to the wafer fabrication. Thus, it would be hard to produce an array of pixels with a large area. The defects are expected to result in low yield. Even though it would already be good enough for the R&D phase, the low yield issue could be resolved by producing a large number of the same device on a large wafer and selecting the good one for study. This can be achieved with the help of the stepper photolithography machine and automatic probe station. Luckily, we have an automatic probe station, as mentioned in Sec. 8.2.1, and the Nikon i10 i-line stepper for the 6-inch wafers.

The AC LGAD simulation is based on the optimized TCAD model of the DC LGAD introduced in Sec. 7.3. The full-size devices with five pixels are simulated. The readout pad used in the simulation is configured to be 100 μm in width and 200 μm in pitch. The transient simulation of the signals is performed with the MIP-like charge deposition of 0.5 fC in the middle of the device as shown by the black arrow in Fig. A.2 (a), and the current response is simulated and shown in Fig. A.2 (b) for each pixel. The scan of the hit position with the step of 50 μm for d is also simulated as the blue curve shown in Fig. A.2 (a), and the responses of the middle pixel for each position are shown in Fig. A.2 (c).

The mask is designed with $10 \times 10 \text{ mm}^2$ for better utilization of the Nikon i10 stepper machine. There are four masks placed on the 6-inch reticle with a total area of $22.5 \times 22.5 \text{ mm}^2$ available for exposure. The 1×1 , 2×2 LGADs with the same layouts used at USTC-IME production are placed as shown in Fig. A.3.

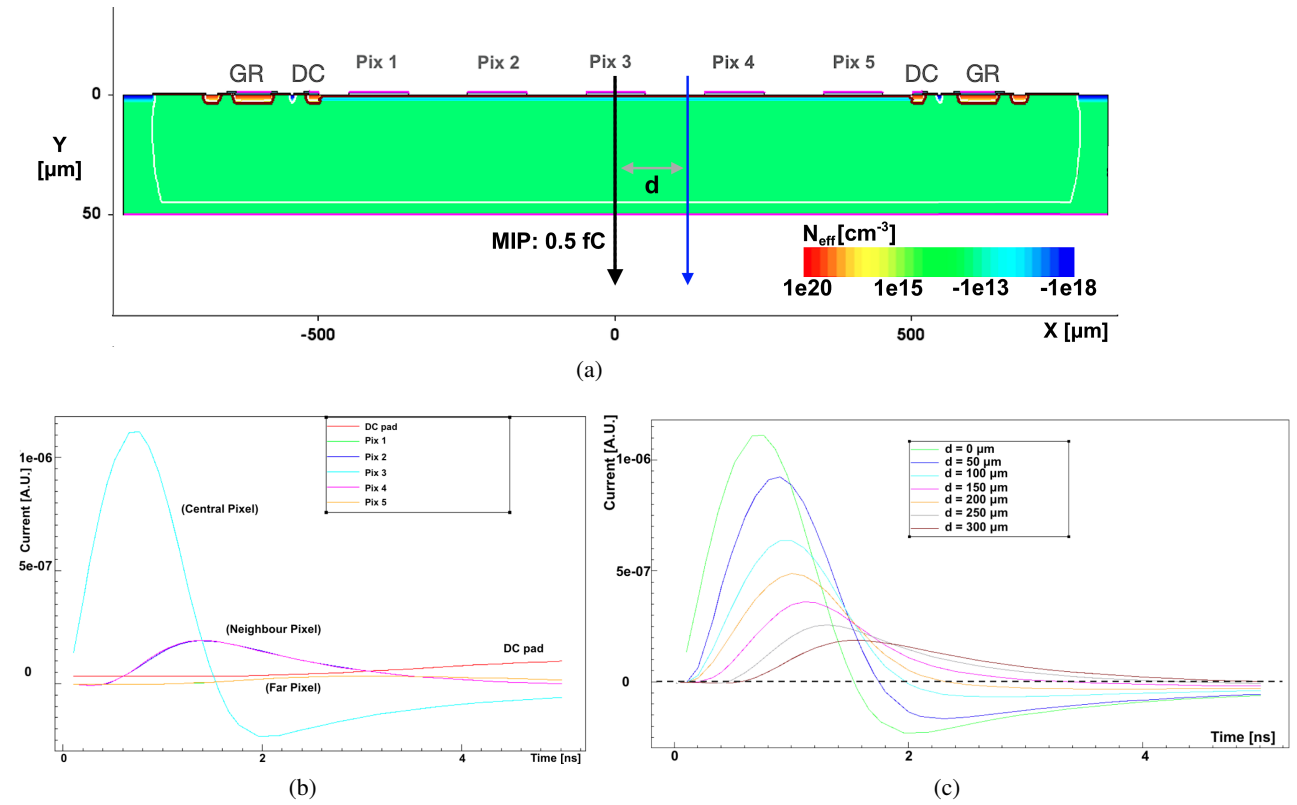


Figure A.2: The simulation of the AC LGAD signal readout with (a) the hit in the middle of the sensor. The hit in the position displaced to the middle by a distance of d is shown by the blue arrow. The signals for the hit in the middle being read out at different pixels are shown in (b). The signals for the hit at different positions with a step of 50 μm and being read out in the middle pixel are shown in (c).

A.3 Design of the AC and DC coupled LGADs

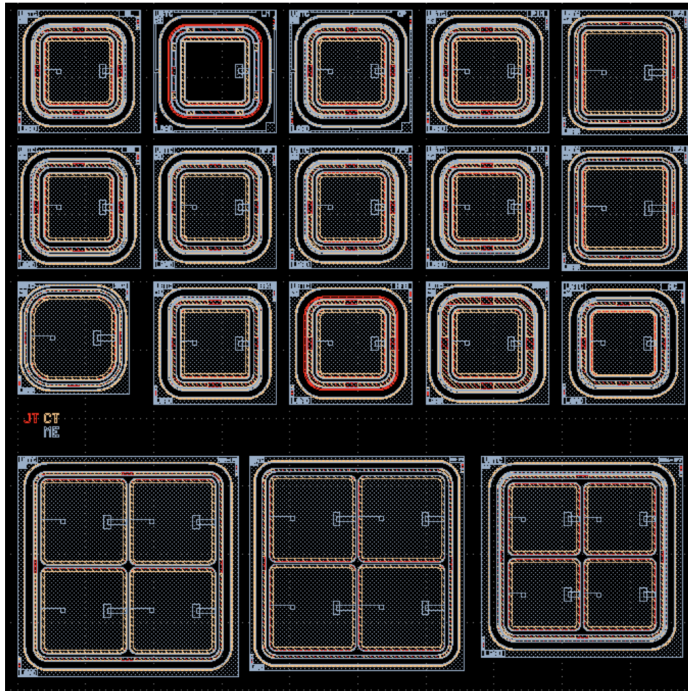


Figure A.3: The designed reticle layout used in the 6-in AC and DC coupled LGADs production on the 6-in wafers at NRFC. The size is designed with $10 \times 10 \text{ mm}^2$ and the LGADs with size of 1×1 , 2×2 are placed for layout optimization.

A.4 Fabrication of the AC and DC LGADs with the 6-inch processes at NRFC

The wafers are split into different groups with different coupling oxide thicknesses and types. The carbon implantation is also realized with different doses. In order to produce more devices with different process parameters to speed up the iterations, the wafers are further split by the photolithographic exposure rows with different implantation doses, referred to as either the even row (ER) or the odd rows (OR). In total, six wafers are produced, and two of them use the AC-LGAD process. The wafers after the fabrications are completed are shown in Fig. A.4 (a).

Apart from the standard LGAD fabrication process and common structures, several changes are implemented for AC-LGAD fabrication. The n^+ layer implantation is limited to the area of the DC ring where bias is needed. The n^- layer is added to cover the center region of the pad with a reduced dose to realize a resistive connection to the readout. A thin layer of the dielectric material film is induced for the AC coupling. Fine electrode segmentation is achieved by the etching of the metal layer in the central region of the pad. For the comparison of the pad pitch and width influences on the timing and spatial resolution of AC-LGAD. The electrodes with different geometries are designed on a single LGAD device, as shown by the microscope photo in Fig. A.4 (b). Both pixel and strip readout have been attempted to reduce the complexity of the readout amplifier requirement and the wire bonding.

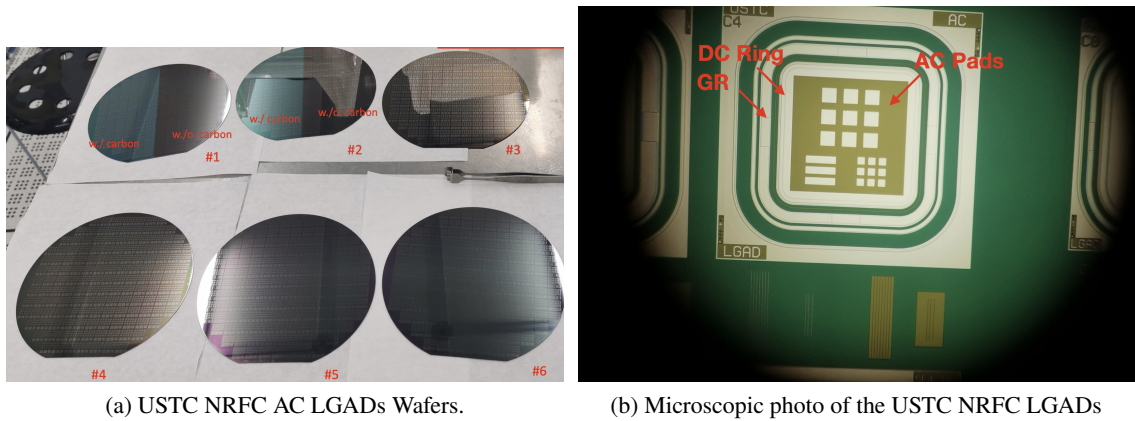


Figure A.4: (a) Photo of the wafer of AC/DC LGADs produced at USTC NRFC. (b) The microscopic photo of the USTC NRFC LGADs.

A.5 Performance of the AC and DC LGADs produced at NRFC

A.5.1 I-V and Timing performance

The performance of the AC and DC LGADs have been characterized by the I-V and C-V test as well as the β -scope and laser TCT measurement, which is introduced in Chapter. 8. The AC-LGAD is

A.5 Performance of the AC and DC LGADs produced at NRFC

under testing on the amplifier board, as shown in Fig. A.5. The breakdown voltages are located in a good range of 150 to 200 V (shown in Fig. A.6 (a)) and the measured timing resolution is better than 40 ps (shown in Fig. A.6 (b))

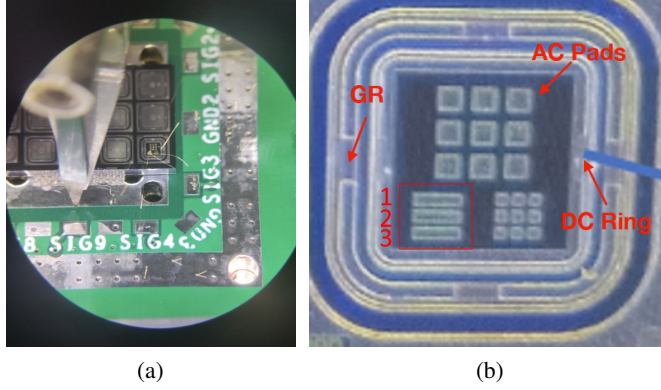


Figure A.5: (a) The bonding of USTC NRFC AC LGAD sensor on the 9-channel pre-amplifier board for the charge collection, position, and timing resolution test. (b) The electrodes in the AC-LGAD used in the TCT test.

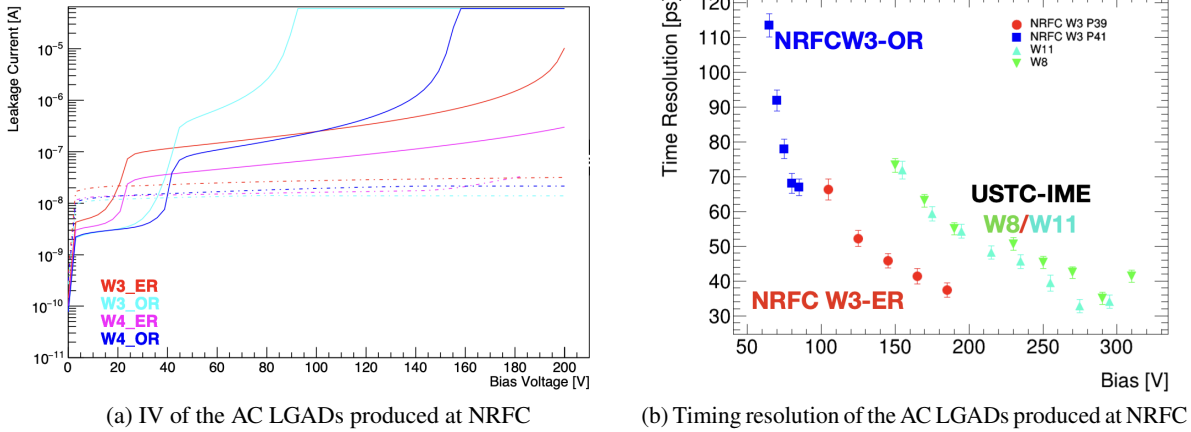


Figure A.6: The test results of the LGAD samples produced by NRFC at USTC. (a) I-V curves measured for the **W3** and **W4** where a V_{BD} in the range of 150 to 220 V is found for the **W3-ER** **W4-OR**. Different depths of the gain layer are realized by the different implantation energies. (b) The timing resolution of the NRFC LGADs measured by the β -scope, a time resolution better than 40 ps is achieved by the **W3-ER**. The LGADs fabricated at USTC-IME are also measured for comparison.

A.5.2 Spatial results from the laser-TCT

The measurement of the spatial resolution is performed with the laser-TCT system. The focused infra-red laser produces a fixed amount of charge deposition, and the fine scan is performed on the interested areas on the sensor surface. The 9-channel amplifier board introduced in [230] has been

A Development of the AC-LGADs at the USTC Nano-Fabrication and Research Center

used for this test. Both strip (shown in A.7) and the pixel (shown in A.8) electrodes on the AC-LGAD sensor are studied.

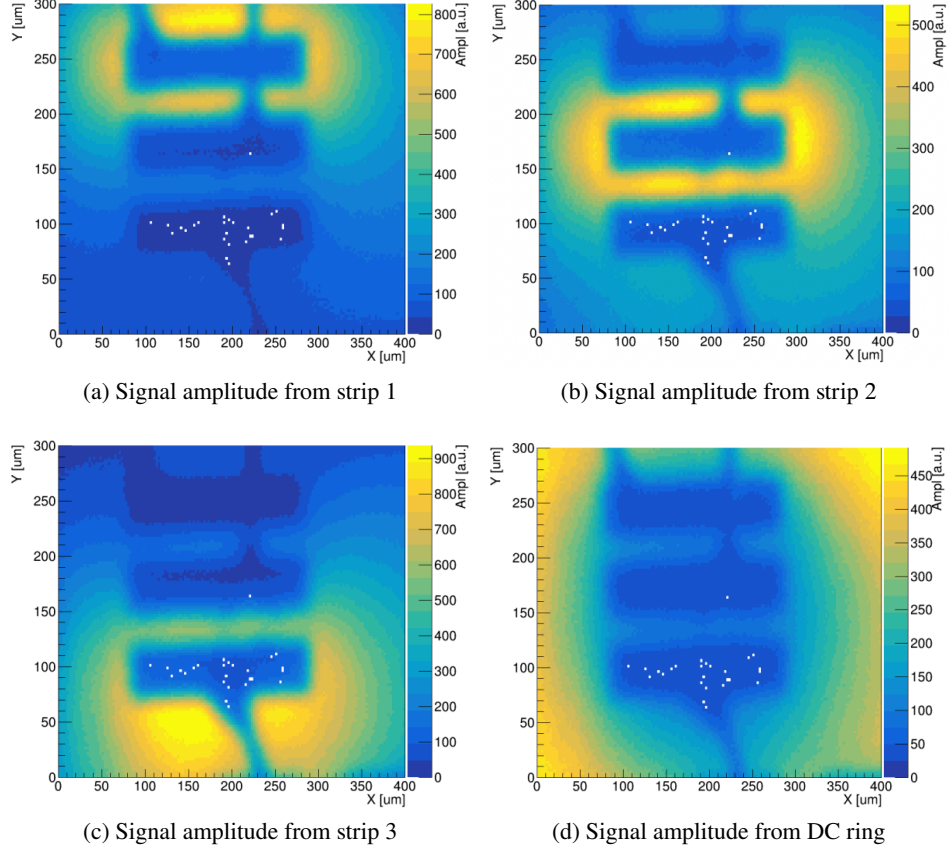


Figure A.7: The average amplitude of the signal obtained from different NRFC AC-LGAD strips as a function of the laser spot position. The signals from the DC ring are also read out for comparison.

The signal amplitudes are used for analysis and obtaining the position of the primary ionization. The observed signal from the different pads for the same hit can be seen in Fig. A.10 (a), where a significant amplitude difference can be noticed. The analysis is performed by the X and Y directions separately. The scan results are shown in Fig. A.9 with the pixel pad width of $100\ \mu\text{m}$ and pitch of $150\ \mu\text{m}$, and performed with $2.5\ \mu\text{m}$ step.

For combining the signal from different electrodes together for position measurement, a fraction function $F(Y)$ is defined as:

$$F(Y) = \frac{A_1(Y) + A_3(Y) - A_2(Y) - A_4(Y)}{A_1(Y) + A_3(Y) + A_2(Y) + A_4(Y)}, \quad (\text{A.1})$$

where $A_i(Y)$ is the average signal amplitude for pad i measured in Fig. A.9. Similar relation can be applied in the X direction. Taking into account that the electrode design is symmetric for the X and Y directions, the results from the Y direction scan can also be applied to the X direction.

A.5 Performance of the AC and DC LGADs produced at NRFC

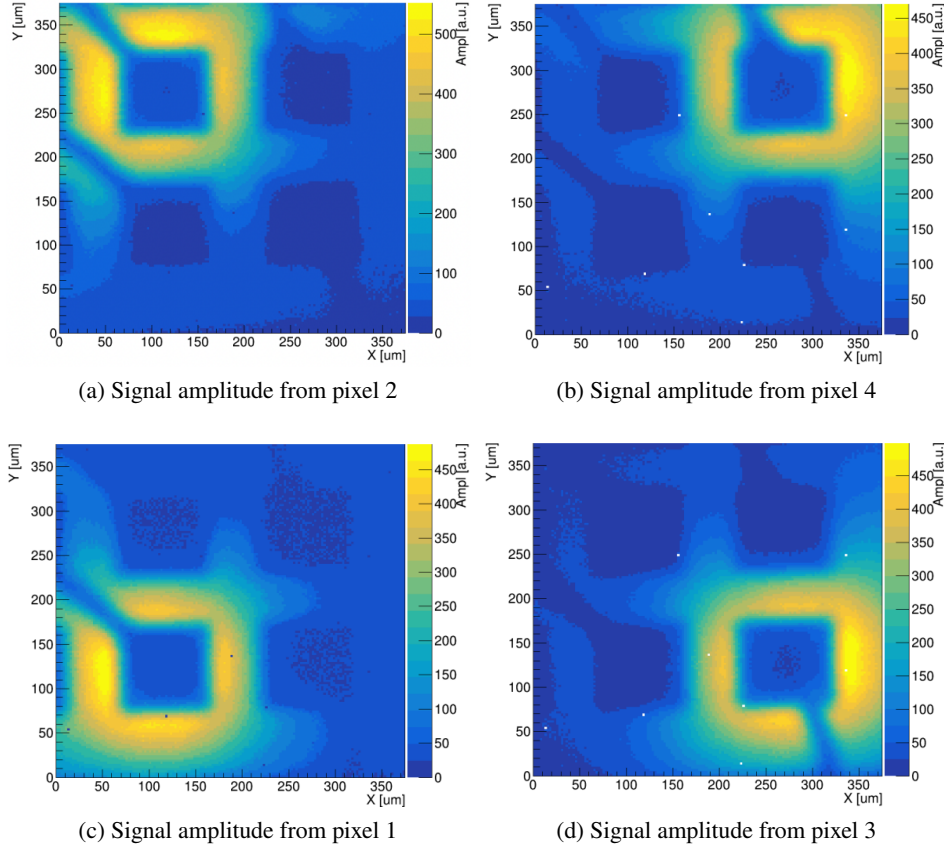


Figure A.8: The average amplitude of the signal obtained from different NRFC AC-LGAD pixels as a function of the laser spot position. The labeling of the pixels can be found in Fig. A.9.

With this function, the position along the Y direction is determined as shown in Fig. A.10 (b). The fitting of this function is performed on the calibration data set where a good linear ship can be found in the range of 150 to 250 μm in the Y direction with the slop to be $\frac{2}{150}\mu\text{m}^{-1} (\frac{2}{\text{pitch}})$. Thus, based on this result, we can reconstruct the position of the signals from the test data with:

$$X_{\text{reco}} = \frac{d_{\text{pitch}}}{2} \cdot F_{\text{measured}}, \quad (\text{A.2})$$

$$Y_{\text{reco}} = \frac{d_{\text{pitch}}}{2} \cdot F_{\text{measured}}. \quad (\text{A.3})$$

The final evaluation is based on the test data for both X and Y directions. The range of 150 to 250 μm is used for the direction in measurement. For the direction not in measurement, the range of 175 to 215 μm is used to ensure good linearity. The root mean square (RMS) of the difference between the laser beam spot and the reconstructed position is quoted as the spatial resolution. The final spatial resolution is measured to be 5.2 μm in X direction and 5.0 μm in Y direction as shown in the Fig. A.11 in the area of interest.

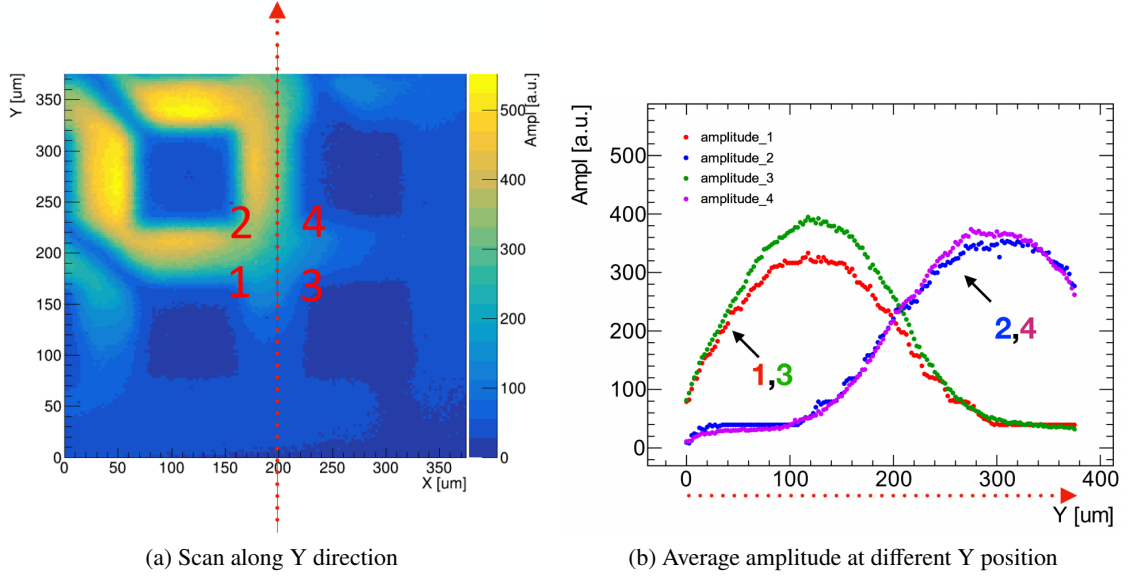


Figure A.9: The scan is performed along the Y direction. The X position is fixed in the center of the two columns of pads ($200 \mu\text{m}$) in the scan.

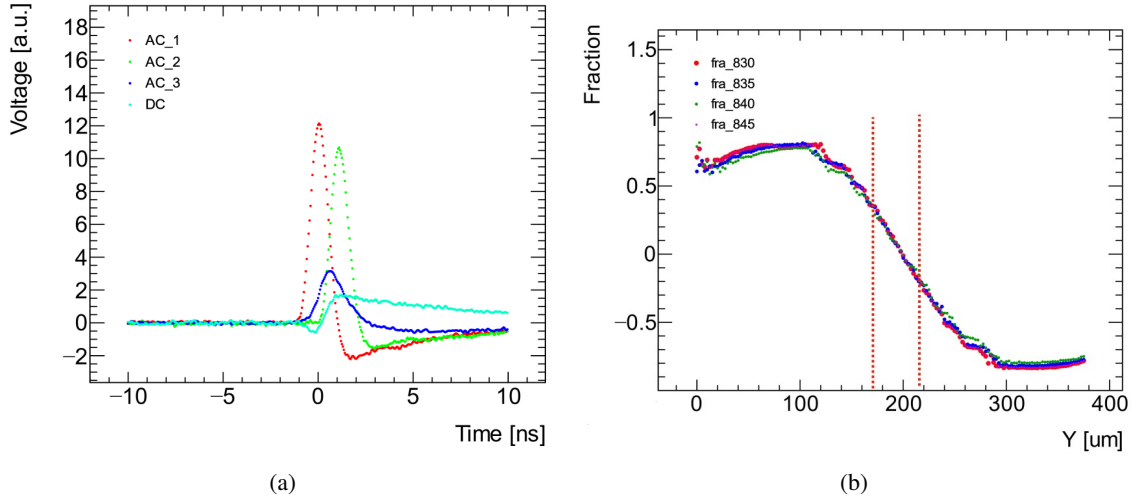


Figure A.10: The signal waveform and the amplitude used for the position determination. (a) The signal observed from different pixel of AC-LGAD for the same hit. (b) The measured $F(Y)$ function with the calibration data.

A.6 Summary

This section presents the development of AC-LGADs at the USTC NRFC. The AC-LGAD, also known as RSD, aims to eliminate the inefficient area (inter-pad gap) with a continuous gain layer, a resistive n^- implant, and a thin layer made by dielectric material for the AC coupled readout to front-end electronics. Such a design can achieve 100% fill factor, thus being favored by several vendors to

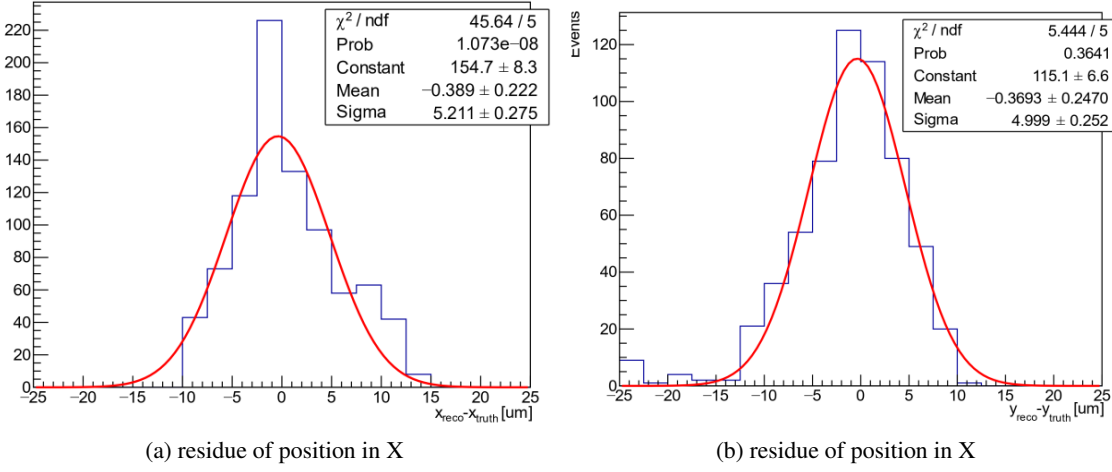


Figure A.11: The measured position resolution with the test data in (a) X direction and (b) Y direction. The 640 points are used in the estimation in the range of 150 to 250 μm for the direction under measurement and 175 to 215 μm for the direction not measured.

explore the silicon detector for 4-D tracking applications.

The USTC NRFC is a support platform that integrates micro- and nano-processing, manufacturing, and testing methods for innovative research and advanced manufacturing in cutting-edge and interdisciplinary fields. The center is equipped with more than 40 sets of advanced micro-nano processing, manufacturing, and characterization equipment, providing an effective and complete process line for 6-inch semiconductor samples or wafers for nanoscale research and development.

The AC and DC coupled LGADs were designed with a mask size of 10 mm \times 10 mm, using the Nikon i10 stepper machine for better alignment precision and photolithographic efficiency. The fabrication of the AC and DC LGADs with the 6-inch processes at NRFC was conducted using six wafers, with two of them using the AC-LGAD process. Several changes were implemented in the fabrication process for AC-LGADs, including limiting the n^+ layer implantation, adding a reduced dose n^- layer, inducing a thin layer of dielectric material film, and etching the metal layer in the central region of the pad.

The performance of the AC and DC LGADs produced at NRFC was characterized by I-V and C-V tests, β -scope, and laser TCT measurements. The breakdown voltages were found to be in a good range of 150 to 200 V, and the timing resolution was better than 40 ps. Spatial resolution measurements were performed using laser-TCT system on the pixel AC-LGAD sensor. The measured position resolution was 5.2 μm in the X direction and 5.0 μm in the Y direction.

In conclusion, the development and fabrication of AC-LGADs at NRFC proved to be a valuable process for understanding LGAD techniques and improving the USTC-IME LGAD design. The produced AC and DC LGADs demonstrated good performance in terms of breakdown voltage, timing resolution, and spatial resolution. The research conducted at USTC NRFC has successfully achieved its objectives, providing valuable insights for future LGAD development. Further in-depth research based on these processes can be expected in the future.

Publications and conference talks

Published journal articles

1. ATLAS Collaboration, *Measurement of the Higgs boson production cross section in association with a vector boson and decaying into WW^* with the ATLAS detector at $\sqrt{s} = 13$ TeV*, ATLAS-CONF-2022-067, 2022, url: <https://cds.cern.ch/record/2842519>. (Contribution: statistical analysis: all channels' combination fitting, hypothesis test, systematics uncertainties analysis. WH 2-lepton same-sign channel background estimation, binning optimization.)
2. X. Yang, S. Alderweireldt and N. Atanov et al., *Layout and performance of HPK prototype LGAD sensors for the High-Granularity Timing Detector*, Nucl. Instrum. Meth. A, 980:164379, 2020. (Contribution: HPK sample preparation, IV/CV test software development, 5x5 LGAD array automatical test with probe-card and digital switch, 5x5 array breakdown and gain layer depletion voltage test and analysis method. paper writing.)
3. X. Yang, K. Ma, X.X. Zheng, and Y. Liu., *Radiation hardness characterization of low gain avalanche detector prototypes for the high granularity timing detector*, Journal of University of Science and Technology of China, 52(1):3, 2022. (Contribution: USTC-IME LGAD sample design and fabrication. IV/CV and beta scope measurement, carbon-diffusion gain layer design. gain-layer radiation hardness analysis method, paper writing.)
4. C.H. Li, X. Yang, and J.J. Ge et al., *Performance of LGAD sensors with carbon enriched gain layer produced by USTC*, Nucl. Instrum. Meth. A, 1039:167008, 2022. (Contribution: LGAD sample design, fabrication assembly and IV/CV, beta test, software development, analysis method, paper edit.)
5. Ge J. J. and Yang X. and Zheng X. X. et al., *Digital switch boards for IV and CV measurements of large-array Low Gain Avalanche Detectors*, Nucl. Instrum. Meth. A, 1005:165400, 2021. (Contribution: LGAD sample fabrication, large array IV/CV probe-card test, automatic test software programming, noise analysis.)

Conference talk and posters

1. *A High-Granularity Timing Detector for the ATLAS Phase-II upgrade* (30')
talk at the 10th International Conference on New Frontiers in Physics (ICNFP 2021) on behalf of the ATLAS Collaboration, Aug. 2021, Crete, Greece
2. *The beam test results of the USTC-IME LGADs at different irradiation fluence at DESY and CERN PS/SPS beam for ATLAS HGTD upgrade* (12')
talk (co-author) at the 8th China LHC Physics Workshop (CLHCP2022), Nov. 2022, Nanjing, China
3. *Performance of USTC LGADs for the ATLAS HGTD Upgrade* (12')
talk at the 7th China LHC Physics Workshop (CLHCP2021), Nov. 2021, Nanjing(online), China

A Development of the AC-LGADs at the USTC Nano-Fabrication and Research Center

4. *Characterization of LGADs for HGTD Upgrade at USTC* (15')
talk at the 6th China LHC Physics Workshop (CLHCP2020), Nov. 2020, online, China
5. *Recent results of the carbonated USTC-IME LGADs and fabrication of the AC-LGADs at USTC NRFC* (25'+5')
talk the 40th RD50 Workshop, Jun. 2022, CERN, Geneva, Switzerland
6. *LGAD Sensor Design at USTC for the ATLAS HGTD Project*
poster at the 5th China LHC Physics Workshop (CLHCP2019), Oct. 2019, Dalian, China
7. *Layout and Performance of HPK Prototype LGAD sensors for the High-Granularity Timing Detector HGTD*
poster on behalf of the ATLAS HGTD group at the 12th International "Hiroshima" Symposium on the Development and Application of Semiconductor Tracking Detectors (HSTD12), Dec. 2019, Hiroshima, Japan
8. *News from High-Granularity Timing Detector Upgrade* (20')
talk on behalf of the HGTD group at ATLAS Upgrade Week, Nov. 2022, CERN
9. *Performance of the USTC first batch LGADs* (20')
talk at the 16th (Virtual) "Trento" Workshop on Advanced Silicon Radiation Detectors, Feb. 2021, online
10. *Preliminary USTC-1 LGAD Results and Large Array Characterization for HGTD* (20')
talk at the 37th RD50 Workshop, Nov. 2020, Zagreb, Croatia
11. *Characterization on the radiation hardness of USTC-1.1 LGADs* (20')
talk (co-author) at the 38th RD50 Workshop, Jun. 2021, online
12. *First demonstration of the full DAQ chain with the ALTIROC2 and FADA at CERN lab* (12')
talk at HGTD (mini) week during ATLAS upgrade week, Nov. 2022, CERN
13. *DAQ improvements for the HGTD test beam* (30')
talk at HGTD week, Sept. 2022, CERN
14. *USTC-IME LGAD sensor testing and design* (20')
talk at HGTD week, Sept. 2022, CERN
15. *VH combination post-mortem* (20')
talk on behalf of the VH team at the HWW Workshop, Jun. 2022, CERN

Bibliography

- [1] F. Abe et al., *Observation of top quark production in $\bar{p}p$ collisions*, *Phys. Rev. Lett.* **74** (1995) 2626, arXiv: [hep-ex/9503002](#) (cit. on pp. 1, 10).
- [2] S. Abachi et al., *Observation of the top quark*, *Phys. Rev. Lett.* **74** (1995) 2632, arXiv: [hep-ex/9503003](#) (cit. on pp. 1, 10).
- [3] S. W. Herb et al.,
Observation of a Dimuon Resonance at 9.5 GeV in 400-GeV Proton-Nucleus Collisions,
Phys. Rev. Lett. **39** (5 1977) 252,
URL: <https://link.aps.org/doi/10.1103/PhysRevLett.39.252> (cit. on p. 1).
- [4] J. E. Augustin et al., *Discovery of a Narrow Resonance in e^+e^- Annihilation*,
Phys. Rev. Lett. **33** (23 1974) 1406,
URL: <https://link.aps.org/doi/10.1103/PhysRevLett.33.1406> (cit. on p. 1).
- [5] J. J. Aubert et al., *Experimental Observation of a Heavy Particle J* ,
Phys. Rev. Lett. **33** (23 1974) 1404,
URL: <https://link.aps.org/doi/10.1103/PhysRevLett.33.1404> (cit. on p. 1).
- [6] G. Arnison et al., *Experimental Observation of Isolated Large Transverse Energy Electrons with Associated Missing Energy at $\sqrt{s} = 540$ GeV*, *Phys. Lett. B* **122** (1983) 103 (cit. on pp. 1, 10).
- [7] M. Banner et al., *Observation of Single Isolated Electrons of High Transverse Momentum in Events with Missing Transverse Energy at the CERN anti- p p Collider*, *Phys. Lett. B* **122** (1983) 476 (cit. on pp. 1, 10).
- [8] R. Brandelik et al. (TASSO Collab.), D. P. Barberet al. (MARK J Collab.) Ch. Berger et al. (PLUTO Collab.), W. Bartel et al. (JADE Collab.),
Evidence for planar events in ee annihilation at high energies,
Physics Letters B **86** (1979) 243, ISSN: 0370-2693,
URL: <https://www.sciencedirect.com/science/article/pii/037026937990830X> (cit. on p. 1).
- [9] Particle Data Group, *Review of Particle Physics*,
Progress of Theoretical and Experimental Physics **2022** (), 083C01, ISSN: 2050-3911,
eprint: <https://academic.oup.com/ptep/article-pdf/2022/8/083C01/49175539/ptac097.pdf>,
URL: <https://doi.org/10.1093/ptep/ptac097> (cit. on pp. 1, 5, 6, 28).
- [10] P. W. Higgs, *Spontaneous symmetry breakdown without massless bosons*,
Physical review **145** (1966) 1156 (cit. on pp. 1, 5).

Bibliography

- [11] P. W. Higgs, *Broken symmetries and the masses of gauge bosons*, Physical review letters **13** (1964) 508 (cit. on pp. 1, 6).
- [12] ATLAS Collaboration, *Observation of a new particle in the search for the standard model Higgs boson with the ATLAS detector at the LHC*, Physics Letters B **716** (2012) 1 (cit. on p. 1).
- [13] CMS Collaboration, *Observation of a new boson at a mass of 125 GeV with the CMS experiment at the LHC*, Physics Letters B **716** (2012) 30 (cit. on p. 1).
- [14] CMS Collaboration, *A portrait of the Higgs boson by the CMS experiment ten years after the discovery*, Nature **607** (2022) 60 (cit. on pp. 1, 31, 33).
- [15] ATLAS Collaboration, *A detailed map of Higgs boson interactions by the ATLAS experiment ten years after the discovery*, Nature **607** (2022) 52 (cit. on pp. 1, 25, 31, 33).
- [16] S. Dimopoulos, S. Raby and F. Wilczek, *Supersymmetry and the scale of unification*, Physical Review D **24** (1981) 1681 (cit. on p. 1).
- [17] J. Wess and J. Bagger, *Supersymmetry and supergravity*, Princeton University Press, 1992 (cit. on p. 1).
- [18] G. Aad et al., *Observation and measurement of Higgs boson decays to WW^* with the ATLAS detector*, Phys. Rev. D **92** (2015) 012006, arXiv: [1412.2641 \[hep-ex\]](https://arxiv.org/abs/1412.2641) (cit. on p. 1).
- [19] J. Alison and J. Alison, *The Fake Factor Method*, The Road to Discovery: Detector Alignment, Electron Identification, Particle Misidentification, WW Physics, and the Discovery of the Higgs Boson (2015) 151 (cit. on p. 2).
- [20] O. S. Brüning et al., *LHC Design Report*, CERN Yellow Reports: Monographs, Geneva: CERN, 2004, URL: <https://cds.cern.ch/record/782076> (cit. on pp. 2, 10).
- [21] ATLAS Collaboration, *ATLAS detector and physics performance technical design report*, tech. rep., CERN-LHCC-99-15, 1999 (cit. on pp. 2, 11).
- [22] CMS Collaboration, *CMS technical design report, volume II: physics performance*, tech. rep., CERN-LHCC-2006-021, 2006 (cit. on p. 2).
- [23] I. Zurbano Fernandez et al., *High-Luminosity Large Hadron Collider (HL-LHC): Technical design report*, **10/2020 (2020)**, ed. by I. Béjar Alonso et al. (cit. on p. 2).
- [24] P. Azzi et al., *Report from Working Group 1: Standard Model Physics at the HL-LHC and HE-LHC*, CERN Yellow Rep. Monogr. **7** (2019) 1, ed. by A. Dainese et al., arXiv: [1902.04070 \[hep-ph\]](https://arxiv.org/abs/1902.04070) (cit. on p. 2).
- [25] Atlas Collaboration, *ATLAS toward the High Luminosity era: Challenges on electronic systems*, Nucl. Instrum. Meth. A **1045** (2023) 167610 (cit. on p. 2).

- [26] ATLAS Collaboration, *Technical Design Report for the ATLAS Inner Tracker Pixel Detector*, tech. rep., CERN, 2017, URL: <https://cds.cern.ch/record/2285585> (cit. on pp. 2, 18).
- [27] ATLAS Collaboration, *Technical Design Report for the ATLAS Inner Tracker Strip Detector*, tech. rep., CERN, 2017, URL: <http://cds.cern.ch/record/2257755> (cit. on pp. 2, 18).
- [28] ATLAS Collaboration, *ATLAS Phase-II Upgrade Scoping Document*, CERN-LHCC-2015-020, LHCC-G-166, 2015, URL: <https://cds.cern.ch/record/2055248> (cit. on p. 2).
- [29] ATLAS Collaboration, *A High-Granularity Timing Detector for the ATLAS Phase-II Upgrade: Technical Design Report*, ATLAS-TDR-031; CERN-LHCC-2020-007, 2020, URL: <https://cds.cern.ch/record/2719855> (cit. on p. 2).
- [30] C. Allaire et al., *A high-granularity timing detector in ATLAS: Performance at the HL-LHC*, Nucl. Instrum. Meth. A **924** (2019) 355 (cit. on p. 2).
- [31] L. C. Garcia, *A High-Granularity Timing Detector for the Phase-II upgrade of the ATLAS Calorimeter system: detector concept, description, R&D and beam test results*, Journal of Instrumentation **15** (2020) C09047 (cit. on p. 3).
- [32] S. Ali et al., *Performance in beam tests of Carbon-enriched irradiated Low Gain Avalanche Detectors for the ATLAS High Granularity Timing Detector*, arXiv preprint arXiv:2303.07728 (2023) (cit. on p. 3).
- [33] S. Weinberg, *A Model of Leptons*, Phys. Rev. Lett. **19** (1967) 1264 (cit. on pp. 5, 6).
- [34] A. Salam, *Weak and Electromagnetic Interactions*, Conf. Proc. C **680519** (1968) 367 (cit. on pp. 5, 6).
- [35] S. L. Glashow, *Partial-symmetries of weak interactions*, Nuclear Physics **22** (1961) 579, ISSN: 0029-5582, URL: <http://www.sciencedirect.com/science/article/pii/0029558261904692> (cit. on pp. 5, 6).
- [36] D. Griffiths, *Introduction to elementary particles*, John Wiley & Sons, 2020 (cit. on p. 5).
- [37] M. Gell-Mann, *A Schematic Model of Baryons and Mesons*, Phys. Lett. **8** (1964) 214 (cit. on pp. 5, 6).
- [38] M. D. Schwartz, *Quantum Field Theory and the Standard Model*, Cambridge University Press, 2013, ISBN: 978-1-107-03473-0 (cit. on p. 5).
- [39] M. E. Peskin and D. V. Schroeder, *An Introduction to Quantum Field Theory*, Westview Press Reading, 1995, ISBN: 978-0-201-50397-5 (cit. on p. 5).
- [40] J. F. Donoghue, E. Golowich and B. R. Holstein, *Dynamics of the Standard Model*, Cambridge University Press, 1992, ISBN: 978-0-511-52437-0 (cit. on p. 5).
- [41] F. B. Englert, *R.(1964). Broken Symmetry and the Mass of Gauge Vector Mesons*, Physical Review Letters **13** () 321 (cit. on p. 6).
- [42] N. Cabibbo, *Unitary Symmetry and Leptonic Decays*, Physical Review Letters **10** (1963) 531 (cit. on p. 9).

Bibliography

- [43] J. Brod, M. Gorbahn and E. Stamou, *Standard-Model Prediction of ϵ_K with Manifest Quark-Mixing Unitarity*, [Phys. Rev. Lett. **125** \(2020\) 171803](#), arXiv: [1911.06822 \[hep-ph\]](#) (cit. on p. 10).
- [44] ATLAS Collaboration, *The ATLAS experiment at the CERN large hadron collider*, [JINST **3** \(2008\) S08003](#) (cit. on pp. 12–15).
- [45] tikz.net, *3D Axis CMS*, https://tikz.net/axis3d_cms/, Accessed: 2023-03-10, 2023 (cit. on p. 12).
- [46] A. La Rosa, *The ATLAS Insertable B-Layer: from construction to operation*, [JINST **11** \(2016\) C12036](#), ed. by C. Gemme and L. Rossi, arXiv: [1610.01994 \[physics.ins-det\]](#) (cit. on p. 13).
- [47] ATLAS Collaboration, *Operation and performance of the ATLAS semiconductor tracker in LHC Run 2*, [JINST **17** \(2022\) P01013](#), arXiv: [2109.02591 \[physics.ins-det\]](#) (cit. on p. 13).
- [48] E. Abat et al., *The ATLAS TRT barrel detector*, [JINST **3** \(2008\) P02014](#) (cit. on p. 13).
- [49] ATLAS Collaboration, ‘The ATLAS liquid argon calorimeter: An overview’, *Journal of Physics: Conference Series*, vol. 160, 1, IOP Publishing, 2009 012043 (cit. on p. 14).
- [50] R. McKenzie, *The ATLAS Tile Calorimeter performance and its upgrade towards the High Luminosity Large Hadron Collider*, [SciPost Phys. Proc. \(2022\) 171](#), URL: <https://scipost.org/10.21468/SciPostPhysProc.8.171> (cit. on p. 14).
- [51] B. Lefebvre, ‘Muon Spectrometer Phase-I Upgrade for the ATLAS Experiment: the New Small Wheel project’, *13th Conference on the Intersections of Particle and Nuclear Physics*, 2018, arXiv: [1810.01394 \[physics.ins-det\]](#) (cit. on p. 14).
- [52] ATLAS Collaboration, *Muon reconstruction performance of the ATLAS detector in proton–proton collision data at $\sqrt{s}=13$ TeV*, *The European Physical Journal C* **76** (2016) 1 (cit. on p. 15).
- [53] O. Brüning and L. Rossi, *The High Luminosity Large Hadron Collider: The New Machine for Illuminating the Mysteries of Universe*, Advanced Series on Directions in High Energy Physics, World Scientific Publishing Company Pte Limited, 2015, ISBN: 9789814675475, URL: <https://books.google.com/books?id=8pJEDwAAQBAJ> (cit. on p. 16).
- [54] ATLAS Collaboration, *Simulated HL-LHC collision event in the ATLAS detector*, General Photo, 2019, URL: <https://cds.cern.ch/record/2674770> (cit. on p. 18).
- [55] ATLAS Collaboration, *ATLAS Liquid Argon Calorimeter Phase-II Upgrade: Technical Design Report*, tech. rep., CERN, 2017, URL: <http://cds.cern.ch/record/2285582> (cit. on p. 18).
- [56] ATLAS Collaboration, *Technical Design Report for the Phase-II Upgrade of the ATLAS Tile Calorimeter*, tech. rep., CERN, 2017, URL: <http://cds.cern.ch/record/2285583> (cit. on p. 18).

- [57] ATLAS Collaboration, *Technical Design Report: A High-Granularity Timing Detector for the ATLAS Phase-II Upgrade*, tech. rep., CERN, 2020, URL: <http://cds.cern.ch/record/2719855> (cit. on pp. 18–22).
- [58] ATLAS Collaboration, *Technical Design Report for the Phase-II Upgrade of the ATLAS Muon Spectrometer*, tech. rep., CERN, 2017, URL: <http://cds.cern.ch/record/2285580> (cit. on p. 18).
- [59] ATLAS Collaboration, *Technical Design Report for the Phase-II Upgrade of the ATLAS TDAQ System*, tech. rep., CERN, 2017, URL: <http://cds.cern.ch/record/2285584> (cit. on p. 18).
- [60] *Technical Proposal: A High-Granularity Timing Detector for the ATLAS Phase-II Upgrade*, tech. rep., CERN, 2018, URL: <http://cds.cern.ch/record/2623663> (cit. on p. 18).
- [61] D. de Florian et al., *Handbook of LHC Higgs Cross Sections: 4. Deciphering the Nature of the Higgs Sector*, **2/2017 (2016)**, arXiv: [1610.07922 \[hep-ph\]](https://arxiv.org/abs/1610.07922) (cit. on pp. 25, 26).
- [62] C. Anastasiou et al., *High precision determination of the gluon fusion Higgs boson cross-section at the LHC*, *Journal of High Energy Physics* **2016 (2016)** 1 (cit. on p. 25).
- [63] P. Bolzoni, F. Maltoni, S.-O. Moch and M. Zaro, *Higgs Boson Production via Vector-Boson Fusion at Next-to-Next-to-Leading Order in QCD*, *Phys. Rev. Lett.* **105 (2010)** 011801, arXiv: [1003.4451 \[hep-ph\]](https://arxiv.org/abs/1003.4451) (cit. on pp. 26, 40).
- [64] O. Brein, A. Djouadi and R. Harlander, *NNLO QCD corrections to the Higgs-strahlung processes at hadron colliders*, *Physics Letters B* **579 (2004)** 149 (cit. on p. 26).
- [65] O. Brein, R. V. Harlander and T. J. Zirke, *vh@ nnlo—Higgs Strahlung at hadron colliders*, *Computer Physics Communications* **184 (2013)** 998 (cit. on p. 26).
- [66] M. Ciccolini, S. Dittmaier and M. Krämer, *Electroweak radiative corrections to associated WH and ZH production at hadron colliders*, *Physical Review D* **68 (2003)** 073003 (cit. on p. 26).
- [67] O. Brein, R. V. Harlander, M. Wiesemann and T. Zirke, *Top-quark mediated effects in hadronic Higgs-Strahlung*, *The European Physical Journal C* **72 (2012)** 1868 (cit. on p. 26).
- [68] LHC Higgs Working Group, *LHC Higgs Working Group: Higgs cross sections and decay branching ratios*, URL: https://twiki.cern.ch/twiki/bin/view/LHCPhysics/LHCHWG#Higgs_cross_sections_and_decay_b (cit. on pp. 27, 28).
- [69] CMS Collaboration, *Search for Higgs boson decays to a Z boson and a photon in proton proton collisions at $\sqrt{s}=13$ TeV*, arXiv preprint arXiv:2204.12945 (2022) (cit. on p. 27).
- [70] ATLAS Collaboration, *A search for the $Z\gamma$ decay mode of the Higgs boson in pp collisions at $\sqrt{s}=13$ TeV with the ATLAS detector*, *Physics Letters B* **809 (2020)** 135754 (cit. on p. 27).
- [71] CMS Collaboration, *A measurement of the Higgs boson mass in the diphoton decay channel*, *Phys. Lett. B* **805 (2020)** 135425, arXiv: [2002.06398 \[hep-ex\]](https://arxiv.org/abs/2002.06398) (cit. on p. 29).

Bibliography

- [72] ATLAS Collaboration, *Measurement of the Higgs boson mass in the $H \rightarrow ZZ^* \rightarrow 4\ell$ decay channel using 139 fb^{-1} of $\sqrt{s} = 13\text{ TeV}$ pp collisions recorded by the ATLAS detector at the LHC*, (2022), arXiv: [2207.00320 \[hep-ex\]](#) (cit. on pp. 29, 30).
- [73] ATLAS Collaboration, *Evidence of off-shell Higgs boson production from ZZ leptonic decay channels and constraints on its total width with the ATLAS detector*, (2023), arXiv: [2304.01532 \[hep-ex\]](#) (cit. on pp. 29, 30).
- [74] CMS Collaboration, *Measurement of the Higgs boson width and evidence of its off-shell contributions to ZZ production*, *Nature Phys.* **18** (2022) 1329, arXiv: [2202.06923 \[hep-ex\]](#) (cit. on p. 29).
- [75] ATLAS Collaboration, *Study of the spin and parity of the Higgs boson in diboson decays with the ATLAS detector*, *Eur. Phys. J. C* **75** (2015) 476, [Erratum: *Eur.Phys.J.C* 76, 152 (2016)], arXiv: [1506.05669 \[hep-ex\]](#) (cit. on p. 30).
- [76] CMS Collaboration, *Constraints on the spin-parity and anomalous HVV couplings of the Higgs boson in proton collisions at 7 and 8 TeV*, *Phys. Rev. D* **92** (2015) 012004, arXiv: [1411.3441 \[hep-ex\]](#) (cit. on p. 30).
- [77] D. Zeppenfeld, *Higgs couplings at the LHC*, eConf **C010630** (2001) P123, ed. by N. Graf, arXiv: [hep-ph/0203123](#) (cit. on p. 35).
- [78] A. Falkowski, S. Rychkov and A. Urbano, *What if the Higgs couplings to W and Z bosons are larger than in the Standard Model?*, *Journal of High Energy Physics* **2012** (2012) 1 (cit. on p. 35).
- [79] ATLAS Collaboration, *Study of $(W/Z)H$ production and Higgs boson couplings using $H \rightarrow WW^*$ decays with the ATLAS detector*, *JHEP* **08** (2015) 137, arXiv: [1506.06641 \[hep-ex\]](#) (cit. on p. 35).
- [80] CMS Collaboration, *Measurement of Higgs boson production and properties in the WW decay channel with leptonic final states*, *JHEP* **01** (2014) 096, arXiv: [1312.1129 \[hep-ex\]](#) (cit. on p. 35).
- [81] CMS Collaboration, *Measurements of the Higgs boson production cross section and couplings in the WW boson pair decay channel in proton–proton collisions at $\sqrt{s} = 13\text{ TeV}$* , (2022), arXiv: [2206.09466 \[hep-ex\]](#) (cit. on p. 35).
- [82] ATLAS Collaboration, *Measurement of the production cross section for a Higgs boson in association with a vector boson in the $H \rightarrow WW^* \rightarrow \ell\nu\ell\nu$ channel in pp collisions at $\sqrt{s} = 13\text{ TeV}$ with the ATLAS detector*, *Phys. Lett. B* **798** (2019) 134949, arXiv: [1903.10052 \[hep-ex\]](#) (cit. on p. 35).
- [83] ATLAS Collaboration, *Higgs boson production cross-section measurements and their EFT interpretation in the 4ℓ decay channel at $\sqrt{s} = 13\text{ TeV}$ with the ATLAS detector*, *Eur. Phys. J. C* **80** (2020) 957, arXiv: [2004.03447 \[hep-ex\]](#) (cit. on pp. 35, 53), Erratum: *Eur. Phys. J. C* **81** (2021) 29.

- [84] CMS Collaboration, *Measurements of production cross sections of the Higgs boson in the four-lepton final state in proton–proton collisions at $\sqrt{s} = 13$ TeV*, *Eur. Phys. J. C* **81** (2021) 488, arXiv: [2103.04956 \[hep-ex\]](#) (cit. on p. 35).
- [85] ATLAS Collaboration, *Measurement of the properties of Higgs boson production at $\sqrt{s} = 13$ TeV in the $H \rightarrow \gamma\gamma$ channel using 139 fb^{-1} of pp collision data with the ATLAS experiment*, (2022), arXiv: [2207.00348 \[hep-ex\]](#) (cit. on p. 35).
- [86] CMS Collaboration, *Measurements of Higgs boson production cross sections and couplings in the diphoton decay channel at $\sqrt{s} = 13$ TeV*, *JHEP* **07** (2021) 027, arXiv: [2103.06956 \[hep-ex\]](#) (cit. on p. 35).
- [87] ATLAS Collaboration, *Measurements of WH and ZH production in the $H \rightarrow b\bar{b}$ decay channel in pp collisions at 13 TeV with the ATLAS detector*, *Eur. Phys. J. C* **81** (2021) 178, arXiv: [2007.02873 \[hep-ex\]](#) (cit. on p. 35).
- [88] CMS Collaboration, *Observation of Higgs boson decay to bottom quarks*, *Phys. Rev. Lett.* **121** (2018) 121801, arXiv: [1808.08242 \[hep-ex\]](#) (cit. on p. 35).
- [89] ATLAS Collaboration, *Measurements of Higgs boson production cross-sections in the $H \rightarrow \tau^+\tau^-$ decay channel in pp collisions at $\sqrt{s} = 13$ TeV with the ATLAS detector*, *JHEP* **08** (2022) 175, arXiv: [2201.08269 \[hep-ex\]](#) (cit. on p. 35).
- [90] CMS Collaboration, *Measurements of Higgs boson production in the decay channel with a pair of τ leptons in proton-proton collisions at $\sqrt{s} = 13$ TeV*, (2022), arXiv: [2204.12957 \[hep-ex\]](#) (cit. on p. 35).
- [91] ATLAS Collaboration, *Direct constraint on the Higgs-charm coupling from a search for Higgs boson decays into charm quarks with the ATLAS detector*, *Eur. Phys. J. C* **82** (2022) 717, arXiv: [2201.11428 \[hep-ex\]](#) (cit. on p. 35).
- [92] CMS Collaboration, *Search for Higgs boson decay to a charm quark-antiquark pair in proton-proton collisions at $\sqrt{s} = 13$ TeV*, (2022), arXiv: [2205.05550 \[hep-ex\]](#) (cit. on p. 35).
- [93] G. Aad et al., *ATLAS data quality operations and performance for 2015–2018 data-taking*, *Journal of instrumentation* **15** (2020) (cit. on p. 37).
- [94] G. Aad et al., *Operation of the ATLAS trigger system in Run 2*, *JINST* **15** (2020) P10004, arXiv: [2007.12539 \[physics.ins-det\]](#) (cit. on p. 37).
- [95] The ATLAS Collaboration, *The ATLAS Experiment TDAQ Public Plots*, URL: <https://twiki.cern.ch/twiki/bin/view/AtlasPublic/ApprovedPlotsDAQ> (cit. on p. 38).
- [96] ATLAS Collaboration, *Luminosity Public Results Run 2*, <https://twiki.cern.ch/twiki/bin/view/AtlasPublic/LuminosityPublicResultsRun2>, 2019 (cit. on p. 38).
- [97] M. L. Ciccolini, S. Dittmaier and M. Krämer, *Electroweak radiative corrections to associated WH and ZH production at hadron colliders*, *Phys. Rev. D* **68** (2003) 073003, arXiv: [hep-ph/0306234 \[hep-ph\]](#) (cit. on pp. 39, 40).
- [98] O. Brein, A. Djouadi and R. Harlander, *NNLO QCD corrections to the Higgs-strahlung processes at hadron colliders*, *Phys. Lett. B* **579** (2004) 149, arXiv: [hep-ph/0307206](#) (cit. on pp. 39, 40).

Bibliography

- [99] O. Brein, R. V. Harlander, M. Wiesemann and T. Zirke,
Top-quark mediated effects in hadronic Higgs-Strahlung, [Eur. Phys. J. C **72** \(2012\) 1868](#),
arXiv: [1111.0761 \[hep-ph\]](#) (cit. on pp. 39, 40).
- [100] A. Denner, S. Dittmaier, S. Kallweit and A. Mück, *HAWK 2.0: A Monte Carlo program for Higgs production in vector-boson fusion and Higgs strahlung at hadron colliders*,
[Comput. Phys. Commun. **195** \(2015\) 161](#), arXiv: [1412.5390 \[hep-ph\]](#) (cit. on pp. 39, 40).
- [101] O. Brein, R. V. Harlander and T. J. E. Zirke, *vh@nnlo – Higgs Strahlung at hadron colliders*,
[Comput. Phys. Commun. **184** \(2013\) 998](#), arXiv: [1210.5347 \[hep-ph\]](#) (cit. on pp. 39, 40).
- [102] M. Bähr et al., *Herwig++ physics and manual*, [Eur. Phys. J. C **58** \(2008\) 639](#),
arXiv: [0803.0883 \[hep-ph\]](#) (cit. on p. 39).
- [103] J. Bellm et al., *Herwig 7.0/Herwig++ 3.0 release note*, [Eur. Phys. J. C **76** \(2016\) 196](#),
arXiv: [1512.01178 \[hep-ph\]](#) (cit. on p. 39).
- [104] L. Altenkamp, S. Dittmaier, R. V. Harlander, H. Rzehak and T. J. E. Zirke,
Gluon-induced Higgs-strahlung at next-to-leading order QCD, [JHEP **02** \(2013\) 078](#),
arXiv: [1211.5015 \[hep-ph\]](#) (cit. on pp. 39, 40).
- [105] R. V. Harlander, A. Kulesza, V. Theeuwes and T. Zirke,
Soft gluon resummation for gluon-induced Higgs Strahlung, [JHEP **11** \(2014\) 082](#),
arXiv: [1410.0217 \[hep-ph\]](#) (cit. on pp. 39, 40).
- [106] S. Actis, G. Passarino, C. Sturm and S. Uccirati,
NLO electroweak corrections to Higgs boson production at hadron colliders,
[Phys. Lett. B **670** \(2008\) 12](#), arXiv: [0809.1301 \[hep-ph\]](#) (cit. on pp. 39, 40).
- [107] M. Bonetti, K. Melnikov and L. Tancredi, *Higher order corrections to mixed QCD-EW contributions to Higgs boson production in gluon fusion*, [Phys. Rev. D **97** \(2018\) 056017](#),
arXiv: [1801.10403 \[hep-ph\]](#) (cit. on pp. 39, 40), Erratum: [Phys. Rev. D **97** \(2018\) 099906](#).
- [108] F. Dulat, A. Lazopoulos and B. Mistlberger, *iHixs 2 – Inclusive Higgs cross sections*,
[Comput. Phys. Commun. **233** \(2018\) 243](#), arXiv: [1802.00827 \[hep-ph\]](#) (cit. on pp. 39, 40).
- [109] S. Actis, G. Passarino, C. Sturm and S. Uccirati,
NNLO computational techniques: The cases $H \rightarrow \gamma\gamma$ and $H \rightarrow gg$,
[Nucl. Phys. B **811** \(2009\) 182](#), arXiv: [0809.3667 \[hep-ph\]](#) (cit. on pp. 39, 40).
- [110] R. V. Harlander and K. J. Ozeren, *Top mass effects in Higgs production at next-to-next-to-leading order QCD: Virtual corrections*, [Phys. Lett. B **679** \(2009\) 467](#),
arXiv: [0907.2997 \[hep-ph\]](#) (cit. on pp. 39, 40).
- [111] R. V. Harlander and K. J. Ozeren,
Finite top mass effects for hadronic Higgs production at next-to-next-to-leading order,
[JHEP **11** \(2009\) 088](#), arXiv: [0909.3420 \[hep-ph\]](#) (cit. on pp. 39, 40).
- [112] A. Pak, M. Rogal and M. Steinhauser,
Finite top quark mass effects in NNLO Higgs boson production at LHC, [JHEP **02** \(2010\) 025](#),
arXiv: [0911.4662 \[hep-ph\]](#) (cit. on pp. 39, 40).
- [113] R. V. Harlander, H. Mantler, S. Marzani and K. J. Ozeren,
Higgs production in gluon fusion at next-to-next-to-leading order QCD for finite top mass,
[Eur. Phys. J. C **66** \(2010\) 359](#), arXiv: [0912.2104 \[hep-ph\]](#) (cit. on pp. 39, 40).

- [114] C. Anastasiou, C. Duhr, F. Dulat, F. Herzog and B. Mistlberger, *Higgs Boson Gluon-Fusion Production in QCD at Three Loops*, *Phys. Rev. Lett.* **114** (2015) 212001, arXiv: [1503.06056 \[hep-ph\]](#) (cit. on pp. 39, 40).
- [115] D. de Florian et al., *Handbook of LHC Higgs Cross Sections: 4. Deciphering the Nature of the Higgs Sector*, (2016), arXiv: [1610.07922 \[hep-ph\]](#) (cit. on pp. 39, 40, 74).
- [116] C. Anastasiou et al., *High precision determination of the gluon fusion Higgs boson cross-section at the LHC*, *JHEP* **05** (2016) 058, arXiv: [1602.00695 \[hep-ph\]](#) (cit. on pp. 39, 40).
- [117] M. Ciccolini, A. Denner and S. Dittmaier, *Strong and Electroweak Corrections to the Production of a Higgs Boson + 2 Jets via Weak Interactions at the Large Hadron Collider*, *Phys. Rev. Lett.* **99** (2007) 161803, arXiv: [0707.0381 \[hep-ph\]](#) (cit. on pp. 39, 40).
- [118] M. Ciccolini, A. Denner and S. Dittmaier, *Electroweak and QCD corrections to Higgs production via vector-boson fusion at the CERN LHC*, *Phys. Rev. D* **77** (2008) 013002, arXiv: [0710.4749 \[hep-ph\]](#) (cit. on pp. 39, 40).
- [119] P. Bolzoni et al., *Higgs production via vector-boson fusion at NNLO in QCD*, *Phys. Rev. Lett.* **105** (2010), arXiv: [1003.4451 \[hep-ph\]](#) (cit. on p. 39).
- [120] C. Anastasiou, L. Dixon, K. Melnikov and F. Petriello, *High-precision QCD at hadron colliders: Electroweak gauge boson rapidity distributions at next-to-next-to leading order*, *Phys. Rev. D* **69** (2004) 094008, arXiv: [hep-ph/0312266](#) (cit. on p. 39).
- [121] F. Buccioni et al., *OpenLoops 2*, *Eur. Phys. J. C* **79** (2019) 866, arXiv: [1907.13071 \[hep-ph\]](#) (cit. on p. 39).
- [122] F. Cascioli, P. Maierhöfer and S. Pozzorini, *Scattering Amplitudes with Open Loops*, *Phys. Rev. Lett.* **108** (2012) 111601, arXiv: [1111.5206 \[hep-ph\]](#) (cit. on p. 39).
- [123] A. Denner, S. Dittmaier and L. Hofer, *COLLIER: A fortran-based complex one-loop library in extended regularizations*, *Comput. Phys. Commun.* **212** (2017) 220, arXiv: [1604.06792 \[hep-ph\]](#) (cit. on p. 39).
- [124] F. Cascioli et al., *Precise Higgs-background predictions: merging NLO QCD and squared quark-loop corrections to four-lepton + 0,1 jet production*, *JHEP* **01** (2014) 046, arXiv: [1309.0500 \[hep-ph\]](#) (cit. on p. 39).
- [125] F. Caola, K. Melnikov, R. Röntschi and L. Tancredi, *QCD corrections to W^+W^- production through gluon fusion*, *Phys. Lett. B* **754** (2016) 275, arXiv: [1511.08617 \[hep-ph\]](#) (cit. on p. 39).
- [126] M. Grazzini, S. Kallweit, M. Wiesemann and J. Y. Yook, *ZZ production at the LHC: NLO QCD corrections to the loop-induced gluon fusion channel*, *JHEP* **03** (2019) 070, arXiv: [1811.09593 \[hep-ph\]](#) (cit. on p. 39).
- [127] T. Binoth, G. Ossola, C. G. Papadopoulos and R. Pittau, *NLO QCD corrections to tri-boson production*, *JHEP* **06** (2008) 082, arXiv: [0804.0350 \[hep-ph\]](#) (cit. on p. 39).

Bibliography

- [128] M. Beneke, P. Falgari, S. Klein and C. Schwinn, *Hadronic top-quark pair production with NNLL threshold resummation*, [Nucl. Phys. B **855** \(2012\) 695](#), arXiv: [1109.1536 \[hep-ph\]](#) (cit. on p. 39).
- [129] M. Cacciari, M. Czakon, M. Mangano, A. Mitov and P. Nason, *Top-pair production at hadron colliders with next-to-next-to-leading logarithmic soft-gluon resummation*, [Phys. Lett. B **710** \(2012\) 612](#), arXiv: [1111.5869 \[hep-ph\]](#) (cit. on p. 39).
- [130] P. Bärnreuther, M. Czakon and A. Mitov, *Percent-Level-Precision Physics at the Tevatron: Next-to-Next-to-Leading Order QCD Corrections to $q\bar{q} \rightarrow t\bar{t} + X$* , [Phys. Rev. Lett. **109** \(2012\) 132001](#), arXiv: [1204.5201 \[hep-ph\]](#) (cit. on p. 39).
- [131] M. Czakon and A. Mitov, *NNLO corrections to top-pair production at hadron colliders: the all-fermionic scattering channels*, [JHEP **12** \(2012\) 054](#), arXiv: [1207.0236 \[hep-ph\]](#) (cit. on p. 39).
- [132] M. Czakon and A. Mitov, *NNLO corrections to top pair production at hadron colliders: the quark-gluon reaction*, [JHEP **01** \(2013\) 080](#), arXiv: [1210.6832 \[hep-ph\]](#) (cit. on p. 39).
- [133] M. Czakon, P. Fiedler and A. Mitov, *Total Top-Quark Pair-Production Cross Section at Hadron Colliders Through $O(\alpha_s^4)$* , [Phys. Rev. Lett. **110** \(2013\) 252004](#), arXiv: [1303.6254 \[hep-ph\]](#) (cit. on p. 39).
- [134] M. Czakon and A. Mitov, *Top++: A program for the calculation of the top-pair cross-section at hadron colliders*, [Comput. Phys. Commun. **185** \(2014\) 2930](#), arXiv: [1112.5675 \[hep-ph\]](#) (cit. on p. 39).
- [135] N. Kidonakis, *Two-loop soft anomalous dimensions for single top quark associated production with a W^- or H^-* , [Phys. Rev. D **82** \(2010\) 054018](#), arXiv: [1005.4451 \[hep-ph\]](#) (cit. on p. 39).
- [136] N. Kidonakis, ‘Top Quark Production’, *Proceedings, Helmholtz International Summer School on Physics of Heavy Quarks and Hadrons (HQ 2013)* (JINR, Dubna, Russia, 15th–28th July 2013) 139, arXiv: [1311.0283 \[hep-ph\]](#) (cit. on p. 39).
- [137] A. Broggio et al., *Top-quark pair hadroproduction in association with a heavy boson at NLO+NNLL including EW corrections*, [JHEP **08** \(2019\) 039](#), arXiv: [1907.04343 \[hep-ph\]](#) (cit. on p. 39).
- [138] J. Campbell, R. K. Ellis and R. Röntsch, *Single top production in association with a Z boson at the LHC*, [Phys. Rev. D **87** \(2013\) 114006](#), arXiv: [1302.3856 \[hep-ph\]](#) (cit. on p. 39).
- [139] F. Maltoni, L. Mantani and K. Mimasu, *Top-quark electroweak interactions at high energy*, [JHEP **10** \(2019\) 004](#), arXiv: [1904.05637 \[hep-ph\]](#) (cit. on p. 39).
- [140] ATLAS and CMS Collaborations, *Combined Measurement of the Higgs Boson Mass in pp Collisions at $\sqrt{s} = 7$ and 8 TeV with the ATLAS and CMS Experiments*, [Phys. Rev. Lett. **114** \(2015\) 191803](#), arXiv: [1503.07589 \[hep-ex\]](#) (cit. on p. 39).
- [141] J. Butterworth et al., *PDF4LHC recommendations for LHC Run II*, [J. Phys. **G43** \(2016\)](#), arXiv: [1510.03865 \[hep-ph\]](#) (cit. on p. 39).

- [142] T. Sjöstrand et al., *An introduction to PYTHIA 8.2*, *Comput. Phys. Commun.* **191** (2015) 159, arXiv: [1410.3012 \[hep-ph\]](#) (cit. on p. 39).
- [143] ATLAS Collaboration, *Measurement of the Z/γ^* boson transverse momentum distribution in pp collisions at $\sqrt{s} = 7$ TeV with the ATLAS detector*, *JHEP* **09** (2014) 145, arXiv: [1406.3660 \[hep-ex\]](#) (cit. on p. 39).
- [144] ATLAS Collaboration, *ATLAS Pythia 8 tunes to 7 TeV data*, ATL-PHYS-PUB-2014-021, 2014, URL: <https://cds.cern.ch/record/1966419> (cit. on p. 40).
- [145] P. Nason, *A new method for combining NLO QCD with shower Monte Carlo algorithms*, *JHEP* **11** (2004) 040, arXiv: [hep-ph/0409146](#) (cit. on p. 40).
- [146] S. Frixione, P. Nason and C. Oleari, *Matching NLO QCD computations with parton shower simulations: the POWHEG method*, *JHEP* **11** (2007) 070, arXiv: [0709.2092 \[hep-ph\]](#) (cit. on p. 40).
- [147] S. Alioli, P. Nason, C. Oleari and E. Re, *A general framework for implementing NLO calculations in shower Monte Carlo programs: the POWHEG BOX*, *JHEP* **06** (2010) 043, arXiv: [1002.2581 \[hep-ph\]](#) (cit. on p. 40).
- [148] G. Luisoni, P. Nason, C. Oleari and F. Tramontano, *$HW^\pm/HZ + 0$ and 1 jet at NLO with the POWHEG BOX interfaced to GoSam and their merging within MiNLO*, *JHEP* **10** (2013) 083, arXiv: [1306.2542 \[hep-ph\]](#) (cit. on p. 40).
- [149] K. Hamilton, P. Nason, E. Re and G. Zanderighi, *NNLOPS simulation of Higgs boson production*, *JHEP* **10** (2013) 222, arXiv: [1309.0017 \[hep-ph\]](#) (cit. on p. 40).
- [150] P. Nason and C. Oleari, *NLO Higgs boson production via vector-boson fusion matched with shower in POWHEG*, *JHEP* **02** (2010) 037, arXiv: [0911.5299 \[hep-ph\]](#) (cit. on p. 40).
- [151] S. Frixione, G. Ridolfi and P. Nason, *A positive-weight next-to-leading-order Monte Carlo for heavy flavour hadroproduction*, *JHEP* **09** (2007) 126, arXiv: [0707.3088 \[hep-ph\]](#) (cit. on p. 40).
- [152] H. B. Hartanto, B. Jäger, L. Reina and D. Wackerroth, *Higgs boson production in association with top quarks in the POWHEG BOX*, *Phys. Rev. D* **91** (2015) 094003, arXiv: [1501.04498 \[hep-ph\]](#) (cit. on p. 40).
- [153] S. Agostinelli et al., *Geant4—a simulation toolkit*, *NIM A* **506** (2003) (cit. on p. 40).
- [154] ATLAS Collaboration, *The ATLAS Collaboration Software and Firmware*, ATL-SOFT-PUB-2021-001, 2021, URL: <https://cds.cern.ch/record/2767187> (cit. on p. 40).
- [155] R. D. Ball et al., *Parton distributions for the LHC Run II*, *JHEP* **04** (2015), arXiv: [1410.8849 \[hep-ph\]](#) (cit. on p. 40).
- [156] ATLAS Collaboration, *The Pythia 8 A3 tune description of ATLAS minimum bias and inelastic measurements incorporating the Donnachie–Landshoff diffractive model*, ATL-PHYS-PUB-2016-017, 2016, URL: <https://cds.cern.ch/record/2206965> (cit. on p. 40).

Bibliography

- [157] ATLAS Collaboration, *Electron efficiency measurements with the ATLAS detector using the 2015 LHC proton–proton collision data*, ATLAS-CONF-2016-024, 2016, URL: <https://cds.cern.ch/record/2157687> (cit. on p. 41).
- [158] ATLAS Collaboration, *Electron and photon performance measurements with the ATLAS detector using the 2015–2017 LHC proton-proton collision data*, *JINST* **14** (2019) P12006, arXiv: [1908.00005 \[hep-ex\]](#) (cit. on pp. 40, 46, 64).
- [159] ATLAS Collaboration, *Muon reconstruction and identification efficiency in ATLAS using the full Run 2 pp collision data set at $\sqrt{s} = 13$ TeV*, *Eur. Phys. J. C* **81** (2021) 578, arXiv: [2012.00578 \[hep-ex\]](#) (cit. on pp. 41, 64).
- [160] M. Cacciari, G. P. Salam and G. Soyez, *The anti- k_t jet clustering algorithm*, *JHEP* **04** (2008) 063, arXiv: [0802.1189 \[hep-ph\]](#) (cit. on p. 41).
- [161] M. Cacciari, G. P. Salam and G. Soyez, *FastJet user manual*, *Eur. Phys. J. C* **72** (2012) 1896, arXiv: [1111.6097 \[hep-ph\]](#) (cit. on p. 41).
- [162] ATLAS Collaboration, *Jet reconstruction and performance using particle flow with the ATLAS Detector*, *Eur. Phys. J. C* **77** (2017) 466, arXiv: [1703.10485 \[hep-ex\]](#) (cit. on p. 41).
- [163] ATLAS Collaboration, *Jet energy scale and resolution measured in proton–proton collisions at $\sqrt{s} = 13$ TeV with the ATLAS detector*, *Eur. Phys. J. C* **81** (2020) 689, arXiv: [2007.02645 \[hep-ex\]](#) (cit. on pp. 41, 64).
- [164] ATLAS Collaboration, *ATLAS b-jet identification performance and efficiency measurement with $t\bar{t}$ events in pp collisions at $\sqrt{s} = 13$ TeV*, *Eur. Phys. J. C* **79** (2019) 970, arXiv: [1907.05120 \[hep-ex\]](#) (cit. on pp. 41, 64).
- [165] ATLAS Collaboration, *Optimisation and performance studies of the ATLAS b-tagging algorithms for the 2017-18 LHC run*, ATL-PHYS-PUB-2017-013, 2017, URL: <https://cds.cern.ch/record/2273281> (cit. on p. 41).
- [166] ATLAS Collaboration, *Performance of missing transverse momentum reconstruction with the ATLAS detector using proton–proton collisions at $\sqrt{s} = 13$ TeV*, *Eur. Phys. J. C* **78** (2018) 903, arXiv: [1802.08168 \[hep-ex\]](#) (cit. on pp. 42, 64).
- [167] ATLAS Collaboration, *Object-based missing transverse momentum significance in the ATLAS Detector*, ATLAS-CONF-2018-038, 2018, URL: <https://cds.cern.ch/record/2630948> (cit. on p. 42).
- [168] ATLAS Collaboration, *Vertex Reconstruction Performance of the ATLAS Detector at $\sqrt{s} = 13$ TeV*, ATL-PHYS-PUB-2015-026, 2015, URL: <https://cds.cern.ch/record/2037717> (cit. on p. 42).
- [169] F. Chollet et al., *Keras*, 2015, URL: <https://keras.io> (cit. on p. 42).
- [170] M. Abadi et al., ‘TensorFlow: A System for Large-Scale Machine Learning’, *12th USENIX Symposium on Operating Systems Design and Implementation (OSDI 16)*, 2016 265, arXiv: [1605.08695 \[cs.DC\]](#) (cit. on pp. 42, 43).

- [171] A. Hoecker et al., *TMVA - Toolkit for Multivariate Data Analysis*, (2008), arXiv: [physics/0703039 \[physics.data-an\]](#) (cit. on pp. 42, 54).
- [172] ATLAS Collaboration, *Measurements of Higgs boson production by gluon–gluon fusion and vector-boson fusion using $H \rightarrow WW^* \rightarrow e\nu\mu\nu$ decays in pp collisions at $\sqrt{s} = 13$ TeV with the ATLAS detector*, (2022), arXiv: [2207.00338 \[hep-ex\]](#) (cit. on p. 43).
- [173] F. Chollet et al., *Keras*, <https://keras.io>, 2015 (cit. on p. 43).
- [174] T. Plehn, D. L. Rainwater and D. Zeppenfeld, *Method for identifying $H \rightarrow \tau^+\tau^- \rightarrow e^\pm\mu^\mp p_T$ at the CERN LHC*, *Phys. Rev. D* **61** (2000) 093005, arXiv: [hep-ph/9911385](#) (cit. on pp. 44, 53).
- [175] S. Hochreiter and J. Schmidhuber, *Long Short-Term Memory*, *Neural Comput.* **9** (1997) 1735, ISSN: 0899-7667 (cit. on p. 47).
- [176] ATLAS Collaboration, *Observation of WWW Production in pp Collisions at $\sqrt{s} = 13$ TeV with the ATLAS Detector*, *Phys. Rev. Lett.* **129** (2022) 061803, arXiv: [2201.13045 \[hep-ex\]](#) (cit. on p. 58).
- [177] ATLAS Collaboration, *Electron and photon energy calibration with the ATLAS detector using 2015–2016 LHC proton–proton collision data*, *JINST* **14** (2019) P03017, arXiv: [1812.03848 \[hep-ex\]](#) (cit. on p. 64).
- [178] ATLAS Collaboration, *Muon reconstruction performance of the ATLAS detector in proton–proton collision data at $\sqrt{s} = 13$ TeV*, *Eur. Phys. J. C* **76** (2016) 292, arXiv: [1603.05598 \[hep-ex\]](#) (cit. on p. 64).
- [179] ATLAS Collaboration, *Performance of electron and photon triggers in ATLAS during LHC Run 2*, *Eur. Phys. J. C* **80** (2020) 47, arXiv: [1909.00761 \[hep-ex\]](#) (cit. on p. 64).
- [180] ATLAS Collaboration, *Performance of the ATLAS muon triggers in Run 2*, *JINST* **15** (2020) P09015, arXiv: [2004.13447 \[physics.ins-det\]](#) (cit. on p. 64).
- [181] G. Avoni et al., *The new LUCID-2 detector for luminosity measurement and monitoring in ATLAS*, *JINST* **13** (2018) P07017 (cit. on p. 64).
- [182] ATLAS Collaboration, *Luminosity determination in pp collisions at $\sqrt{s} = 13$ TeV using the ATLAS detector at the LHC*, ATLAS-CONF-2019-021, 2019, URL: <https://cds.cern.ch/record/2677054> (cit. on p. 64).
- [183] S. Höche, F. Krauss, M. Schönherr and F. Siegert, *QCD matrix elements + parton showers. The NLO case*, *JHEP* **04** (2013) 027, arXiv: [1207.5030 \[hep-ph\]](#) (cit. on p. 65).
- [184] S. Schumann and F. Krauss, *A parton shower algorithm based on Catani–Seymour dipole factorisation*, *JHEP* **03** (2008) 038, arXiv: [0709.1027 \[hep-ph\]](#) (cit. on p. 65).
- [185] S. Hoeche, S. Schumann and F. Siegert, *Hard photon production and matrix-element parton-shower merging*, *Phys. Rev. D* **81** (2010) 034026, arXiv: [0912.3501 \[hep-ph\]](#) (cit. on p. 65).

Bibliography

- [186] G. Cowan, K. Cranmer, E. Gross and O. Vitells,
Asymptotic formulae for likelihood-based tests of new physics, *Eur. Phys. J. C* **71** (2011) 1554,
arXiv: [1007.1727 \[physics.data-an\]](https://arxiv.org/abs/1007.1727) (cit. on pp. 68, 70),
Erratum: *Eur. Phys. J. C* **73** (2013) 2501.
- [187] ATLAS Collaboration, *Search for the $b\bar{b}$ decay of the Standard Model Higgs boson in associated (W/Z) H production with the ATLAS detector*,
Journal of High Energy Physics **2015** (2015) 69 (cit. on p. 68).
- [188] F. Hartmann, *Evolution of Silicon Sensor Technology in Particle Physics*, vol. 275,
Springer Tracts in Modern Physics, Springer, 2017,
ISBN: 978-3-319-64434-9, 978-3-319-64436-3 (cit. on pp. 83, 92, 112, 166).
- [189] L. Rossi, P. Fischer, T. Rohe and N. Wermes,
Pixel Detectors: From Fundamentals to Applications, Particle Acceleration and Detection,
Springer Berlin Heidelberg, 2006, ISBN: 9783540283331,
URL: <https://books.google.nl/books?id=AKGIXQOm0-EC>
(cit. on pp. 83, 129, 147, 150).
- [190] G. Kramberger, *Signal development in irradiated silicon detectors*,
PhD thesis: Stefan Inst., Ljubljana, 2001 (cit. on pp. 83, 188).
- [191] B. J. Baliga, *Fundamentals of power semiconductor devices*,
Springer Science & Business Media, 2010 (cit. on pp. 85, 86, 110, 111).
- [192] *What is an SiPM and how does it work?*,
<https://hub.hamamatsu.com/us/en/technical-notes/mppc-sipms/what-is-an-SiPM-and-how-does-it-work.html>, Accessed: 2023-03-10, 2023 (cit. on p. 85).
- [193] S. Ramo, *Currents induced by electron motion*, *Proceedings of the IRE* **27** (1939) 584
(cit. on p. 88).
- [194] F. Cenna et al., *Weightfield2: A fast simulator for silicon and diamond solid state detector*,
Nucl. Instrum. Meth. A **796** (2015) 149 (cit. on pp. 89, 97, 98).
- [195] V. A. Van Lint, T. Flanagan, R. Leadon and J. A. Naber,
Mechanisms of radiation effects in electronic materials. Vol. 1, (1980) (cit. on p. 91).
- [196] A. International, ‘ASTM E722-14, Standard Practice for Characterizing Neutron Fluence Spectra in Terms of an Equivalent Monoenergetic Neutron Fluence for Radiation-Hardness Testing of Electronics’, 2014 (cit. on p. 91).
- [197] M. Moll, *Radiation damage in silicon particle detectors: Microscopic defects and macroscopic properties*, PhD thesis: Hamburg U., 1999 (cit. on p. 92).
- [198] H. F.-W. Sadrozinski, *Charge Multiplication in Si Sensors*,
<https://indico.cern.ch/event/265941/contributions/1601822/>,
Accessed: 2023-03-10, 2013 (cit. on p. 95).
- [199] G. Pellegrini et al., *Technology developments and first measurements of Low Gain Avalanche Detectors (LGAD) for high energy physics applications*,
Nucl. Instrum. Meth. A **765** (2014) 12 (cit. on pp. 95, 107).

- [200] X. Yang et al., *Layout and performance of HPK prototype LGAD sensors for the High-Granularity Timing Detector*, Nucl. Instrum. Meth. A **980** (2020) 164379 (cit. on pp. 95, 172).
- [201] G. Paternoster et al., *Developments and first measurements of Ultra-Fast Silicon Detectors produced at FBK*, Journal of Instrumentation **12** (2017) C02077 (cit. on p. 95).
- [202] N. Moffat et al., *Low Gain Avalanche Detectors (LGAD) for particle physics and synchrotron applications*, Journal of Instrumentation **13** (2018) C03014 (cit. on p. 95).
- [203] G. Giacomini, W. Chen, F. Lanni and A. Tricoli, *Development of a technology for the fabrication of Low-Gain Avalanche Diodes at BNL*, Nucl. Instrum. Meth. A **934** (2019) 52 (cit. on pp. 95, 107).
- [204] Y. Fan et al., *Radiation hardness of the low gain avalanche diodes developed by NDL and IHEP in China*, Nuclear Instruments and Methods in Physics Research Section A: Accelerators, Spectrometers, Detectors and Associated Equipment **984** (2020) 164608 (cit. on p. 95).
- [205] K. Wu et al., *Design of Low Gain Avalanche Detectors (LGAD) with 400 keV ion implantation energy for multiplication layer fabrication*, Nuclear Instruments and Methods in Physics Research Section A: Accelerators, Spectrometers, Detectors and Associated Equipment **984** (2020) 164558 (cit. on p. 95).
- [206] H. F. Sadrozinski, A. Seiden and N. Cartiglia, *4D tracking with ultra-fast silicon detectors*, Reports on Progress in Physics **81** (2017) 026101 (cit. on pp. 96, 98).
- [207] R. McIntyre, *Multiplication noise in uniform avalanche diodes*, IEEE Transactions on Electron Devices (1966) 164 (cit. on p. 96).
- [208] Y. Gurinskaya et al., *Radiation damage in p-type EPI silicon pad diodes irradiated with protons and neutrons*, Nuclear Instruments and Methods in Physics Research Section A: Accelerators, Spectrometers, Detectors and Associated Equipment **958** (2020) 162221 (cit. on pp. 100, 102).
- [209] M. Moll, *SISSA: Acceptor removal-Displacement damage effects involving the shallow acceptor doping of p-type silicon devices*, PoS (2020) 027 (cit. on pp. 100, 102).
- [210] M. Ferrero et al., *Radiation resistant LGAD design*, Nuclear Instruments and Methods in Physics Research Section A: Accelerators, Spectrometers, Detectors and Associated Equipment **919** (2019) 16 (cit. on p. 101).
- [211] A. S. Nicolo Cartiglia Hartmut Sadrozinski, 'The effect of temperature and irradiation on the LGAD gain mechanism', The 34th RD50 Workshop, 2019, URL: <https://indico.cern.ch/event/812761/contributions/3459057/> (cit. on p. 101).
- [212] J. F. Ziegler and J. P. Biersack, *The stopping and range of ions in matter*, Springer, 1985 (cit. on p. 101).

Bibliography

- [213] G. Laštovička-Medin et al., *Studies of LGAD performance limitations, Single Event Burnout and Gain Suppression, with Femtosecond-Laser and Ion Beams*, Nuclear Instruments and Methods in Physics Research Section A: Accelerators, Spectrometers, Detectors and Associated Equipment **1041** (2022) 167388 (cit. on pp. 102, 103).
- [214] G. Pellegrini et al., *Recent technological developments on LGAD and iLGAD detectors for tracking and timing applications*, Nucl. Instrum. Meth. A **831** (2016) 24 (cit. on pp. 104, 107).
- [215] G. Paternoster et al., *Trench-isolated low gain avalanche diodes (ti-lgads)*, IEEE Electron Device Letters **41** (2020) 884 (cit. on p. 104).
- [216] G. Paternoster et al., *Novel strategies for fine-segmented low gain avalanche diodes*, Nucl. Instrum. Meth. A **987** (2021) 164840 (cit. on p. 104).
- [217] Y. Zhao et al., ‘A new approach to achieving high granularity for silicon diode detectors with impact ionization gain’, *Journal of Physics: Conference Series*, vol. 2374, 1, IOP Publishing, 2022 012171 (cit. on p. 105).
- [218] G. Giacomini, W. Chen, G. D’Amen and A. Tricoli, *Fabrication and performance of AC-coupled LGADs*, Journal of Instrumentation **14** (2019) P09004 (cit. on p. 105).
- [219] K. Nakamura, S. Kita, T. Ueda, K. Hara and H. Suzuki, ‘First prototype of finely segmented HPK AC-LGAD detectors’, *Proceedings of the 29th International Workshop on Vertex Detectors (VERTEX2020)*, 2021 010016 (cit. on p. 105).
- [220] P. Fernández-Martínez et al., *Design and fabrication of an optimum peripheral region for low gain avalanche detectors*, Nucl. Instrum. Meth. A **821** (2016) 93 (cit. on p. 107).
- [221] M. Carulla et al., *50 μ m thin Low Gain Avalanche Detectors (LGAD) for timing applications*, Nucl. Instrum. Meth. A **924** (2019) 373 (cit. on p. 108).
- [222] G. Giacomini, L. Bosisio and I. Rashevskaya, *Measurement of Johnson noise induced by p-stops in silicon microstrip detectors*, IEEE Transactions on Nuclear Science **60** (2013) 4022 (cit. on p. 109).
- [223] *Power Semiconductor Device Electric Field Optimization Technology*, University of Electronic Science and Technology Press, 2015, ISBN: 9787564732622, URL: <https://books.google.com/books?id=CjNDzAEACAAJ> (cit. on p. 110).
- [224] S. Inc., *Sentaurus Device User Guide*, **Version M-2016.12** (2016) (cit. on pp. 113, 115).
- [225] E. Curras Rivera and M. Moll, *Study of impact ionization coefficients in silicon with Low Gain Avalanche Diodes*, (2022), arXiv: [2211.16543](https://arxiv.org/abs/2211.16543) [physics.ins-det] (cit. on p. 115).
- [226] IME,CAS, *Institute of Microelectronics of the Chinese Academy of Sciences*, URL: <http://english.ime.cas.cn/> (cit. on p. 135).

- [227] H. Föll, *Spiking and Epitaxial Si in Contact Holes*,
https://www.tf.uni-kiel.de/matwis/amat/elmat_en/, Accessed: 2023-03-10,
2019 (cit. on p. 150).
- [228] J. Ge et al., *Digital switch boards for IV and CV measurements of large-array Low Gain Avalanche Detectors*, Nucl. Instrum. Meth. A **1005** (2021) 165400 (cit. on pp. 161, 164, 165).
- [229] A. Chilingarov,
Recommendations towards a standardization of the macroscopic parameter measurements,
2009 (cit. on p. 166).
- [230] J. Ge et al., *An ultra-fast low-noise preamplifier for Low Gain Avalanche Detectors*,
Nucl. Instrum. Meth. A **1040** (2022) 167222 (cit. on pp. 168, 209).
- [231] H. Jansen et al., *Performance of the EUDET-type beam telescopes*,
EPJ Techniques and Instrumentation **3** (2016) 1 (cit. on p. 181).
- [232] University of Science and Technology of China,
USTC Center for Micro and Nanoscale Research and Fabrication,
URL: <http://nano.ustc.edu.cn/> (cit. on p. 203).